UNIVERSITY OF GLAMORGAN

Faculty of Advanced Technology

Department of Engineering

THE EFFECT OF IMPACT DAMAGE ON THE FATIGUE LIFE OF STEEL

by

Suzanne Louise Thomas

MEng, BEng (Hons), PGCE, AMIMechE

This thesis is submitted in partial fulfilment of the requirements of the University of Glamorgan/Prifysgol Morgannwg for the degree of

Doctor of Philosophy

October 2008

CERTIFICATE OF RESEARCH

This is to certify that, apart from where specific reference to other publications is made, the work presented in this thesis is the result of the investigations undertaken by the candidate.

S. L. Thomas

S. L. Thomas
(Candidate)

12/11/08
(Date)

Rae S Gord

Dr. R. S. Gordon
(Director of Studies)

12/11/08
(Date)

K. L. Fra

Dr. K. L. Franklin
(Supervisor)

12/11/08
(Date)

S J. Wilcox

Professor S. J. Wilcox
(Supervisor)

12th November 2008
(Date)

DECLARATION

I declare that neither this thesis, nor any part of it, has been submitted in candidature for any degree at any other academic institution.

S. L. Thomas

S. L. Thomas
(Candidate)

12/11/08

(Date)

DEDICATION

To Paul and to my mum and dad

ACKNOWLEDGEMENTS

I am indebted to many people who have helped me during the course of this study. First of all, I wish to record my gratitude to my Director of Studies, Dr Rae Gordon and also my supervisors, Dr Kathryn Franklin and Professor Steven Wilcox, for their guidance and supervision throughout all my academic studies. Their wisdom, experience and professionalism have been truly inspirational.

I am also very grateful to the staff of the laboratories, in particular Mr Gareth Betteney, Mr Brian Huish, Mr Paul Marshman, Mr Clive Monks, Mr Robert Watkins, Mr Edward Watts and Mr Huw Williams for their assistance in manufacturing and experimental work.

I would also like to thank Mr Clive Bennett and Mr Terry Powell for their assistance in document preparation, and also Mr Toby Bradshaw, Mr Andrew Davies, Mr Robert Evans and Mr Steve Hunter for all their IT knowledge and assistance.

Finally, I would like to thank Paul and my parents for all their support and patience.

ABSTRACT

The aim of the research was to investigate the effect of impact damage on the fatigue life of steel using both experimental and finite element methods. Any component that is subjected to a single impact may have not only noticeable surface damage, but also residual stresses in its surface and subsurface layers. These residual stresses may reduce or possibly improve the fatigue life of the component. The objectives of the research were, therefore, to investigate what effect the size of an impacting object has on the fatigue life of a specimen and also to evaluate experimentally how the amount of single impact energy affects the fatigue life of specimens. Furthermore, three dimensional, non-linear transient numerical models were developed, which were used to show the surface and subsurface residual stresses produced as a result of the impact.

The specimens used in the experimental programme were made from two different types of cold-rolled, mild steel strip; namely Bending Quality Bright Steel (BS1449), and '070M20' Carbon Steel (BS970). To investigate what effect the size of an impacting object has on the fatigue life of a specimen, the impactors were produced in six sizes; 10mm, 11mm, 12mm, 18mm, 25mm and 40mm radii, and in order to determine how the amount of impact energy affects the fatigue life of a specimen, the height of the impactor hammer head was adjusted to impact heights of 410mm, 276mm, 163mm and 87mm, thus altering the amount of impact energy imparted into the specimen.

The current study found that the fatigue life of a specimen is greatly reduced due to a single impact and that the greater the height of the impact, and consequently the higher the impact energy, then the lower the fatigue life of the specimen becomes. It was also noted that the reduction in fatigue life due to the single impact is not affected by the size of impactor but by the energy of the impact, as a single impact at the chosen impact energy for this study will impart residual stresses in the specimen which causes a normalisation in the reduction in the fatigue life of the specimen.

LIST OF CONTENTS

LIST OF FIGURES

LIST OF TABLES

NOTATIONS

2D	Two-dimensional
3D	Three-dimensional
ε	Strain
$\dot{\varepsilon}$	Strain Rate
σ	Standard deviation
σ_r	Maximum radial stress
σ_y	Uniaxial yield stress
C	Cowper-Symonds strain rate parameter
CAD	Computer aided design
CLA	Centre line average
COR	Coefficient of restitution
CVEL	Elastic wave propagation speed
c	Width of impact
ρ	Density
DOF	Degrees of freedom
DPN	Diamond pyramid number
E	Young's Modulus
F.E.	Finite element
F.E.A.	Finite element analysis
F.O.D.	Foreign object damage
h	Depth of impact
N	Life to failure (cycles)
NoE	Number of elements
n	Number of data

P	Cowper-Symonds strain rate parameter
P_o	Maximum pressure
S	Alternating stress amplitude
SD	Standard deviation
TEL	Time step increment
t	T-test value
U.T.S.	Ultimate tensile strength
υ	Poisson's ratio
Ø	Diameter
$\bar{x}$	mean

Chapter 1: INTRODUCTION

The word *fatigue* derives from the Latin expression *fatīgārе* which means 'to tire', (Suresh, 1994). It is estimated that around 90% of failures that occur in mechanical systems are due to fatigue, (Mann, 1967). Fatigue is caused by a cyclic load, which can initiate a crack and, consequently, lead to component failure. This is of particular concern, as component failure can be catastrophic and occur without warning and well below the ultimate tensile stress of the material.

The major factors which may affect the properties of materials and components, and can subsequently lead to fatigue failure, are listed below:

- The primary manufacturing process, e.g. casting and rolling
- The design of the component
- The machining or fabrication of the component
- Heat treatment or mechanical working of the component
- Surface treatments such as plating or anodizing
- Inspection procedures
- Identification marks
- Environmental conditions

There are three main reasons why a fatigue fracture will occur at the surface of a component that is subjected to cyclic stresses, namely:

1) The surface is always weaker than the subsurface of the material.
2) Surface irregularities such as scratches and poor surface finish can result in stress concentrations and, hence, cause cracks to initiate.
3) The tensile stress is a maximum at the surface of the component. A tensile stress will tend to open a crack and spread it in a direction perpendicular to that of the tensile stress.

The main reason why a fatigue fracture may originate in the subsurface of a component is due to excessive surface compressive residual stresses, which are introduced into the component by, for example, heat treatment, forming or finishing processes or by mechanical prestressing.

The cyclic load applied to a component, which results in fatigue failure, can take many different forms; for example, a sinusoidal load cycle, which achieves an alternating maximum-minimum stress. Depending on the component being tested, the magnitude of the load and its frequency will affect the number of cycles to component failure; for example, low cycle fatigue failure may occur because the cyclic load is too high for the component material and/or structure. Conversely, either no failure or high cycle fatigue failure may occur because the load is too low for the component material and/or structure. Hence, both the load and the frequency at which it is applied are specific to the component under test. In low cycle, high stress fatigue situations, failure of the component can occur up to 10^3 cycles. In this region, high stresses cause considerable plastic deformation prior to the failure of the component. In high cycle, low stress fatigue situations, failure of the component occurs beyond 10^3 cycles. In this region, low stresses cause the material to deform elastically.

The stress-life, or S-N method, can be used to quantify metal fatigue. A plot of the alternating stress amplitude, S, versus life to failure (number of cycles), N, can be produced. This data can be presented on a linear, semi log or log-log plot. For example a typical S-N curve for 4140 Chromium-molybdenum steel is shown in Figure 1.1, (Mann,1967). Note: 40,000 PSI to 55,000 PSI equates to 275.8MN/m^2 to 379.2MN/m^2.

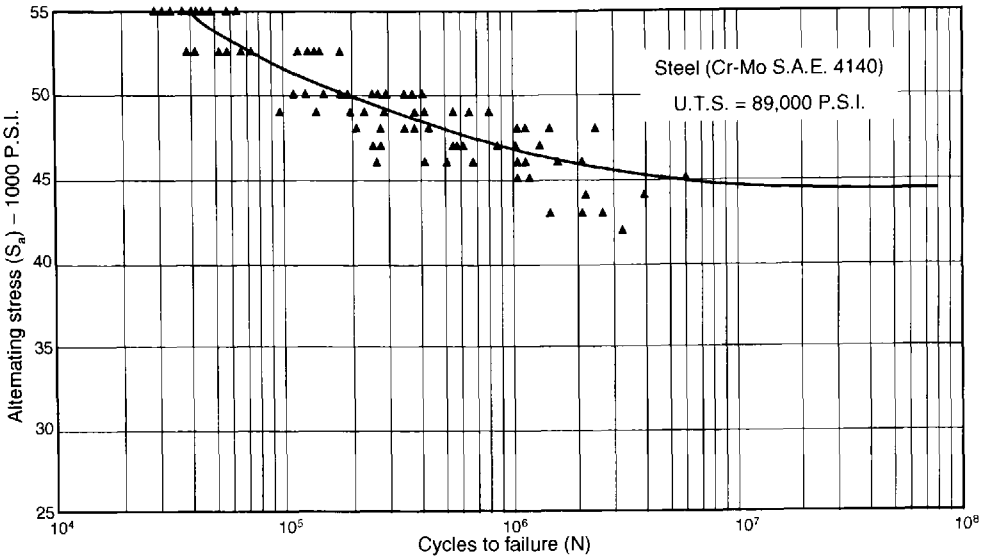

Figure 1.1: Typical S-N curve for 4140 Chromium-molybdenum steel

An example of component failure due to metal fatigue is that of the world's first passenger jet airliner, the De Havilland Comet. It was designed and built in Great Britain in 1954, as a sight-seeing aeroplane with large, square windows. After a successful first year, disaster struck when two planes were lost at sea and, as a result, all Comets were grounded so that safety checks could be carried out. It was found that the effect of pressurising and depressurising the cabin was causing cracks to initiate in the corners of the square windows, which led to catastrophic failure.

Fatigue failures, due to single or repeated impact loading, are frequently reported, as an impact can cause surface damage to a component that will affect its fatigue life. Impact fatigue loads can usually be divided into two categories: regularly-repeated impact load and randomly-repeated impact load. Previous research on impact fatigue by Yu *et al.* (1999) highlighted the following points.

a) The fatigue strength of impacted specimens is lower than the fatigue strength of non-impacted specimens.
b) The crack growth rate is usually higher in impacted specimens than in non-impacted specimens.

c) Stress concentrations cause the fatigue life of materials to decrease.
d) The difference in the endurance fatigue limit between impact and non-impact fatigue increases with the hardness.
e) The crack initiation life in smooth specimens is higher in impact fatigue than in non-impact fatigue. However, the crack initiation life of notched specimens is shorter in impact than in non-impact fatigue.
f) The impact fatigue life of a specimen significantly improves with an increase in the distance between the minimum cross section and impact loading point. As the distance increases, the effect of the impact plastic wave decreases, and, hence, there is an increase in impact fatigue life.

When a metal component is subjected to an impact from another, harder object it will normally result in an indentation or crater on the surface of the metal. This indentation is the result of local plastic yielding, which will tend to expand but is restrained by adjacent, deeper metal that was not plastically deformed by the impact. Residual compressive stresses are induced in the metal, the depth of which depends on the hardness and ductility of the metal, the size and velocity of impact and also the state of the strain in the metal at the time of impact.

Residual stresses can affect the fatigue behaviour of materials, as they can alter the mean level of the fatigue cycle and the fatigue life for crack nucleation. Residual stresses are induced in a ductile material when the material is unloaded after previously being loaded. This action results in a non-uniform stress distribution and, where the initial loading is sufficiently large, the maximum residual stress exceeds the yield stress of the material. Residual stresses are thought to be favourable if compressive but detrimental if tensile (Suresh, 1994), hence the reason why the process of shot-peening is widely used to improve the fatigue life of many engineered structural parts. In the shot-peening process, small, hard spheres (usually 0.1mm to 1mm in diameter) are shot at the surface of a component, with a velocity in the order of 60m/s. Depending on the velocity and size of shot used, duration of treatment, coverage, the material properties of the shot and the surface being treated, a compressive residual stress layer of

varying depths will be generated on the surface of the component due to the localised plastic deformation of the surface layer of the component. Shot-peening is used to improve the fatigue life of many engineering components such as gears, shafts and valves springs.

An example of component failure due to repeated impact damage can be found in pulse-jet engines. Pulse-jets are a very simple type of engine with only one moving part, the reed valve. The reed valve flexes back and forth against a retainer plate, allowing air into the combustion chamber. When there is a build up of pressure, the valve stops the exhaust gases escaping through the inlet. As the reed valve can flex around a hundred times a second, each time hitting against the retainer plate, this can lead to impact fatigue failure of the reed valve.

One possible way to predict the residual stresses present in a component which has been subjected to an impact is with the use of finite element analysis. In the late 1800s, Lord John William Strutt Rayleigh developed a method for predicting the natural frequency of simple structures. This method was developed further by Walter Ritz, becoming known as the Rayleigh-Ritz method, and was used to predict the stress and displacement behaviour of structures. The Rayleigh-Ritz method proved difficult to use on complex shapes, so by the 1940s numerical methods had been developed by Alberto Castigliano and William Rowan to predict the behaviour of more general structures. In 1943 Richard Courant proposed the use of triangular elements, which could be used to predict the behaviour in more complex structures. The development of analogue computers in the 1950s enabled a team from Boeing to demonstrate that complex surfaces could be analysed with a matrix of triangular shapes. The benefit of structural analysis to the aerospace industry became clear and structural analysis methods on computers were developed. In 1960 Dr. Ray Clough coined the term "finite element" and finite element analysis (F.E.A.) was carried out on digital computers, which were much faster than the analogue computers previously used. As the speed of computers grew so the F.E.A. software was developed further. In the 1980s F.E.A. was linked with computer aided design (CAD)

packages and from the 1990s the F.E.A. software could be found built into many CAD packages, (Adams *et al.*, 1999). Today F.E.A. is used in many areas of modern engineering design to assist the engineer when carrying out stress analyses on heat conduction, electrical fields, magnetic fields and fluid flow; for example, on very complex geometries and structures. A further advantage of using F.E.A. when carrying out investigations into areas such as stress analysis is that F.E.A. is non-destructive, unlike other techniques such as hole-drilling and layer removal, which are used to measure residual stresses.

1.1 Aims and Objectives

The aim of the research was to investigate the effect of a single impact on the fatigue life of steel. A component subjected to a single impact may have not only noticeable surface damage but also residual stresses in the surface and subsurface layers. These residual stresses may improve, or possibly reduce, the fatigue life of the component. The objectives of the research were, therefore, to investigate what effect the size of an impacting object has on the fatigue life of a specimen, which can be achieved by varying the size of spherical impact, and also to evaluate experimentally, by varying the height of impact, how the amount of single impact energy affects the fatigue life of specimens. Various numerical models were developed for the different sizes of spherical impactor tested, which can be used to show the surface and subsurface stresses produced as a result of the impact. The data acquired from material testing during the experimental programme were used as initial conditions to produce an accurate numerical model.

1.2 Structure of the Thesis

The subsequent Chapters of this thesis, in brief, cover the following topics:

Chapter 2: A comprehensive literature review on the technical aspects of metal impact fatigue and relevant numerical modelling is presented. Included is a summary of the salient points raised in previous research, together with some of the unexplored areas, and the aims behind the current research are outlined.

Chapter 3: Presents the experimental apparatus, the single impact and fatigue tests undertaken, and also details the materials used and methodology followed.

Chapter 4: Comprises a summary of all impact and fatigue test results and, where appropriate a discussion on how these results were interpreted and the possible factors that may have influenced them.

Chapter 5: Presents both two-dimensional and three-dimensional non-linear models, which have been developed using the ANSYS finite element software, to simulate a specimen which has been subjected to a single impact and to observe the residual stresses produced in the specimen. Comparisons are made between the numerical and experimental results in order to validate the numerical results obtained.

Chapter 6: Provides a discussion on the experimental results obtained in Chapter 4 and the numerical results obtained in Chapter 5. Any concerns or factors that may have influenced the results are also discussed.

Chapter 7: Finally, a summary of the research project, accompanied by the major conclusions from the study, is presented. Additionally, the limitations of the present work are identified and suggestions for further work are also included.

Chapter 2: LITERATURE REVIEW

This Chapter presents a comprehensive literature review of the technical aspects of metal impact fatigue and relevant numerical modelling, which includes a summary of the salient points raised in previous research, as well as outlining some of the unexplored areas and the significance of the current research.

The preliminary review carried out has highlighted many areas that may be considered when carrying out research into the fatigue induced in an object that has been subjected to impact. It has therefore been decided to separate this review into the related areas; namely, spherical impacts, finite element analysis and case studies.

The trademarks of the various software packages discussed within the literature review are listed below:

- ABAQUS is a commercial software package for finite element analysis developed by SIMULIA, a brand of Dassault Systemes S.A.
- ADINA is a commercial software package for finite element analysis developed by ADINA R&D, Inc.
- ANSYS is a commercial software package for finite element analysis developed by ANSYS, Inc.
- DYNA2D is a commercial software package for finite element analysis developed by Hydrosoft International (HI).
- LS-DYNA is a multiphysics simulation software package, actively developed by the Livermore Software Technology Corporation (LSTC).
- MARC2000 is a finite element code developed by MSC Software Corporation.
- PW/WHAM is a finite element code developed by Henry Teichman based on the WHAM software package for finite element analysis.
- ZéBuLoN is a commercial software package for finite element analysis developed by Northwest Numerics, Inc.

2.1 Spherical Impacts

Tabor (1948) carried out an experimental investigation using various metals that were impacted by conical and spherical indenters under both static and dynamic load conditions, to determine the effect on material hardness. Steel conical and spherical indenters, with radii varying from 0.05mm to 0.159mm, were used to indent specimens of steel, aluminium alloy, brass and bronze. Static loads of between 2,453N and 29,430N (250kg and 3,000kg), and impact velocities of between 0m/s and 9m/s were used. The results showed that the conical indentation had no effect on the hardness value of the materials tested, unlike the materials impacted with spherical indenters, which produced work-hardening. For the very soft metals tested, the dynamic hardness was found to be much higher than the static hardness. With the materials indented with the spherical indenter, it was noted that the work hardening increased with the size of indenter.

Goldsmith *et al.* (1960) carried out an experimental investigation to determine the force-indentation relationship of hard steel balls on tool steel, lead and aluminium bars, under both static and dynamic load conditions. Steel balls of 12.7mm radius were impacted into the metal specimens using an air gun, with impact velocities of between 7.1m/s and 89.2m/s. The position of the impact on the specimen was not accurate and, consequently, was not repeatable. The energies before and after impact were found, and it was noted that work hardening occurred in the static compressive test specimens, particularly at low velocities, compared with the dynamic test specimens. The dimensions of the impact crater were calculated using strain data and also equations that treated the metal bars as one-dimensional members. The strain data was obtained between 50mm to 203mm from the impact site, which does not give an accurate representation of the strain at the location of impact as the strain will alter along the length of the sample. A good correlation was found between the calculated impact craters and the actual impact craters produced.

Using a two-dimensional, axi-symmetric finite element analysis, Hardy *et al.* (1971) carried out a study of the deformations and stresses produced when a rigid sphere was pressed into an elastic-perfectly-plastic half-space. It was found that the radius of indentation produced experimentally in previous literature was very similar to that predicted by the F.E.A. used in the study. The pressure distribution in the contact region was noted to change from an elastic elliptical shape to a rectangular shape as the static load increases, as shown in Figure 2.1. It was noted that there was a thin elastic inclusion imbedded in the plasticised material under the applied load and some residual radial and tangential tensile stresses existed over the contact area.

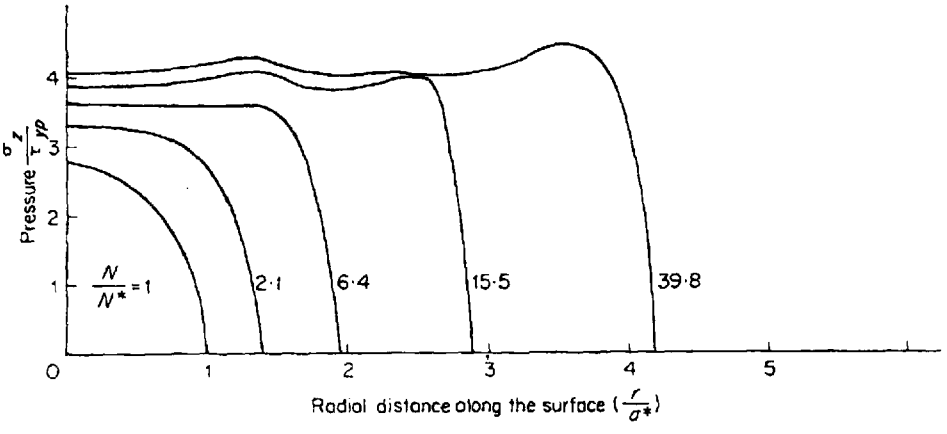

Figure 2.1: Pressure distribution in contact area (Hardy *et al.*, 1971)

Experiments were carried out by Studman *et al.* (1977) to support the hypothesis that high residual stresses develop just outside the contact area of a flat surface that has been statically loaded with a spherical indenter. In the experiments, a flat, carbon steel (EN44B) surface, 10mm thick and with a hardness of 800DPN, was impacted with a tungsten carbide sphere of 5mm radius, with the load applied at a constant stress rate of usually 250N/sec. Additionally, the maximum load of 25kN was held constant for 20 seconds, after which photographs were taken and notes made. The applied load was then reduced to approximately half

the loading rate and further photographs were taken and notes made. Radial and circumferential cracks in the steel were found to extend after load removal, implying the presence of high tensile circumferential residual stresses. Under these loading conditions the 25kN load would have a contact time of 20 seconds; the current research will concentrate on dynamic impacts with a contact time of approximately 0.2ms.

Further experimental work was carried out by Iguchi *et al.* (1979), on smooth round bars and notched flat specimens of annealed carbon steel (JIS S20C equivalent to AISI 1020) using an axial load impact fatigue testing machine. The load was applied in a similar manner to a forced falling hammer, the weight of which was not noted, and the specimens received 4 impacts every second. The fracture surface was examined using scanning electron microscopy and the X-ray diffraction technique, and the residual stresses were determined using X-ray diffraction. It was found that the fatigue life of impacted smooth round bars was longer than that of the non-impacted smooth round bars. The fatigue life of the impacted notched flat specimens was much shorter than the non-impacted notched flat specimens. It was noted that the larger the stress concentration produced due to impact, the shorter the fatigue life. Also, the rate of crack growth in impact fatigue was higher than that in non-impact fatigue, when compared at the same maximum stress intensity factor.

Kral *et al.* (1993) investigated the deformation characteristics and residual stresses produced from the repeated indentation of a half-space by a rigid sphere. The half-space was modelled using the finite element code ABAQUS, with varying material properties and the rigid spherical indenter, of radius 0.0015mm. A two-dimensional, axi-symmetric model was developed were the load was applied in steps until a maximum load of 300 times the initial yield load was applied, and it was found that the surface and subsurface stresses varied with material hardness. For non hardened materials, a spherical band of tensile hoop stress develops from the axis of symmetry to the surface, which produces a peak tensile hoop stress at the surface, and subsequently increases the materials

susceptibility to surface radial cracking. In hardened materials, as the loading increased, a decrease in both the compressive radial and tensile hoop stresses at the contact edge was found, with the surface stresses remaining unchanged. The use of such a small indenter indicates that this research may have been merely an exercise in the use of ABAQUS.

Finite element solutions comparing the normal contact of an elastic-plastic layered medium under loading by a rigid and also a deformable indenter, were carried out by Faulkner *et al.* (1998), with a two-dimensional, axi-symmetric model produced using the ANSYS program. The layered plate consisted of a stiff hard layer rigidly bonded to a softer substrate, which was indented by a sphere of radius 100mm to represent the indentation made by a Rockwell indenter. The results produced showed that varying the properties of the indenter affected the point at which yielding commenced. The results obtained were not supported by any experimental work.

Johnson (1999) reported on the theories postulated by Heinrich Hertz in 1882. Hertz produced mathematical models of the stresses produced when two spherical elastic bodies make contact. The assumptions made by Hertz when carrying out these analyses can be summarised as follows:

a) The surfaces are frictionless
b) Strains are small
c) Each solid can be considered as an elastic half-space
d) The contact surfaces are continuous and non-conforming.

The pressure distribution within the contact area between two spheres was noted to be hemispherical in shape and between two cylinders was noted to be elliptical in shape. At the surface within the contact area all stress components are compressive, except at the very edge of the contact area where the radial stress is tensile, and have a maximum value which can be calculated using equation 2.1.

$$\sigma_r = \frac{1}{3}(1\text{-}2\,\nu)\,P_o \qquad (2.1)$$

where σ_r = maximum radial stress

ν = Poisson's ratio

P_o = maximum pressure

A numerical study of the normal impact of elastoplastic spheres with a rigid wall was produced by Li *et al.* (2000), who used DYNA2D to write an axi-symmetric, non-linear, explicit, two-dimensional F.E. code. A typical steel sphere with a 10mm radius was modelled impacting three materials which are elastic, elastoplastic and elastic-perfectly-plastic. Contact force and displacement were analysed and also both material behaviour and the coefficient of restitution (COR) were considered. It was found that the more elastic the material was, then the shorter the contact time of the impact and the higher the rebound velocity was. The contact force was found to be the greatest in the elastic material and the COR was found to decrease with impact velocities greater than 20m/s. The strain hardening was also noted to increase with impact velocity, demonstrating that work hardening had taken place. The results obtained were not supported by any experimental work. This work was later developed by Wu *et al.* (2003) and compared with the experimental results produced by other researchers, namely Tabor (1948) and Goldsmith *et al.* (1960), and the F.E. results were found to compare well with the experimental results. The COR was found to decrease with increasing velocity and to be proportional to (impact velocity)$^{-1/4}$.

Further work by Yan *et al.* (2003) used the F.E.A. code MARC2000 to produce a two-dimensional, axi-symmetric model of the contact between a rigid sphere of radius 50mm and a deformable half-space, using typical steel material properties. The work carried out investigated the pressure distribution during unloading. It was found that beyond the elastic limit the deformation during unloading is perfectly elastic, and that the reloading curve follows exactly the unloading curve

for the same contact force. The F.E.A. results were compared against those calculated using Hertz's Law and agreed favourably. However, no frictional properties were considered in this work.

Wu *et al.* (2005) developed a two-dimensional, axi-symmetric model using DYNA2D, to determine the energy dissipation during the normal impact of an elastic spherical particle with both an elastic and an elastic-perfectly-plastic substrate. A bilinear model was produced with no strain hardening or frictional affects considered. The impactor was 10mm in radius and the impact velocity ranged between 5m/s and 150m/s. The substrate was square in cross-section and was modelled in two sizes; 20mm x 20mm and also 100mm x 100mm. The numerical results obtained for the elastic to elastic contact compared well with those calculated from Hertzian theory for elastic contacts (Johnson, 1999). It was noted that with the elastic to elastic contact, as the velocity increases both the contact time and the COR decreases, indicating an increase in the amount of kinetic energy dissipation and possibly an increase in the amount of elastic stress waves generated. It was also noted that substrate size was found to have an affect on the energy dissipation. In the smaller substrate there was found to be more than one reflection of the stress waves generated, thus causing the energy dissipation due to stress wave propagation to be negligible. In the larger substrate size there was no reflection of the stress waves generated and so there was significant energy dissipation due to stress wave propagation. The elastic to elastic-perfectly-plastic contact indicated that the energy loss due to stress wave propagation is negligible and kinetic energy is mainly dissipated due to plastic deformation. It was also noted that as the impact velocity increases the COR decreases. No experimental work was carried out to verify the results obtained.

Previous research into spherical impacts, discussed above, has not considered the residual stresses in the test specimens due to either static or dynamic loading, and their subsequent effect on the fatigue life of the specimens. The current study will consider the effect of dynamic loading on the fatigue life of specimens and the residual stresses produced. The current research work will use a rigid

spherical indenter, varying from 10mm to 40mm in radius, with a mass of 3.52kg and an impact velocity of approximately 3m/s, as research to date indicates that low impact velocities with varying sizes in indenter have not been considered. The hardness of the material will be tested both before and after impact, to determine whether any work hardening of the impacted material has taken place. Also where possible, the experimental results will be used to validate the numerical results.

Previous research has shown that finite element analysis has primarily centred around two-dimensional, axi-symmetric models, which ignore time dependant effects and assume the material to be elastic-perfectly-plastic. The current research aims to determine both experimentally and with the use of a three-dimensional model, how the size of an indenter will affect the fatigue life of a specimen. The model, which will consider time dependant effects, will be used to show the residual stresses in specimens after a single impact and also any effect to the properties and geometry on the periphery of the specimens.

2.2 Finite Element Analysis using ANSYS

The finite element program ANSYS was used by Orbison *et al.* (1989) in the development of fatigue crack initiation studies in specimens. The two-dimensional, axi-symmetric model was found to be very useful in determining principal and yield stresses. Firmin *et al.* (1994) showed that the ANSYS program can be used to predict both the stress and strain distribution in a component under either static loading or time varying loads. However, it was suggested by the authors that there is no reliable way to accurately predict the onset of fatigue failure in a component.

ANSYS has also been used by Slavik *et al.* (2000) to predict the stress intensity in aircraft engine components. The ultimate strength characteristics of steel plates under axial compressive loads were determined and the plates were struck with circular and conical shape impactors to determine how the effect of shape, size and location of impact will affect the ultimate strength behaviour. A series of elastic-plastic, large deflection, finite element analyses were carried out in ANSYS using four node plate shell elements, with a finer mesh used in the vicinity of the impact area. A two-dimensional plane stress and also a plane strain model were produced, as well as an axi-symmetric, three-dimensional model. The results produced compare well with other finite element programs and theoretical literature, although ANSYS generated slightly higher stress intensity results.

Compressive testing carried out by Paik *et al.* (2003) using spherical and conical indenters into steel plates, showed that the shape of the impactor did not appear to affect the ultimate compressive strength. However, as the diameter and depth of the resulting impact crater increased, the ultimate compressive strength decreased. It was also noted that as the impact location becomes closer to the edge of the steel plate, the ultimate compressive strength will decrease. The experimental results were then verified with the use of a plane stress, two-dimensional, non-linear numerical model developed using ANSYS.

Her *et al.* (2004) used the LS-DYNA software to model the effect of a low velocity impact on composite laminates of cylindrical and spherical shells, in order to determine the contact force during impact and the resulting deflection of the composite structure. The plane stress, two-dimensional model that was produced simulated a rigid spherical steel indenter impacting the composite material ASH3501 with a velocity of 30m/s and the model ignored the effect of friction during contact. The numerical results were compared with results found in existing literature and were noted to be in good agreement.

Four different types of fibre reinforced composite plates were studied by Hosseinzadeh *et al.* (2006), after being impacted by a standard drop weight with different impact energies. Carbon fibre, carbon/glass fibre, thin glass fibre and thick glass fibre reinforced composite plates were impacted with spherical hardened steel impactors of radius 9.5mm with impact energies of 30J, 50J and 100J, weighing either 2.5kg and 5.5kg. The damage zones were studied using a non-destructive inspection (N.D.I.) technique which uses two ultra-sonic probes, called the A-Scan. It was found that the carbon fibre reinforced composite plates showed the best structural behaviour under low impact velocities, with the carbon/glass fibre performing best under high impact velocities. The experimental results were then compared with numerical results produced by plate impacts modelled using LS-DYNA V6.1. However, the plane stress, two-dimensional analysis did not produce results which were in agreement with the experimental results. The damage to the plates produced by the model was not similar to that produced experimentally, as the software cannot accurately model the post-failure behaviour of the composite plates.

2.3 Case Studies

This section will consider case studies where impacts can enhance the fatigue life of components, such as in the shot peening process, and also reduce the fatigue life of components, such as aircraft structures, boat propeller blades and ice axes.

2.3.1 Shot Peening

Shot peening is a well recognised process, which is used to enhance the fatigue characteristics of metal components and to help eliminate the problems of stress corrosion cracking. The process involves the bombardment of the surface of a material with small spherical media, also called "shot", to produce a thin layer of

high magnitude residual compressive stress. The compressive stresses that help to prevent crack initiation are generated when the impact of each particle of shot on the component produces a small indentation which compresses the material beneath the indent. The purpose of introducing compressive stresses into a component is to prevent fatigue failures, which usually propagate through a component in regions of tensile stress. Changing tensile stresses to compressive stresses at the surface of a component, where fatigue cracks typically occur, limits their propagation, (Lawerenz, 1991 and Brickwood, 2002). Tyler (1987) determined that the resulting residual compressively stressed layer is equal to approximately 50% to 60% of the ultimate tensile strength of the metal, which results in a component with enhanced fatigue strength of between 10% and 35%, depending on the material used.

Hills *et al.* (1983) have shown experimentally that the residual stresses obtained in quenched aluminium and annealed stainless steel cylindrical specimens during shot peening at various velocities and with shot of radius 0.3mm to 0.4mm, are directly proportional to the material hardness. The depth of material affected was also found to be directly proportional to the velocity of the shot.

Metallographic studies by Murray (1984) have shown that shot peening breaks up the surface layer grains and changes the structure of the grain boundaries, in such a way that it develops slip planes and dislocations. The modified structure provides nucleation sites for the available carbon, which precipitates as fine chromium carbide particles along the slip planes. Shot peening also reduces the size of grain boundary carbides and the chromium depletion zone, and it prevents the formation of continuous grain boundary networks of the chromium depleted material; thus the material is no longer susceptible to intergranular corrosion.

Research carried out by Niku-Lari (1987) using various materials of shot, including steel, cast iron, glass and ceramics, of between 0.05mm and 0.65mm in radius, which were fired at steel specimens, showed that the maximum residual compressive stress in a material increases with the hardness of the shot, as shown

in Figure 2.2. However, this does appear to stabilise out once it reaches an optimum level. It was also found that the stress gradient reduces with increasing shot size and that the harder the material of shot, the greater the depth of impact. The current research will use impactors of the same hardness to ensure that the results obtained are due to the size of the impactor and not its material properties.

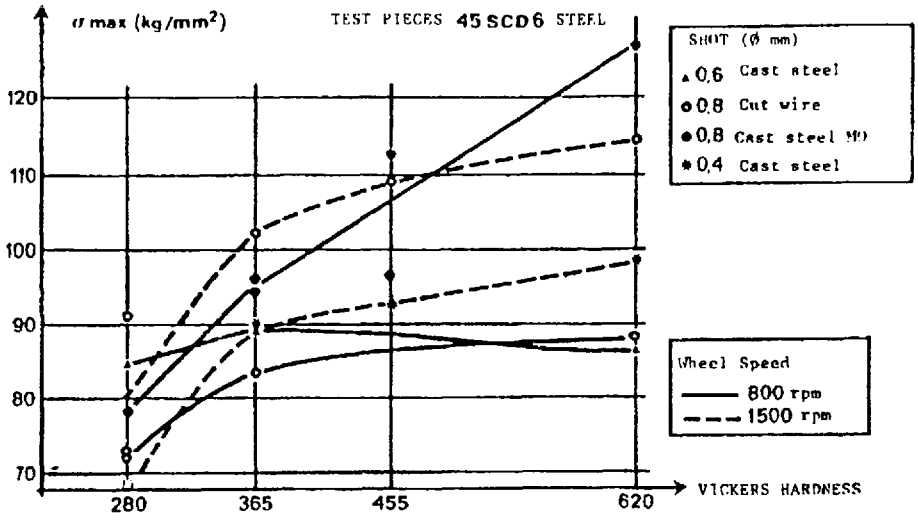

Figure 2.2: Variation in the maximum residual compressive stress as a function of the hardness of the material, for various shot diameters (Niku-Lari, 1987)

Gillespie *et al.* (1992) highlighted the importance of using the correct size and shape media when shot peening. Improperly sized shot will give either too little, too much or inconsistent layers of compressive stress, and may cause surface damage and poor fatigue properties, so 'Image Analysis' was used to determine the correct peening media. This process uses digital image processing to evaluate the size and shape of media, and appears to provide a much better control of peening media when compared to the use of different sized sieves currently used to categorise shot in size and shape.

Fatigue tests were carried out by Hara (1992) on shot peened and non-shot peened specimens of precipitation hardened stainless steel at different percentages of yield. It was found that there is a direct relationship between fatigue failure and surface residual stresses; the higher the compressive stress, the greater the life of the component. Shot peening was found to remove the residual tensile stresses in the surface layer of specimens, which resulted in a significant improvement in fatigue strength in the order of 25% for the shot peened specimens.

A mathematical model was developed by Diepart (1993), which can be used to predict the optimum peening parameters required to produce the necessary level of residual compressive stresses in a metal component to improve the fatigue performance and prevent stress corrosion cracking. The model showed that it is possible to vary the shot size and velocity to determine the residual stresses in a component.

Mitsubayashi *et al.* (1994) shot peened specimens of JIS SCr420 steel using shot of 0.4mm radius at a velocity of 29m/s, to determine the effect of shot peening on the fatigue strength of transmission gears. They verified both theoretically and experimentally that the compressive residual stress layer formed by shot peening can suppress the propagation of fatigue cracking.

Research carried out by Farrahi *et al.* (1995) on 531 HV spring steel, has shown that the value of surface stress is not affected by the kinetic energy of the shot, and that the residual stress is not greatly affected by the shot size. However, the maximum stress occurred at a lower subsurface level as the shot size increased, and a linear relationship was found between the depth at which maximum residual stress occurred and the size of the shot. It was also found that shot peening does improve the fatigue strength, but that shot size has little effect on the endurance limit. However, the endurance limit was said to be reduced by using a harder shot material, but this is not true in all tests carried out. The depth of the plastically deformed layer and the depth of the maximum residual stress

increases with shot peening time, projection pressure and shot size. This fatigue life improvement can be attributed to the maximum residual stress and also to the depth of the plastically deformed layer. The residual stresses were determined using SIEMENS X-ray stress measurement apparatus. The saturation of the surface with shot was also tested, and it was determined that once total saturation (100% coverage) had been reached, further impacts had no effect on the fatigue life. The accuracy of shot was not repeatable making it difficult to make any suppositions concerning single impacts.

In order to clarify the mechanism of the creation of compressive residual stresses by shot peening, Kobayashi *et al.* (1998) performed both a static compression test and a dynamic impact test using a single steel ball against a flat steel plate. The tests used a 25mm radius steel ball with a 50mm thick flat steel plate and also a 38mm radius steel ball with a 75mm thick flat steel plate. In the static test a force of 49kN was applied to the ball, and in the dynamic test a velocity of 6.3m/s was applied to the ball through a drop height of 2m. As the dynamic test was a repeated impact test, observations were made after the 1^{st}, 10^{th}, 20^{th} and 30^{th} impacts; it should be noted that these were just impacts to the specimen and not repeated impacts to the same location on the specimen. The shape of the impact craters produced showed that the depth of impact was larger in the static tests but the swell around the indentation was greater in the dynamic tests. In the static compression test, compressive residual stresses were created near the centre of the ball indentation mark, whereas in the dynamic impact test, tensile residual stresses were created near the centre of the ball indentation mark and compressive residual stresses are created on the outside of the indentation. Also, the tensile residual stress in the centre of the first ball indentation mark changed to compressive stress as the frequency of the ball indentations surrounding the first ball indentation mark increased. Thus, the compressive residual stress created by shot peening is considered to be the result of the superposition of the residual stresses produced by surrounding shots.

Kirk (1999) postulated that the diameter of the shot used can produce a residual stress layer of the same depth, and that larger shot produce a deeper layer of compressive stress. However, he has not validated his theories.

Wick *et al.* (2000) has found that shot peening at elevated temperatures (290°C) can increase the fatigue strength of quenched and tempered steel (AISI 4140), where compared to conventional shot peening temperatures. The warm peened steel samples have only a slightly higher compressive residual stress than those which are conventionally peened. These stresses are due to the strain ageing processes, which lead to a more diffuse dislocation structure. Annealing after conventional shot peening reduces the fatigue strength because the residual stresses are decreased.

By carrying out rotating bend fatigue tests on steel (AISI 4340) subjected to the shot peening process, Torres *et al.* (2002) found that an increase in the shot peening intensity results in an increase in the compressive residual stress field, but did not necessarily increase the fatigue life of the steel samples. It was also found that the relaxation of induced compressive stresses during the fatigue process, in medium and high cycle fatigue of shot peened samples, will initiate cracks below the surface of the specimen. In low cycle fatigue of shot peened samples cracks initiated on the surface of the sample.

Teodosio *et al.* (2003) found that shot peening produces compressive stresses in the superficial layers of steel, which can improve the resistance to fatigue crack initiation. Of the two materials tested, namely a high strength low alloy steel and a duplex stainless steel, both showed an improved resistance to fatigue crack initiation after shot peening.

A literature review was conducted by Shen *et al.* (2006) on previous research carried out, which considered the residual stresses induced by shot peening. It was noted that very few studies considered the effects of multiple indentation and that many analyses were concerned with static rather than dynamic impacts, with

little consideration into the velocity of the shot and material characteristics. Therefore, the authors decided to develop a mathematical model to predict the distribution of residual stresses due to shot peening. The materials tested included Al7075 and Ti-6Al-4V, with shot of size S170 (0.216mm radius). It was found that the model could not show the tensile residual stress field due to an incorrect assumption; namely, that the target material could be considered as semi-infinite. However, it was felt that the model could be developed further in order to accurately determine the residual stresses induced in a material due to multiple impacts.

In a study carried out by Park *et al.* (2006), to determine the affect of shot velocity on material characteristics, cylindrical test specimens of aluminium alloy (Al6061-T651) were impacted with shot of 0.4mm radius, at velocities of 40m/s, 50m/s and 70m/s. The experimental results obtained showed that surface roughness, hardness, compressive residual stress and fatigue life all increase as shot velocity increases. The author did not carry out any finite element analyses to verify the residual stresses produced.

Rotating bend fatigue tests were carried out by Kawagoishi *et al.* (2007), in order to investigate the effects of shot peening and double shot peening on the fatigue strength of 18% Ni maraging steel. Round specimens of 2.5mm radius were impacted with shot made from steel (0.15mm, 0.3mm and 5.5mm radius) or cemented carbide (0.025mm radius). An X-ray diffraction technique was used to determine residual stresses and it was found that fracture initiated from the surface of the specimen. Also, the fatigue life of the specimen increased due to the shot peening. It was noted that the smaller the shot size was, then the higher the fatigue strength. Double shot peening was found to not only increase the fatigue life of the specimen but also to reduce the scatter of results. Additionally, double shot peening increase both the hardness of the specimen and the amount of compressive residual stress near the specimen surface.

2.3.2 Shot Peening and Finite Element Analysis

A plane stress, two-dimensional model, developed by Levers *et al.* (1998), allows the analyst to analyse the impact of shot against the surface of thin plate structures. Shot is impacted into a specimen of aluminium alloy using F.E. code in ABAQUS. The analyst is then able to examine the effect of varying the shot size and velocity, to visualise the residual stress profile produced with 100% coverage. The resulting simulation can be used to predict the shape of large flexible structures, such as an aircraft wing, after the peening process. However, no experimental work was carried out to verify the numerical results.

Finite element analysis has also been used to predict the development, magnitude and distribution of residual stresses in accordance with shot velocity, shot diameter and material parameters. The models, developed by Schiffner *et al.* (1999) in ADINA 7.1, was used to simulate in 2D and 3D the perpendicular impact of an elastic sphere on an elastic-plastic surface and also to investigate the effect of multiple impacts. Steel shot (42CrMo4) of 0.2mm to 1mm radius was impacted with a velocity of up to 100m/s into steel specimens (54CrSi6). The two-dimensional model developed was axi-symmetric and the three-dimensional model was quasi-static.

Baragetti (2001) used ABAQUS 5.4 to produce both axi-symmetric and 3D models of the shot peening process. A steel shot was modelled impacting a low alloy steel sample. The shot was modelled with a velocity of 100m/s at varying angles of impact (0 degrees, 30 degrees and 45 degrees, with respect to the normal of the impacted surface). Single and multiple impacts were modelled and it was found that after impact compressive stresses existed near the surface of the sample and tensile stresses were present in the inner parts of the sample. No experimental work was carried out to verify the numerical results.

Finite element analysis has also been used to model and simulate the residual stress field resulting from the shot peening process on welded joints on aircraft structures. Meo *et al.* (2003) produced an axial-symmetric, three-dimensional model using ANSYS to simulate a steel shot peening ball of 1.5mm radius impacting a welded 2024-T6 aluminium specimen, at a velocity of 36m/s. The impact time was between 9μs and 10μs, and it was noted that altering the coefficient of friction between 0.1 and 0.5 had no effect on the residual stresses and plastic strains produced. The model showed that there was a tensile stress beneath the impact site, with a compressive stress on the surface of the specimen. This work was verified by experimental work and there was good agreement with the numerical results. The research showed that shot peening can be seen to reduce the tensile residual stresses induced by the welding process and therefore increase the fatigue life of welded aircraft structures.

Research carried out by Guagliano *et al.* (2004) initially involved carrying out rotating bend fatigue tests on un-notched cylindrical specimens of 39NiCrMo3 steel in order to determine the fatigue limit of the material being tested. Notched specimens were then produced and shot peened with 0.15mm and 0.3mm radius shot. It was found experimentally, and also by using finite element analysis, that the fatigue limit increased with the larger diameter shot size. Axial-symmetric, three-dimensional numerical models were produced using ABAQUS to verify the experimental results. The research indicates that the depth at which maximum compressive residual stress occurs is an important factor in determining the fatigue life of the component. Greater compressive stress is produced by the larger shot size, which in turn produces a higher fatigue limit, indicating that the smaller the depth of impact the greater the fatigue life of the component.

A three-dimensional, elastoplastic finite element model was produced by ElTobgy *et al.* (2004), to determine the resulting residual stresses from the shot peening process. Specimens of AISI4340 steel, which were impacted with a deformable steel shot of 0.2mm, 0.35mm and 0.5mm radius, at velocities of

20m/s, 25m/s, 40m/s and 60m/s, were modelled using ABAQUS. The numerical results compared well with the experimental results of previous work carried out by Torres *et al.* (2002). The compressive stress and penetration depth were found to increase with both shot size and velocity, and a slight decrease in surface stress was observed with an increase in shot size. Multiple impacts were also modelled but did not show any substantial effect on the resulting residual stress profile.

A two-dimensional, axi-symmetric model was produced by Cochennec *et al.* (2006), using the ZéBuLoN F.E. package. The model simulated 7075T13 aluminium alloy plate impacted with a steel shot of 1.5mm radius at velocities of between 0.2m/s and 20m/s. Frictional effects were not considered. The model was compared with the results of previous experimental research and was found to overestimate both the COR and also the indentation diameter produced. For high impact velocities the residual stress profile shows good agreement with the experimental results. A tensile residual stress is observed just below the top surface of the specimen for velocities below 15m/s; however, this was not validated experimentally. Differences between the experimental and the numerical results may be due to inaccuracies in the numerical model. For instance, the plate being impacted is highly constrained in the model when compared to the experimental rig, which will result in a difference in impact energy absorbed. Also, the impact diameter measurements were carried out using an optical microscope, which may not be as accurate as the results produced by the model. The height of rebound was measured using a digital camera, which may also produce errors depending on the exposure speed of the shot taken and accuracy of height measurements. The accuracy of the model may be enhanced by taking into account the kinematic hardening effects.

Frija *et al.* (2006) have developed a three-dimensional elastic-plastic numerical model, using ABAQUS, to predict the induced residual stress, plastic deformation profiles and superficial damage caused by shot peening. An aeronautical Nickel-based, super-alloy material, Waspaloy, was impacted with

cast steel shot of size S230 (0.3mm to 0.42mm in radius), at a velocity of 52m/s. The model simulated 100% surface coverage with shot peening. The obtained residual stress and plastic deformation profiles are in good agreement with the X-ray diffraction analysis that was also carried out and the maximum surface damage was located in the border of the indentation zone. It was noted that as the frictional coefficient increases, the surface compressive stress decreases. A slight relaxation of the residual stresses due to the shot peening process was also found.

Overall, previous research into components which have been shot peened show an increase in the fatigue life of a component, with tensile residual stresses present below the surface of the impact and compressive residual stresses on the surface of the component. However, previous work has concentrated on either the experimental aspect of the research with small spherical indenters impacting at high velocity, or the prediction of residual stresses with the use of a numerical model. The current research aims to determine both experimentally and with the use of a three-dimensional model, how the size of an indenter will affect the fatigue life of a specimen. However, unlike shot peening which uses spherical shot of up to 0.5mm radius impacting at a high velocity, the current research will use spherical indenters of varying radius sizes between 10mm and 40mm, impacting at a velocity of approximately 3m/s.

2.3.3 Shot Peening and Springs

Research carried out by Bell (1984) to investigate the shot peening of springs, showed that the larger the size of shot, the greater the increase in fatigue life. It was also found that double shot peening can also affect fatigue life. In double shot peening a large shot size followed by a small shot size was found to have little affect. However, a small shot size followed by a large shot size can increase the fatigue life of a component.

The properties of helical compression springs of various metals and sizes after the shot peening process were analysed by Bird *et al.* (1986). The shot used was cast steel with a shot size of between S70 and S550. It was found that shot peening improved the endurance limit of springs, with the smaller shot resulting in the best improvement. It was noted that the larger the shot, then the greater the relaxation of the compressive stresses, resulting in decreased fatigue resistance. This could also be due to the fact that smaller shot results in better coverage on the awkward geometry of a spring.

A review of previous research on the properties of leaf springs was carried out by Kaiser (1987). It was noted that the amount of residual stress produced by shot peening on the surface of the material is determined by the tensile strength or hardness of the material, the velocity of the shot, the degree of coverage and also the diameter of shot used. Residual compressive stresses were found below the surface of the shot peened material and the thickness of the surface layer containing residual compressive stresses increased for all material hardness values, with increasing velocity of shot, size of shot, and rate of coverage. Also, the poorer the surface finish, the greater the improvement in fatigue strength that can be provided by shot peening, with a 20% increase for polished specimens, 65% increase for surface decarbonised specimens and 100% increase for surface oxidized specimens. Residual compressive stresses induced by shot peening clearly increase with an increasing prestress and, therefore, also improve the fatigue strength. Additionally, minor surface defects can be eliminated or compensated for by shot peening.

2.3.4 Impacts on Aircraft Structures

Foreign objects, such as hail, ice, birds and debris, can cause a threat to aeroplane components such as jet engines (Weaver, 1990). The damage caused by foreign objects is known as Foreign Object Damage (F.O.D.). One area of particular concern is the F.O.D. to the leading edges of jet engine blades. In order to predict

the performance of materials, it has been necessary to simulate the impact of the object.

To determine the maximum deflection and the ultimate strength of a fan blade under the impact from a bird, experiments were carried out by Tsai *et al.* (1974) on the impact of cantilever beams by silicone rubber cylinders, at a velocity of 102m/s, to represent bird impacts. The results of the experiments were used to produce a model that can now be used to predict the structural response of the fan blades due to such impacts. The model was found to compare well with the experimental results.

Experimental work to evaluate the F.O.D. resistance of various materials for fan blades was carried out by Wong *et al.* (1978). Impacted cantilevered and simply supported specimens of materials such as Ti, Al, Boron Al and Boron Ti, were impacted with impactors that were made of gelatine in order to simulate the soft body impacts of birds. The impactors weighed between 55g and 789g, and were fired at the specimens at a velocity of 253m/s. Strain gauges were fitted to the specimens to measure the strains which resulted from the impacts. It was not clear from notes as to where on the specimens the strain gauges were located, which consequently makes it difficult to comment on the validity of the results obtained, as the resulting stresses will change over the length of the specimen. It was noted that the thicker the specimen was, then the lower the stresses resulting from the impact were.

Another investigation by Bertke *et al.* (1979) involved non-rotating impact tests on small test specimens of blade materials. This investigation involved three tests; fixed-fixed, cantilever, and free-free methods of mounting. The soft material gelatine was used to represent a bird, and was impacted on the edge of the test specimens. The titanium specimens had either flat or tapered edges. The impactors weighed between 2g and 6g, and were fired at the specimens at a velocity of between 140m/s and 480m/s. It was found that an increase in impactor size would increase the damage on the specimen, and that by

decreasing the incidence angle of the impact, the damage would be reduced. The effect of different methods of mounting was found to be negligible, as the results were very similar for all three methods. Increasing the leading edge thickness decreased the amount of bending and damage in the impact area. The tests on the impacted specimens agreed with actual blade impacts; however, it was found that using a tapered edge specimen was more precise than a flat edge specimen, which in any case did not accurately resemble the real blade. It was also noted that increasing the velocity increased the damage to the specimen.

Further single impact tests were carried out by Nicholas *et al.* (1980), on titanium leading edge specimens, using small spheres of 0.4mm to 1.6mm radius that were made of varying materials such as sand and glass, impacting with a velocity of between 240m/s and 490m/s. An attempt was made to measure the stress on the specimens with the use of strain gauges but this was not achieved. It was difficult to obtain repeatability with the impacts as many of the impactors broke up on impact and it was also difficult to achieve the same position of impact on each specimen tested. It was found that as the impact velocity increased, the amount of denting or bulging of the leading edge also increased. The fatigue tests also indicated that the maximum damage, and the greatest reduction in fatigue life, occurred at the critical velocity when the blade had been dented and a tear was formed.

Martin (1990) developed a plane stress, two-dimensional, transient, non-linear impact analysis using the PW/WHAM F.E. program to determine the response of a soft body projectile impact on a solid body, which simulated the impact of a bird on a fan blade. The model was said to compare well with the test data and can be used as a design tool for most structural components concerned with soft body impacts.

Experimental work using gelatine spheres of 12.7mm to 15.9mm in radius, which were fired with an incident angle of 15 degrees at titanium alloy (Ti-6Al-4V) specimens, was carried out by Hughes (1992, 1994), in order to simulate bird

impacts on the leading edge of fan blades. The impact velocity ranged between 470m/s and 617m/s. It was noted that as the size of impactor increases, so does the damage, and an increase in the velocity of impact will also increase the damage. Increasing the specimen thickness was found to decrease the amount of impact damage. A three-dimensional finite element analysis was conducted using the DYNA3D code to determine whether it is possible to calculate the critical failure velocity and it was found that the thicker the specimen the higher the critical velocity.

In order to validate a finite element model, experiments in which carbon/epoxy composite panels were impacted by ice spheres of 12.7mm, 21.35mm and 25.4mm radius, at velocities of between 30m/s and 200m/s, were conducted to simulate hail on aircraft structures. The model, created by Kim *et al.* (2000), used F.E. code DYNA3D to simulate the impacts. A linear relationship was found between high velocity impacts, kinetic energy and the impact force. It was also found that the larger impact craters were produced by the smaller projectiles. The numerical results were found to compare well with the experimental results produced.

A three-dimensional finite element analysis was also used by Chen *et al.* (2001, 2002) to determine the relationship between the residual stress intensity factor, the crack size, and the indentation width, due to F.O.D. by metal spheres on titanium alloy blades. A hardened steel sphere of 1.6mm radius was impacted into Ti-6Al-4V alloy specimens at a velocity of between 200m/s and 300m/s. Strain hardening was not considered in the analysis. It was found that at 200m/s, crack initiation occurred underneath the impact crater. It was also postulated that shallow indents can reduce the critical crack size by as much as 60%. No experimental work was carried out to verify these observations; never the less the F.E.A. results did compare well with theoretical results using Hertz's Law.

A different aluminium alloy was investigated by Steif *et al.* (2001), to determine its suitability for use in turbine engines. The material tested was γ-TiAl. A steel sphere of mass $1.64x10^{-5}$kg and 0.8mm radius, travelling at 300m/s with energy of 0.74J, was impacted into the Ti alloy specimen. ABAQUS was used to simulate the impacts. It was noted that impacts near the leading edge of the specimen produced a crack running from the edge of the specimen into the centre. Also, the thicker the specimen tested, the greater its resistance to cracking. Due to the large scatter of fatigue data produced, only a rough correlation between the fatigue strength and the crack size was found, and it was also shown that the fatigue strength is a function of the thickness of the material tested. Additionally, it was postulated that the particle energy has a critical influence on fatigue strength. Predictions of impact crater size were found to be made and were within 10% of experimental results. No other experimental observations were made.

Another study by Ruschau *et al.* (2001) focussed on the influence of high-speed, glass bead impacts on the fatigue strength of simulated airfoil samples, that were made of titanium alloy (Ti-6Al-4V). The glass beads were fired at the samples at a velocity of 305m/s and at varying impact angles of between 0 and 60 degrees. At an impact angle normal to the specimen (0 degrees), compressive residual stresses are located in the region surrounding the impact and residual tensile stresses are located beneath the impact site. However, no F.E.A. was carried out to verify these claims. A large degree of scatter in the results makes it difficult to show trends, but fatigue strength was found to decrease as the impact angle increased. The thickness of samples tested does not appear to affect the fatigue strength after impact; however, it was noted that the deeper the impact crater, the lower the fatigue strength.

A finite element analysis by Boyce *et al.* (2001) on the residual stress distribution associated with a spherical hard body impact, was modelled. The two-dimensional, axi-symmetric, elastic-perfectly-plastic model used a high impact velocity of 300m/s, but a low impact energy, around 6.1J. The model ignored

time dependant effects such as strain rate sensitivity. It showed that compressive stresses are formed in a large area directly beneath the crater and that the most intense stress is located half a crater radius below the crater floor. Also, tensile stresses were to be found at the surface immediately outside the crater rim, with the maximum tensile stresses located one crater radius away from the crater. There was a large discrepancy found between the numerical results and experimental measurements taken. More recent experimental studies by Boyce *et al.* (2003) with titanium alloy blades that had been subjected to impacts by hardened Cr steel spheres, of 0.5mm and 1.6mm radius at velocities between 200m/s and 300m/s, and loads of 9kN to 22kN, were modelled using ABAQUS to visualise the residual stresses within the sample. It was found that the lower the velocity of impact, the greater the fatigue strength.

The fatigue strength of the leading edges of titanium blades that had been impacted with glass beads was found by Martinez *et al.* (2002). Glass beads of 0.5mm radius were impacted into TiAl alloy samples at a velocity of 305m/s, at angles of between 0 and 30 degrees. The samples were diamond in cross-section. Impacted specimens show a reduction in fatigue strength of between 10% and 15%, regardless of the depth of impact produced. Also, there was found to be a reduction in fatigue strength when the impact angle was 30 degrees compared to 0 degrees. However, as only 26 specimens were tested, no clear correlation was found between either notch depth or leading edge thickness and fatigue strength.

Foreign object damage was simulated by firing small radius (0.5mm and 1.6mm) steel spheres at high a velocity of between 200m/s and 300m/s, at a flat specimen of titanium alloy, at angles of between 0 degrees and 30 degrees, by Peters *et al.* (2002). ABAQUS was used to determine the residual stresses for the varying angles of impact. It was found that the angle of impact had no effect on the residual stresses and that the larger diameter sphere caused a greater reduction in fatigue strength. It was postulated that the damage was due to stress concentration, micro crack formation, impact-induced plasticity and tensile

residual stresses around the indent. Fatigue crack growth initiated not only at the impact site but also at locations far from the impact site, in regions of high tensile residual stress.

Further research was carried out by Chen (2005) to produce a more realistic F.O.D. simulation on the leading edge of turbine blades, with the use of a three-dimensional numerical model developed using ABAQUS. The model was produced to simulate a 2mm radius steel sphere impacting Ti-6Al-4V thin sheet at 300m/s. From the numerical results, it was noted that the stress concentration is a maximum at the crater base and is believed to be responsible for fatigue cracking. Residual tensile stress is likely to promote fatigue cracking at the bulge tip and outside the indent where the stress concentration effect is absent. Also, beneath the crater, micro structural damage such as micro-cracks and shear bands, provide a potential site for fatigue cracks to nucleate under high-cycle fatigue loading.

Oakley *et al.* (2007) carried out research to enable predictions to be made on the residual fatigue life of aircraft engine blades after F.O.D., by using an elastic predictive approach based on the arrest of short cracks propagating from a notch. In the experimental work, specimens of Ti-6Al-4V alloy were impacted with 3.2mm cubes of hardened steel, which were fired at a velocity of 180m/s using a gas gun at an impact angle of 135 degrees. In order to determine the residual stresses around the impact area, an X-ray diffraction technique was used. Oakley reported that compressive stresses were found beneath the impact damage. It was also noted that provided the residual stresses were accounted for when predicting the fatigue life of the samples, then the experimental fatigue results were in good agreement with the predicted fatigue results. Due to the fact that a gas gun was used to fire the projectiles, it would not be possible to achieve consistency on the location of impact on the specimen.

Further research in this area was carried out by Dúo *et al.* (2007). Ti-6Al-4V specimens were impacted with cubes (properties unknown) using a gas gun and the residual stresses produced due to impact were measured with a Bruker D8 X-ray diffractometer. These results were then compared with numerical results from previous research undertaken using the LS-DYNA software package. The X-ray results highlighted that there was a compressive residual stress in the area of the impact. However, the three-dimensional model was unable to verify this as the model was only able to show stresses on the front impact side. The F.E. results predicted higher stress values than the experimental results, in some cases up to twice the value, which may have been due to differences in material properties.

To date, research into the foreign object damage of aircraft structures has shown that a single impact can have a detrimental effect on fatigue life. It was also noted that residual stresses have been found outside the impact area, which may have an effect on the fatigue life of a component. Additionally, the research mainly involves high speed, low energy impacts, with small spherical impactors. To date there has been no link made to determine how the size of an indenter will affect the fatigue life of a component.

2.3.5 Failure of Boat Propeller Blades in Ice

Propeller ice-impacts occur frequently on ships that navigate in ice. The impact process raises a strength issue for propeller design and many papers have been published that investigate the propeller response to ice interaction pressures, mainly using the finite element method.

Work has been carried out by Bulat *et al.* (1985), to determine whether scale models of propellers can accurately determine the response of an actual propeller in ice. It was found that the majority of results obtained for both thrust and

torque, were accurate. Synthetic ice was also compared with saline ice and was found to produce the same forces and deformed in similar ways.

Chernuka *et al.* (1989) applied a finite element model to the ice block as well as the propeller blades. Several different propeller geometries were tested, such as rectangular, wedge, circular and elliptical shapes, the results of which showed that pressure distribution is dependant on the indenter shape. The model produced was able to accurately predict pressures when compared with actual indentation tests.

A further propeller ice contact model was produced by Soininen (1998), which looks at the pressure distributions on the ice and propeller blade. However, this paper concentrates more on the pressures and destruction of the ice rather than the effect of impact on the propeller blade.

Research was also conducted by Veitch *et al.* (1993), into the ice blockage affect on propellers. The forces on propeller blades due to an ice blockage are considered, with the opportunity to develop optimum blade designs to minimise the blockage. This area was later developed by Veitch (1994) to see how different shaped propeller blades impact with ice, with the main emphasis on the forces and damage of the ice.

Previous research, which has used numerical modelling to determine the effect of propeller blades impacting ice, has not considered the possibility of any water surrounding the ice, the flow of the ice due to the action of the propeller and the angle of approach of the ice to the propeller blade. To date, the effect of the impact on the fatigue life of the propeller blade has not been considered.

2.3.6 Failure of Ice-Axes

Due to an increase in the popularity of ice climbing, numerous investigations have been carried out into the failures of ice-axes. The research carried out by Haake *et al.* (1997) investigated the dynamic stresses experienced by an ice-axe in normal usage. Photoelastic images were used to try to show evidence of the stress waves and impact; however, this was inconclusive. It was noted that it could be possible to strengthen the axe by widening the pick face and also the addition of teeth, which would reduce the second moment of area and, consequently, increase the stress in the axe.

Further research was carried out by Gordon *et al.* (2006), using F.E.A. to investigate the possible cause of fatigue failure in ice-axes. A two-dimensional, plane stress, bi-linear model with isotropic hardening was developed using ANSYS V9, to simulate the steel (EN24) pick striking a thin layer of ice covering granite rock. The pick was modelled as impacting the semi-rigid surface with a velocity of 9m/s and striking at an angle to the tip of 20 degrees. The weight of the pick was 0.7kg with an impact force of 9.8kN. From the model, it was noted that the time of impact was 0.64ms and the kinetic energy on impact was 28.35J. The rebound velocity was found to be 3.8m/s and the energy absorbed by the pick on impact was 23.31J. These results were compared to those found by Haake *et al.* (1997) and it was noted that the impacted energy was slightly less than that used in the earlier study. Tensile residual stresses were found at the root of a number of the teeth, which could possibly cause a fatigue crack to develop, and also a line of high tensile stress just below the top of the pick was shown. The presence of residual stresses outside the area of impact is in agreement with research carried out by Peters *et al.* (2002), where it was noted that spherical impacts on a specimen of aluminium alloy produced tensile residual stresses at a distance from the impact site.

The research into the failure of ice axes, and the dynamic stresses which result due to impact with the ice, could be linked with the research into propeller blade impacts on ice, which has not considered the effect of the impact on the fatigue life of the propeller blade.

The current research shows that when an impact takes place, the resulting residual stresses are not always located exclusively in the area of impact and it is possible that residual stresses will be found remote of the impact site.

2.3.7 Failure of Reed Valves

Many of the reed valve failures in refrigeration systems are due to impact fatigue. The fatigue originates as surface damage on the reed valve contact surface, which has resulted from impact or twisting of the reed valve. It was reported by Glaeser (1999) that the reed must be free from surface defects, such as dents and scratches, to minimise fatigue. A rough valve seat can also cause stress-raising dents in the reed during impact. Bending of the reed should also be minimised during this process. Extensive work has been carried out into reed valve design to reduce the damage factors that can occur, such as reed overshoot during opening, valve flutter and excessive pressure differentials across the valves. It has been concluded that reeds should be tumbled to reduce sharp edges and shot peening used to improve resistance against fatigue.

2.4 Deficiencies in Previous Research

Research to date has shown that impacts on a component can have significantly different effects on its fatigue life. Overall, previous research into components which have been shot peened show an increase in fatigue life. However, research into foreign object damage of aircraft structures has shown that a single impact can have a detrimental effect on fatigue life. This may be due to the fact that shot peening uses small spherical impactors that are fired at a high velocity, whereas Foreign Object Damage (F.O.D.) mainly uses larger impactors and a lower velocity. Thus far, the effect of the size of indenter and impact energy on the fatigue life of the component has not been determined.

Previous finite element analysis has centred around two-dimensional, axi-symmetric models, which ignore time dependant effects and assume the material to be elastic-perfectly-plastic. The current research aims to determine both experimentally and with the use of a three-dimensional numerical model, how the size of an indenter will affect the fatigue life of a specimen. Low speed, high energy impacts will be considered in the investigation. The transient dynamic finite element model, which will consider time dependent effects, will be used to show the residual stresses in specimens after a single impact and also any effect on the properties and geometry on the periphery of the specimens.

By determining the effect of the size of indenter on the fatigue life of the component and consequently highlighting sizes of indenter which could prove either detrimental or beneficial to the component, the outcomes of the study could be used in many engineering applications; such as shot peening, aircraft structures and components, boat propellers, car body panels and parts, and numerous other applications in which a metal structure or component may be subjected to an impact.

Chapter 3: EXPERIMENTAL METHODOLOGY

This chapter will describe the experimental apparatus, the single impact and fatigue tests undertaken, and will also detail the materials used and methodology followed.

3.1 Specimens

The specimens used in the experimental programme were made from two different types of cold-rolled, mild steel strip. Preliminary tests were carried out on the first material, Bending Quality Bright Steel (BS1449), in order to determine the validity of measurements taken. The second material tested was '070M20' Carbon Steel (BS970). Figures 3.1 and 3.2 show the size and shape of the specimens used in testing.

The materials were chosen as they are both types of mild steel that are not only easily obtainable but also widely used for many engineering components. It was important that the materials tested were cold rolled, as the cold working of metals is frequently used in the finishing stage of production to achieve a smooth finish. When a metal is cold worked, the lattice crystal structure is deformed and the grains are elongated in the direction the material is being rolled. Consequently, the surface of the metal becomes harder and smoother, and the ductility is lessened. The resulting hardness is due to the residual compressive stresses produced by the pressure of the rollers on the surface of the metal. If a light roller pressure is applied a shallow layer of residual compressive stress will occur on the surface of the metal, with small residual tensile stresses induced in the core. However, if a high roller pressure is applied a deep layer of residual compressive stresses will occur on the surface of the metal, with large residual tensile stresses in the core, which can lead to subsurface fatigue cracks.

The size, shape, preparation and surface finish of all specimens were in accordance with *BS3518-3:1963 Methods of Fatigue Testing – Part 3: Direct stress fatigue tests.*

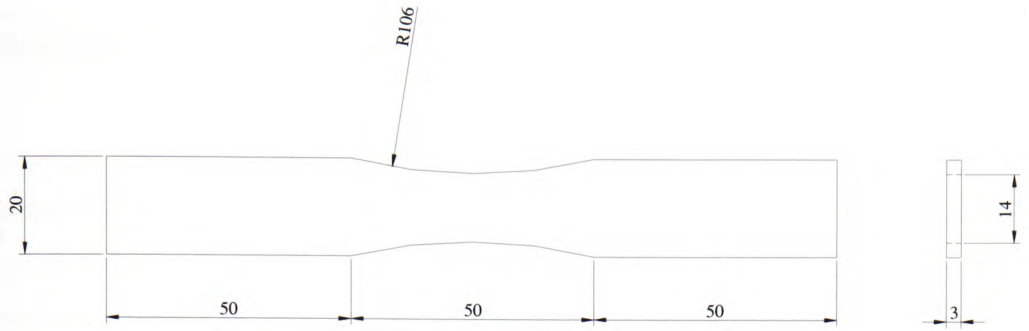

Figure 3.1: Dimensions (in mm) of a typical specimen

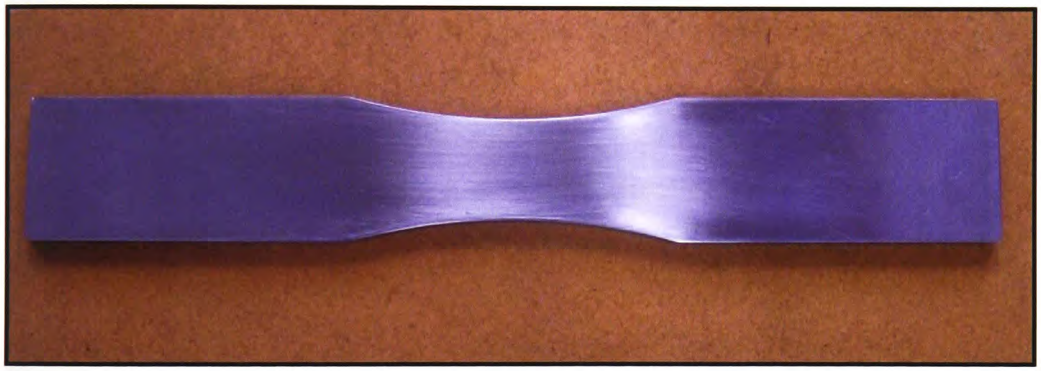

Figure 3.2: Polished specimen

The specimens were first ground and then hand polished with 600 grit silicon carbide paper, so that the finished test piece had a surface texture, measured as the Centre Line Average (CLA), of no greater than 5μm. As recommended in BS3518-3, the polishing was carried out in both transverse and longitudinal directions, with the direction of final polishing in the longitudinal direction. The preparation of the specimen was very important because the free surface of a specimen, or component, is a common site for the nucleation of fatigue cracks. Therefore, the way the surface is prepared during manufacture has a significant

effect on the initiation of cracks and, consequently, the fatigue life of the component. As well as the surface roughness, residual stresses may be induced in the surface layer by the manufacturing process. If these stresses are tensile they can have a detrimental effect on fatigue life and polishing helps to reduce these stresses.

Using a Talysurf 5-20 Taylor-Hobson machine, which is shown in Figure 3.3, the surface texture both before and after polishing was measured, with each value recorded being the average of three readings taken at random places on the transverse surface of the specimen. From every batch of six polished specimens, one specimen was chosen at random to test the surface texture. The width and thickness of the specimen were also recorded to ensure that all specimens had been consistently manufactured. Following the measurements, the tested specimen was discarded as the surface became heavily marked by the Talysurf's stylus arm, which could have resulted in the initiation of surface cracks and thus would have had a detrimental effect on fatigue life.

It was noted that the tests carried out in the experimental programme had no effect on the surface texture, and it was therefore decided that the surface texture could be determined for every specimen after tests were completed, to ensure that they meet the requirements previously mentioned. At all stages of the experimental programme the polished specimens were handled using latex gloves, in order to prevent scratching and corrosion due to skin oils.

Tensile tests were carried out on the two mild steels to determine the material properties, which would be used as initial conditions for the numerical model and also would enable a suitable load to be determined for fatigue tests, that would be below the yield point. Nine specimens from each batch of material were produced as detailed in Figure 3.4 and then tensile tested using a Hounsfield H20K-W Tensometer, as shown in Figure 3.5.

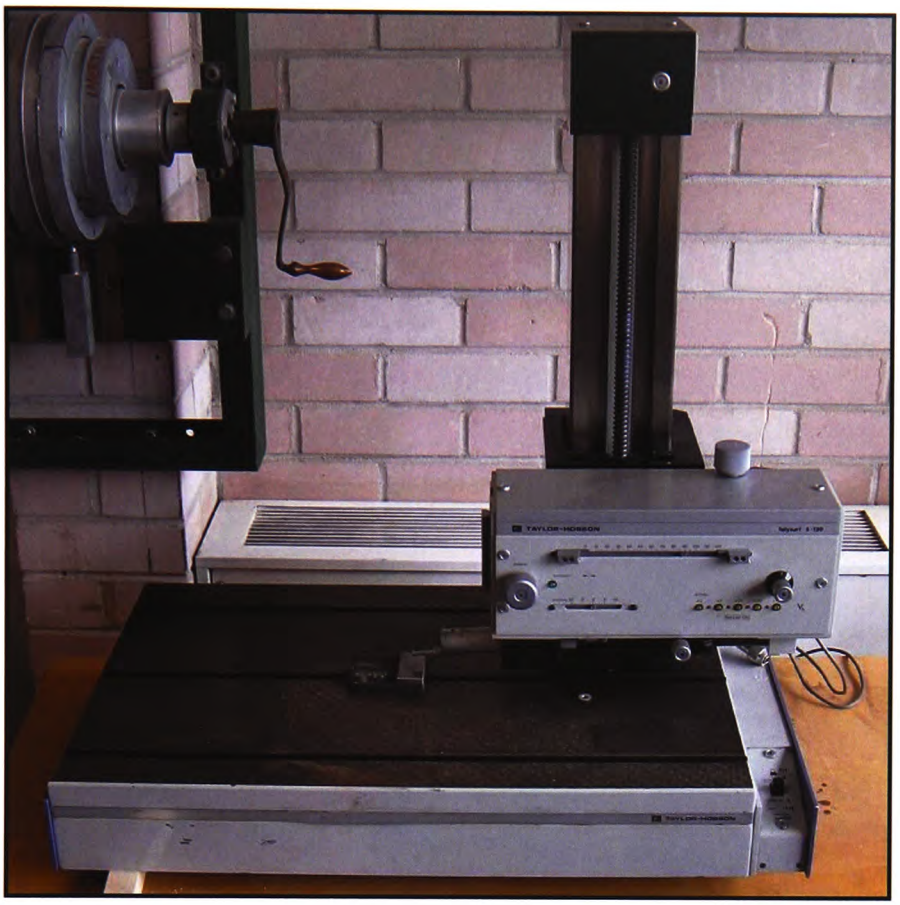

Figure 3.3: Talysurf 5-20 Taylor-Hobson machine

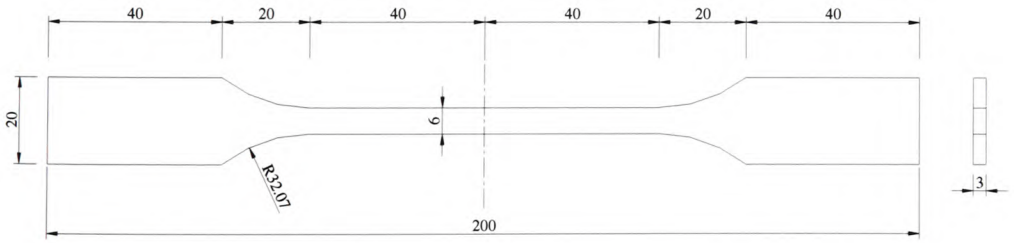

Figure 3.4: Dimensions (in mm) of tensile test specimen

Figure 3.5: Hounsfield H20K-W Tensometer

It was important to determine the hardness of each specimen at the end of the experimental work. The term "hardness" [of a material] can refer to the resistance to indentation, abrasion, machining or scratching, (Bailey, 1964). The hardness of a material is found to be related to both the yield strength and the tensile strength of the material. Rockwell hardness tests, first introduced by Rockwell in 1922, were carried out using a Wilson Rockwell Hardness Tester, as shown in Figure 3.6. The Rockwell hardness number is a measure of the depth of penetration of a standard indenter. There are nine scales of hardness which could be used in this test; the most common scale used is scale 'C'. In scale 'C', a minor load of 98.1N (or 10kgf) is applied to a 120 degrees diamond cone indenter, the dial indicator set to zero and the load is then increased to 1471.5N (or 150kgf). Once the load has been applied and the dial indicator has settled, the load is removed and the hardness value can be read off the dial indicator. Testing the hardness of the specimens made it possible to ascertain whether any work-softening or work-hardening of the material had taken place during the

fatigue test. It is also necessary to ensure the consistency of the material tested, as a change in the hardness of the material due to manufacturing and finishing processes would cause a spread of results.

Figure 3.6: Wilson Rockwell Hardness Tester

3.2 Impact Rig

The manufacturing drawings for the impact rig designed by the candidate can be found in Appendix 1. The impact rig was made primarily from mild steel sections. However, the back plate, which the specimen was held against during impact, was made from polished, hardened gauge steel; this was to ensure that the specimen remained flat during the impact and helped to eliminate surface damage to the specimen.

The single row, deep groove ball bearings used on the impactor arm axle were chosen because they could withstand the dynamic loading produced by the impact, and also allow free movement of the impactor arm. Figure 3.7 shows the manufactured impact rig.

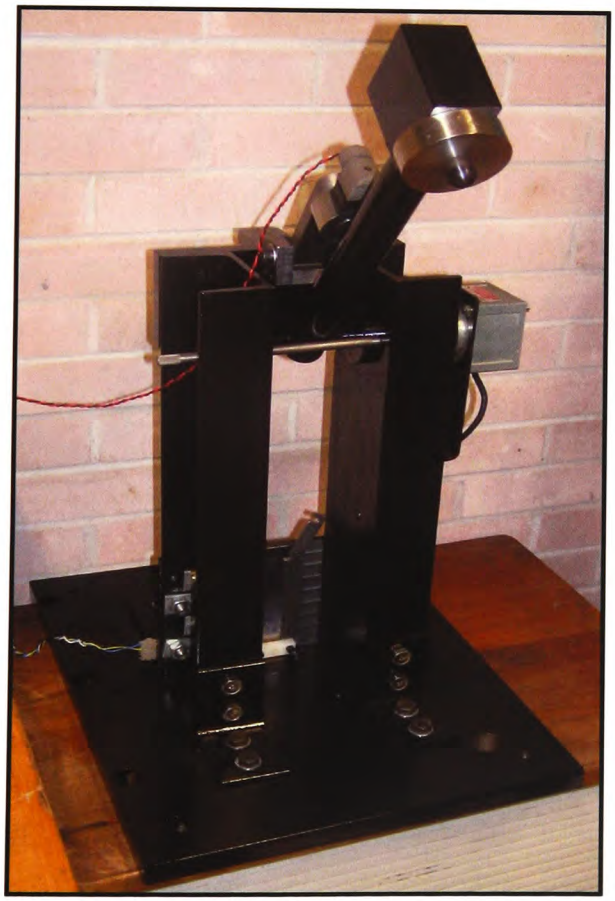

Figure 3.7: Impact rig

The impactor hammer head was held at the specified angle for impact by the use of a Stephenson Gobin Magnet Type 58 electromagnet, as shown in Figure 3.8. When the power supply to the electromagnet was switched off, the impactor hammer head was released and fell freely.

To ensure the specimen was placed safely in the holder on the impact rig, a safety bar was used in conjunction with the electromagnet. The bar could then be removed before the test started and when the electromagnet was switched off, the impact of the specimen took place.

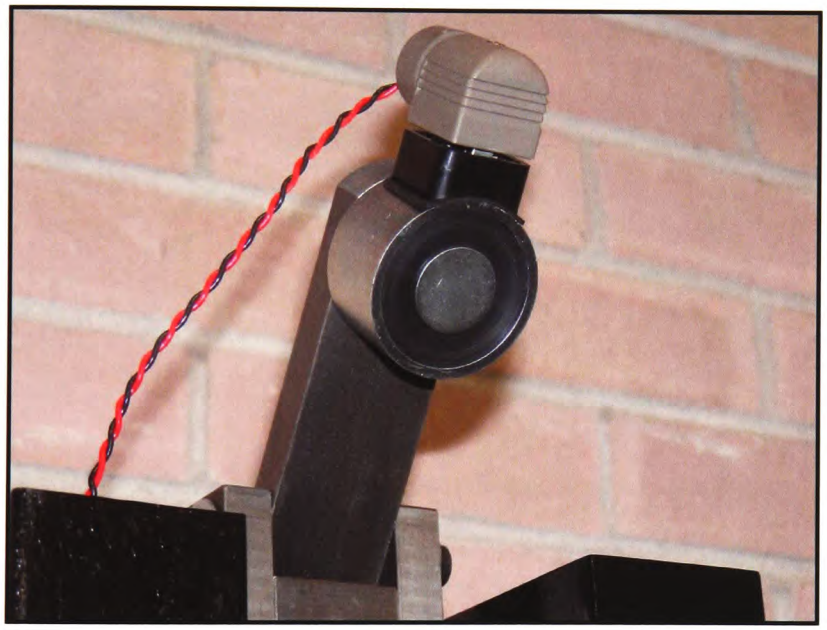

Figure 3.8: Stephenson Gobin Magnet Type 58 electromagnet

3.3 Impactor Hammer Heads

The impactor hammer heads consisted of hardened, silver steel (BS1407), hammer heads which located into a base/holder of stainless steel. The silver steel hammer heads were hardened to ensure that the surface had a greater hardness than the surface of the specimen. If the hammer head had a hardness value

which was the same or lower than the hardness value of the specimen, the hammer head would deform on impact and repeat tests would become inconsistent. Also, less impact energy would be dissipated into the specimen, as some energy would be used in the deformation of the hammer head. Hardness tests were carried out using a Wilson Rockwell Hardness Tester, (Figure 3.6).

The hammer heads were manufactured to the required dimensions, as illustrated in Figure 3.9. They were then heated to 800°C and held at that temperature for 60 minutes. The final step in the hardening process was to rapidly quench the hammer heads to 300°C in oil; this transformed the austenite structure on the surface of the hammer head to martensite, which is the hardest structure in steel. The hammer heads were then allowed to cool in air to room temperature.

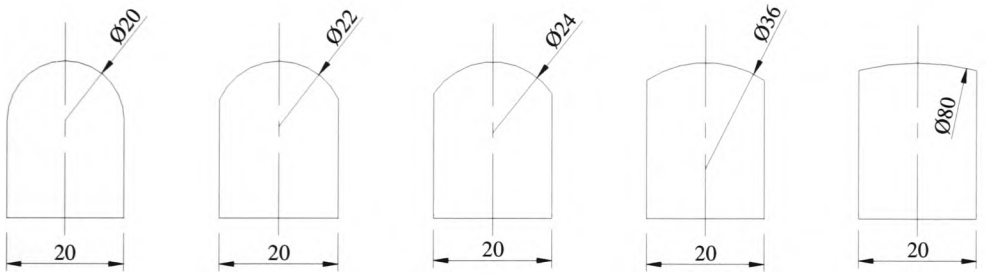

Figure 3.9: Dimensions (in mm) of impactor hammer heads

Tensile tests using the Hounsfield H20K-W Tensometer and Extensometer were carried out on eleven sample specimens of the hardened, silver steel used to make the hammer heads. The tensile test specimens produced were 5.05mm diameter and 25.5 mm long, as shown in Figure 3.10.

Figure 3.10: Silver steel before hardening process (top of picture) and hardened silver steel (bottom of picture) tensile test specimens

To investigate what effect the size of an impacting object has on the fatigue life of a specimen, the hammer heads were produced in five sizes; 10mm, 11mm, 12mm, 18mm and 40mm radii. A selection of impactor hammer heads is shown in Figure 3.11. The 10mm and 40mm radii hammer heads were chosen to provide a considerable difference in the surface area of the head that would be in contact with the deformed specimen during impact. The 12mm radius hammer head was chosen because it was calculated to produce a contact surface area which is double that produced by the 10mm hammer head and half that produced by the 40mm hammer head. The 11mm and 18mm radius hammer heads produce a contact surface area which is equidistant between the contact areas produced by the 10mm and 12mm, and the 12mm and 40mm impact hammer heads respectively.

The impactor hammer heads were designed so that they all have the same mass and the same length, 48.6 grams and 42mm respectively. This was to ensure that they impacted the specimen not only with the same energy and velocity, but also in the same position. An impactor hammer head in position before an impact test

is shown in Figure 3.12, and a specimen which has been subjected to a single impact is shown in Figure 3.13.

In order to determine whether it was possible to use the experimental results obtained for the five sizes of impactor heads to calculate experimental results for different sized impactor heads, a 25mm radius impactor hammer head was produced and tested so that a comparison could be made between the calculated and the experimental results.

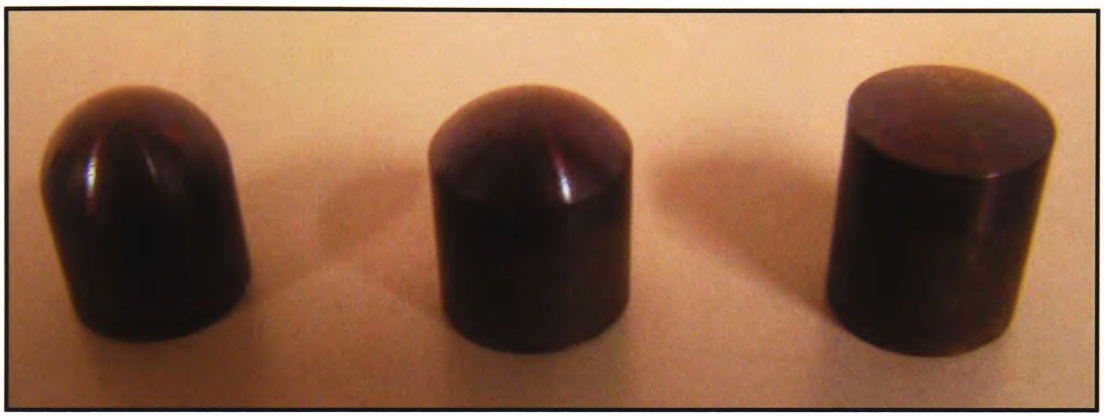

Figure 3.11: Selection of the impactor hammer heads (left to right: 10mm, 12mm and 40mm radii)

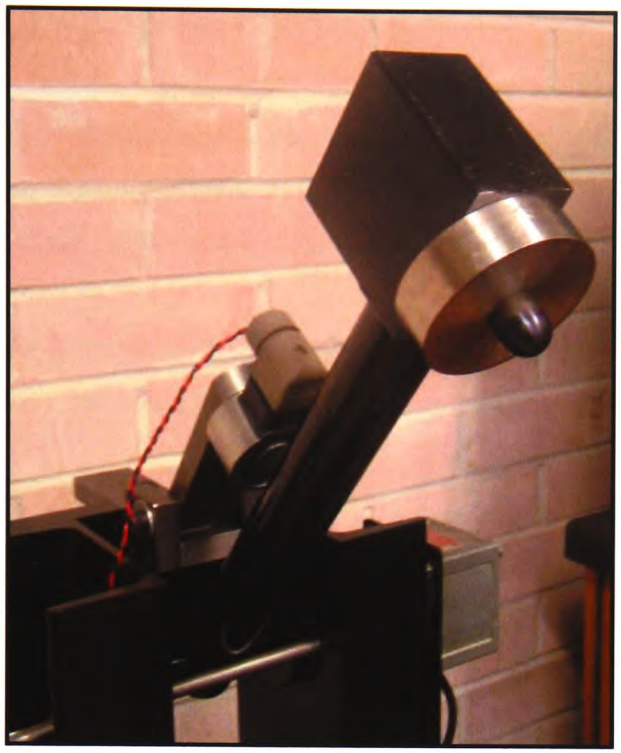

Figure 3.12: Impactor hammer head on impact rig

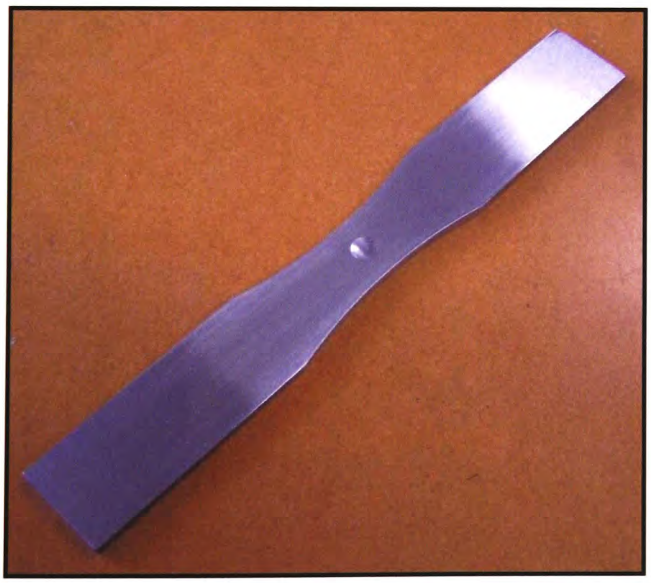

Figure 3.13: A specimen subjected to a single impact using the 10mm radius impactor hammer head

3.4 Depth and Width of Impact Crater

From every batch of thirteen specimens that were impacted using the same size impactor hammer head, one specimen was chosen at random to measure the depth and width of the impact crater produced.

Using a 'Metallux 2' microscope, as shown in Figure 3.14, the width of impact crater that had been produced by the different size impactor hammer heads was measured.

Figure 3.14: A 'Metallux 2' microscope

The depth of the impact crater produced was measured using a 'Mitutoyo Absolute 1D-F125E' linear variable displacement transducer, as shown in Figure 3.15. This specimen was then discarded, as the surface became heavily marked by the transducer and was unable to be used in any further testing.

Figure 3.15: A 'Mitutoyo Absolute 1D-F125E' linear variable displacement transducer

3.5 Velocity and Energy of Impact

The height and angle of the impact arm can be easily adjusted but remained in a fixed position for the initial part of the research programme. This was to ensure that the position, velocity and input energy for each impact was consistent throughout each section of the experimental programme. The mass of the impactor hammer head is 3.52kg.

3.5.1 Material 1 - Bending Quality Bright Steel

For the single impacts on the bending quality bright steel specimens, the height of the impact arm was set to 0.5m, at an angle of 105 degrees. From conservation of energy calculations, the potential energy possessed by the impactor was determined to be 17.27J and the velocity of impact 3.13m/s. The velocity will be verified using the instrumentation on the impact rig, as detailed in Section 3.6.

3.5.2 Material 2 - '070M20' Carbon Steel

With the second material, '070M20' Carbon Steel, the height of the impact arm was set to 0.41m, at an angle of 90 degrees. The height of the impact arm was altered from that used for the first batch of material (the Bending Quality Bright Steel), as it was found that the initial impact energy was too high for the material, which resulted in a slight bending in the specimens after impact. The fatigue tests on the specimens, which were carried out after impact, were performed on an axial loading machine, and so it was important that the specimens were not laterally deformed, as any bending would result in the specimen not being uniformly stressed and would cause specimens to buckle during the fatigue tests. From conservation of energy calculations, the potential energy possessed by the impactor was determined to be 14.16J and the velocity of impact 2.84m/s. The

velocity will be verified using the instrumentation on the impact rig, as detailed in Section 3.6.

3.6 Instrumentation

In order that the numerical model produced realistic results, it was important to define parameters such as the time of the impact, which can be determined using an accelerometer. The acceleration of the impactor hammer head was measured by the Bruel and Kjaer accelerometer type 4344 (resolution of ±5%), which was located on the impact rig behind the specimen. It was possible to analyse the accelerometer data produced to determine the contact time of impact.

One of the results produced by the numerical model was the exit velocity of the impact and in order to determine the accuracy of these results, it was necessary to measure the actual exit velocity of the impact. It was possible to do this and also measure the actual entry velocity of the impact, with the use of a potentiometer (Penny and Giles Industrial Angular Position Sensor 762, which is a hybrid track, industrial sensor with a 355^0 electrical angle). The voltage change measured by the potentiometer can be used to calculate the angular distance travelled by the impactor arm. This angular distance can then be used to calculate both the entry and exit velocity of the impact. The calculations performed using the potentiometer results are discussed further in Chapter 4.2.2 and the potentiometer used on the impact rig is shown in Figure 3.16.

Additionally, the values for the entry velocity of the impact can be used to calculate the energy of the impact and the values of the exit velocity can be used to determine the energy absorbed during impact.

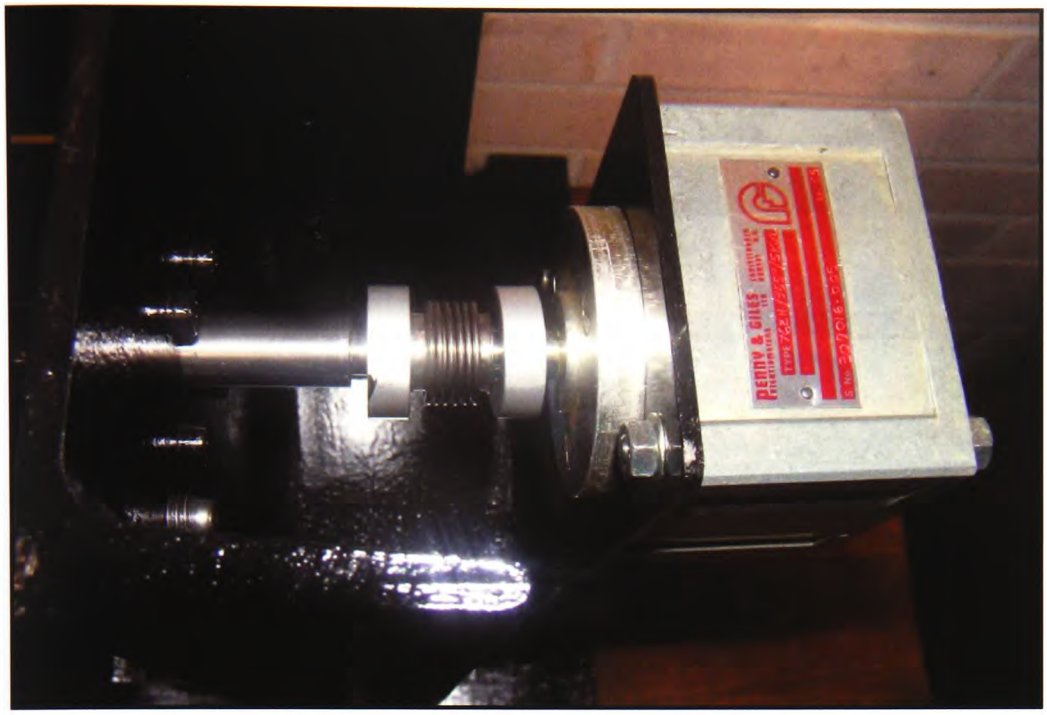

Figure 3.16: Potentiometer - Penny and Giles Industrial Angular Position Sensor 762

3.7 Fatigue Testing

The Instron FastTrack 8502 Axial Torsion floor model, shown in Figure 3.17, was used to carry out the fatigue tests on the specimens. From guidelines set out in *BS3518-1:1993 Methods of Fatigue Testing - Part 1: Guide to General Principles*, it was decided that twelve specimens should be used for each test. In the initial section of the experimental programme it was necessary to obtain control data for the fatigue tests. Specimens were located in the Instron's hydraulic jaws, with the use of spacers to ensure consistency in the span between the jaws and, thus, the length of specimen being loaded during the fatigue tests. A control specimen under fatigue test is shown in Figures 3.18 and 3.19. A control specimen which has fractured after being subjected to fatigue testing is shown in Figure 3.20. The experimental procedure followed for the initial fatigue tests was then repeated for specimens that had been subjected to a single

impact using one of the specified impactor hammer heads. Twelve specimens were impacted, and fatigue tests carried out, for each of the five impactor hammer heads. A specimen subjected to a single impact and then fatigue tested to failure is shown in Figure 3.21. The data obtained from all of the fatigue tests can then be plotted on an S-N diagram and comparisons made.

Figure 3.17: Instron FastTrack 8502 Axial Torsion floor model

Figure 3.18: Control specimen under fatigue test

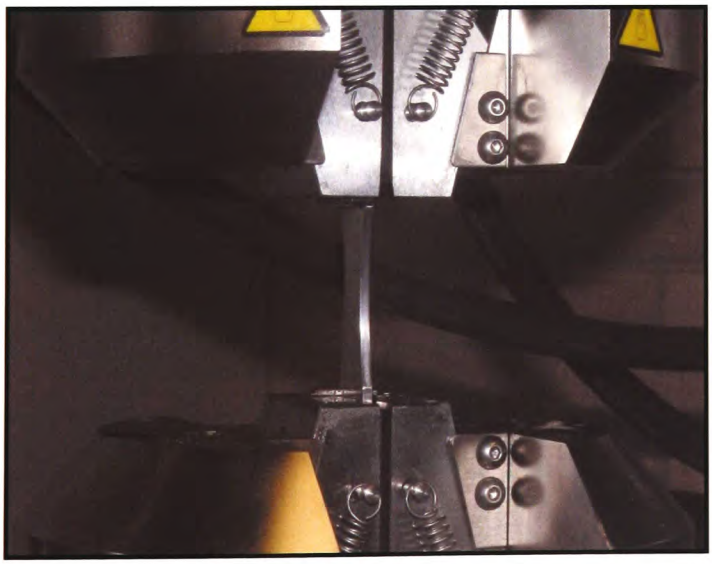

Figure 3.19: Control specimen under fatigue test (enlarged)

Figure 3.20: Control specimen subjected to fatigue test

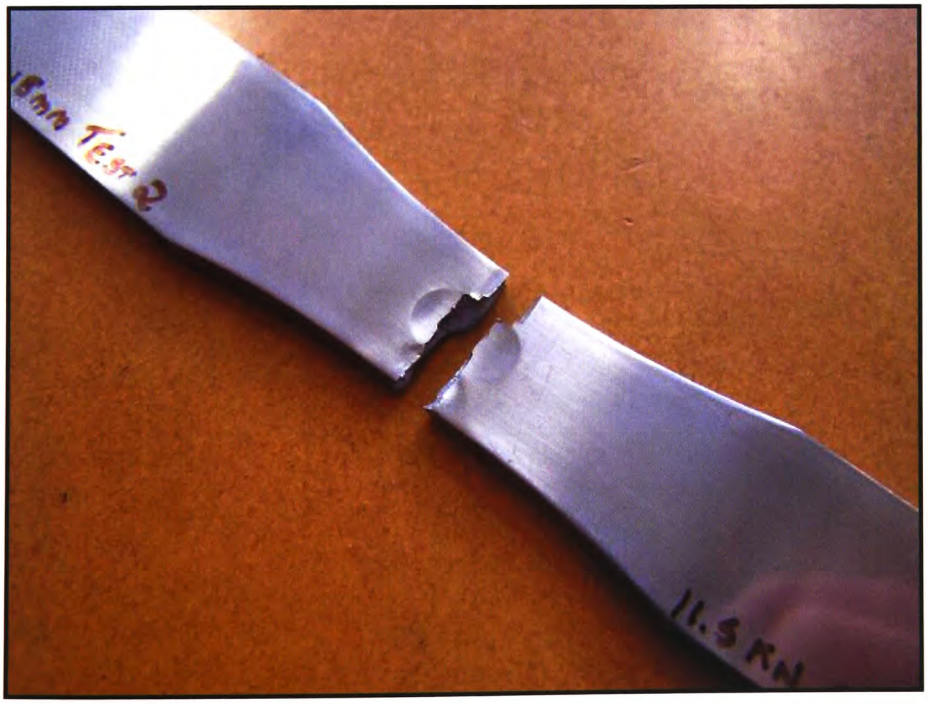

Figure 3.21: An impacted specimen subjected to fatigue test

3.8 Summary of Experimental Methodology

A summary of the parameters measured, the equipment and reasons for the measurements taken, are shown in Table 3.1.

Parameter Measured	Equipment	Purpose
Exit Velocity of Impact	Potentiometer (Penny and Giles IAPS 762)	To validate finite element model results.
Impact Contact Time	Accelerometer (Bruel and Kjaer type 4344)	
Depth of Impact Crater	Linear variable displacement transducer (Mitutoyo Absolute 1D-F125E)	
Width of Impact Crater	Microscope (Metallux 2)	
Material properties (tensile tests)	Tensometer (Hounsfield H20K-W Tensometer)	Parameters required for finite element model.
Entry Velocity of Impact	Potentiometer (Penny and Giles IAPS 762)	
Cycles to failure	Fatigue testing (Instron FastTrack 8502)	For analysis of fatigue results.
Specimen dimensions	Digital callipers (Mitutoyo Absolute Digimatic)	
Surface finish	Surface texture measurer (Talysurf 5-20 Taylor-Hobson)	
Specimen hardness	Rockwell hardness tester (Wilson)	
Entry Impact Energy	Potentiometer (Penny and Giles IAPS 762)	
Exit Impact Energy	Potentiometer (Penny and Giles IAPS 762)	

Table 3.1: Summary of experimental methodology

Chapter 4: EXPERIMENTAL RESULTS

This chapter will present both the experimental results obtained and the observations made during the experimental programme for all material, impact and fatigue tests carried out and, where appropriate, a discussion on how these results were interpreted and the possible factors that may have influenced them.

Please note that results which were deemed invalid due to experimental or human error will be shown as a blank result. A summary of the parameters measured, together with the equipment used including calibration information and possible errors, can be found in Appendix 2.

4.1 Impactor Hammer Head Material Properties

Tensile tests to determine the Young's Modulus of the hardened, silver steel that was used to make the hammer heads were carried out using the Hounsfield H20K-W Tensometer and Extensometer, on eleven sample specimens. The results are presented in Table 4.1. The average Young's Modulus of the hardened, silver steel was found to be 202.227GN/m^2 (SD 5.901), which was used as a set-up parameter for the impactor hammer head in the numerical models.

The stress/strain graph obtained for specimen number three is shown in Figure 4.1. The non-linearity of the graph up to 30.1MN/m^2 is due to the slack in the load train at the start of the test.

The hardness of the material was found to be 59 Rockwell C (SD 2) which is equivalent to 741 DPN. The hardness results are presented in Table 4.2. These results were necessary to make certain that the impactor hammer heads were harder than that of the specimens; this was to ensure that no deformation of the

impactor hammer head occurred on impact for the repeatability of impact tests, as previously mentioned in Section 3.3.

Specimen Number	Young's Modulus (GN/m^2)
1	194.583
2	208.559
3	203.206
4	210.724
5	201.587
6	199.577
7	205.398
8	206.890
9	203.950
10	191.119
11	198.907
Average	**202.227**
SD	**5.901**

Table 4.1: Young's Modulus results for hardened silver steel

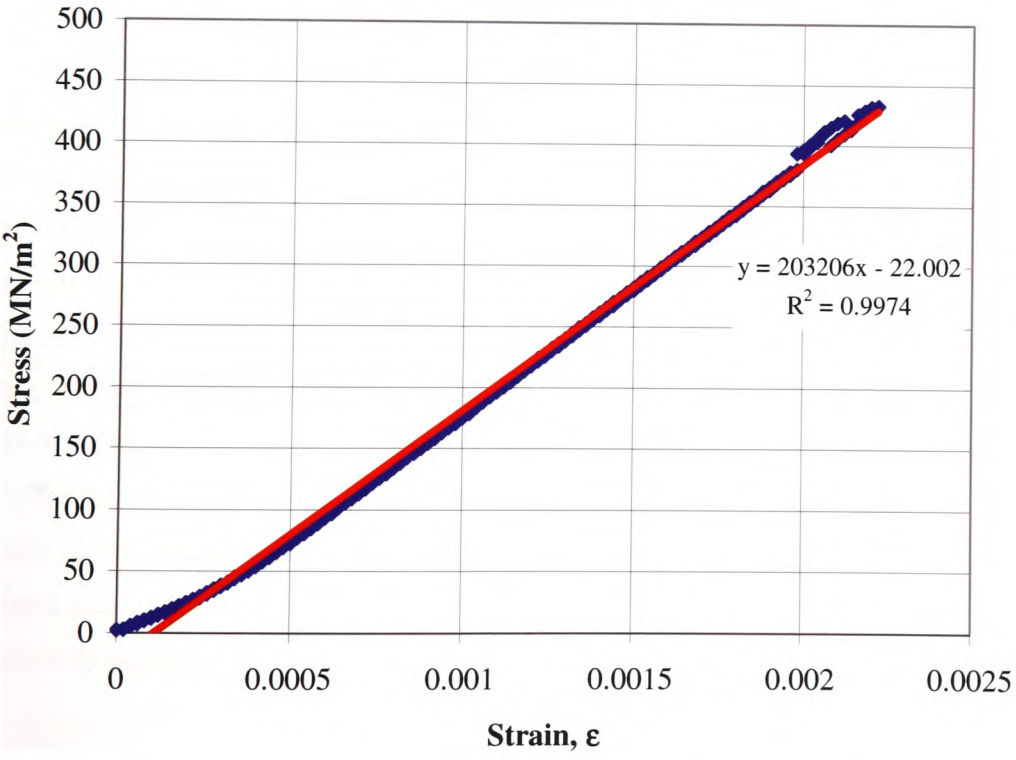

Figure 4.1: Hardened silver steel specimen stress/strain graph

Specimen Number	Hardness (Rockwell C)
1	59
2	56
3	61
4	60
5	58
6	60
7	55
8	59
9	60
10	61
11	59
Average	**59**
SD	**2**

Table 4.2: Hardness results for hardened silver steel

4.2 Specimen Material 1 – Bending Quality Bright Steel

Preliminary tests were carried out on bending quality bright steel specimens, in order to verify both the experimental test procedures used and the results obtained. Initially, tensile tests using the Hounsfield H20K-W Tensometer and Extensometer were carried out on seven sample specimens of the bending quality bright steel that was used to make the specimens, in order to determine both the Young's Modulus and yield stress of the material. These tests were conducted at a rate of 2mm per minute. It is important to identify the rate of straining, as this will alter the structure and properties of a material that is strain rate dependant. A high strain rate will decrease the materials ductility whilst increasing its hardness and strength. A low strain rate will increase the materials ductility and decrease its hardness and strength.

The results are presented in Table 4.3. The average Young's Modulus was found to be 194.136GN/m^2 (SD 13.706) and the average yield stress 372.29MN/m^2 (SD 37.99). These values have been used as set-up parameters for the specimen in the numerical model. The stress/strain graphs obtained for specimen number four are shown in Figures 4.2 and 4.3.

Specimen Number	Young's Modulus (GN/m^2)	Yield Stress (MN/m^2)
1	166.158	424.24
2	193.514	333.33
3	195.152	424.24
4	193.635	333.33
5	196.628	363.63
6	204.800	363.63
7	209.062	363.63
Average	**194.136**	**372.29**
SD	**13.706**	**37.99**

Table 4.3: Tensile test results for bending quality bright steel

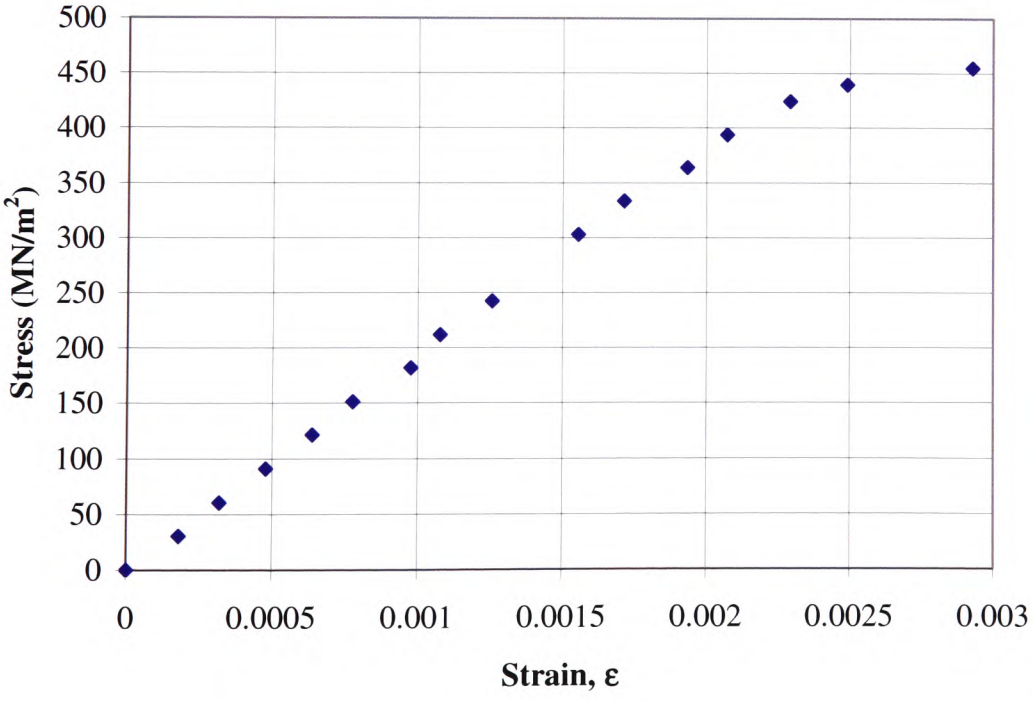

Figure 4.2: Bending quality bright steel specimen stress/strain graph (1)

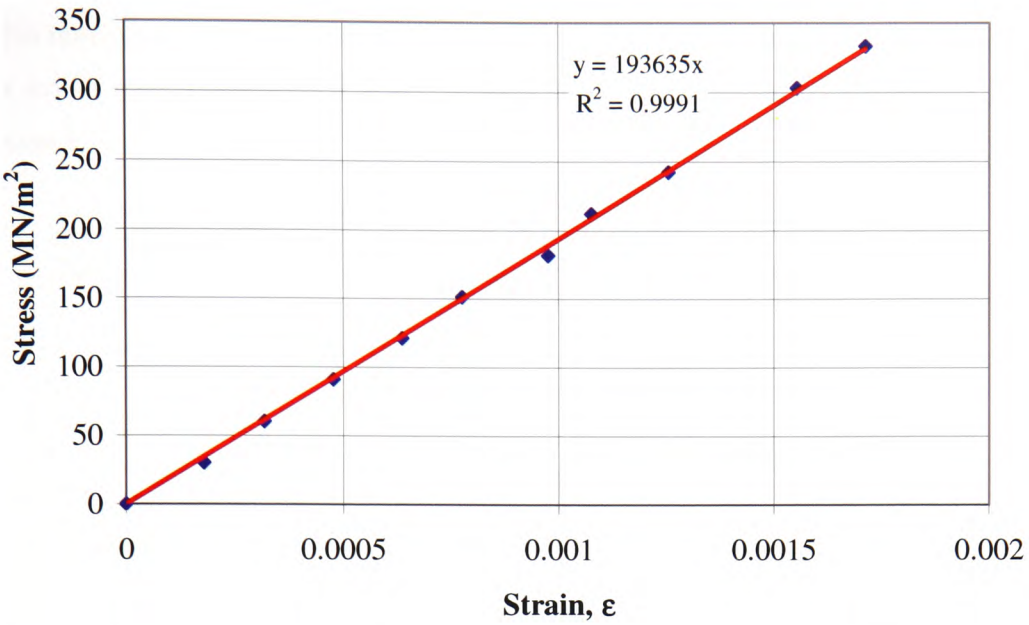

Figure 4.3: Bending quality bright steel specimen stress/strain graph (2) linear section only to determine Young's Modulus

Fatigue tests were carried out on the test specimens, shown in Figure 3.1, of bending quality bright steel, at a sinusoidal load of ±16kN, equivalent to a stress of 381MN/m^2, at 2 cycles a second, or 2Hz. This load was chosen so that the specimen would fail in fatigue whilst ensuring that the load would remain within the elastic limit of the material. The fatigue load of 16kN was calculated by using the yield stress obtained from the tensile tests together with the cross-sectional area of the specimen which was calculated from the design dimensions to be 42mm^2.

The failure stress for each specimen to be fatigue tested was then calculated using the fatigue load of 16kN and the actual cross-sectional area of the specimens, which was measured to be approximately 41mm^2. The control specimen dimensions and calculated failure stresses are shown in Table 4.4. The failure stresses calculated are very close to the yield stress of the material, this is probably due to the experimental errors that occur when measuring the dimensions of the specimens and calculating the yield stress. Accurate measurement of the specimens' dimensions proved difficult using digital

callipers, as it was important not to mark the surface of the specimens in any way as this may cause marking that might result in the initiation of surface cracks and thus would have a detrimental effect on fatigue life, as previously mentioned in Section 3.1.

Specimen Number	Width of Specimen (mm)	Depth of Specimen (mm)	Cross-sectional Area of Specimen (mm^2)	Stress (MN/m^2)
1	14.10	3.00	42.30	378.25
2	14.13	2.96	41.82	382.55
3	14.07	2.91	40.94	390.78
4	14.07	2.96	41.65	384.18
5	14.10	2.97	41.88	382.07
6	14.07	2.93	41.23	388.11
7	14.15	2.97	42.03	380.72
8	14.03	2.96	41.53	385.27
9	14.03	2.97	41.67	383.98
10	14.07	2.96	41.65	384.18
11	14.04	2.96	41.56	385.00
12	14.05	2.93	41.17	388.67
13	14.03	2.92	40.97	390.55
14	14.02	2.92	40.94	390.83
15	14.02	2.92	40.94	390.83
16	14.04	2.92	40.99	390.27
17	14.02	2.96	41.50	385.55
18	14.10	2.93	41.31	387.29
19	14.00	2.92	40.88	391.39
20	14.06	2.92	41.06	389.72
21	14.08	2.93	41.25	387.84
22	14.05	2.91	40.89	391.34
23	14.10	2.95	41.60	384.66
24	14.07	2.96	41.65	384.18
25	14.08	2.92	41.11	389.16
26	14.07	2.97	41.79	382.88
27	14.10	2.90	40.89	391.29
28	14.04	2.91	40.86	391.61
29	14.09	2.94	41.42	386.24
30	14.08	2.94	41.40	386.52
31	14.03	2.90	40.69	393.25
Average	**14.06**	**2.94**	**41.34**	**387.07**
SD	**0.03**	**0.02**	**0.40**	**3.77**

Table 4.4: Initial control specimen dimensions and failure stresses

Using a Talysurf 5-20 Taylor-Hobson machine, the surface texture, measured as the Centre Line Average (CLA) of the specimens after polishing was found to be 0.112μm (SD 0.006). This was achieved by taking three readings at random places on the surface of the specimen and an average calculated, as shown in Table 4.5. The surface texture results of the control specimens after fatigue testing are shown in Table 4.6. It can be seen that the average surface texture, measured as the CLA is 0.21μm (SD 0.061). This value was found to be slightly higher than the specimens which were not fatigue tested, but it is still less than 5μm as recommended by BS3518-3.

	Surface Texture after Polishing (μm)
Reading 1	0.117
Reading 2	0.113
Reading 3	0.106
Average	**0.112**
SD	**0.006**

Table 4.5: Surface texture results for bending quality bright steel prior to testing

Shown in Table 4.7 and Figure 4.4 are the fatigue test results for the initial control tests and it can be seen that the average number of cycles to failure is 66,530 cycles (SD 18,748). These results can be used to determine the effect of a single impact on the fatigue life of a specimen.

The impacted specimen dimensions and calculated failure stresses are shown in Table 4.8. The surface texture results of the impacted specimens are shown in Table 4.9. It can be seen that the average surface texture, measured as the CLA, is 0.215μm (SD 0.046). This value was found to be slightly higher than specimens which were not fatigue tested, but is still less than 5μm as recommended by BS3518-3. The surface texture results also indicate that there is no difference between the surface texture of the impacted and the control specimens so the surface of the specimens do not incur any surface damage during impact. With the equipment available it is not possible to measure the

surface texture of the impacted area of the specimens in order to determine whether any significant surface damage has been sustained due to the impact.

Specimen Number	Surface Texture (μm)
1	0.224
2	0.188
3	0.253
4	0.144
5	0.256
6	0.126
7	0.274
8	0.187
9	0.163
10	0.150
11	0.186
12	0.165
13	0.254
14	0.177
15	0.189
16	0.210
17	0.183
18	0.179
19	0.170
20	0.173
21	0.266
22	0.243
23	0.296
24	0.177
25	0.212
26	0.378
27	0.132
28	0.149
29	0.225
30	0.346
31	0.225
Average	**0.21**
SD	**0.061**

Table 4.6: Surface texture results for initial control specimens

Specimen Number	Cycles to Failure
1	78,185
2	86,348
3	48,349
4	98,045
5	50,760
6	61,449
7	75,611
8	64,525
9	57,026
10	99,246
11	91,597
12	67,509
13	36,584
14	83,272
15	63,691
16	34,792
17	92,689
18	68,106
19	86,612
20	62,357
21	49,723
22	54,871
23	75,005
24	42,419
25	49,084
26	91,346
27	41,415
28	58,295
29	64,493
30	80,932
31	48,119
Average	**66,530**
SD	**18,748**

Table 4.7: Number of cycles to failure for initial control specimens

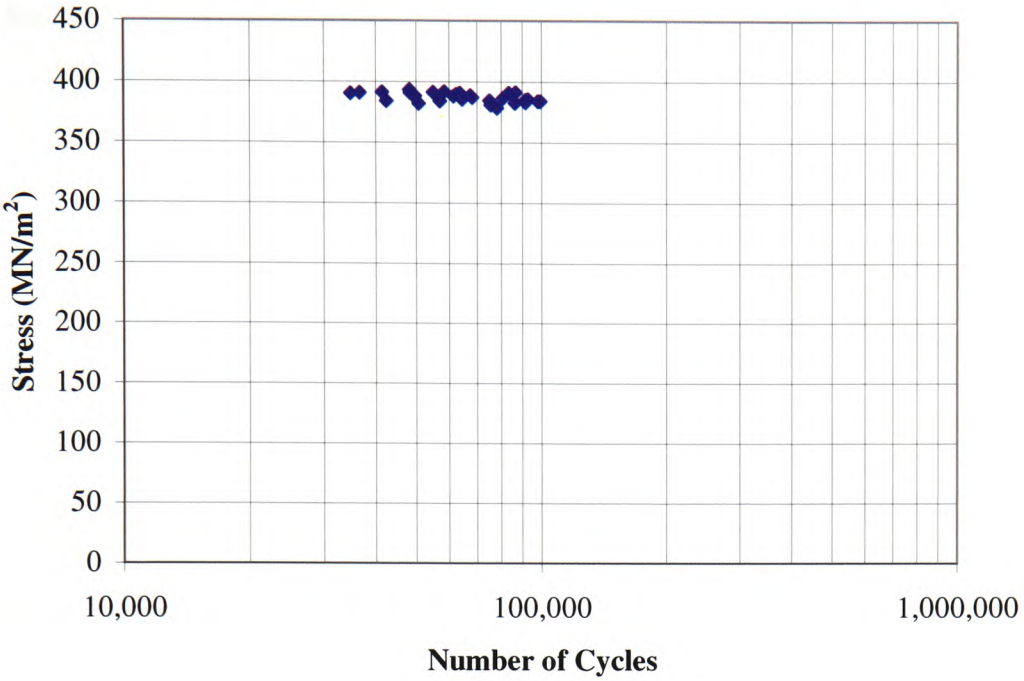

Figure 4.4: S-N Diagram for initial control fatigue tests for bending quality bright steel

Specimen Number	Width of Specimen (mm)	Depth of Specimen (mm)	Cross-sectional Area of Specimen (mm^2)	Stress (MN/m^2)
1	14.11	2.92	41.20	388.34
2	14.08	2.91	40.97	390.50
3	14.11	2.94	41.48	385.70
4	14.07	2.93	41.22	388.11
5	14.08	2.97	41.82	382.61
6	14.09	2.94	41.42	386.24
7	14.18	2.97	42.11	379.92
8	13.99	3.00	41.97	381.22
9	14.11	2.93	41.34	387.01
10	14.06	2.92	41.05	389.72
11	14.14	2.96	41.85	382.28
12	14.11	2.97	41.91	381.80
Average	**14.10**	**2.95**	**41.53**	**385.29**
SD	**0.05**	**0.03**	**0.39**	**3.59**

Table 4.8: Specimen dimensions and failure stresses for specimens impacted with a 10mm impactor hammer head

Specimen Number	Surface Texture Reading 1 (μm)	Surface Texture Reading 2 (μm)	Average Surface Texture (μm)
1	0.229	0.189	0.209
2	0.182	0.182	0.182
3	0.242	0.286	0.264
4	0.168	0.288	0.228
5	0.150	0.229	0.189
6	0.253	0.147	0.200
7	0.321	0.318	0.319
8	0.292	0.183	0.238
9	0.116	0.139	0.128
10	0.208	0.238	0.223
11	0.213	0.187	0.200
12	0.281	0.123	0.202
Average	**0.221**	**0.209**	**0.215**
SD	**0.060**	**0.061**	**0.046**

Table 4.9: Surface texture results for impacted specimens using a 10mm impactor hammer head

Shown in Table 4.10 and Figure 4.5 are the fatigue test results for the impacted specimens. It can be seen that the average number of cycles to failure for the 10mm impactor hammer head is 11,701 cycles (SD 4,015). These results can be used to determine the effect of a single impact on the fatigue life of a specimen.

Specimen Number	Cycles to Failure
1	10,562
2	9,771
3	16,577
4	10,302
5	9,736
6	20,839
7	11,396
8	14,633
9	9,574
10	9,580
11	12,178
12	5,275
Average	**11,701**
SD	**4,015**

Table 4.10: Number of cycles to failure for impacted specimens using a 10mm impactor hammer head

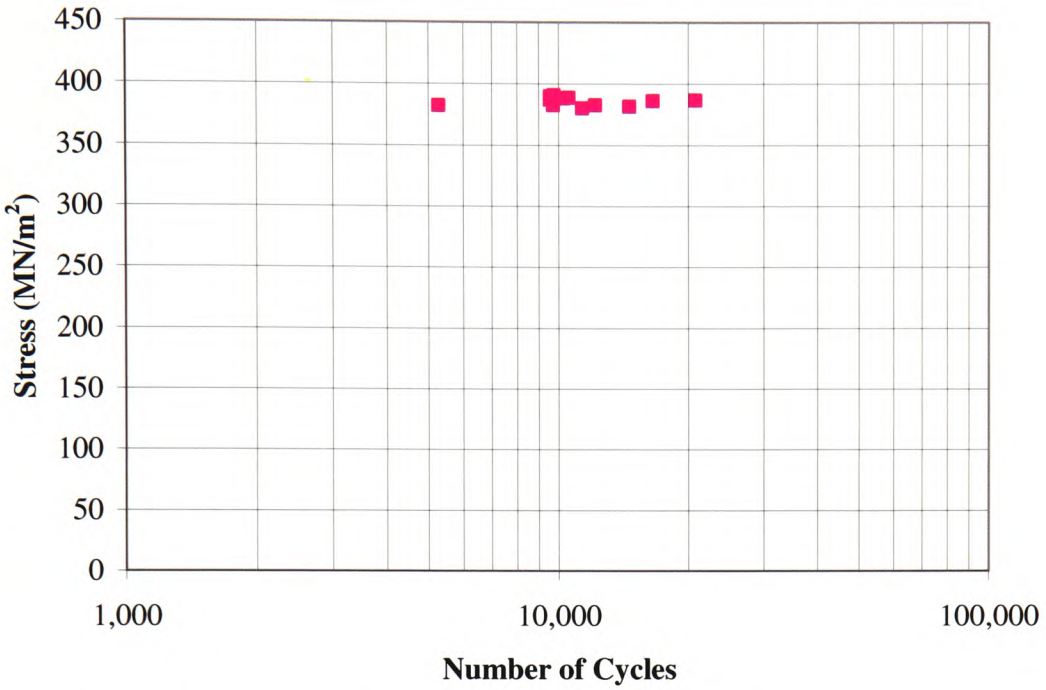

Figure 4.5: S-N Diagram for fatigue tests on bending quality bright steel with a single impact using a 10mm impactor hammer head

When combining the S-N diagrams for the initial fatigue control tests and the impact fatigue tests as shown in Figure 4.6, it can be seen that a single impact with a 10mm radius impactor hammer head can lower the fatigue life of the specimen from an average of 66,530 cycles to 11,701 cycles, which is an average reduction of 82.4%.

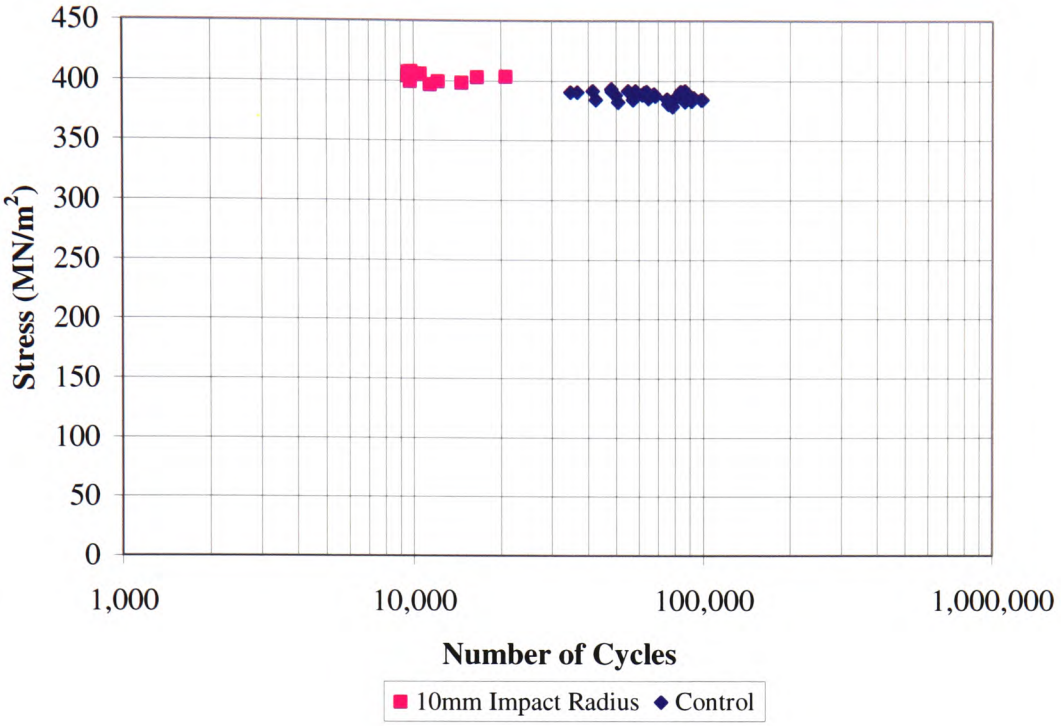

Figure 4.6: S-N Diagram for bending quality bright steel for initial control and 10mm impactor hammer head single impact fatigue tests

4.2.1 Hardness of Material

After fatigue testing, each specimen was hardness tested and the values compared to those obtained for the non-impacted control specimens, in order to determine whether a single impact can effect the hardness of a specimen, which may in turn effect its fatigue life. The hardness results for the non-impacted control specimens are shown in Table 4.11 and the results for the impacted specimens are presented in Table 4.12. Before fatigue testing the non-impacted control specimens, which had been tested at random places over the length of the specimen, were found to have an average hardness of 15 Rockwell C (SD 0.5), which is equivalent to 202 DPN. After fatigue testing, these specimens were found to have a hardness of approximately 13 Rockwell C (SD 3) or 197 DPN

close to the fracture, but remained unchanged at other positions on the specimen surface. The specimens that had been subjected to a single impact were found to have an average hardness value of 10 Rockwell C (SD 3) or 187 DPN near to the shoulder of the specimen and an average hardness of 9 Rockwell C (SD 3) or 183 DPN close to the fracture.

Specimen Number	Hardness (Rockwell C) – Bottom of Specimen				Hardness (Rockwell C) – Top of Specimen			
	Side 1		Side 2		Side 1		Side 2	
	Shoulder	Fracture	Shoulder	Fracture	Shoulder	Fracture	Shoulder	Fracture
1	13.0		17.0		10.0		13.1	
2	17.0		18.0		13.8		18.1	
3	15.8		16.0		15.0		15.2	
4	15.0		17.9		16.9		16.2	
5	12.0		13.6		15.7		18.1	
6	14.7		16.0		16.8		16.0	
7	14.0		17.8		6.8		9.0	
8	10.7		17.1		4.0		8.6	
9	12.7		17.2		14.0		15.0	
10	10.3		15.5		9.1		14.1	
11	16.0		17.0		11.0		13.0	
12	14.0		17.0		11.0		14.9	
13	12.9	7.9	16.7	14.0	14.8	8.8	15.6	14.8
14	17.0	13.3	17.2	16.3	17.5	13.0	16.0	18.0
15	13.8	11.0	16.0	14.2	16.0	11.0	13.6	14.5
16	16.0	12.5	14.5	15.0	12.0	11.0	13.5	13.5
17	15.5	4.2	15.3	13.2	17.3	16.0	15.0	13.0
18	16.4	17.0	14.5	13.1	15.9	15.1	15.6	14.0
19	15.0	14.8	14.0	13.9	16.9	12.0	14.1	11.0
20	16.5	11.4	15.1	14.6	14.4	15.8	16.0	12.1
21	16.0	12.0	16.5	13.0	15.5	12.0	14.5	11.5
22	17.0	10.0	17.0	14.0	16.5	15.5	16.5	16.0
23	16.0	18.0	14.5	9.0	17.5	6.0	15.5	17.5
24	11.0	14.0	17.5	14.0	15.0	13.0	17.0	7.5
25	16.0	15.5	14.5	12.0	17.0	13.5	16.5	14.5
26	17.0	9.0	9.5	10.5	17.5	16.5	13.0	4.5
27	17.5	16.0	11.5	7.5	16.5	16.0	10.0	9.0
28	17.5	16.5	9.5	8.5	17.5	15.5	10.0	8.5
29	16.5	16.0	14.5	1.5	17.5	16.0	9.0	12.5
30	12.0	15.0	14.0	8.5	17.5	15.5	14.5	13.5
Average	**14.8**	**13.0**	**15.4**	**11.8**	**14.6**	**13.5**	**14.2**	**12.6**
SD	**2.1**	**3.6**	**2.2**	**3.6**	**3.5**	**2.9**	**2.6**	**3.5**

Table 4.11: Hardness values of initial control specimens

Specimen Number	Hardness (Rockwell C) – Bottom of Specimen				Hardness (Rockwell C) – Top of Specimen			
	Side 1		Side 2		Side 1		Side 2	
	Shoulder	Fracture	Shoulder	Fracture	Shoulder	Fracture	Shoulder	Fracture
1	10.8	9.5	6.9	7.1	7.0	8.8	11.5	4.5
2	11.0	9.5	9.5	6.9	10.8	10.0	8.5	4.5
3	11.5	10.5	6.5	10.5	12.0	10.5	9.8	5.5
4	9.2	9.8	6.0	6.2	11.0	10.5	10.0	8.0
5	12.5	9.0	10.0	7.8	11.0	9.8	7.0	5.8
6	11.5	8.0	8.0	11.0	11.0	10.0	12.5	8.0
7	12.0	10.0	10.0	10.0	11.8	10.5	9.0	8.0
8	12.0	10.5	11.5	10.0	12.0	10.0	7.0	5.0
9	12.0	10.5	10.0	5.0	10.5	10.0	9.5	6.8
10	11.8	9.0	9.0	6.0	11.8	9.5	11.0	6.0
11	12.2	9.8	8.8	10.0	10.6	9.2	7.8	9.0
12								
Average	**11.5**	**9.6**	**8.7**	**8.2**	**10.9**	**9.9**	**9.4**	**6.5**
SD	**0.9**	**0.8**	**1.7**	**2.1**	**1.4**	**0.5**	**1.8**	**1.6**

Table 4.12: Hardness values of impacted specimens subjected to a single impact with a 10mm impactor hammer head

4.2.2 Entry Velocity of Impact

An oscilloscope records the voltage change produced by the potentiometer against time, as shown in Figure 4.7. Calibration of the potentiometer showed that over an angle of 90 degrees there was a voltage difference recorded of 1.11947 Volts; therefore, for every 1V of voltage change recorded, the impact arm had moved an angular distance of 80.395 degrees. By converting the voltage change to represent an angular displacement, this can be plotted against time to produce a graph illustrating the angular displacement of the impact arm (radians) against time of impact (seconds). The angular resolution of the potentiometer is ±2 degrees, which is due to the setting up of the impact height on the impact rig. By analysing the initial peak on the graph it was possible to calculate the velocity at impact and also the velocity immediately following impact. The gradient of positive slope of this initial peak, just before it levels out, represents the angular velocity of the impact. The gradient of the negative

slope just after the peak levels out represents the angular velocity upon exit. The angular velocities were then converted to linear velocities.

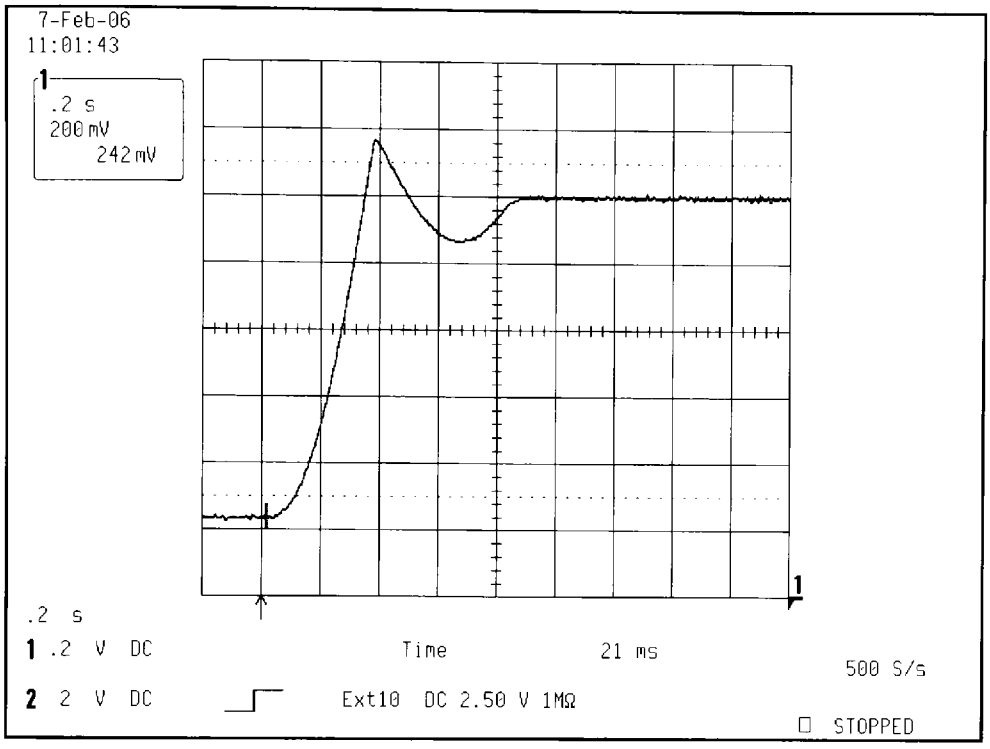

Figure 4.7: Typical oscilloscope display produced by the potentiometer showing voltage change against time

The average entry velocity of impact for the 10mm impactor hammer head is 3.11m/s (SD 0.11); this value is the average of twelve potentiometer readings, which are shown in Table 4.13. This value compares well with the theoretical entry velocity of 3.13m/s, as calculated in Section 3.5.1. The difference between the values is possibly due to the inaccuracy of the angular resolution of the potentiometer and also frictional losses in the impact rig. The experimental entry velocity can be used as a set-up parameter in the numerical model.

Specimen Number	Entry Velocity (m/s)
1	3.13
2	3.18
3	3.24
4	3.11
5	3.14
6	3.15
7	2.95
8	2.92
9	2.96
10	3.18
11	3.20
12	3.20
Average	**3.11**
SD	**0.11**

Table 4.13: Entry velocities for 10mm impactor hammer head

4.2.3 Exit Velocity after Impact

The average exit velocity immediately after impact for the 10mm impactor hammer head was 1.02m/s (SD 0.05). This value was the average of twelve potentiometer readings, which are shown in Table 4.14, and can be used to validate the results of the numerical model.

Specimen Number	Exit Velocity (m/s)
1	1.05
2	1.13
3	1.04
4	1.02
5	0.99
6	1.01
7	0.94
8	1.02
9	1.03
10	0.98
11	0.97
12	1.02
Average	**1.02**
SD	**0.05**

Table 4.14: Exit velocities for 10mm impactor hammer head

4.2.4 Coefficient of Restitution

The coefficient of restitution (COR) is represented as the ratio of the differences in velocities before and after collision, as shown in equation 4.1. A collision with a COR of 1 is a perfectly elastic collision and, conversely, a collision with a COR of 0 is a perfectly plastic, or inelastic, collision. By calculating the COR it is possible to determine whether the impact is elastic or plastic.

The average coefficient of restitution for the specimen impacts using the 10mm radius impactor hammer head is:

$$\text{COR} = \frac{\text{Velocity of object after impact}}{\text{Velocity of object before impact}} \qquad (4.1)$$

$$\text{COR}_{10\text{mm}} = \frac{1.02}{3.11}$$

$$\text{COR}_{10\text{mm}} = 0.33$$

The coefficient of restitution for each of the impacted specimens is shown in Table 4.15. As the average COR is greater than 0 but less than 1, the impact can be said to be partially plastic, with some kinetic energy being transformed into the deformation of material, sound and possibly other forms of energy, such as heat.

Specimen Number	Coefficient of Restitution
1	0.34
2	0.36
3	0.32
4	0.33
5	0.31
6	0.32
7	0.32
8	0.35
9	0.35
10	0.31
11	0.30
12	0.32
Average	**0.33**
SD	**0.02**

Table 4.15: Coefficient of restitution for 10mm impactor hammer head

4.2.5 Entry Impact Energy

The average entry energy of impact for the 10mm impactor hammer head was 17.08J (SD 1.19). This value was the average of twelve potentiometer readings, which are shown in Table 4.16. This value compares well with the theoretical entry energy of 17.27J, as calculated in Section 3.5.1. The difference between the values is possibly due to the inaccuracy of the angular resolution of the potentiometer and frictional losses in the impact rig.

Specimen Number	Entry Impact Energy (J)
1	17.20
2	17.83
3	18.50
4	16.97
5	17.36
6	17.49
7	15.32
8	15.00
9	15.41
10	17.82
11	18.03
12	18.06
Average	**17.08**
SD	**1.19**

Table 4.16: Entry impact energies for 10mm impactor hammer head

4.2.6 Exit Energy after Impact

The average exit energy after impact for the 10mm impactor hammer head was 1.82J (SD 0.18). This value was the average of twelve potentiometer readings, as shown in Table 4.17.

Specimen Number	Exit Energy after Impact (J)
1	1.95
2	2.26
3	1.89
4	1.82
5	1.71
6	1.78
7	1.55
8	1.82
9	1.87
10	1.70
11	1.65
12	1.81
Average	**1.82**
SD	**0.18**

Table 4.17: Exit energies after impact for 10mm impactor hammer head

4.2.7 Depth of Impact Crater

The depth of impact crater produced by the 10mm impactor hammer head was measured as 0.41mm using one specimen from the batch of specimens impacted. This result can be used to validate the numerical model.

4.2.8 Width of Impact Crater

The width of impact crater produced by the 10mm impactor hammer head was measured as 5.0mm using one specimen from the batch of specimens impacted. This result can be used to validate the numerical model.

4.2.9 Volume of Impact Crater

The volume of the impact crater produced by the 10mm impactor hammer head can be calculated using Equation 4.2, for the volume of a spherical cap segment, as shown below.

$$\text{Volume of a spherical segment} = \pi h\left(\frac{c^2}{8}+\frac{h^2}{6}\right) \qquad (4.2)$$

where c = width of impact
h = depth of impact

$$\text{Therefore, volume of impact crater}_{(10mm)} = \pi\times 0.41\left(\frac{5^2}{8}+\frac{0.41^2}{6}\right)$$

$$= 5.23\text{mm}^3$$

4.2.10 Impact Contact Time

An oscilloscope records the voltage change produced by the accelerometer against time, as shown in Figure 4.8. The impact contact time can be measured by calculating the difference between the start and end time of the initial peak recorded by the accelerometer, as the initial peak detected is due to a voltage change generated by the first vibration due to impact. Subsequent pulses recorded are noise due to vibrations present in the impact rig as a result of the impact. The average impact contact time recorded by the accelerometer was 9.53E-05 seconds (SD 4.23E-06). This value is the average of three accelerometer readings, as shown in Table 4.18, and can be used to validate the numerical model. Only three of the twelve accelerometer readings have been recorded; this was due to operational error. The resolution of the accelerometer is ±5%.

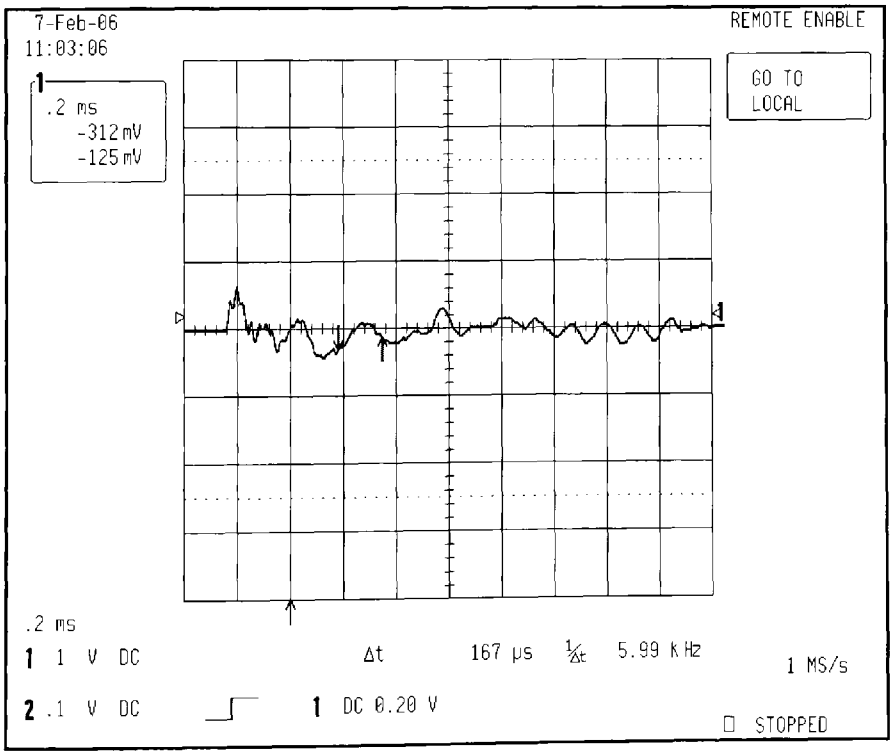

Figure 4.8: Typical oscilloscope display produced by the accelerometer showing voltage change against time

Specimen Number	Impact Contact Time recorded by Accelerometer (seconds)
1	9.00E-05
2	1.00E-04
3	9.60E-05
4	
5	
6	
7	
8	
9	
10	
11	
12	
Average	**9.53E-05**
SD	**4.23E-06**

Table 4.18: Impact contact times calculated from the accelerometer readings

4.3 Specimen Material 2 – '070M20' Carbon Steel

Once the experimental procedures and results from the preliminary study had been assessed and verified, the main study was carried out using '070M20' carbon steel. Initially, tensile tests using the Hounsfield H20K-W Tensometer and Extensometer were carried out on seven sample specimens of the '070M20' carbon steel used to make the specimens, the results of which are shown in Table 4.19. These tests were carried out at rate of 2mm per minute. The average Young's Modulus was found to be 154.312GN/m^2 (SD 12.294) and the corresponding average yield stress was found to be 391.93MN/m^2 (SD 34.29). The experimental value for Young's Modulus is low in comparison with published theoretical values, however this is most likely due to the wide range of specifications for the chemical composition of this material and also the cold-working process during manufacture. These results can be used as set-up parameters for the material properties of the specimen in the numerical models.

The stress/strain graphs obtained for specimen number four are shown in Figures 4.9 and 4.10.

Specimen Number	Young's Modulus (GN/m^2)	Yield Stress (MN/m^2)
1	170.754	390.59
2	157.067	403.99
3	161.210	354.49
4	157.843	404.53
5	156.896	373.80
6	133.546	455.47
7	142.868	360.62
Average	**154.312**	**391.93**
SD	**12.294**	**34.29**

Table 4.19: Tensile test results for '070M20' carbon steel

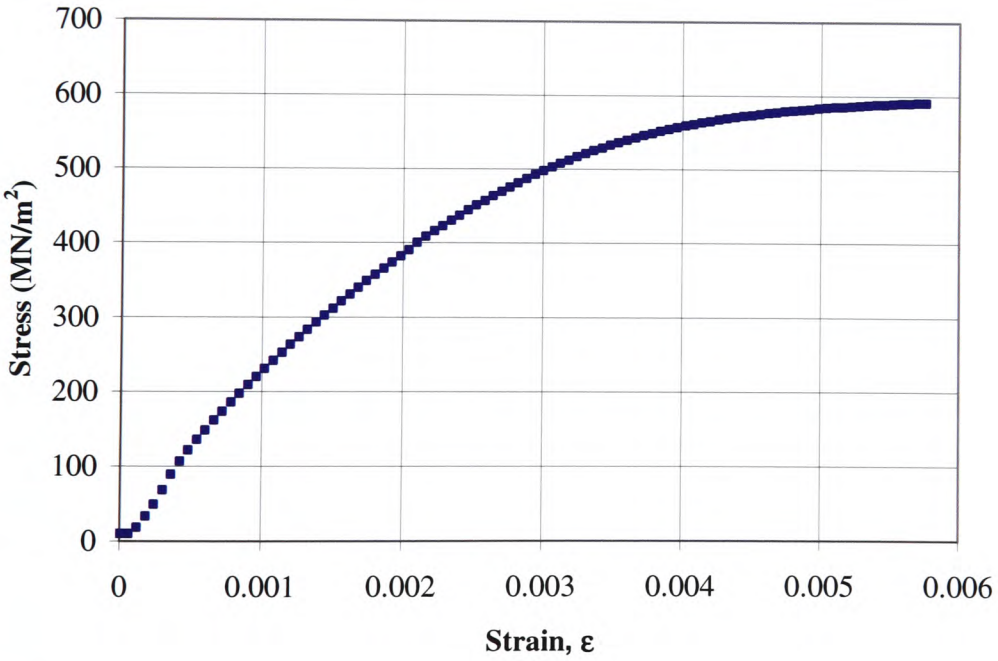

Figure 4.9: '070M20' carbon steel specimen stress/strain graph (1)

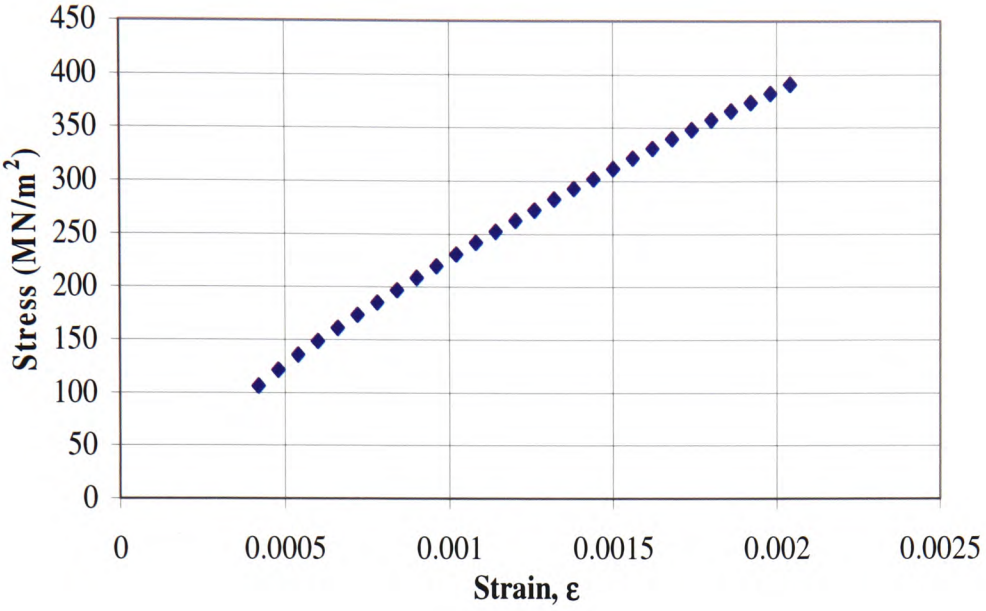

Figure 4.10: '070M20' carbon steel specimen stress/strain graph (2) linear section only to determine Young's Modulus

The fatigue tests were carried out on specimens of the '070M20' carbon steel as shown in Figure 3.1, at a sinusoidal load of ±11.5kN, equivalent to a stress of 273.8MN/m^2, at 2Hz. This load was chosen so that the specimen would fail in fatigue whilst ensuring that the load would remain within the elastic limit of the material. The fatigue load of 11.5kN was calculated by using the yield stress obtained from the tensile tests along with the cross-sectional area of the specimen used in the fatigue tests, which was calculated from the design dimensions as 42mm^2.

The failure stress for each specimen was calculated using the fatigue load of 11.5kN and the actual cross-sectional area of the specimens that were used for the fatigue tests, which was measured to be approximately 41mm^2. The control specimen dimensions and calculated failure stresses are shown in Table 4.20.

The surface texture results of the control specimens are shown in Table 4.21. It can be seen that the average surface texture, measured as the CLA, is 0.148μm (SD 0.03).

Shown in Table 4.22 and Figure 4.11 are the fatigue test results for the initial control tests. It can be seen that the average number of cycles to failure is 520,822 cycles (SD 181,054). These results can be used to determine the effect of a single impact on the fatigue life of a specimen.

Specimen Number	Width of Specimen (mm)	Depth of Specimen (mm)	Cross-sectional Area of Specimen (mm^2)	Stress (MN/m^2)
1	14.11	2.94	41.48	277.219
2	14.00	2.91	40.74	282.278
3	14.14	2.92	41.29	278.526
4	14.14	2.91	41.15	279.483
5	14.10	2.9	40.89	281.242
6	14.14	2.92	41.29	278.526
7	14.02	2.88	40.38	284.811
8	14.11	2.91	41.06	280.077
9	14.08	2.92	41.11	279.713
10	14.11	2.92	41.20	279.118
11	14.09	2.91	41.00	280.475
12	14.08	2.91	40.97	280.674
Average	**14.09**	**2.91**	**41.05**	**280.178**
SD	**0.04**	**0.01**	**0.29**	**1.99**

Table 4.20: Control specimen dimensions and failure stresses

Specimen Number	Surface Texture Reading 1 (μm)	Surface Texture Reading 2 (μm)	Average Surface Texture (μm)
1	0.142	0.136	0.139
2	0.162	0.107	0.135
3	0.184	0.148	0.166
4	0.197	0.171	0.184
5	0.193	0.131	0.162
6	0.235	0.195	0.215
7	0.117	0.145	0.131
8	0.132	0.108	0.120
9	0.111	0.135	0.123
10	0.104	0.105	0.105
11	0.162	0.144	0.153
12	0.122	0.169	0.146
Average	**0.155**	**0.141**	**0.148**
SD	**0.04**	**0.03**	**0.03**

Table 4.21: Surface texture of control specimens

Specimen Number	Cycles to Failure
1	817,848
2	333,639
3	712,357
4	614,729
5	417,931
6	541,566
7	784,501
8	578,713
9	301,238
10	374,303
11	353,578
12	419,467
Average	**520,822**
SD	**181,054**

Table 4.22: Number of cycles to failure for control specimens

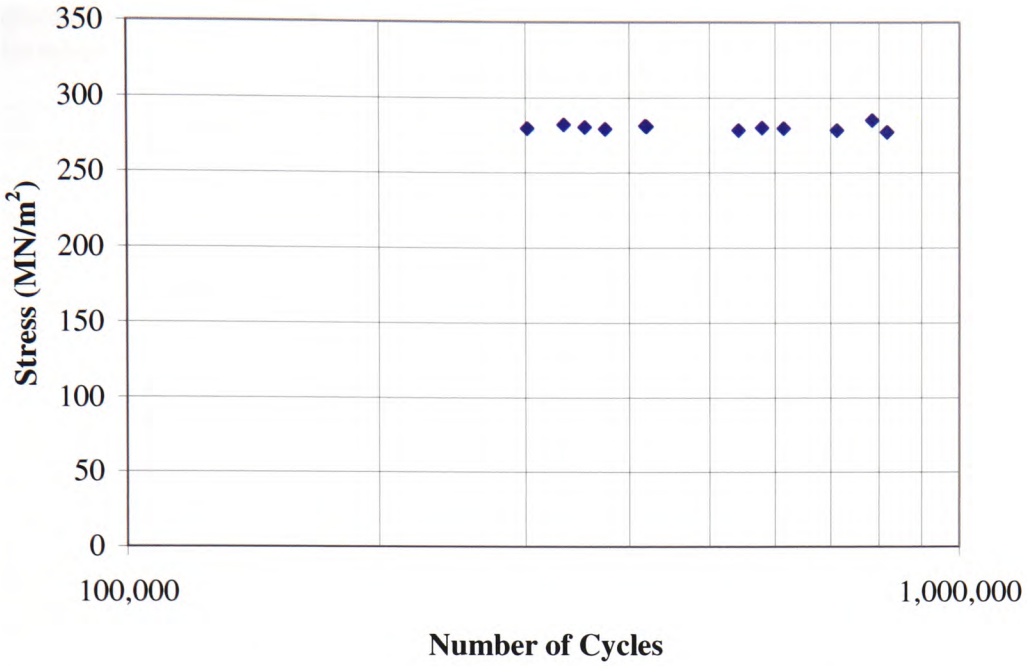

Figure 4.11: S-N Diagram for initial control fatigue tests for '070M20' carbon steel

The impacted specimen dimensions and calculated failure stresses for all sizes of impactor hammer head are shown in Tables 4.23 to 4.27.

The surface texture results of the impacted specimens are shown in Tables 4.28 to 4.32. The average surface texture, measured as the CLA, can be calculated as 0.176μm (SD 0.01). This value was found to be slightly higher than specimens which were not fatigue tested, but is still less than 5μm as recommended by BS3518-3. The slight difference between the surface texture results of the impacted and control specimens also indicates that the specimens do not sustain any surface damage during impact.

Table 4.33 and Figure 4.12 show the fatigue test results for all of the impacted specimens. It can be calculated from these results that the average number of cycles to failure for all the impactor hammer head sizes tested is 47,455 cycles (SD 7,913). These results can be used to determine the effect of a single impact on the fatigue life of a specimen.

Specimen Number	Width of Specimen (mm)	Depth of Specimen (mm)	Cross-sectional Area of Specimen (mm^2)	Stress (MN/m^2)
1	14.12	2.93	41.37	277.968
2	14.06	2.91	40.91	281.073
3	14.06	2.91	40.91	281.073
4	14.08	2.93	41.25	278.758
5	14.14	2.91	41.15	279.483
6	14.13	2.93	41.40	277.772
7	14.13	2.93	41.40	277.772
8	14.18	2.95	41.83	274.916
9	14.08	2.91	40.97	280.674
10	14.07	2.91	40.94	280.873
11	14.07	2.91	40.94	280.873
12	14.10	2.90	40.89	281.242
Average	**14.10**	**2.92**	**41.16**	**279.37**
SD	**0.04**	**0.01**	**0.29**	**1.973**

Table 4.23: Specimen dimensions and failure stresses for specimens impacted with 10mm impactor hammer head

Specimen Number	Width of Specimen (mm)	Depth of Specimen (mm)	Cross-sectional Area of Specimen (mm^2)	Stress (MN/m^2)
1	13.97	2.92	40.79	281.915
2	14.06	2.92	41.06	280.111
3	14.01	2.91	40.77	282.076
4	14.06	2.92	41.06	280.111
5	14.01	2.92	40.91	281.110
6	13.96	2.90	40.48	284.063
7	14.04	2.92	41.00	280.510
8	14.01	2.90	40.63	283.049
9	14.04	2.90	40.72	282.444
10	14.07	2.92	41.08	279.912
11	14.02	2.93	41.08	279.951
12	14.06	2.89	40.63	283.018
Average	**14.02**	**2.91**	**40.85**	**281.522**
SD	**0.04**	**0.01**	**0.21**	**1.432**

Table 4.24: Specimen dimensions and failure stresses for specimens impacted with 11mm impactor hammer head

Specimen Number	Width of Specimen (mm)	Depth of Specimen (mm)	Cross-sectional Area of Specimen (mm^2)	Stress (MN/m^2)
1	14.18	2.91	41.26	278.695
2	14.17	2.92	41.38	277.936
3	14.10	2.92	41.17	279.316
4	14.12	2.92	41.23	278.920
5	14.11	2.90	40.92	281.043
6	14.14	2.91	41.15	279.483
7	14.12	2.89	40.81	281.816
8	14.17	2.89	40.95	280.821
9	14.15	2.89	40.89	281.218
10	14.07	2.88	40.52	283.799
11	14.07	2.91	40.94	280.873
12	14.13	2.91	41.12	279.681
Average	**14.13**	**2.90**	**41.03**	**280.300**
SD	**0.04**	**0.01**	**0.23**	**1.613**

Table 4.25: Specimen dimensions and failure stresses for specimens impacted with 12mm impactor hammer head

Specimen Number	Width of Specimen (mm)	Depth of Specimen (mm)	Cross-sectional Area of Specimen (mm^2)	Stress (MN/m^2)
1	14.02	2.91	40.80	281.875
2	14.12	2.92	41.23	278.920
3	14.09	2.88	40.58	283.396
4	14.09	2.89	40.72	282.416
5	14.09	2.88	40.58	283.396
6	14.10	2.88	40.61	283.195
7	14.05	2.92	41.03	280.310
8	14.14	2.88	40.72	282.394
9	14.06	2.87	40.35	284.991
10	14.10	2.91	41.03	280.276
11	14.06	2.88	40.49	284.001
12	14.07	2.89	40.66	282.817
Average	**14.08**	**2.89**	**40.73**	**282.33**
SD	**0.03**	**0.02**	**0.25**	**1.74**

Table 4.26: Specimen dimensions and failure stresses for specimens impacted with 18mm impactor hammer head

Specimen Number	Width of Specimen (mm)	Depth of Specimen (mm)	Cross-sectional Area of Specimen (mm^2)	Stress (MN/m^2)
1	14.17	2.90	41.09	279.853
2	14.05	2.91	40.89	281.273
3	14.07	2.91	40.94	280.873
4	14.12	2.98	42.08	273.305
5	14.15	2.98	42.17	272.725
6	14.05	2.91	40.89	281.273
7	14.09	2.91	41.00	280.475
8	14.11	2.90	40.92	281.043
9	14.06	2.90	40.77	282.042
10	14.13	2.90	40.98	280.645
11	14.08	2.87	40.41	284.586
12	14.07	2.87	40.38	284.788
Average	**14.09**	**2.91**	**41.04**	**280.240**
SD	**0.04**	**0.03**	**0.55**	**3.704**

Table 4.27: Specimen dimensions and failure stresses for specimens impacted with 40mm impactor hammer head

Specimen Number	Surface Texture Reading 1 (μm)	Surface Texture Reading 2 (μm)	Average Surface Texture (μm)
1	0.285	0.114	0.200
2	0.159	0.153	0.156
3	0.110	0.223	0.167
4	0.127	0.390	0.259
5	0.112	0.113	0.113
6	0.154	0.157	0.156
7	0.208	0.132	0.170
8	0.187	0.143	0.165
9	0.174	0.251	0.213
10	0.178	0.232	0.205
11	0.123	0.158	0.141
12	0.178	0.179	0.179
Average	**0.166**	**0.187**	**0.177**
SD	**0.049**	**0.078**	**0.036**

Table 4.28: Surface texture for specimens impacted with 10mm impactor hammer head

Specimen Number	Surface Texture Reading I (μm)	Surface Texture Reading 2 (μm)	Average Surface Texture (μm)
1	0.230	0.107	0.169
2	0.351	0.233	0.292
3	0.131	0.138	0.135
4	0.247	0.104	0.176
5	0.117	0.104	0.111
6	0.185	0.286	0.236
7	0.166	0.189	0.178
8	0.258	0.128	0.193
9	0.112	0.141	0.127
10	0.138	0.237	0.188
11	0.138	0.164	0.151
12	0.147	0.144	0.146
Average	**0.185**	**0.165**	**0.175**
SD	**0.072**	**0.059**	**0.049**

Table 4.29: Surface texture for specimens impacted with 11mm impactor hammer head

Specimen Number	Surface Texture Reading 1 (μm)	Surface Texture Reading 2 (μm)	Average Surface Texture (μm)
1	0.134	0.199	0.167
2	0.142	0.280	0.211
3	0.128	0.198	0.163
4	0.246	0.118	0.182
5	0.118	0.134	0.126
6	0.275	0.129	0.202
7	0.168	0.137	0.153
8	0.158	0.146	0.152
9	0.255	0.134	0.195
10	0.225	0.329	0.277
11	0.123	0.123	0.123
12	0.105	0.132	0.119
Average	**0.173**	**0.172**	**0.172**
SD	**0.06**	**0.068**	**0.045**

Table 4.30: Surface texture for specimens impacted with 12mm impactor hammer head

Specimen Number	Surface Texture Reading 1 (μm)	Surface Texture Reading 2 (μm)	Average Surface Texture (μm)
1	0.198	0.292	0.245
2	0.262	0.101	0.182
3	0.183	0.125	0.154
4	0.146	0.286	0.216
5	0.217	0.252	0.235
6	0.112	0.162	0.137
7	0.199	0.168	0.184
8	0.318	0.155	0.237
9	0.147	0.233	0.190
10	0.162	0.126	0.144
11	0.294	0.298	0.296
12	0.152	0.127	0.140
Average	**0.199**	**0.194**	**0.196**
SD	**0.063**	**0.073**	**0.05**

Table 4.31: Surface texture for specimens impacted with 18mm impactor hammer head

Specimen Number	Surface Texture Reading 1 (μm)	Surface Texture Reading 2 (μm)	Average Surface Texture (μm)
1	0.148	0.142	0.145
2	0.276	0.231	0.254
3	0.187	0.164	0.176
4	0.199	0.129	0.164
5	0.141	0.183	0.162
6	0.126	0.169	0.148
7	0.122	0.154	0.138
8	0.186	0.112	0.149
9	0.219	0.119	0.169
10	0.183	0.155	0.169
11	0.147	0.192	0.170
12	0.120	0.107	0.114
Average	**0.171**	**0.155**	**0.163**
SD	**0.046**	**0.036**	**0.033**

Table 4.32: Surface texture for specimens impacted with 40mm impactor hammer head

Specimen Number	Cycles to Failure				
	10mm Impactor Hammer Head	11mm Impactor Hammer Head	12mm Impactor Hammer Head	18mm Impactor Hammer Head	40mm Impactor Hammer Head
1	48,400	52,403	59,042	40,259	48,682
2	71,661	42,157	40,431	53,801	68,841
3	45,334	40,045	45,162	46,151	52,417
4	48,221	53,890	42,213	60,651	55,988
5	49,172	47,166	48,935	49,476	52,990
6	51,455	40,735	37,568	32,350	55,761
7	38,372	41,842	44,566	48,107	35,719
8	69,815	46,936	38,238	52,732	43,632
9	47,662	48,978	37,691	54,072	39,853
10	45,236	41,011	41,709	60,436	39,153
11	55,294	32,037	40,216	52,824	50,261
12	42,219	47,398	37,980	48,351	43,608
Average	**51,070**	**44,549**	**42,812**	**49,934**	**48,908**
SD	**10,136**	**6,076**	**6,190**	**7,957**	**9,206**

Table 4.33: Number of cycles to failure for impacted specimens

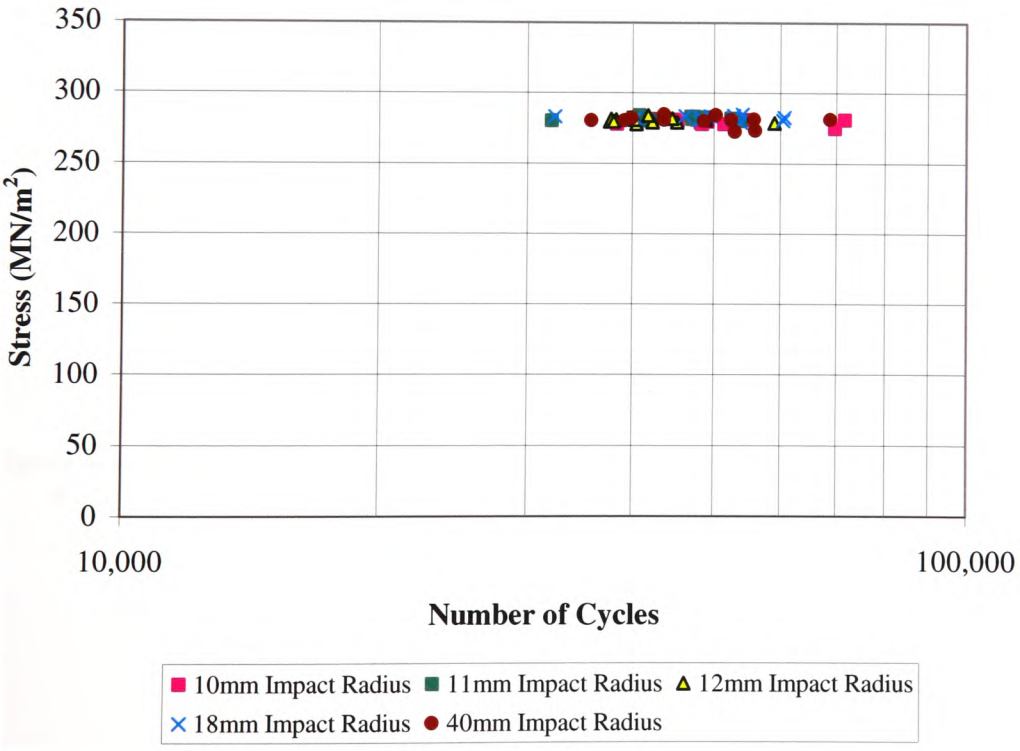

Figure 4.12: S-N Diagram for impact fatigue tests for '070M20' carbon steel

When combining the S-N diagrams for the initial fatigue control tests with the impact fatigue tests as shown in Figure 4.13, it can be seen that the action of impacting lowers the average fatigue life of the specimen by 90.89%. By comparing the standard deviations over which failure can occur for the initial fatigue tests as shown in Table 4.22, and the impact fatigue tests, as shown in Table 4.33, it can be seen that the average range of standard deviations over which failure could occur reduces by 18.09% for specimens subjected to a single impact.

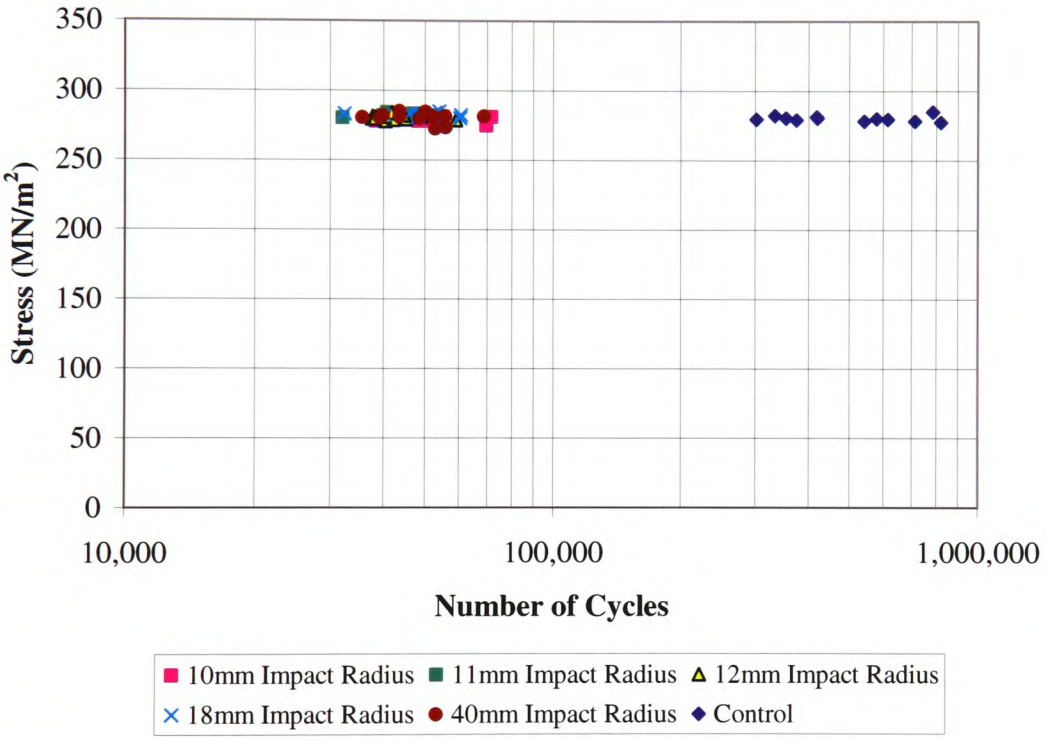

Figure 4.13: S-N Diagram for control and impact fatigue tests for '070M20' carbon steel

4.3.1 Hardness of Material

After fatigue testing, each specimen was hardness tested and the values were compared to those obtained for the non-impacted control specimens, in order to determine whether a single impact can effect the hardness of a specimen, which may in turn effect its fatigue life. The hardness results for the control specimens are shown in Table 4.34, and for the impacted specimens are shown in Tables 4.35 to 4.39. Before fatigue testing, the specimens, which had been tested at random places, were found to have an average hardness of 2.5 Rockwell C (SD 5), which is equivalent to 161 DPN. After fatigue testing the control specimens were found to have an average hardness of approximately 0.2 Rockwell C (SD 3.6) or 154 DPN close to the fracture and -2.0 Rockwell C (SD 4.6) or 146 DPN near the shoulder of the specimen. The impacted specimens were found to have an average hardness of approximately 2.0 Rockwell C (SD 3.6) or 159 DPN close to the fracture and 3.1 Rockwell C (SD 6.1) or 163 DPN near the shoulder of the specimen.

Specimen Number	Hardness (Rockwell C) – Bottom of Specimen				Hardness (Rockwell C) – Top of Specimen			
	Side 1		Side 2		Side 1		Side 2	
	Shoulder	Fracture	Shoulder	Fracture	Shoulder	Fracture	Shoulder	Fracture
1	3.0	3.0			3.0			
2	3.5	4.0			4.5	2.0		
3	5.0	3.5			3.5	1.5		
4	4.5	2.0	1.5		1.5			
5	4.5	2.5	-2.5	-2.0	3.5	1.5	-3.5	-2.5
6	3.5	2.5	-7.5	-3.5	4.5	2.5	-9.5	-2.5
7	4.5	2.0	-7.0	-3.0	3.5	3.0	2.0	-8.5
8	3.5	3.5	-1.5	-1.5	2.5	2.5	-3.5	-8.5
9	3.0	3.5	0.0	-2.5	4.0	2.0	-3.0	-5.5
10	4.0	4.0	-2.0	-3.5	3.0	4.0	3.5	-10.0
11	4.0	4.0	-7.0	-5.0	-6.5	-12.5	2.0	-4.0
12	4.0	1.5	-11.0	-26.5	3.0	2.0	0.5	-7.0
Average	**3.9**	**3.0**	**-4.1**	**-5.9**	**2.5**	**0.8**	**-1.4**	**-6.0**
SD	**0.6**	**0.9**	**4.1**	**8.4**	**2.9**	**4.8**	**4.3**	**2.9**

Table 4.34: Hardness values of initial control specimens

Specimen Number	Hardness (Rockwell C) – Bottom of Specimen				Hardness (Rockwell C) – Top of Specimen			
	Side 1		Side 2		Side 1		Side 2	
	Shoulder	Fracture	Shoulder	Fracture	Shoulder	Fracture	Shoulder	Fracture
1	1.5	2.5	2.5	-2.0	0.5	2.0	-7.5	-7.5
2	-1.0	-1.5	-1.0	-7.5	-0.5	1.5	-9.5	3.0
3	11.5	1.5	-6.0	-2.0	15.0	2.0	-6.5	0.0
4	12.0	1.5	3.5	-10.0	6.0	2.5	0.5	
5	12.5	1.5	3.0		9.0	2.0	4.5	-7.0
6	-1.0	2.0	-2.5	-7.0	0.5	1.5	-7.5	-6.0
7	14.0	1.5	2.0	11.5	10.5	1.5	1.5	-5.5
8	-1.5	2.5	-2.5	-11.5	1.5	3.0	-7.5	-6.5
9	7.0	1.5	1.5	-14.0	13.0	1.0	1.5	-5.5
10	11.5	2.0	-7.5	-16.5	11.0	2.0	-4.5	-6.5
11	14.5	2.0	-6.5	-6.5	14.5	2.0	1.5	-6.5
12	4.0	0.5	-2.5	-27.5	2.5	2.0	2.5	-9.0
Average	**7.1**	**1.5**	**-1.3**	**-8.5**	**7.0**	**1.9**	**-2.6**	**-5.2**
SD	**6.3**	**1.1**	**3.9**	**10.1**	**5.9**	**0.5**	**5.0**	**3.9**

Table 4.35: Hardness values of specimens impacted with 10mm impactor hammer head

Specimen Number	Hardness (Rockwell C) – Bottom of Specimen				Hardness (Rockwell C) – Top of Specimen			
	Side 1		Side 2		Side 1		Side 2	
	Shoulder	Fracture	Shoulder	Fracture	Shoulder	Fracture	Shoulder	Fracture
1	-1.5	1.0	-2.0	-34.0	-8.0	1.5	-2.5	-10.0
2	4.0	1.5	-3.0	-21.0	-5.5	2.5	-7.0	-19.0
3	-9.0	1.5	-7.0	-22.0	-6.0	2.0	-5.0	-4.0
4	-6.0	1.5	-7.0	-20.0	-6.0	1.5	-3.0	-7.5
5	-4.0	1.5	-9.0	-6.0	-5.5	2.0	-4.5	-14.0
6	-12.0	2.5	-10.0	-6.0	1.0	0.5	-7.0	-5.5
7	-9.5	0.5	-4.5	-20.0	-7.0	3.0	-8.0	-7.0
8	0.0	1.5	-7.0		-4.5	1.5	3.5	
9	-4.5	0.0	-9.0	-17.0	-2.0	1.5	-3.0	-4.5
10	-7.0	0.5	0.5	-23.0	-6.0	11.0	-3.0	-9.0
11	2.0	3.0	-2.5		-3.5	2.5	-5.5	-16.0
12	0.0	2.0	-9.5	2.0	3.0	2.0	-7.5	-10.0
Average	**-4.0**	**1.4**	**-5.8**	**-16.7**	**-4.2**	**2.6**	**-4.4**	**-9.7**
SD	**4.9**	**0.8**	**3.4**	**13.1**	**3.3**	**2.7**	**3.1**	**5.7**

Table 4.36: Hardness values of specimens impacted with 11mm impactor hammer head

Specimen Number	Hardness (Rockwell C) – Bottom of Specimen				Hardness (Rockwell C) – Top of Specimen			
	Side 1		Side 2		Side 1		Side 2	
	Shoulder	Fracture	Shoulder	Fracture	Shoulder	Fracture	Shoulder	Fracture
1	3.5	1.5	3.5		3.5	2.0	-1.5	-24.5
2	1.5	2.0	0.0		3.5	2.0	2.5	-5.0
3	6.0	0.5	-22.5	-13.0	-6.0	1.5	3.0	-3.0
4	-10.0	0.5	0.0	-11.5	-7.5	2.0	0.5	-10.5
5	0.5	1.5	-7.5	-4.0	-3.0	2.5	0.5	-14.0
6	-5.0	1.5	-1.0	-11.0	-4.5	2.5	3.5	-3.5
7	8.5	1.0	1.0	-14.5	-8.5	0.0	-6.0	-26.0
8	-5.0	1.5	1.5	-9.0	0.5	2.0	-4.5	-8.5
9	-3.0	2.5	-1.0	-21.0	4.5	2.5	-3.5	0.5
10	-10.0	2.0	-7.5	-4.5	-12.0	2.5	-3.0	-6.5
11	-4.5	0.0	-6.0	-5.0	1.0	2.5	-7.0	-6.0
12	-1.0	2.0	-4.5	-12.0	0.0	2.0	-7.0	-11.5
Average	**-1.5**	**1.4**	**-3.7**	**-10.6**	**-2.4**	**2.0**	**-1.9**	**-9.9**
SD	**5.8**	**0.7**	**6.9**	**7.2**	**5.4**	**0.7**	**3.9**	**8.2**

Table 4.37: Hardness values of specimens impacted with 12mm impactor hammer head

Specimen Number	Hardness (Rockwell C) – Bottom of Specimen				Hardness (Rockwell C) – Top of Specimen			
	Side 1		Side 2		Side 1		Side 2	
	Shoulder	Fracture	Shoulder	Fracture	Shoulder	Fracture	Shoulder	Fracture
1	-8.0	1.5	2.5	-19.5	-8.5	1.5	4.0	-13.5
2	-3.5	1.5	-4.5	-6.5	-10.5	2.5	-9.0	-14.0
3	-11.5	1.5	-1.5	-21.0	-8.5	2.5	3.0	-15.5
4	1.5	-2.0	1.5	33.5	-1.5	55.5	-8.5	-21.5
5	-9.5	1.0	0.0	60.0	-8.5	2.0	0.0	-10.0
6	-4.5	2.5	-2.5	-30.0	-8.5	-1.5	-1.0	-15.5
7	-4.5	2.5	-7.0	-40.5	-3.5	1.5	-1.0	-10.0
8	-7.0	1.5	-4.5	-10.0	0.0	2.5	-4.5	-4.0
9	-3.0	1.5	-5.0	30.0	-5.0	2.5	-7.5	-9.0
10	4.5	1.0	3.5	-10.0	0.0	-5.0	-6.5	-9.0
11	3.0	2.0	-8.0	-4.5	3.5	3.0	-5.5	-6.0
12	-8.5	2.5	1.5	-23.0	-11	2.5	1.0	-3.5
Average	**-4.2**	**1.4**	**-2.0**	**-3.5**	**-5.8**	**5.8**	**-2.9**	**-10.9**
SD	**5.1**	**1.2**	**3.8**	**29.6**	**4.8**	**15.8**	**4.5**	**5.3**

Table 4.38: Hardness values of specimens impacted with 18mm impactor hammer head

Specimen Number	Hardness (Rockwell C) – Bottom of Specimen				Hardness (Rockwell C) – Top of Specimen			
	Side 1		Side 2		Side 1		Side 2	
	Shoulder	Fracture	Shoulder	Fracture	Shoulder	Fracture	Shoulder	Fracture
1	3.5	1.0	-7.5	0.5	2.5	11.5	-4.5	-9.0
2	2.5	-10.5	-8.5	-9.0	3.5	2.0	-1.5	-8.0
3	1.5	-14.0	-10.0	-8.0	1.5	2.0	-3.0	-27.5
4	3.5	3.0	-3.0	-0.5	0.0	1.5	-9.0	-4.5
5	-1.5	-2.0	-9.5	4.5	-2.0	3.0	-0.5	22.5
6	3.0	1.5	1.0	-8.0	1.5	2.0	-7.0	-8.0
7	-5.0	2.0	-6.5	20.0	-6.5	-1.5	2.5	32.0
8	0.5	0.5	-6.0	-5.5	-1.5	0.5	-8.5	0.5
9	0.5	1.5	-4.5	-12.0	-0.5	1.0	-6.0	0.5
10	1.0	0.5	-4.5	-4.5	3.0	3.0	-6.5	-1.5
11	1.5	0.5	-6.5	-4.5	3.0	3.0	3.5	-38.5
12	3.0	2.5	-10.0	-12.5	3.5	3.5	-3.0	1.5
Average	**1.2**	**-1.1**	**-6.3**	**-3.3**	**0.7**	**2.6**	**-3.6**	**-3.3**
SD	**2.4**	**5.4**	**3.2**	**8.9**	**3.0**	**3.1**	**4.1**	**18.8**

Table 4.39: Hardness values of specimens impacted with 40mm impactor hammer head

4.3.2 Entry Velocity of Impact

The entry velocities for the impactor hammer head sizes tested are shown in Table 4.40 and also on the graph in Figure 4.14 and were calculated as previously described in Section 4.2.2. These values compare well with the theoretical entry velocity of 2.84m/s, as calculated in Section 3.5.2. The difference between the values was possibly due to the inaccuracy of the angular resolution of the potentiometer and frictional losses in the impact rig. The average entry velocity was 2.66m/s (SD 0.02); the slight deviation from the mean demonstrates the consistency of impacts produced using the impact rig. The graph has a straight trend line showing that for any impactor hammer head size between 10mm and 40mm, the entry velocity is 2.66m/s. This value can be used as set-up parameter for the velocity of impact in the numerical model.

Specimen Number	Entry Velocity (m/s)				
	10mm Impactor Hammer Head	11mm Impactor Hammer Head	12mm Impactor Hammer Head	18mm Impactor Hammer Head	40mm Impactor Hammer Head
1	2.83	2.64	2.58	2.56	2.65
2	2.68	2.66	2.79	2.56	2.62
3	2.65	2.65	2.76	2.58	2.61
4	2.67	2.79	2.67	2.67	2.53
5	2.58	2.65	2.60	2.70	2.67
6	2.60	2.65	2.61	2.69	2.70
7	2.56	2.65	2.61	2.66	2.73
8	2.66	2.66	2.66	2.82	2.60
9	2.69	2.62	2.68	2.70	2.64
10	2.74	2.57	2.55	2.79	2.65
11		2.56	2.58	2.71	2.60
12			2.67	2.73	2.64
Average	**2.67**	**2.65**	**2.65**	**2.68**	**2.64**
SD	**0.08**	**0.06**	**0.08**	**0.08**	**0.05**

Table 4.40: Entry velocities for specimens subjected to a single impact

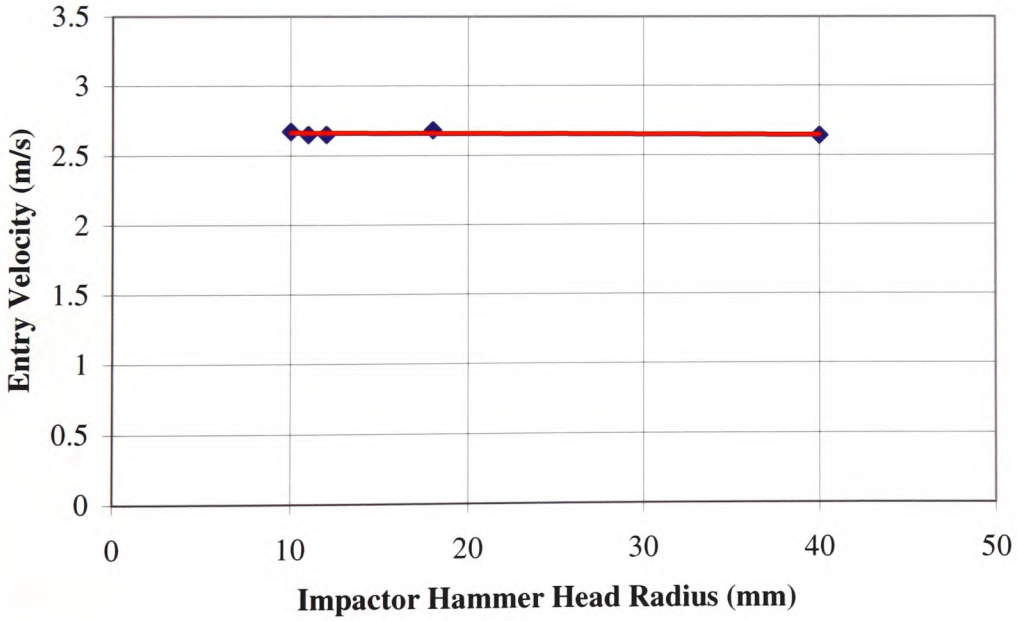

Figure 4.14: Entry impact velocity against impactor hammer head radius

4.3.3 Exit Velocity after Impact

The exit velocities for all of the impactor hammer head sizes are shown in Table 4.41 and on the graph in Figure 4.15. The exit velocity was shown to increase with the impactor hammer head size, indicating that less energy is absorbed by the specimen on impact. The trend line of the graph is logarithmic and can be used to predict the exit velocity for any impactor head radius between 10mm and 40mm, with a correlation of 96.02%. The results for exit velocity can be used to validate the results of the numerical models.

	Exit Velocity after Impact (m/s)				
Specimen Number	**10mm Impactor Hammer Head**	**11mm Impactor Hammer Head**	**12mm Impactor Hammer Head**	**18mm Impactor Hammer Head**	**40mm Impactor Hammer Head**
1	0.80	0.78	0.80	0.89	1.09
2	0.78	0.80	0.87	0.91	1.05
3	0.77	0.76	0.82	0.92	1.05
4	0.85	0.86	0.86	0.96	1.02
5	0.76	0.82	0.83	0.94	1.06
6	0.75	0.83	0.84	0.95	1.05
7	0.78	0.82	0.85	0.94	1.08
8	0.75	0.84	0.81	1.01	1.04
9	0.78	0.83	0.81	0.96	1.08
10	0.83	0.77	0.81	0.99	1.05
11		0.81	0.78	0.97	1.03
12			0.80	0.97	1.02
Average	**0.79**	**0.81**	**0.82**	**0.95**	**1.05**
SD	**0.03**	**0.03**	**0.03**	**0.03**	**0.02**

Table 4.41: Exit velocities for specimens subjected to a single impact

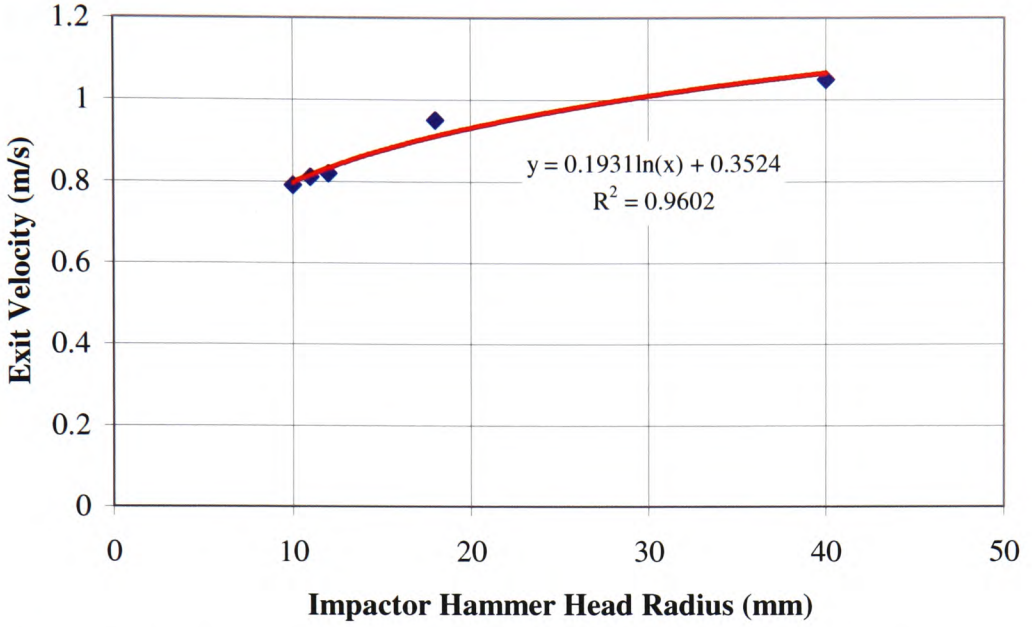

Figure 4.15: Exit velocity after impact against impactor hammer head radius

4.3.4 Coefficient of Restitution

The coefficient of restitution for specimens impacted with the various sizes of impactor hammer head is calculated using equation 4.1. An example of the calculation for the 10mm radius impactor hammer head is shown below.

$$COR_{10mm} = \frac{0.79}{2.67}$$

$$COR_{10mm} = 0.29$$

Specimen Number	Coefficient of Restitution				
	10mm Impactor Hammer Head	11mm Impactor Hammer Head	12mm Impactor Hammer Head	18mm Impactor Hammer Head	40mm Impactor Hammer Head
1	0.28	0.30	0.31	0.35	0.41
2	0.29	0.30	0.31	0.36	0.40
3	0.29	0.29	0.30	0.36	0.40
4	0.32	0.31	0.32	0.36	0.40
5	0.30	0.31	0.32	0.35	0.40
6	0.29	0.31	0.32	0.35	0.39
7	0.31	0.31	0.32	0.35	0.40
8	0.28	0.31	0.30	0.36	0.40
9	0.29	0.32	0.30	0.35	0.41
10	0.30	0.30	0.32	0.35	0.40
11		0.32	0.30	0.36	0.39
12			0.30	0.36	0.39
Average	**0.30**	**0.31**	**0.31**	**0.35**	**0.40**
SD	**0.01**	**0.01**	**0.01**	**0.00**	**0.01**

Table 4.42: Coefficient of restitution of specimens subjected to a single impact

The COR for all specimen impacts using the different impactor hammer head sizes are shown in Table 4.42. The impact can be said to be partially plastic, with some kinetic energy being transformed into the deformation of material, sound and possibly other forms of energy, such as heat. The trend line of the graph, shown in Figure 4.16, is logarithmic and can be used to predict the coefficient of restitution for any impactor hammer head radius between 10mm and 40mm for the impact rig under the same conditions, with a correlation of 99.05%.

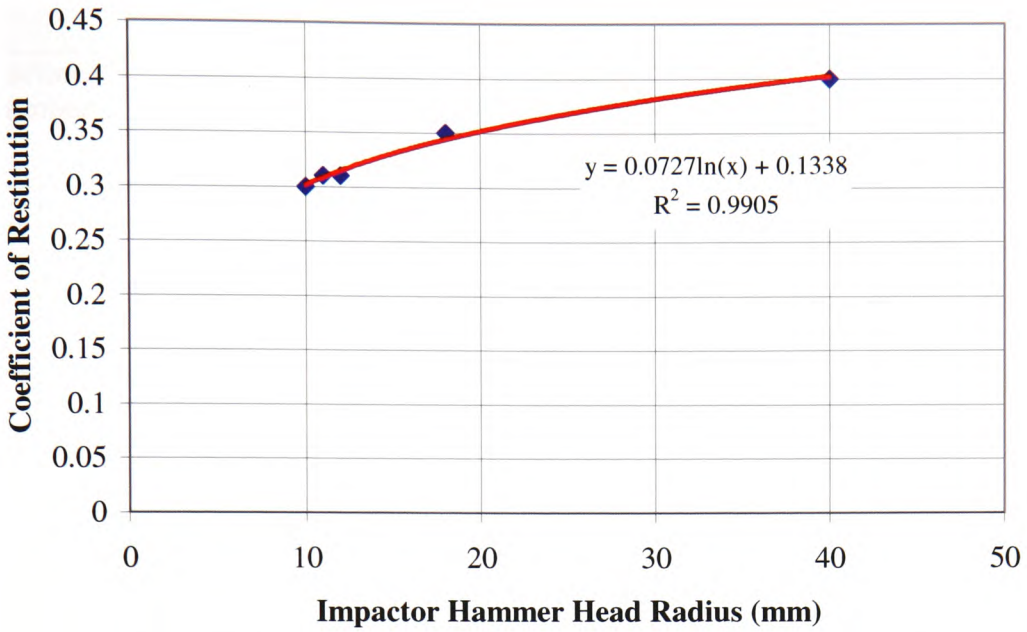

Figure 4.16: Coefficient of restitution against impactor hammer head radius

4.3.5 Entry Impact Energy

The entry energies for all the impactor hammer head sizes tested are shown in Table 4.43 and on the graph in Figure 4.17. These values compare well with the theoretical entry energy of 14.16J, as calculated in Section 3.5.2. The difference between the values is possibly due to inaccuracies in the potentiometer readings and frictional losses in the impact rig. The graph has a linear trend line, as the velocity values used when calculating the entry impact energy are very close, showing that for any size of impactor hammer head with a radius between 10mm and 40mm, the entry energy imparted on the specimen will be approximately 12.46J (SD 0.16). This value can be used in the analysis of experimental work which will determine the effect of impact energy on the fatigue life of a specimen.

Specimen Number	Entry Impact Energy (J)				
	10mm Impactor Hammer Head	11mm Impactor Hammer Head	12mm Impactor Hammer Head	18mm Impactor Hammer Head	40mm Impactor Hammer Head
1	14.13	12.28	11.69	11.49	12.40
2	12.64	12.48	13.74	11.51	12.09
3	12.38	12.40	13.44	11.69	11.95
4	12.57	13.74	12.57	12.55	11.25
5	11.73	12.37	11.93	12.87	12.55
6	11.91	12.31	11.96	12.72	12.79
7	11.52	12.32	11.97	12.49	13.08
8	12.44	12.42	12.49	14.03	11.89
9	12.77	12.07	12.60	12.84	12.27
10	13.18	11.60	11.42	13.67	12.38
11		11.55	11.69	12.95	11.91
12			12.58	13.09	12.23
Average	**12.53**	**12.32**	**12.34**	**12.66**	**12.23**
SD	**0.75**	**0.57**	**0.71**	**0.79**	**0.47**

Table 4.43: Entry impact energies for specimens subjected to a single impact

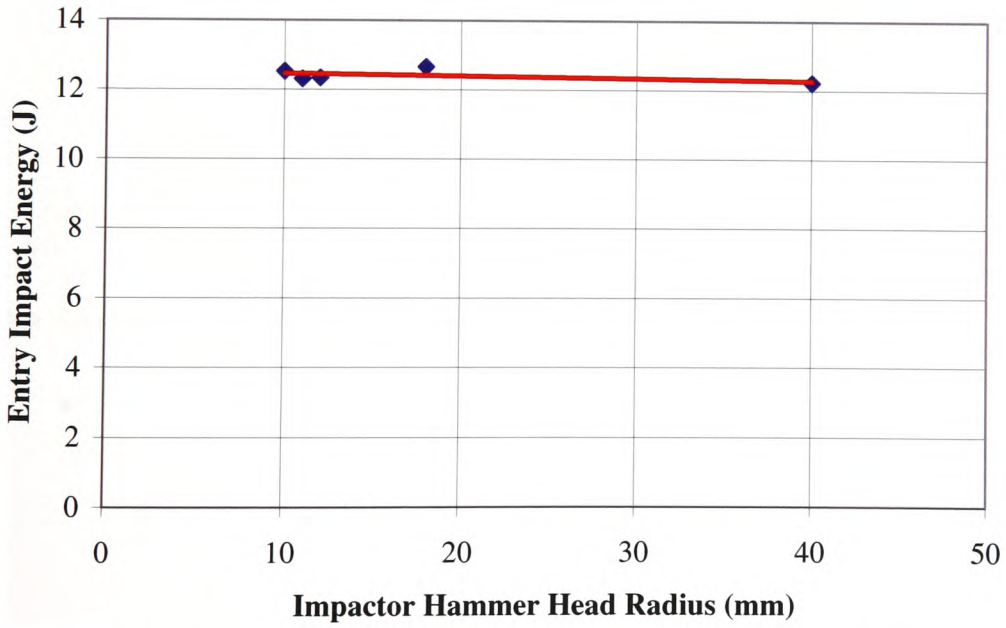

Figure 4.17: Entry impact energy against impactor hammer head radius

4.3.6 Exit Energy after Impact

The exit energy for all impactor hammer head sizes tested is shown in Table 4.44 and Figure 4.18. The exit energy was shown to increase with the impactor hammer head size, indicating that as the size of impactor hammer head increases less energy is absorbed by the specimen on impact. The trend line of the graph is logarithmic and can be used to predict the exit energy for any impactor head radius between 10mm and 40mm, with a correlation of 97.24%.

	Exit Energy after Impact (J)				
Specimen Number	**10mm Impactor Hammer Head**	**11mm Impactor Hammer Head**	**12mm Impactor Hammer Head**	**18mm Impactor Hammer Head**	**40mm Impactor Hammer Head**
1	1.14	1.08	1.11	1.41	2.10
2	1.06	1.12	1.32	1.46	1.93
3	1.05	1.02	1.19	1.49	1.94
4	1.27	1.29	1.31	1.63	1.84
5	1.03	1.19	1.23	1.55	1.98
6	1.00	1.22	1.24	1.59	1.93
7	1.08	1.20	1.26	1.57	2.06
8	1.00	1.23	1.16	1.78	1.92
9	1.06	1.21	1.17	1.61	2.06
10	1.22	1.05	1.15	1.72	1.95
11		1.15	1.08	1.64	1.86
12			1.12	1.66	1.84
Average	**1.09**	**1.16**	**1.19**	**1.59**	**1.95**
SD	**0.09**	**0.08**	**0.08**	**0.11**	**0.09**

Table 4.44: Exit energies after impact for specimens subjected to a single impact

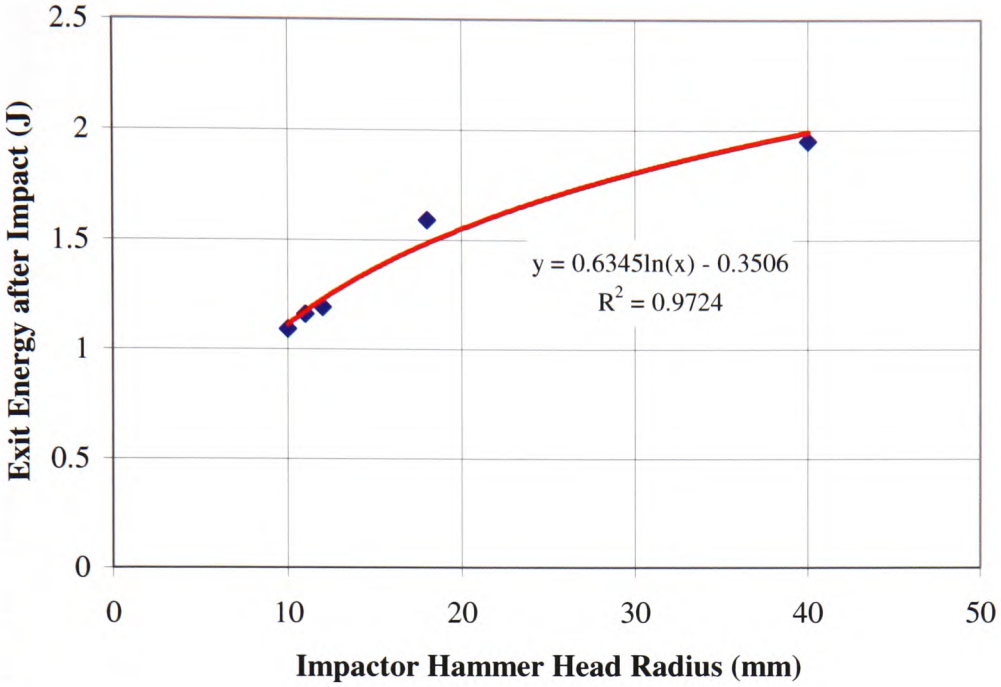

Figure 4.18: Exit energy after impact against impactor hammer head radius

4.3.7 Depth of Impact Crater

The depths of craters produced for the different impactor hammer head sizes tested are shown in Table 4.45 and on the graph in Figure 4.19. These values can be used to validate the results produced by the numerical models. The depth of crater produced was shown to decrease with a corresponding increase in impactor hammer head size. The trend line of the graph can be used to predict the depth of crater produced for any impactor hammer head radius between 10mm and 40mm.

Impactor Hammer Head Radius (mm)	Depth of Impact Crater (mm)
10	0.38
11	0.36
12	0.34
18	0.25
40	0.18

Table 4.45: Depth of impact craters of specimens subjected to a single impact

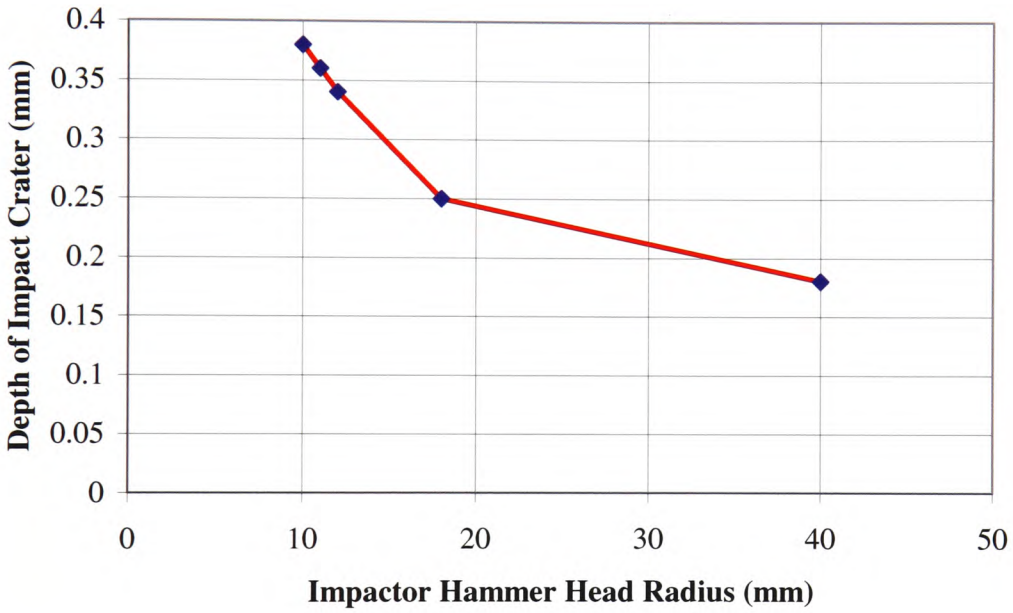

Figure 4.19: Depth of impact crater against impactor hammer head radius

4.3.8 Width of Impact Crater

The width of craters produced for the various impactor hammer head sizes tested are shown in Table 4.46 and on the graph in Figure 4.20. These values can be used to validate the results produced by the numerical models. The crater width produced was shown to increase with a corresponding increase in impactor hammer head size. The trend line of the graph is logarithmic and can be used to

predict the width of crater produced for any impactor hammer head radius between 10mm and 40mm, with a correlation of 99.74%.

Impactor Hammer Head Radius (mm)	Width of Impact Crater (mm)
10	5.6
11	5.75
12	5.9
18	6.5
40	7.5

Table 4.46: Width of impact craters of specimens subjected to a single impact

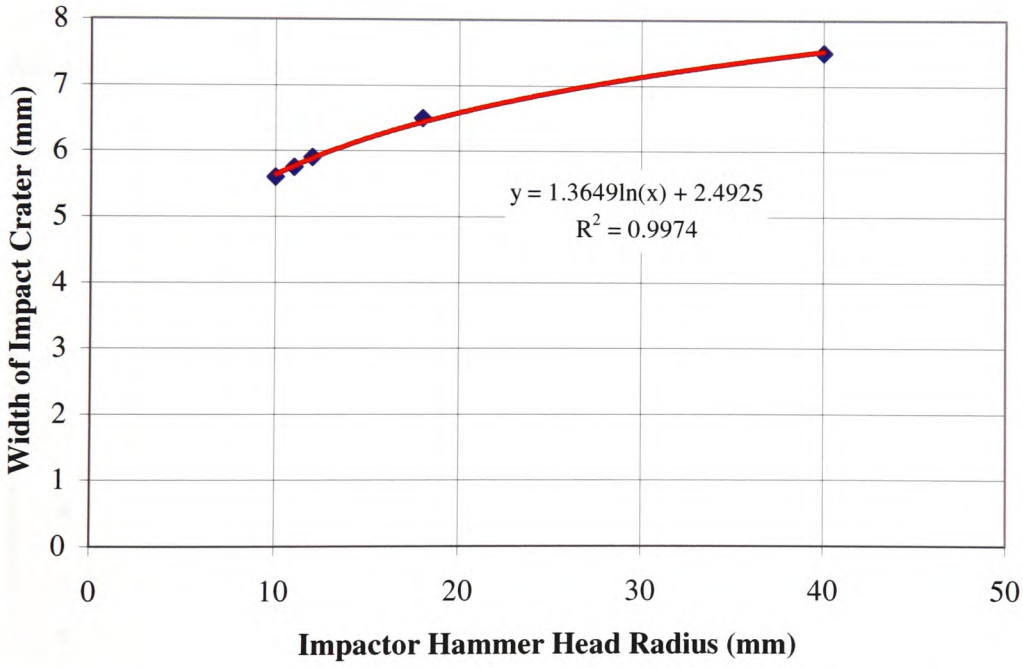

Figure 4.20: Width of impact crater against impactor hammer head radius

4.3.9 Volume of Impact Crater

The volumes of the craters produced for the different impactor hammer head sizes tested were calculated using equation 4.2 and are shown in Table 4.47 and on the graph in Figure 4.21. The volume of crater produced was shown to decrease with a corresponding increase in the impactor hammer head size. The trend line of the graph which can be used to predict the volume of crater produced for any impactor hammer head radius between 10mm and 40mm.

Impactor Hammer Head Radius (mm)	Volume of Impact Crater (mm^3)
10	4.71
11	4.70
12	4.67
18	4.16
40	3.98

Table 4.47: Volume of impact craters of specimens subjected to a single impact

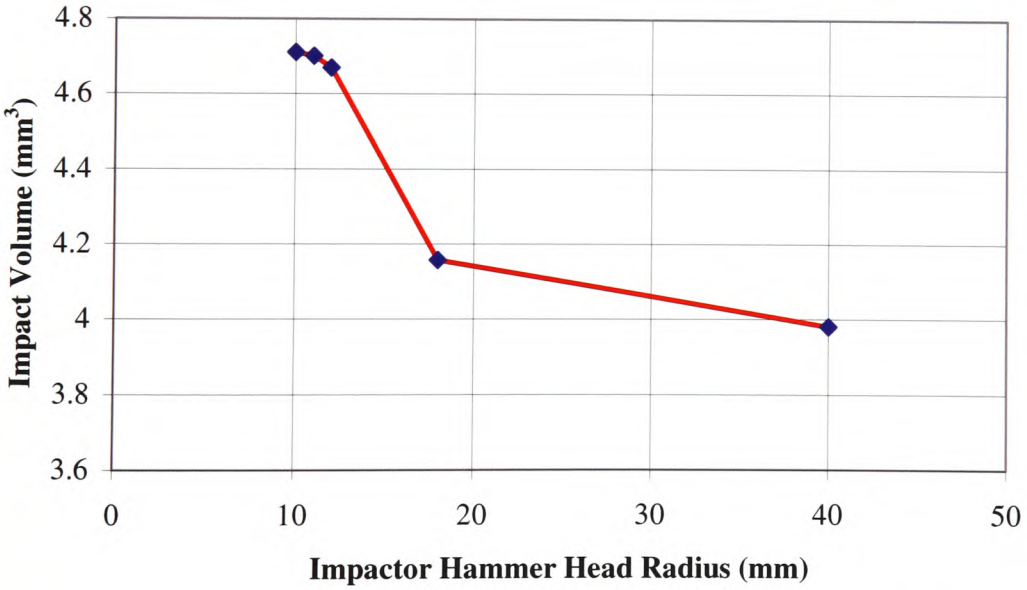

Figure 4.21: Volume of impact crater against impactor hammer head radius

4.3.10 Impact Contact Time

The impact contact times calculated from the accelerometer readings for each of the specimens tested are shown in Table 4.48 and were calculated as previously described in Section 4.2.10. Any readings not recorded were due to operational error. These results can be used to validate the impact contact times produced by the numerical models.

	Impact Contact Time (seconds)				
Specimen Number	**10mm Impactor Hammer Head**	**11mm Impactor Hammer Head**	**12mm Impactor Hammer Head**	**18mm Impactor Hammer Head**	**40mm Impactor Hammer Head**
1	9.00E-5	1.08E-4	1.11E-04	1.06E-04	1.10E-04
2	9.00E-5	1.09E-4	1.08E-04	1.08E-04	1.34E-04
3	9.30E-5	1.04E-4	1.06E-04	1.05E-04	1.25E-04
4	8.70E-5	1.21E-4	1.05E-04	1.09E-04	1.20E-04
5	9.20E-5	1.17E-4	1.00E-04	1.11E-04	1.08E-04
6		5.00E-5	1.05E-04	1.12E-04	1.08E-04
7		1.09E-4	1.11E-04	1.05E-04	1.10E-04
8		1.13E-4	1.03E-04	1.05E-04	1.26E-04
9		1.16E-4	1.09E-04	1.09E-04	1.27E-04
10		1.06E-4		1.01E-04	
11		1.08E-4			
12					
Average	**9.04E-5**	**1.06E-04**	**1.06E-04**	**1.07E-04**	**1.19E-04**
SD	**1.41E-06**	**1.92E-20**	**1.41E-06**	**3.54E-06**	**1.20E-05**

Table 4.48: Impact contact times calculated from the accelerometer readings

4.4 Impact Prediction

In order to determine whether it was possible to use the experimental results obtained and graphical information to make predictions for different sized impactor hammer heads, a 25mm radius impactor hammer head was manufactured and tested using the same experimental procedure. However, due to a restriction on material available, only four specimens were tested using the 25mm impactor hammer head. In certain instances only three of the four experimental results obtained have been recorded; this was due to operational error.

The average surface texture of the specimens tested, measured as the CLA, was found to be 0.158μm (SD 0.013), as shown in Table 4.49. The dimensions and failure stresses for specimens impacted with the 25mm impactor hammer head are shown in Table 4.50.

Specimen Number	Surface Texture Reading 1 (μm)	Surface Texture Reading 2 (μm)	Average Surface Texture (μm)
1	0.186	0.106	0.146
2	0.121	0.219	0.170
3	0.141	0.154	0.148
4	0.182	0.155	0.169
Average	**0.158**	**0.159**	**0.158**
SD	**0.032**	**0.046**	**0.013**

Table 4.49: Surface texture of specimens impacted with 25mm impactor hammer head

Specimen Number	Width of Specimen (mm)	Depth of Specimen (mm)	Cross-sectional Area of Specimen (mm^2)	Stress (MN/m^2)
1	14.06	2.90	40.77	282.042
2	14.13	2.91	41.12	279.681
3	14.06	2.98	41.90	274.471
4	14.10	2.90	40.89	281.242
Average	**14.09**	**2.92**	**41.17**	**279.359**
SD	**0.03**	**0.02**	**0.04**	**3.403**

Table 4.50: Specimen dimensions and failure stresses for specimens impacted with 25mm impactor hammer head

4.4.1 Cycles to Failure

The average number of cycles to failure for all the impactor hammer head sizes tested was 47,455 cycles (SD 3,582), and it was predicted that the 25mm radius impactor hammer head would cause specimens to fail within two standard deviations i.e. between 40,291 and 54,619 cycles. It was found that the average experimental number of cycles to failure for specimens impacted with the 25mm radius impactor hammer head was 38,789 cycles (SD 5,696), which does not lie within the predicted region, as shown in Table 4.51 and Figure 4.22. It was also noted that this value does not lie between the experimental number of cycles to failure for specimens impacted with the 18mm and the 40mm impactor hammer heads, namely 49,934 and 48,908 cycles respectively, as shown in Table 4.33. It is felt that more data is required in order to determine the exact trend.

Specimen Number	Cycles to Failure
1	41,740
2	45,319
3	33,319
4	34,780
Average	**38,789**
SD	**5,696**

Table 4.51: Cycles to failure for specimens subjected to a single impact with the 25mm impactor hammer head

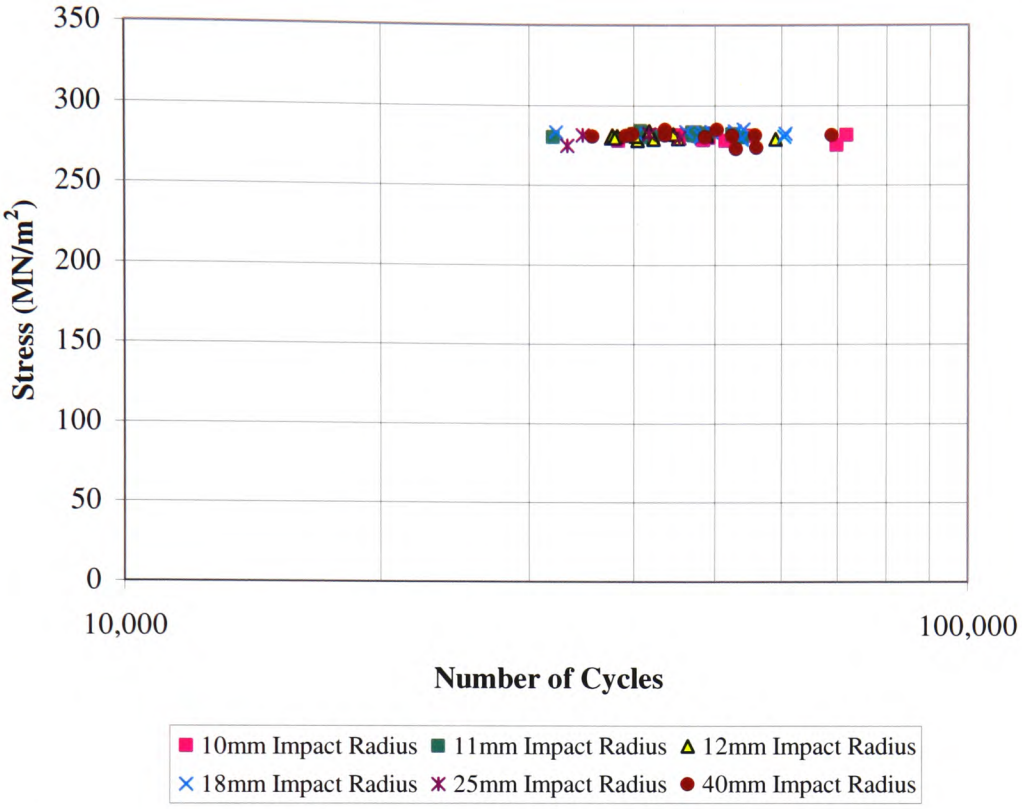

Figure 4.22: S-N Diagram for impact fatigue tests for '070M20' carbon steel (including 25mm impact radius)

4.4.2 Hardness of Material

The specimens impacted with the 25mm radius hammer head were found to have average hardness values of approximately 3.3 Rockwell C (SD 10.08) or 164 DPN close to the fracture and -4.15 Rockwell C (SD 3.7) or 140 DPN near the shoulder of the specimen as shown in Table 4.52. These hardness values are comparable with those for specimens impacted with the various sizes of impactor hammer head tested.

Specimen Number	Hardness (Rockwell C) – Bottom of Specimen				Hardness (Rockwell C) – Top of Specimen			
	Side 1		Side 2		Side 1		Side 2	
	Shoulder	Fracture	Shoulder	Fracture	Shoulder	Fracture	Shoulder	Fracture
1	4.5	0.5	-5.0	32.5	-1.0	46.0	-8.0	-6.0
2	1.0	2.5	-7.5	-7.5	-2.0	1.0	-4.0	-5.5
3	0.5	1.0	-5.5	-12.0	-1.0	0.5	-7.0	-6.0
4	-2.5	0.5	3.0	26.0	-27.0	1.5	-4.5	-22.5
Average	**0.9**	**1.1**	**-3.8**	**9.8**	**-7.8**	**12.3**	**-5.9**	**-10.0**
SD	**2.9**	**0.9**	**4.6**	**22.7**	**12.8**	**22.5**	**1.9**	**8.3**

Table 4.52: Hardness values for specimens subjected to a single impact with the 25mm impactor hammer head

4.4.3 Entry Velocity of Impact

The average entry velocity for any size impactor hammer head between 10mm and 40mm radius was found to be 2.66m/s (SD 0.02). Therefore, it is possible to predict that the entry velocity for a 25mm radius impactor hammer head will be 2.66m/s (SD 0.02). The actual average value for the entry impact velocity for the 25mm impactor hammer head was found to be 2.67m/s (SD 0.03), as shown in Table 4.53, which is very close to the predicted value and within the range of the experimental results. Figure 4.23 shows the entry velocity for all sizes of impactor hammer heads tested.

Specimen Number	Entry Velocity (m/s)
1	2.68
2	2.65
3	2.69
Average	**2.67**
SD	**0.03**

Table 4.53: Entry impact velocities for specimens subjected to a single impact with the 25mm impactor hammer head

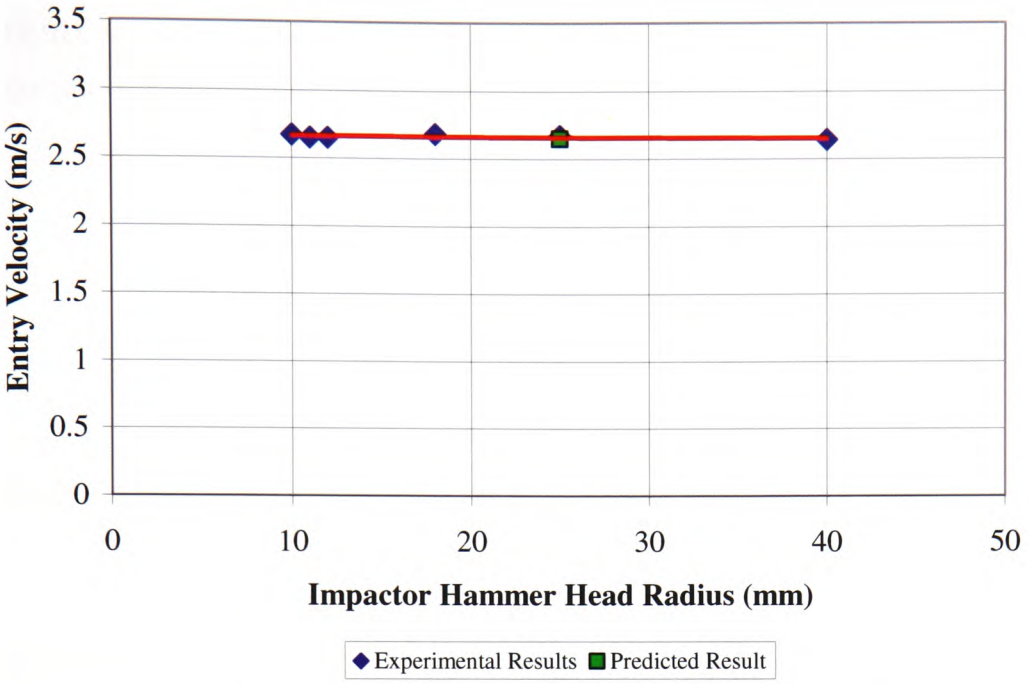

Figure 4.23: Entry impact velocity against impactor hammer head radius (predicted and experimental results)

4.4.4 Exit Velocity after Impact

From the formula (equation 4.3), obtained from the graph of exit impact velocities in Figure 4.15, the exit velocity after impact for a 25mm radius impactor hammer head was predicted to be 0.97m/s as shown.

$$y = 0.1931\ln(x) + 0.2524 \qquad (4.3)$$

when $x = 25\text{mm}$

$$y = 0.1931\ln(25) + 0.2524$$

$$y = 0.97\text{m/s}$$

The actual average value for exit velocity after impact was found to be 0.96m/s (SD 0.01), as shown in Table 4.54, which is within the range of the experimental results and very close to the predicted value.

Specimen Number	Exit Velocity (m/s)
1	0.95
2	0.96
3	0.96
Average	**0.96**
SD	**0.01**

Table 4.54: Exit velocities after impact for specimens subjected to a single impact with the 25mm impactor hammer head

Plotting the experimental results for all sizes of impactor hammer head tested as shown in Figure 4.24, produced a more accurate logarithmic trend and formula (equation 4.4) for predicting the exit velocity after impact for impactor hammer heads between 10mm and 40mm radius. The formula which should now be used is:

$$y=0.1894\ln(x) + 0.3604 \qquad (4.4)$$

where x is the impactor hammer head radius (mm) and y is the exit velocity after impact (m/s).

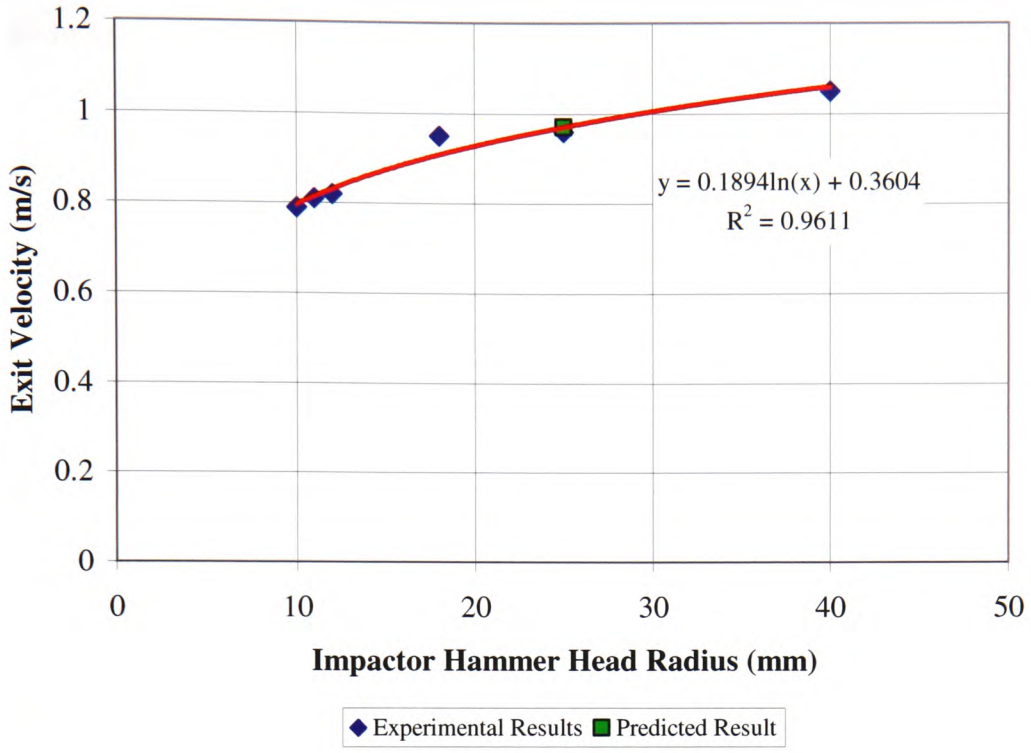

Figure 4.24: Exit velocity after impact against impactor hammer head radius (predicted and experimental results)

4.4.5 Coefficient of Restitution

Using the formula (equation 4.5), obtained from the graph of coefficient of restitution in Figure 4.16, the coefficient of restitution for a 25mm radius impactor hammer head is predicted to be 0.37 as shown below.

$$y = 0.0727 \ln(x) + 0.1338 \qquad (4.5)$$

when $x = 25\text{mm}$

$$y = 0.0727 \ln(25) + 0.1338$$

$$y = 0.37$$

The actual average value for the coefficient of restitution was 0.36 (SD 0.00), as shown in Table 4.55, which is close to the predicted value.

Specimen Number	Coefficient of Restitution
1	0.35
2	0.36
3	0.36
Average	**0.36**
SD	**0.00**

Table 4.55: Coefficients of restitution for specimens subjected to a single impact with the 25mm impactor hammer head

Plotting the experimental results for all sizes of impactor hammer heads tested as shown in Figure 4.25, produced a more accurate logarithmic trend and formula (equation 4.6) for predicting the coefficient of restitution for impactor hammer heads between 10mm and 40mm radius. The formula which should now be used is:

$$y = 0.0707\ln(x) + 0.1383 \qquad (4.6)$$

where x is the impactor hammer head radius (mm) and y is the coefficient of restitution.

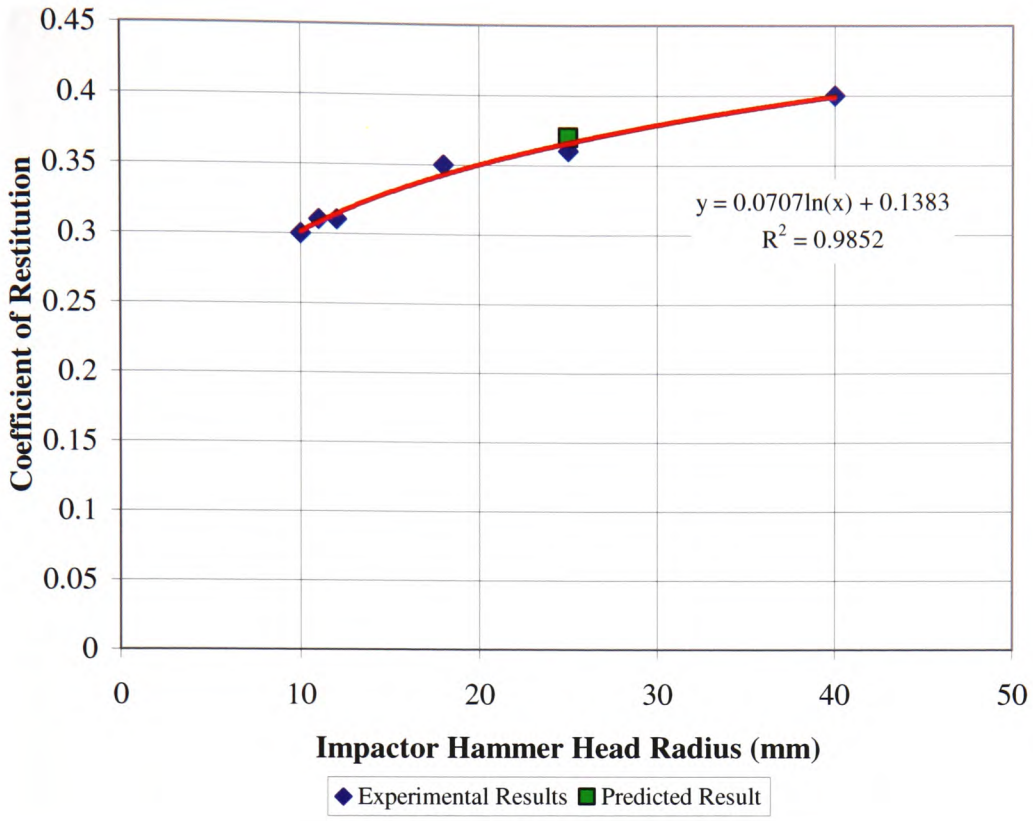

Figure 4.25: Coefficient of restitution against impactor hammer head radius (predicted and experimental results)

4.4.6 Entry Impact Energy

The average entry impact energy for any size impactor hammer head between 10mm and 40mm radius was found to be 12.46J (SD 0.16). Therefore, it is possible to predict that the entry impact energy for a 25mm radius impactor hammer head will be 12.46J (SD 0.16). The actual average value for the entry impact energy for the 25mm impactor hammer head was found to be 12.58 (SD 0.20), as shown in Table 4.56, which is within the range of the experimental results. Figure 4.26 shows the entry impact energy for all sizes of impactor hammer heads tested.

Specimen Number	Entry Impact Energy (J)
1	12.64
2	12.36
3	12.74
Average	**12.58**
SD	**0.20**

Table 4.56: Entry impact energies for specimens subjected to a single impact with the 25mm impactor hammer head

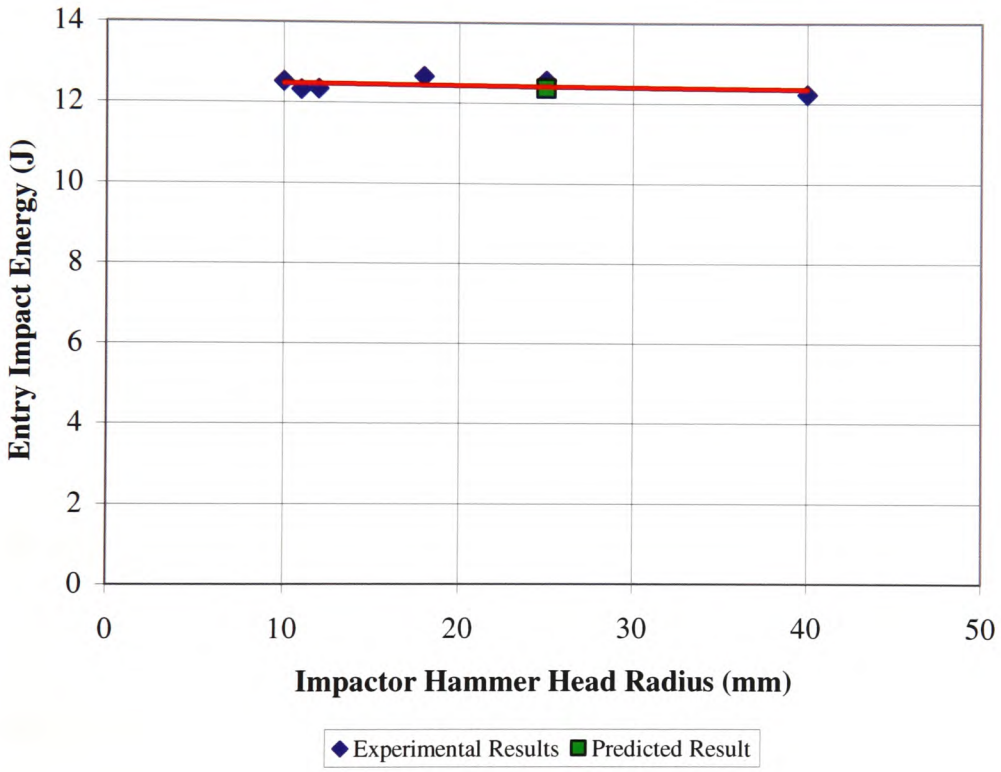

Figure 4.26: Entry impact energy against impactor hammer head radius (predicted and experimental results)

4.4.7 Exit Energy after Impact

From the formula (equation 4.7), obtained from the graph of exit energy after impact as shown in Figure 4.18, the exit energy for a 25mm radius impactor hammer head was predicted to be 1.69J as shown below.

$$y = 0.6345\ln(x) - 0.3506 \quad (4.7)$$

when $x = 25mm$

$$y = 0.6345\ln(25) - 0.3506$$

$$y = 1.69J$$

The actual average value for exit energy after impact was 1.61J (SD 0.02), as shown in Table 4.57, which is close to the predicted value.

Specimen Number	Exit Energy after Impact (J)
1	1.59
2	1.61
3	1.63
Average	**1.61**
SD	**0.02**

Table 4.57: Exit energies after impact for specimens subjected to a single impact with the 25mm impactor hammer head

Plotting the experimental results for all sizes of impactor hammer head tested, as shown in Figure 4.27, produced a more accurate logarithmic trend and formula (equation 4.8) for predicting the exit energy after impact for impactor hammer heads between 10mm and 40mm radius. The formula which should now be used is:

$$y = 0.613\ln(x) - 0.3034 \quad (4.8)$$

where x is the impactor hammer head radius (mm) and y is the exit energy after impact (J).

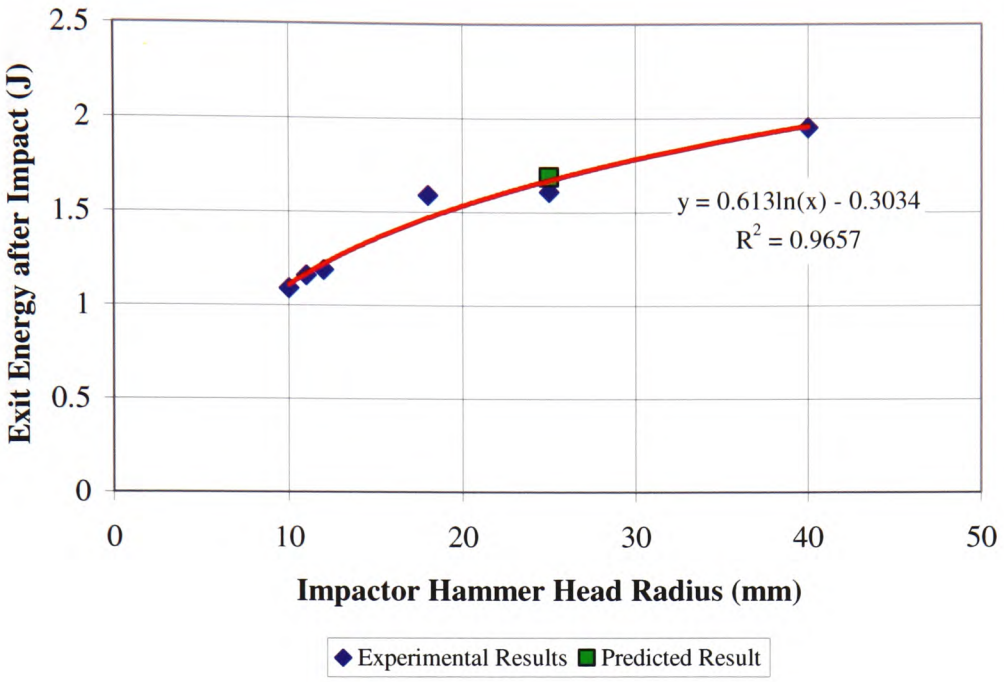

Figure 4.27: Exit energy after impact against impactor hammer head radius (predicted and experimental results)

4.4.8 Depth of Impact Crater

From the graph showing the depth of impact crater produced by the various sizes of impactor hammer heads in Figure 4.19, the depth of impact crater produced by a 25mm radius impactor hammer head was predicted to be approximately 0.225mm. The actual value for the depth of impact crater produced by a 25mm radius impactor hammer head was 0.22mm, which is close to the predicted value. Plotting the experimental results for all sizes of impactor hammer heads tested, as shown in Figure 4.28, produced a more accurate trend for predicting the depth of impact crater produced for impactor hammer heads with a radius between 10mm and 40mm.

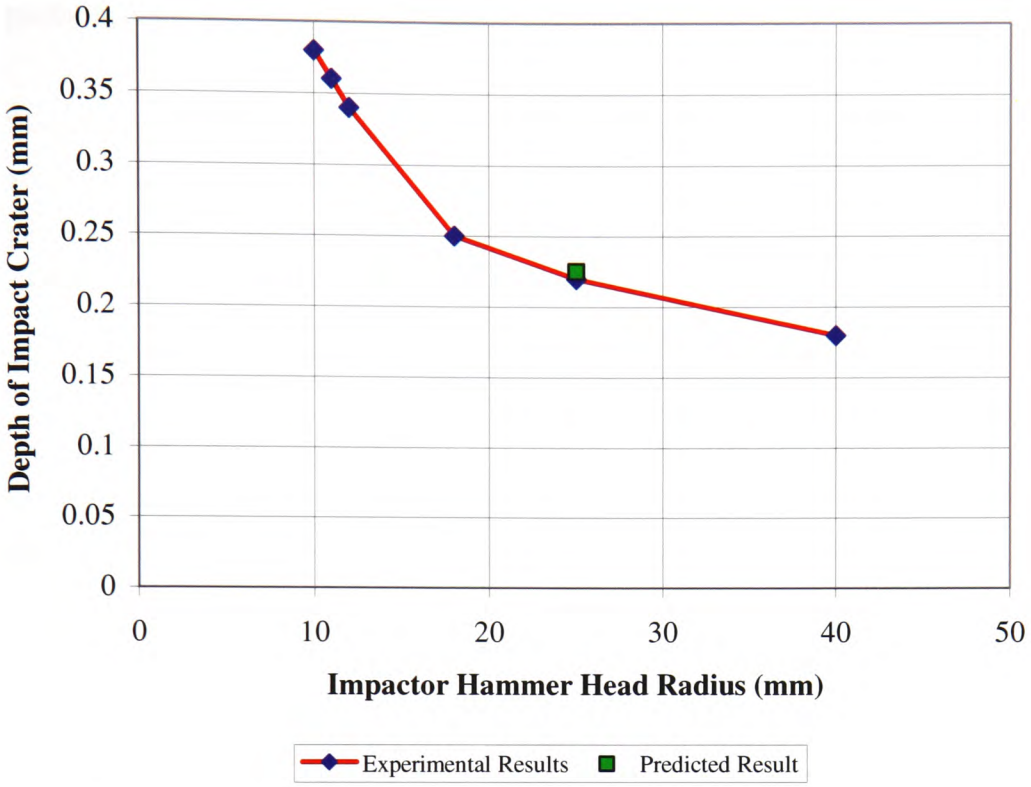

Figure 4.28: Depth of impact crater against impactor hammer head radius (predicted and experimental results)

4.4.9 Width of Impact Crater

From the formula (equation 4.9), obtained from the graph showing the width of impact craters produced by the various sizes of impactor hammer head in Figure 4.20, the width of crater produced by a 25mm radius impactor hammer head was predicted to be 6.886mm as shown below.

$$y = 1.3649\ln(x) + 2.4925 \qquad (4.9)$$

when $x = 25\text{mm}$

$$y = 1.3649\ln(25) + 2.4925$$

$$y = 6.886\text{mm}$$

The actual value for the width of impact crater produced by a 25mm radius impactor hammer head was 6.8mm, which is close to the predicted value.

Plotting the experimental results for all sizes of impactor hammer heads tested, as shown in Figure 4.29, produced a more accurate logarithmic trend and formula (equation 4.10) for predicting the width of impact crater for impactor hammer heads between 10mm and 40mm radius. The formula which should now be used is:

$$y = 1.3423\ln(x) + 2.5422 \qquad (4.10)$$

where x is the impactor hammer head radius (mm) and y is the width of impact crater (mm).

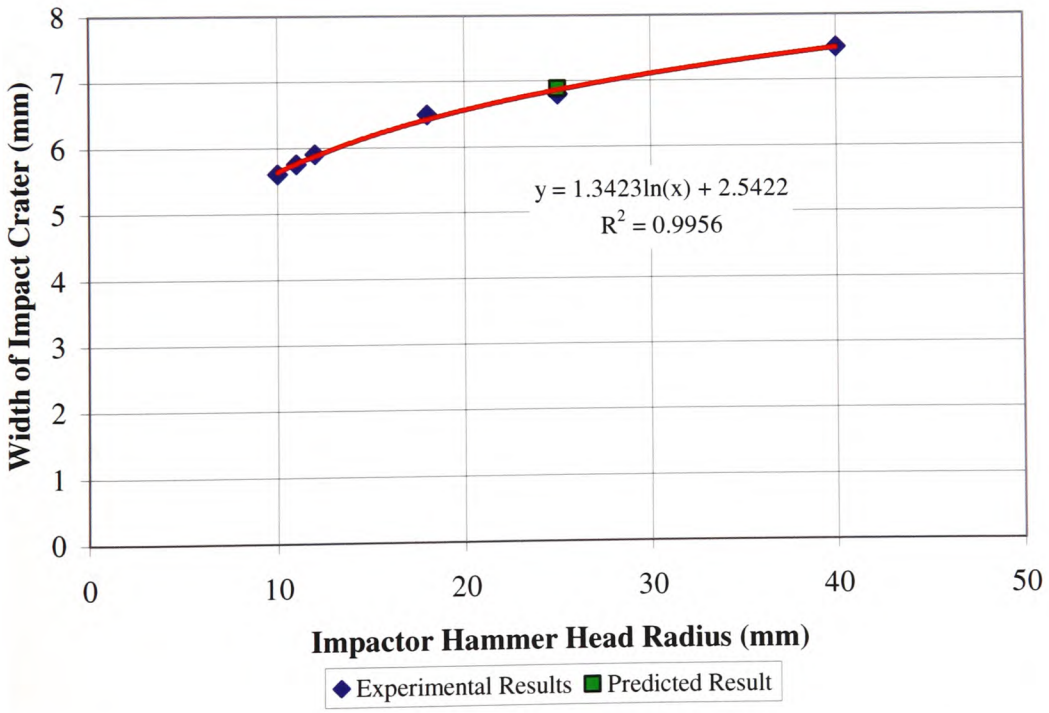

Figure 4.29: Width of impact crater against impactor hammer head radius (predicted and experimental results)

4.4.10 Volume of Impact Crater

From the graph showing the volume of impact crater produced by the various sizes of impactor hammer heads in Figure 4.21, the volume of impact crater produced by a 25mm radius impactor hammer head was predicted to be approximately 4.1mm^3. The actual value for the volume of impact crater produced by a 25mm radius impactor hammer head was 4mm^3, which is close to the predicted value. Plotting the experimental results for all sizes of impactor hammer heads tested, as shown in Figure 4.30, produced a more accurate trend for predicting the impact volume for impactor hammer heads between 10mm and 40mm radius.

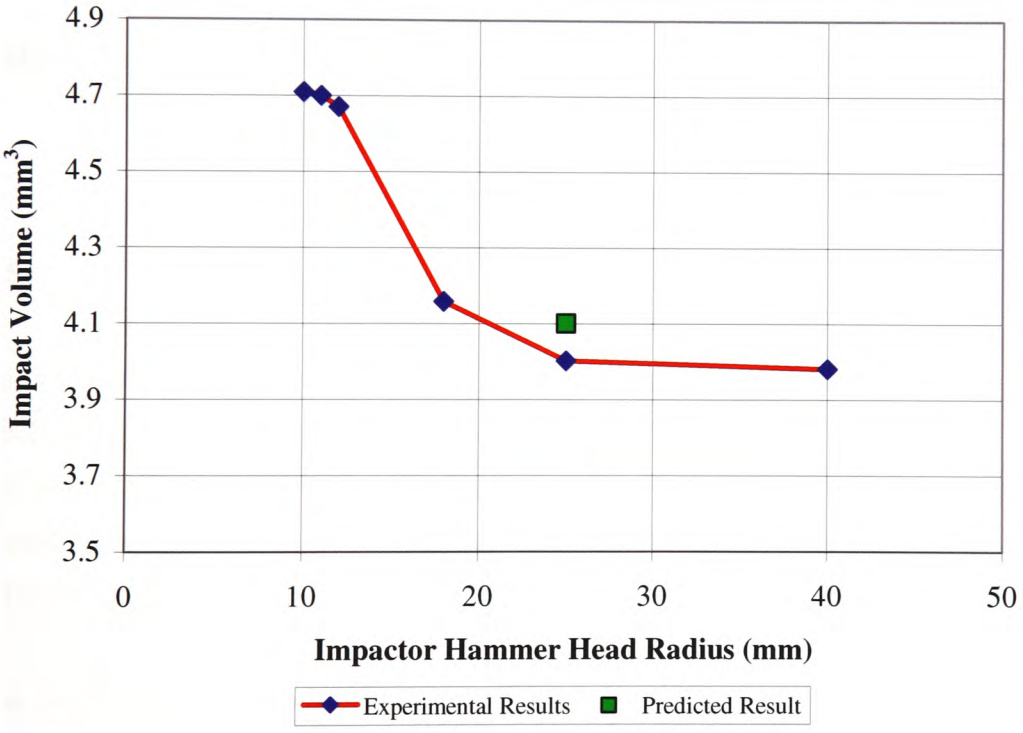

Figure 4.30: Volume of impact crater against impactor hammer head radius (predicted and experimental results)

4.4.11 Impact Contact Time

The average impact contact time recorded by the accelerometer was 1.12E-4 seconds (SD 2.12E-06). This value was the average of the accelerometer readings as shown in Table 4.58, and compares well with the other impacted specimens.

Specimen Number	Impact Contact Time (seconds)
1	1.09E-04
2	1.21E-04
3	1.07E-04
4	1.12E-04
Average	**1.12E-04**
SD	**2.12E-06**

Table 4.58: Impact contact times for specimens subjected to a single impact with the 25mm impactor hammer head

4.5 T-Test

The t-test was developed in 1908 by W. S. Gossett, to look at the interference in small samples of data, as the interpretation of small samples may be inaccurate due to the lack of available data. By using the t-test it is possible to compare the means of two small data groups and to determine whether they are statistically different from each other.

The t-test for the fatigue cycle data on the 10mm and 12mm impact radius is shown below:

n = number of data for each list

$\bar{x}$ = mean

σ = standard deviation

t = T - test value

DOF = degrees of freedom

The number of specimens tested for each impact radius is:

$$n_{10} = 12$$
$$n_{12} = 12$$

The mean of the fatigue cycle values for each impact radius is:

$$\bar{x}_{10} = 5.107x10^4$$
$$\bar{x}_{12} = 4.281x10^4$$

The standard deviation for each impact radius is:

$$\sigma_{10} = 1.014x10^4$$
$$\sigma_{12} = 6.19x10^3$$

The variance of the difference between the two means is shown below in equation 4.11:

$$\sigma_d^2 = \frac{\sigma_{10}^2}{n_1} + \frac{\sigma_{12}^2}{n_2} \qquad (4.11)$$

$$\sigma_d^2 = \left(\frac{1.014x10^4}{12}\right)^2 + \left(\frac{6.19x10^3}{12}\right)^2$$

$$\sigma_d^2 = 10109016.33 + 3193008.33$$

$$\sigma_d^2 = 13302024.66$$

$$\sigma_d = 3647.19$$

The t value is shown below in equation 4.12:

$$\frac{t = \bar{x}_{10} + \bar{x}_{12}}{\sigma_d} \qquad (4.12)$$

$$t = \frac{5.107x10^4 - 4.281x10^4}{3647.19}$$

$$t = 2.26$$

The degree of freedom is shown below in equation 4.13:

$$DOF = n_{10} + n_{12} - 2 \qquad (4.13)$$

$$DOF = 12 + 12 - 2$$

$$DOF = 22$$

If the calculated t value exceeds the tabulated t value for the calculated degree of freedom, then the means are significantly different.

To determine the significance of the data, a risk level, also known as an alpha level, must be set. In the majority of research an alpha level of 0.05 is set, which means there is a 95% chance of the means being significantly different. Using this alpha level, the tabulated t value in above set of data is 1.717 and the calculated value is 2.26. As the calculated value exceeds the tabulated value the means are significantly different.

4.5.1 T-Test on Entry Velocity of Impact

T-tests were carried out on the entry impact velocity for each set of data for all the various impactor hammer head sizes tested. It was found that there was no significant difference between the means apart from the case which compared the 40mm with the 25mm radius impactor hammer head, as shown in Table 4.59. This indicates that the entry impact velocity for one size of impactor hammer head is not statistically different from any other size of impactor hammer head, which again demonstrates the consistency of impacts produced using the impact

rig. However, in the case of the 40mm and 25mm radius impactor hammer head which shows a significant difference between the means, the t-test result is considered to be invalid. This discrepancy is possibly due to the small amount of data available for the impacts made using the 25mm radius impactor hammer head, as there was agreement between the experimental results for the entry velocity for all sizes impactor hammer heads produced.

Impactor Hammer Head Radius (mm)	Impactor Hammer Head Radius (mm)	Significant Difference	Percentage Accuracy (%)
10	12	No	45.1
10	40	No	71.7
12	40	No	31.4
10	18	No	30.2
12	18	No	69.2
40	18	No	87.1
10	11	No	1.7
12	11	No	44.1
18	11	No	27.1
40	11	No	67.4
10	25	No	58.1
11	25	No	50
12	25	No	81.2
18	25	No	37.5
40	25	Yes	96.2

Table 4.59: T-test results on entry impact velocities

4.5.2 T-Test on Exit Velocity after Impact

T-tests were also carried out on the exit velocity after impact for each set of data, for all the various impactor hammer head sizes tested. It was found that there was a significant difference between the means, as shown in Table 4.60. This indicates that the exit velocity for one size of impactor hammer head is statistically different from any other size of impactor hammer head. However, in the comparison of the 12mm with the 11mm radius impactor hammer head there was shown to be no significant difference between the means. In this case the

percentage accuracy is so low that the t-test result is considered invalid and more data is required.

Impactor Hammer Head Radius (mm)	Impactor Hammer Head Radius (mm)	Significant Difference	Percentage Accuracy (%)
10	12	Yes	99.3
10	40	Yes	100
12	40	Yes	100
10	18	Yes	100
12	18	Yes	100
40	18	Yes	100
10	11	Yes	95
12	11	No	15.8
18	11	Yes	100
40	11	Yes	100
10	25	Yes	100
11	25	Yes	100
12	25	Yes	100
18	25	No	27.7
40	25	Yes	100

Table 4.60: T-test results on exit velocities after impact

4.5.3 T-Test on Fatigue Cycles

T-tests were carried out on the fatigue cycles for each set of data for the various impactor hammer head sizes tested. The t-test results show that the relationship between fatigue cycles is inconclusive, as 53% of results show a significant difference between the means and 47% show no significant difference, as shown in Table 4.61. However, the percentage accuracies for the t-test results which indicate that there is no significant difference between the means are very low, indicating that the results may be invalid and that more data is required.

Impactor Hammer Head Radius (mm)	Impactor Hammer Head Radius (mm)	Significant Difference	Percentage Accuracy (%)
10	12	Yes	97.5
10	40	No	41
12	40	Yes	93
10	18	No	23.7
12	18	Yes	97.7
40	18	No	22.7
10	11	Yes	93.1
12	11	No	50.5
18	11	Yes	92.4
40	11	No	81.5
10	25	Yes	96.1
11	25	No	88.2
12	25	No	72.8
18	25	Yes	97.7
40	25	Yes	94

Table 4.61: T-test results on fatigue cycles

4.5.4 T-Test on Absorbed Energy

T-tests were carried out on the absorbed energy for each set of data for the various impactor hammer head sizes tested. The t-test results show that there is a significant difference between the means for t-tests carried out using the 40mm impactor hammer head. This indicates that the absorbed energy for the 40mm hammer head is statistically different from any other size of impactor hammer head, as shown in Table 4.62. However, the percentage accuracies for the t-test results on the 10mm, 11mm, 12mm, 18mm and 25mm impactor hammer heads are very low, indicating that the results may be invalid and more data is required.

Impactor Hammer Head Radius (mm)	Impactor Hammer Head Radius (mm)	Significant Difference	Percentage Accuracy (%)
10	12	No	66.4
10	40	Yes	100
12	40	Yes	99.9
10	18	No	76.8
12	18	No	21.8
40	18	Yes	99.7
10	11	No	67.4
12	11	No	5.3
18	11	No	28.4
40	11	Yes	100
10	25	No	64.9
11	25	No	34.1
12	25	No	24.4
18	25	No	9.6
40	25	Yes	98.5

Table 4.62: T-test results on absorbed energy

4.6 Height of Impact

It was decided to extend the experimental programme to determine how the amount of impact energy affects the fatigue life of a specimen of '070M20' carbon steel.

Using only the 10mm radius impactor hammer head, the same procedures were followed as in the original experimental programme. However, for these tests the height of the impactor hammer head was adjusted, thus altering the amount of impact energy imparted onto the specimen.

Previously in the experimental programme, tests were carried out at 410mm (90 degrees angle of impact). The follow-on tests were conducted at 276mm (67.5 degrees angle of impact), 163mm (45 degrees angle of impact), and 87mm (22.5 degrees angle of impact), to give a good range of results between 0 degrees and 90 degrees.

It was only possible to test six specimens for each of the three different impact heights due to restrictions on material availability. The surface texture results of the specimens are shown in Tables 4.63 to 4.65. The impacted specimen dimensions and calculated failure stresses for the specimens are shown in Tables 4.66 to 4.68.

Specimen Number	Surface Texture Reading 1 (μm)	Surface Texture Reading 2 (μm)	Average Surface Texture (μm)
1	0.288	0.249	0.269
2	0.308	0.366	0.337
3	0.320	0.254	0.287
4	0.165	0.142	0.154
5	0.179	0.142	0.161
6	0.123	0.294	0.209
Average	**0.231**	**0.241**	**0.236**
SD	**0.085**	**0.087**	**0.073**

Table 4.63: Surface texture for specimens impacted from a height of 87mm

Specimen Number	Surface Texture Reading 1 (μm)	Surface Texture Reading 2 (μm)	Average Surface Texture (μm)
1	0.235	0.142	0.189
2	0.289	0.373	0.331
3	0.240	0.295	0.268
4	0.336	0.129	0.233
5	0.161	0.161	0.161
6	0.216	0.139	0.178
Average	**0.246**	**0.207**	**0.226**
SD	**0.060**	**0.102**	**0.064**

Table 4.64: Surface texture for specimens impacted from a height of 163mm

Specimen Number	Surface Texture Reading 1 (μm)	Surface Texture Reading 2 (μm)	Average Surface Texture (μm)
1	0.157	0.157	0.157
2	0.198	0.160	0.179
3	0.143	0.151	0.147
4	0.175	0.132	0.154
5	0.149	0.141	0.145
6	0.178	0.258	0.218
Average	**0.167**	**0.167**	**0.167**
SD	**0.021**	**0.046**	**0.028**

Table 4.65: Surface texture for specimens impacted from a height of 276mm

Specimen Number	Width of Specimen (mm)	Depth of Specimen (mm)	Cross-sectional Area of Specimen (mm^2)	Stress (MN/m^2)
1	14.06	2.89	40.63	283.018
2	14.16	2.91	41.21	279.088
3	14.10	2.91	41.03	280.276
4	14.10	2.88	40.61	283.195
5	14.10	2.89	40.75	282.216
6	14.16	2.90	41.06	280.051
Average	**14.11**	**2.90**	**40.88**	**281.307**
SD	**0.04**	**0.01**	**0.25**	**1.725**

Table 4.66: Specimen dimensions and failure stresses for specimens impacted from a height of 87mm

Specimen Number	Width of Specimen (mm)	Depth of Specimen (mm)	Cross-sectional Area of Specimen (mm^2)	Stress (MN/m^2)
1	14.06	2.86	40.21	285.987
2	14.15	2.91	41.18	279.286
3	14.13	2.91	41.12	279.681
4	14.06	2.91	40.91	281.073
5	14.13	2.88	40.69	282.594
6	14.06	2.93	41.20	279.155
Average	**14.10**	**2.90**	**40.89**	**281.296**
SD	**0.04**	**0.02**	**0.38**	**2.645**

Table 4.67: Specimen dimensions and failure stresses for specimens impacted from a height of 163mm

Specimen Number	Width of Specimen (mm)	Depth of Specimen (mm)	Cross-sectional Area of Specimen (mm^2)	Stress (MN/m^2)
1	13.98	2.86	40.21	285.987
2	14.09	2.91	41.18	279.286
3	14.16	2.91	41.12	279.681
4	14.11	2.91	40.91	281.073
5	14.11	2.88	40.69	282.594
6	14.18	2.93	41.20	279.155
Average	**14.10**	**2.90**	**40.88**	**281.296**
SD	**0.07**	**0.02**	**0.38**	**2.645**

Table 4.68: Specimen dimensions and failure stresses for specimens impacted from a height of 276mm

4.6.1 Cycles to Failure

The number of cycles to failure for the differing impact heights can be seen in Table 4.69. When combining the S-N diagrams for the control and impact fatigue test results at the various heights, as shown in Figure 4.31, it can be seen that subjecting a specimen to a single impact from a height of 87mm will lower the average fatigue life of the specimen by 6.4% when compared with non-impacted control specimens, and also decrease the average range of standard deviations over which failure could occur by 13.03%.

By comparing the fatigue results for the impacted specimens alone, it can be seen that the greater the height of the impact, and therefore the higher the impact energy, the lower the fatigue life of the specimen. Increasing the height of the impactor hammer head from 87mm to 410mm can lower the average fatigue life of the specimen by 89.5% and, additionally, the average range of standard deviations over which failure can occur is decreased by 1.88%.

This is highlighted further in Figure 4.32, which illustrates the cycles to failure for the differing impact heights, including the fatigue test results for the control specimens, which are considered to be at impact height of 0mm as no impact

took place. It will be possible to predict other rates of failure for impact heights between 0mm and 410mm, with the use of this graph.

Specimen Number	Cycles to Failure		
	Height of Impact 276mm (67.5 degrees)	Height of Impact 163mm (45 degrees)	Height of Impact 87mm (22.5 degrees)
1	81,685	172,661	454,044
2	75,975	176,624	619,673
3	82,430	157,641	446,011
4	81,002	256,688	325,482
5	67,765	140,112	494,479
6	50,775	182,319	584,987
Average	**73,272**	**181,007**	**487,446**
SD	**12,313**	**40,091**	**105,936**

Table 4.69: Cycles to failure for differing impact heights

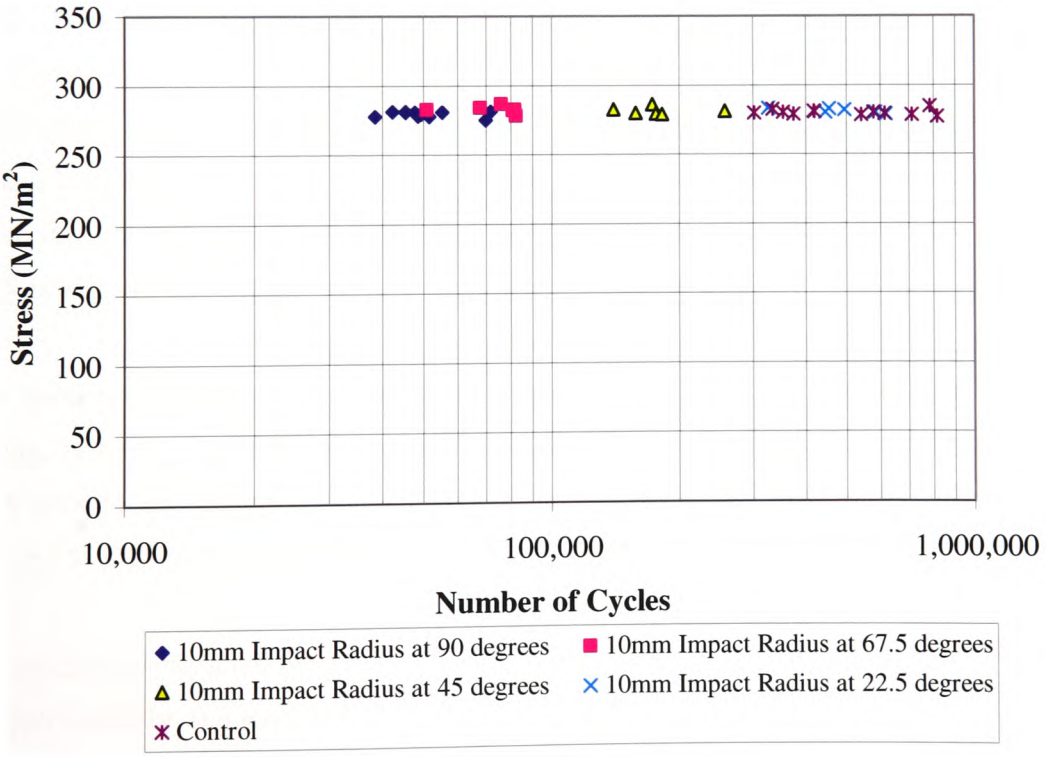

Figure 4.31: S-N Diagram for control and impact fatigue tests for '070M20' carbon steel for varying heights of impactor hammer head

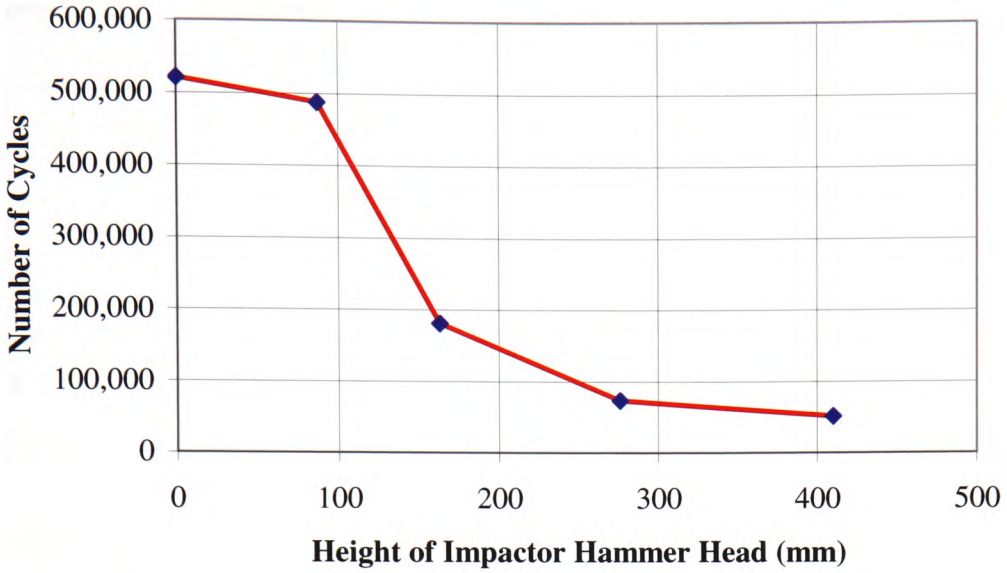

Figure 4.32: Cycles to failure against height of impactor hammer head

4.6.2 Hardness of Material

After fatigue testing, the specimens impacted from a height of 87mm were found to have a hardness of approximately -0.6 Rockwell C (SD 5.1) or 151 DPN close to the fracture and a hardness of approximately -3.1 Rockwell C (SD 2.7) or 143 DPN near to the shoulder of the specimen, as shown in Table 4.70.

The specimens impacted from a height of 163mm were found, after fatigue testing, to have a hardness of approximately -1.5 Rockwell C (SD 3.2) or 147 DPN close to the fracture and a hardness of approximately -2.5 Rockwell C (SD 5.1) or 144 DPN near to the shoulder of the specimen, as shown in Table 4.71.

The specimens impacted from a height of 276mm were found to have a hardness of approximately -0.8 Rockwell C (SD 4.4) or 150 DPN close to the fracture and a hardness of approximately -3.9 Rockwell C (SD 2.7) or 140 DPN near to the shoulder of the specimen, after fatigue testing, as shown in Table 4.72.

Specimen Number	Hardness (Rockwell C) – Bottom of Specimen				Hardness (Rockwell C) – Top of Specimen			
	Side 1		Side 2		Side 1		Side 2	
	Shoulder	Fracture	Shoulder	Fracture	Shoulder	Fracture	Shoulder	Fracture
1	3.0	1.5	1.5	0.5	-7.0	-2.5	-9.5	-8.5
2	5.0	2.5	-4.5	-5.0	4.0	4.0	-3.5	1.5
3	-5.5	-21.0	-7.0	-4.0	4.5	3.0	-10.0	-16.5
4	4.0	-3.0	3.5	-9.0	0.5	-10.5	-9.5	-6.5
5	3.0	0.0	3.0	-2.0	4.5	3.0	-5.5	-3.0
6	4.0	3.5	-7.0	0.0	3.0	3.5	-12.0	-6.5
Average	**2.3**	**-2.8**	**-1.8**	**-3.3**	**1.6**	**0.1**	**-8.3**	**-6.6**
SD	**3.9**	**9.2**	**5.0**	**3.5**	**4.5**	**5.7**	**3.2**	**6.0**

Table 4.70: Hardness values of specimens impacted from a height of 87mm

Specimen Number	Hardness (Rockwell C) – Bottom of Specimen				Hardness (Rockwell C) – Top of Specimen			
	Side 1		Side 2		Side 1		Side 2	
	Shoulder	Fracture	Shoulder	Fracture	Shoulder	Fracture	Shoulder	Fracture
1	4.5	2.5	-7.5	-1.0	3.0	-0.5	-2.5	-8.5
2	3.5	2.5	-5.5	-4.5	3.0	2.0	-9.0	-7.0
3	6.5	2.5	-8.0	-3.0	3.5	2.0	-6.5	-5.0
4	3.0	1.0	1.5	-2.5	4.0	1.5	7.0	-9.5
5	3.5	0.5	2.5	13.0	-2.0	-15.5	-6.0	-7.0
6	-7.5	3.0	-10.0	-7.0	-11.0	2.0	-6.5	-22.5
Average	**2.3**	**2.0**	**-4.5**	**-0.8**	**0.1**	**-1.4**	**-3.9**	**-9.9**
SD	**4.9**	**1.0**	**5.2**	**7.1**	**5.8**	**7.0**	**5.7**	**6.3**

Table 4.71: Hardness values of specimens impacted from a height of 163mm

Specimen Number	Hardness (Rockwell C) – Bottom of Specimen				Hardness (Rockwell C) – Top of Specimen			
	Side 1		Side 2		Side 1		Side 2	
	Shoulder	Fracture	Shoulder	Fracture	Shoulder	Fracture	Shoulder	Fracture
1	-1.0	2.0	-7.5	-16.5	1.0	3.0	-6.5	-10.5
2	5.5	2.5	-7.0	-5.5	2.0	1.5	-7.5	-5.0
3	1.0	34.0	-4.5	36.5	1.0	0.5	1.0	42.0
4	2.0	0.0	-4.5	-8.5	2.0	2.0	-6.0	-7.5
5	-1.0	3.5	-2.0	-19.5	5.5	0.5	-1.5	-1.0
6	11.0	1.5	-6.5	44.0	6.5	2.5	-3.5	-8.5
Average	**2.9**	**7.3**	**-5.3**	**5.1**	**3.0**	**1.7**	**-4.0**	**1.6**
SD	**4.6**	**13.1**	**2.1**	**27.8**	**2.4**	**1.0**	**3.3**	**20.1**

Table 4.72: Hardness values of specimens impacted from a height of 276mm

4.6.3 Entry Velocity of Impact

The entry velocities of impact for the different test heights, as well as the theoretical values, are shown in Table 4.73 and Figure 4.33. It can be seen that as the height of the impactor hammer head decreases, so the velocity of impact also decreases. The difference between the experimental and the theoretical values was possibly due to the inaccuracy of the angular resolution of the potentiometer and frictional losses in the impact rig. It is possible to use the graph produced to predict the velocity of impact for other impact heights between 87mm and 410mm.

	Entry Velocity (m/s)		
Specimen Number	**Height of Impact 276mm (67.5 degrees)**	**Height of Impact 163mm (45 degrees)**	**Height of Impact 87mm (22.5 degrees)**
1	2.05	1.41	0.71
2	1.99	1.39	0.75
3	2.03	1.40	0.77
4	2.08	1.42	0.84
5	2.06	1.48	0.76
6	2.06		0.85
Average	**2.04**	**1.42**	**0.78**
SD	**0.03**	**0.03**	**0.06**
Theoretical Values	**2.33**	**1.79**	**1.31**

Table 4.73: Entry impact velocities for differing impact heights

4.6.4 Exit Velocity after Impact

The exit velocities after impact for the different test heights are shown in Table 4.74 and Figure 4.34. It can be seen that as the height of the impactor hammer head decreases, so the exit velocity also decreases. It is possible use the graph produce to predict the exit velocity for other impact heights between 87mm and 410mm.

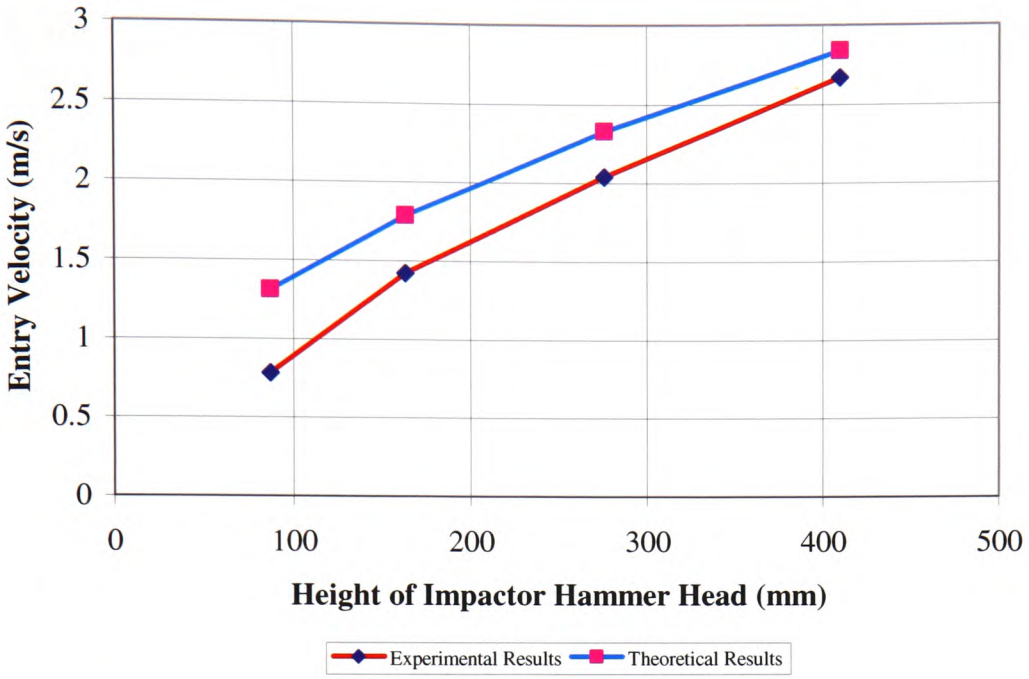

Figure 4.33: Entry impact velocity against height of impactor hammer head

Specimen Number	Exit Velocity (m/s)		
	Height of Impact 276mm (67.5 degrees)	Height of Impact 163mm (45 degrees)	Height of Impact 87mm (22.5 degrees)
1	0.66	0.47	0.30
2	0.66	0.55	0.29
3	0.65	0.56	0.36
4	0.68	0.53	0.37
5	0.67	0.55	0.39
6	0.70		0.37
Average	**0.67**	**0.54**	**0.35**
SD	**0.02**	**0.04**	**0.04**

Table 4.74: Exit velocities after for differing impact heights

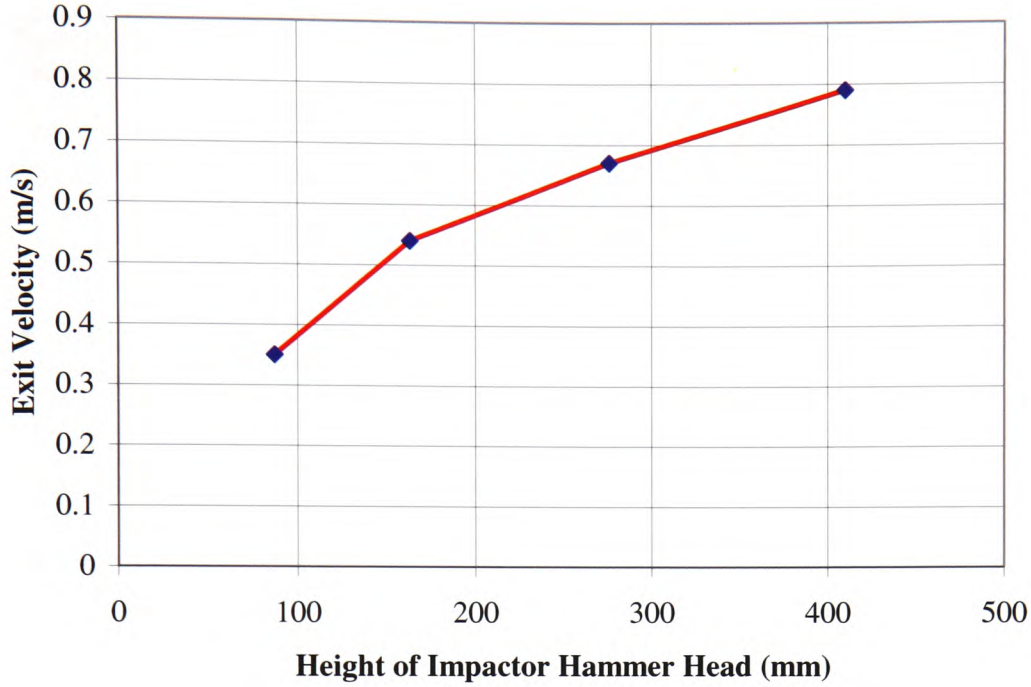

Figure 4.34: Exit velocity after impact against height of impactor hammer head

4.6.5 Coefficient of Restitution

The coefficients of restitution for the different test heights are shown in Table 4.75 and Figure 4.35. It can be seen that as the height of the impactor hammer head decreases, so the coefficient of restitution increases. Therefore, the higher the impact energy, then the less plastic the material becomes. It is possible to predict the coefficient of restitution for other impact heights between 87mm and 410mm using the graph produced.

Specimen Number	Coefficient of Restitution		
	Height of Impact 276mm (67.5 degrees)	Height of Impact 163mm (45 degrees)	Height of Impact 87mm (22.5 degrees)
1	0.32	0.34	0.43
2	0.33	0.40	0.39
3	0.32	0.40	0.47
4	0.33	0.38	0.44
5	0.32	0.38	0.52
6	0.34		0.44
Average	**0.33**	**0.38**	**0.45**
SD	**0.01**	**0.02**	**0.04**

Table 4.75: Coefficient of restitution for differing impact heights

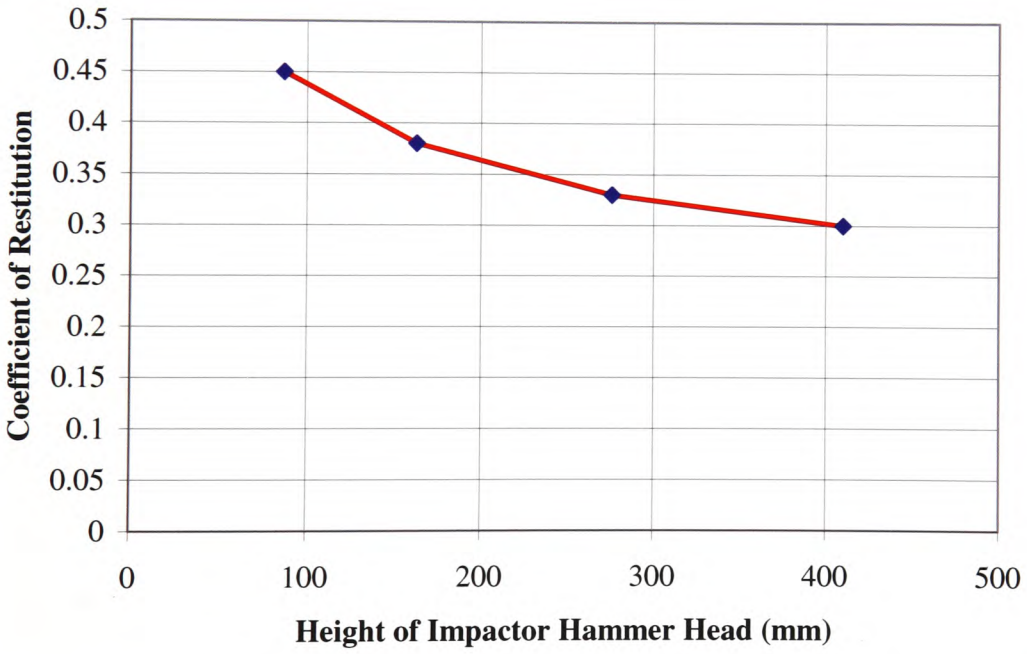

Figure 4.35: Coefficient of restitution against height of impactor hammer head

4.6.6 Entry Impact Energy

The entry energy of impact for the different test heights, as well as the theoretical values, are shown in Table 4.76 and Figure 4.36. It can be seen that as the height of the impactor hammer head decreases, so the energy of impact also decreases. The difference between the experimental and the theoretical values was possibly due to the inaccuracy of the angular resolution of the potentiometer and frictional losses in the impact rig. It is possible to predict the energy of impact for other impact heights between 87mm and 410mm using the graph produced.

	Entry Impact Energy (J)		
Specimen Number	**Height of Impact 276mm (67.5 degrees)**	**Height of Impact 163mm (45 degrees)**	**Height of Impact 87mm (22.5 degrees)**
1	7.38	3.48	0.88
2	7.00	3.40	1.00
3	7.22	3.47	1.05
4	7.60	3.57	1.25
5	7.49	3.83	1.03
6	7.43		1.28
Average	**7.35**	**3.55**	**1.08**
SD	**0.21**	**0.17**	**0.15**
Theoretical Values	**9.53**	**5.61**	**2.99**

Table 4.76: Entry impact energies for differing impact heights

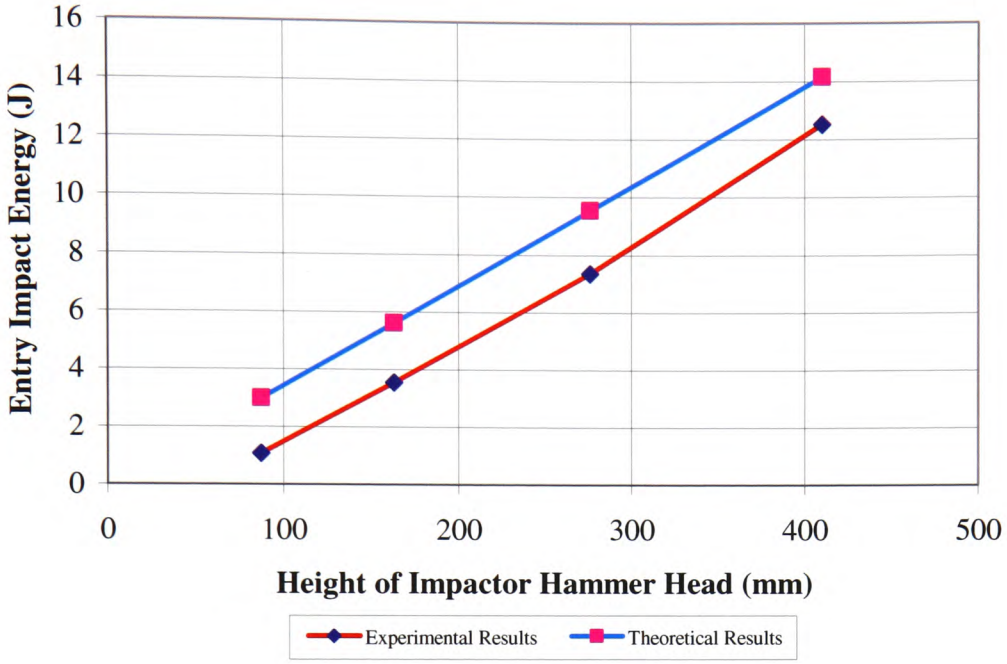

Figure 4.36: Entry impact energy against height of impactor hammer head

4.6.7 Exit Energy after Impact

The exit energy after impact for the different test heights is shown in Table 4.77 and Figure 4.37. It can be seen that as the height of the impactor hammer head decreases, so the energy after impact also decreases. It is possible to use the graph produced to predict the exit energy of impact for other impact heights between 87mm and 410mm.

Specimen Number	Exit Impact Energy (J)		
	Height of Impact 276mm (67.5 degrees)	Height of Impact 163mm (45 degrees)	Height of Impact 87mm (22.5 degrees)
1	0.77	0.40	0.16
2	0.78	0.53	0.15
3	0.75	0.56	0.23
4	0.81	0.50	0.24
5	0.78	0.54	0.27
6	0.87		0.24
Average	**0.79**	**0.51**	**0.22**
SD	**0.04**	**0.06**	**0.05**

Table 4.77: Exit energies after for differing impact heights

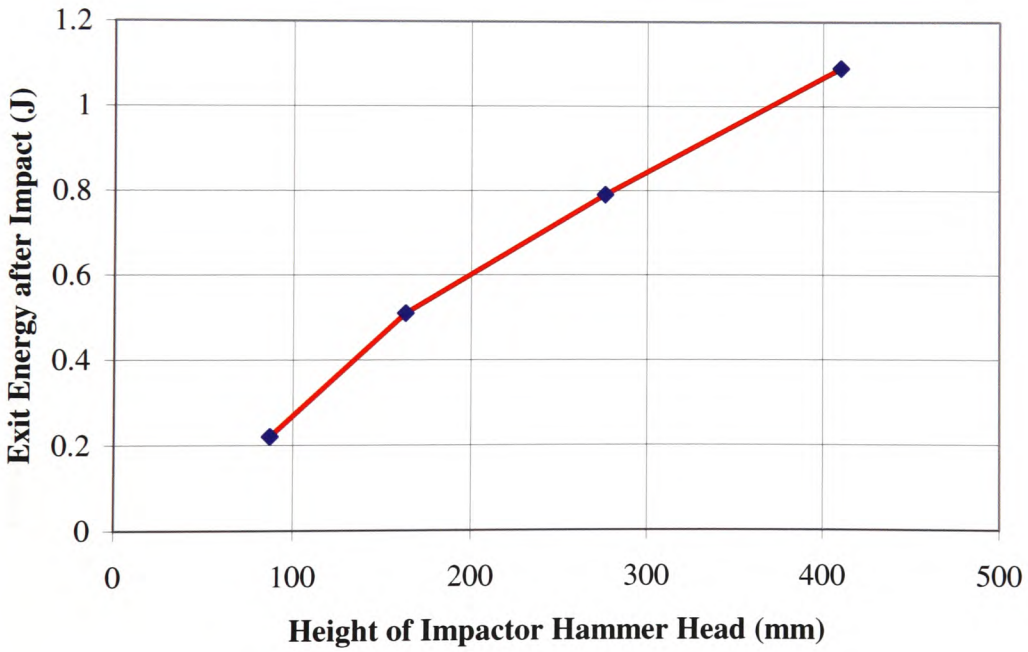

Figure 4.37: Exit energy after impact against height of impactor hammer head

4.6.8 Depth of Impact Crater

The depth of impact crater produced for the different test heights is shown in Table 4.78 and Figure 4.38. It can be seen that as the height of the impactor hammer head decreases, so the impact crater depth also decreases. It is possible to predict the depth of impact crater produced for other impact heights between 87mm and 410mm using the graph produced.

Height of Impact (mm)	Depth of Impact Crater (mm)
276	0.28
163	0.19
87	0.10

Table 4.78: Depth of impact crater for differing impact heights

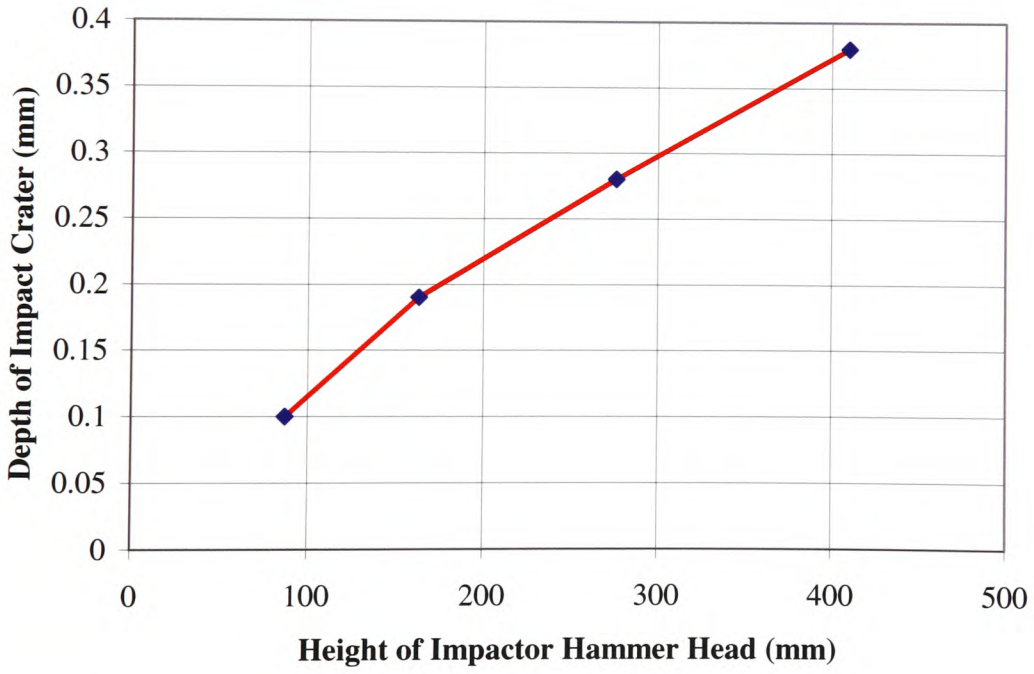

Figure 4.38: Depth of impact crater against height of impactor hammer head

4.6.9 Width of Impact Crater

The width of impact crater produced for the different test heights is shown in Table 4.79 and Figure 4.39. It can be seen that as the height of the impactor hammer head decreases, so the width also decreases. Using the graph produced it is possible to predict the width of impact crater produced for other impact heights between 87mm and 410mm.

Height of Impact (mm)	Width of Impact Crater (mm)
276	4.74
163	3.93
87	3.05

Table 4.79: Width of impact crater for differing impact heights

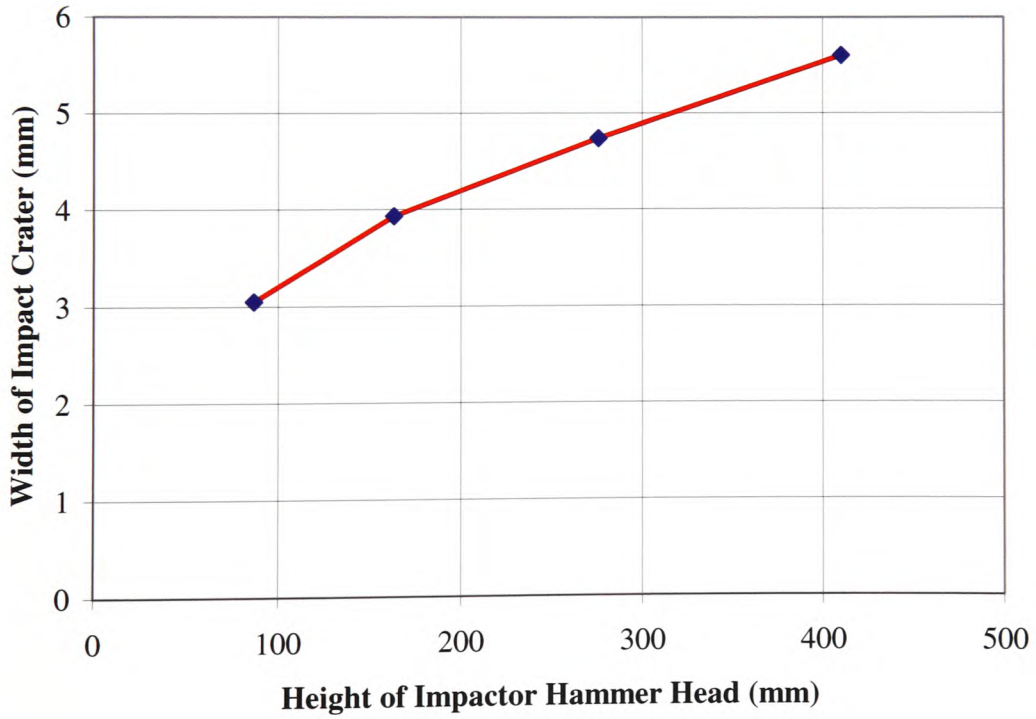

Figure 4.39: Width of impact crater against height of impactor hammer head

4.6.10 Volume of Impact Crater

The volume of the impact crater produced for the different test heights is shown in Table 4.80 and Figure 4.40. It can be seen that as the height of the impactor hammer head decreases, so the width also decreases. Using the graph produced it is possible to predict the volume of the impact crater produced for other impact heights between 87mm and 410mm.

Height of Impact (mm)	Volume of Impact Crater (mm^3)
276	2.48
163	1.16
87	0.37

Table 4.80: Volume of impact crater for differing impact heights

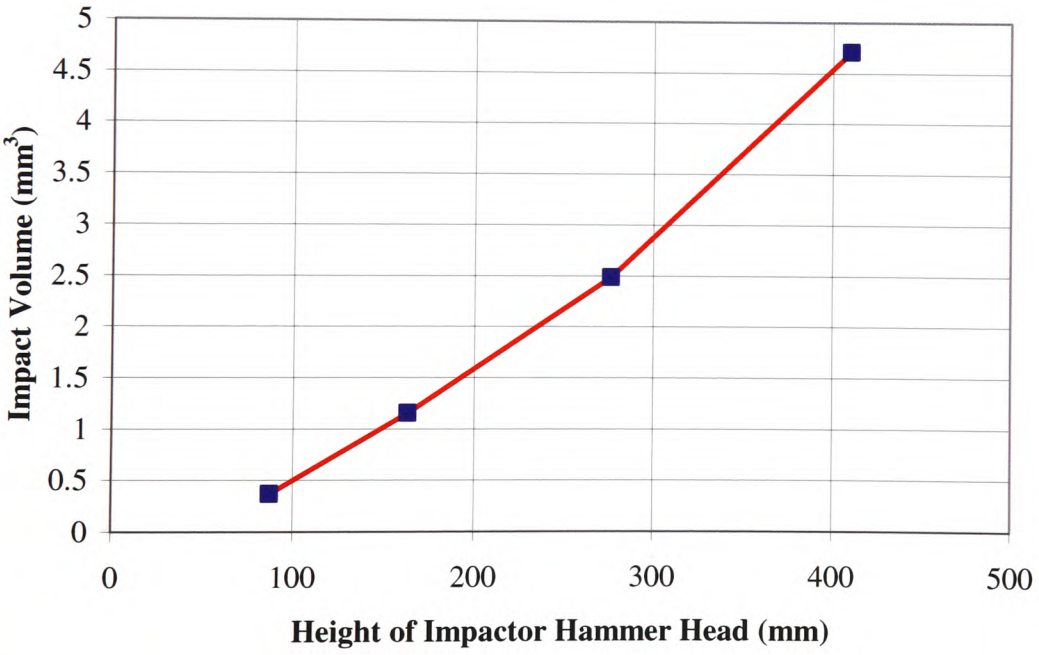

Figure 4.40: Volume of impact crater against height of impactor hammer head

4.6.11 Impact Contact Time

The impact contact times calculated from the accelerometer readings for each of the specimens tested are presented in Table 4.81. Readings were taken for each of the specimens tested; however, due to errors some of the results were invalid.

Specimen Number	Height of Impact 276mm (67.5 degrees)	Height of Impact 163mm (45 degrees)	Height of Impact 87mm (22.5 degrees)
1	1.05E-04	9.80E-05	1.10E-04
2	9.10E-05	1.06E-04	1.06E-04
3	9.20E-05	1.06E-04	1.48E-04
4	1.03E-04	8.50E-05	1.07E-04
5	8.22E-05	1.13E-04	
6	8.40E-05	9.80E-05	
Average	**9.29E-05**	**1.01E-04**	**1.18E-04**
SD	**1.49E-05**	**2.12E-08**	**2.04E-06**

Table 4.81: Impact contact times calculated from accelerometer readings

4.7 Microstructure of Specimen Surface

Using a 'Metallux 2' microscope with a magnification and aperture of 100x/0.9, the surface of both impacted and non-impacted specimens were photographed to inspect the surface finish and also the impact crater produced by the impactor hammer heads.

As can be seen from Figures 4.41 and 4.42 the surface finish is very consistent, with the direction of final polishing in the longitudinal direction.

Some of the specimens have surface irregularities as shown in Figures 4.43 and 4.44, which are possibly due to inclusions in the initial steel casting process.

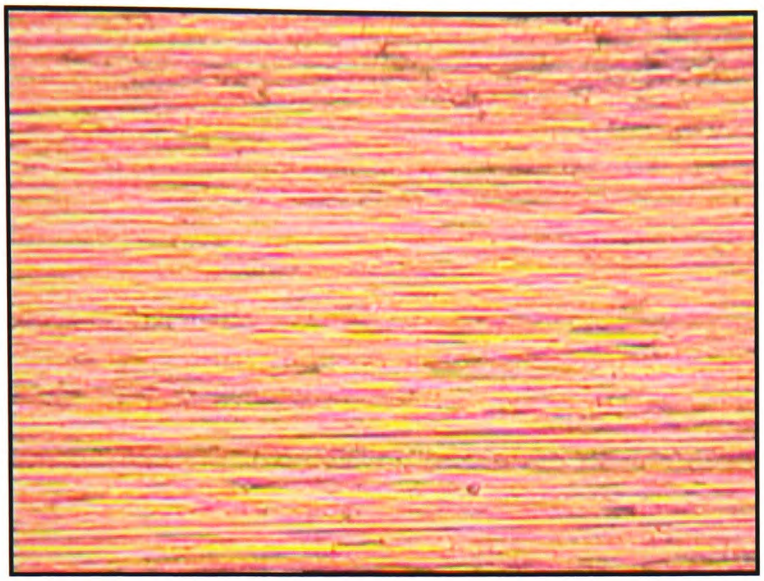

Figure 4.41: Surface finish on a typical specimen (1)

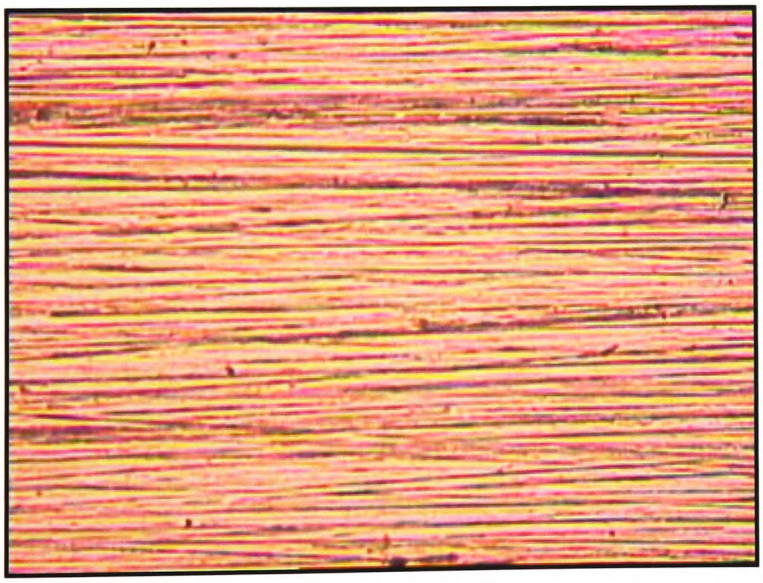

Figure 4.42: Surface finish on a typical specimen (2)

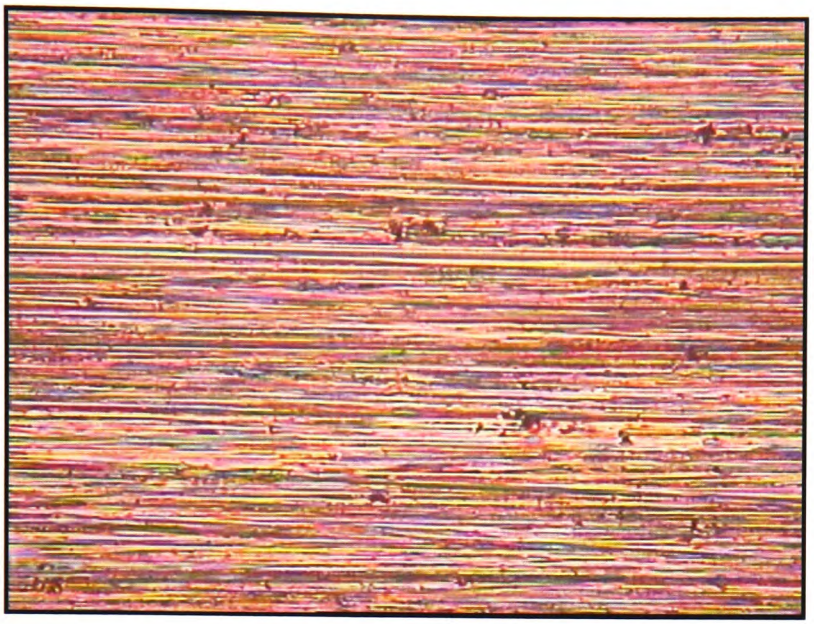

Figure 4.43: Surface finish on a control specimen showing inclusions (1)

Figure 4.44: Surface finish on a control specimen showing inclusions (2)

Figures 4.45 to 4.47 show sections of the craters produced due to a single impact. Distortion of the specimen is seen in terms of flow lines in the form of concentric circles, which correspond to the disposition of the specimen in relation to the pressure from the impactor hammer head. It is also possible that some irregularities on the surface finish of the impactor hammer head may be reproduced on the surface of the specimen during impact. However, any such markings will be consistent for all tests using the same hammer head.

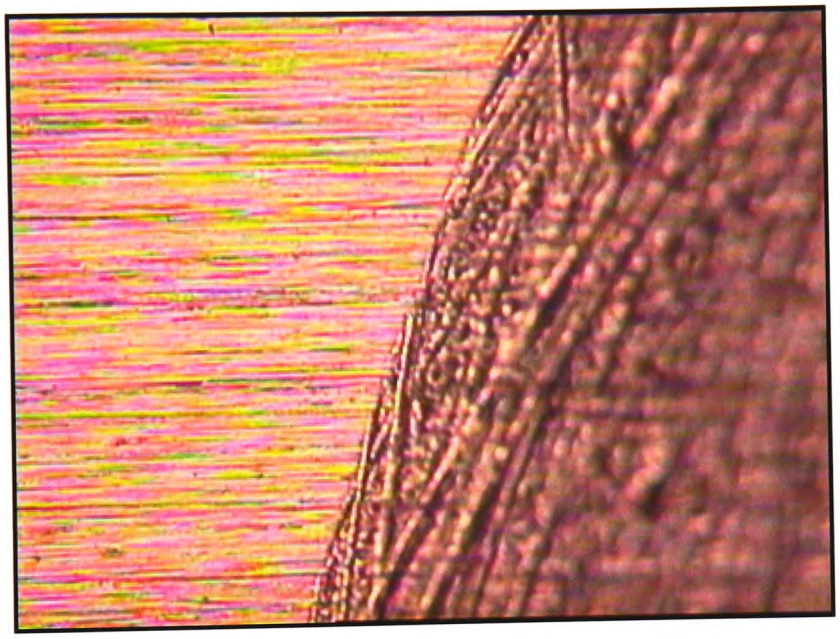

Figure 4.45: Surface finish on a specimen subjected to a single impact with a 10mm radius impactor hammer head - edge of impact crater shown

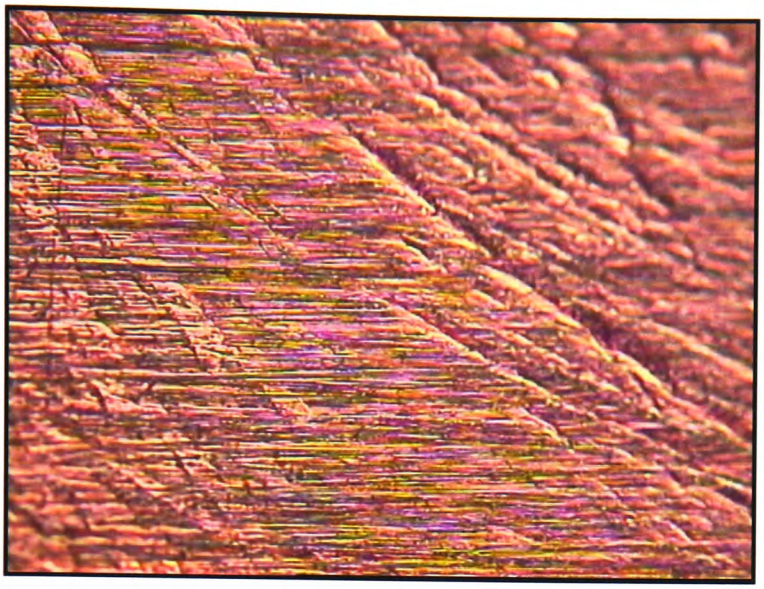

Figure 4.46: Surface finish on a specimen subjected to a single impact with a 25mm radius impactor hammer head - impact crater shown

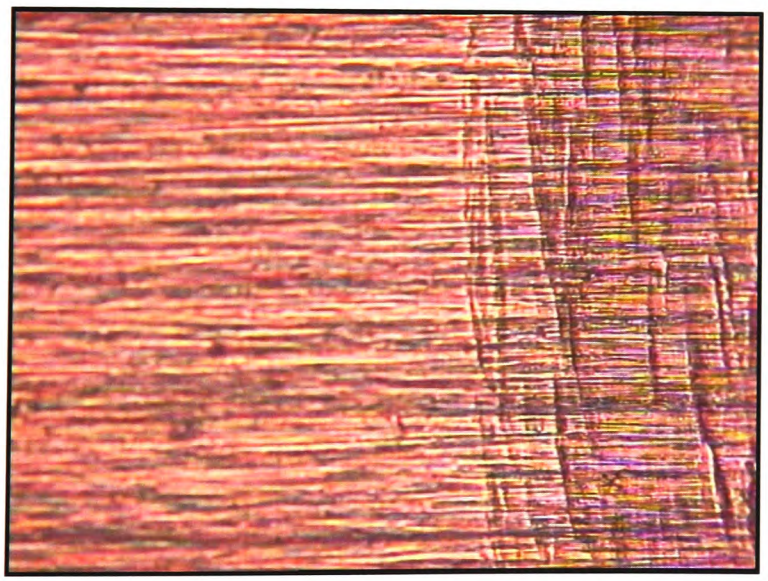

Figure 4.47: Surface finish on a specimen subjected to a single impact with a 25mm radius impactor hammer head - edge of impact crater shown

4.8 Macrostructure of Fatigue Cracks

A fatigue crack initiates at a point of stress concentration and gradually extends across the specimen until the remaining area cannot sustain the load and suddenly tears. The fractured surface of the specimen consists of two areas; one area is relatively smooth with some ripple marks across the surface of the crack, and the second area has a fibrous appearance.

These two areas can clearly be seen in Figure 4.48, which shows a control specimen that has failed in fatigue. The fractured surface at Area 1 is where the fatigue crack initiated and, as can be seen, the surface area is relatively smooth with some ripple marks emanating towards the centre of the specimen. Area 2 is where the specimen suddenly tears, as can be seen by the fibrous appearance of the fractured surface.

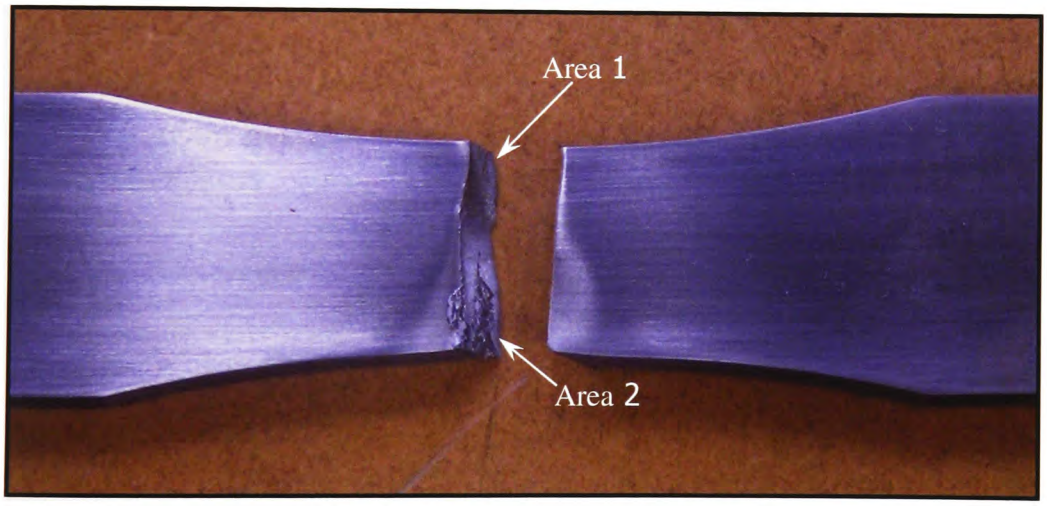

Figure 4.48: A control specimen which has failed in fatigue

Figure 4.49 shows a specimen that has had a single impact from a 40mm radius impactor hammer head, about to fail by tearing.

Figure 4.49: An impacted specimen which was about to fail by tearing

Figure 4.50 shows a specimen which has had a single impact from a 40mm impactor hammer head, clearly showing the smooth and fibrous areas associated with fatigue failures.

It can also be seen that on some of the specimens that have had a single impact, the structure is slightly distorted, as shown in Figure 4.51. Flow lines in the form of concentric circles appear to radiate from the central point of the specimen which is directly beneath the impact site. These flow lines are possibly conchoidal growth rings which radiate inwards from the origin of failure. The rings indicate the progressive nature of the fatigue crack propagation.

In the control specimens the structure appears smooth, as shown in Figure 4.52. The origin of failure on these specimens mainly occurs at the region of the greatest stress concentration, which is where the cross sectional area is the smallest.

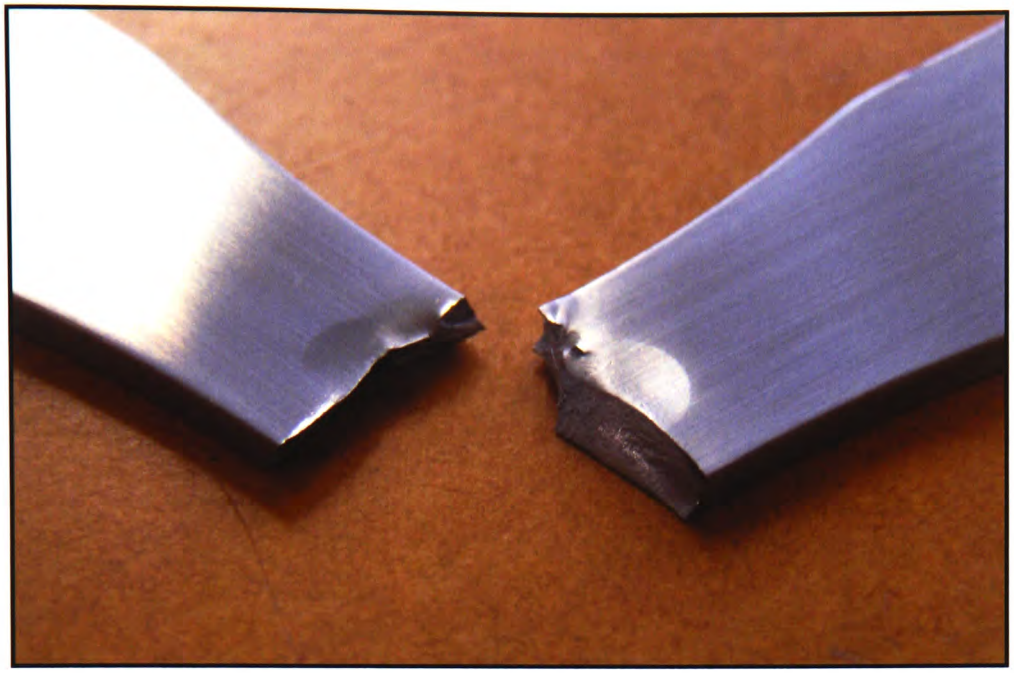

Figure 4.50: An impacted specimen which has failed in fatigue - view of tear (1)

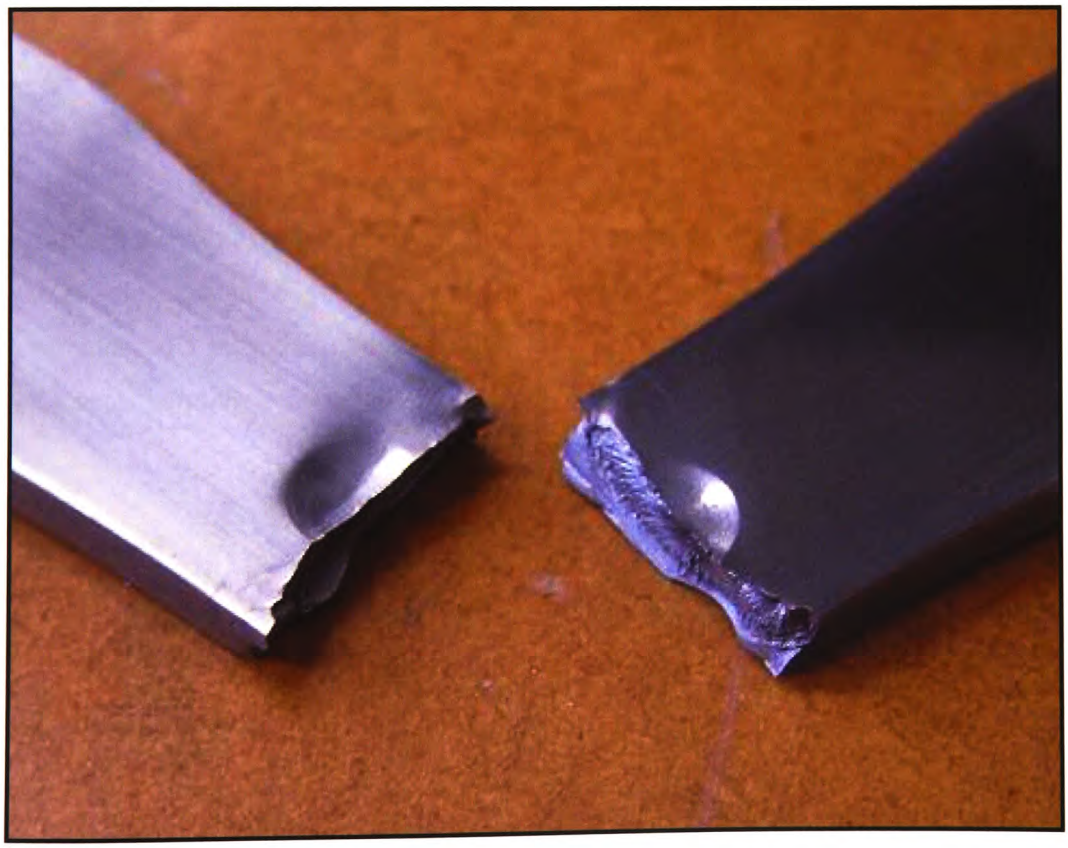

Figure 4.51: An impacted specimen which has failed in fatigue - view of tear (2)

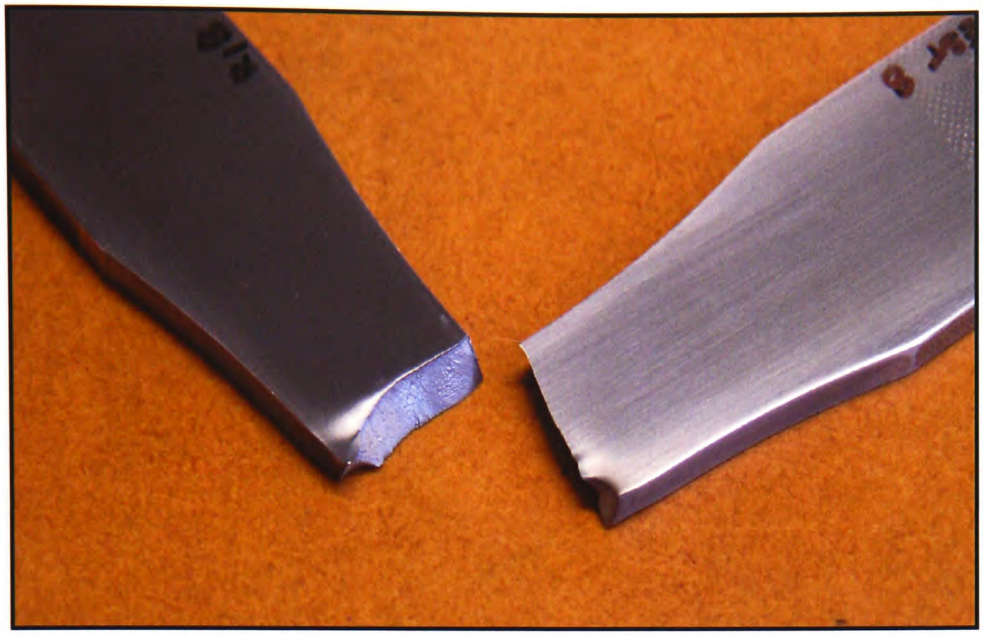

Figure 4.52: A control specimen which has failed in fatigue - view of tear

4.9 Summary of Experimental Results

Table 4.82 shows a summary of the experimental results for all the specimen tests using the various impactor hammer head sizes, whilst Table 4.83 shows a summary of the experimental results for all the specimen tests using various impactor hammer head heights.

Material Batch	Impactor Hammer Head Radius (mm)	Average Fatigue Life (cycles)	Entry Velocity of Impact (m/s)	Exit Velocity after Impact (m/s)	Coefficient of Restitution	Depth of Impact Crater (mm)	Width of Impact Crater (mm)	Impact Contact Time (seconds)	Impact Volume (mm^3)	Entry Impact Energy (J)	Exit Energy after Impact (J)	Energy Diff (J)
1)Bending Quality Bright Steel	N/A (Control)	66,530										
	10	11,701	3.11	1.02	0.33	0.41	5.00	9.53E-05	5.23	17.08	1.82	15.26
2)'070M20' Carbon Steel	N/A (Control)	520,822										
	10	51,070	2.67	0.79	0.30	0.38	5.60	9.04E-05	4.71	12.53	1.09	11.44
	11	44,549	2.65	0.81	0.31	0.36	5.75	0.000106	4.70	12.32	1.16	11.16
	12	42,812	2.65	0.82	0.31	0.34	5.90	0.000106	4.67	12.34	1.19	11.15
	18	49,934	2.68	0.95	0.35	0.25	6.50	0.000107	4.16	12.66	1.59	11.07
	25	38,789	2.67	0.96	0.36	0.22	6.80	0.000112	4.00	12.58	1.61	10.97
	40	48,908	2.64	1.05	0.40	0.18	7.50	0.000119	3.98	12.23	1.95	10.28

= Total number of specimens tested is four.
= No results available.

Table 4.84: Summary of specimen test results using varying sized impactor hammer heads

Material Batch	Impactor Hammer Head Radius (mm)	Angle of Impactor Hammer Head (degrees)	Height of Impactor Hammer Head (mm)	Average Fatigue Life (cycles)	Entry Velocity of Impact (m/s)	Exit Velocity after Impact (m/s)	Coefficient of Restitution	Depth of Impact Crater (mm)	Width of Impact Crater (mm)	Impact Contact Time (seconds)	Impact Volume (mm^3)	Entry Impact Energy (J)	Exit Energy after Impact (J)	Energy Diff (J)
'070M20' Carbon Steel	10	90	410	51,070	2.67	0.79	0.30	0.38	5.60	9.04E-05	4.71	12.53	1.09	11.44
		67.5	276	73,272	2.04	0.67	0.33	0.28	4.74	9.29E-05	2.48	7.35	0.79	6.56
		45	163	181,007	1.42	0.54	0.38	0.19	3.93	1.01E-04	1.16	2.96	0.42	2.54
		22.5	87	487,446	0.78	0.35	0.45	0.10	3.05	1.18E-04	0.37	1.08	0.22	0.86

= Total number of specimens tested is six.

Table 4.85: Summary of specimen test results for varying impact heights

Chapter 5: NUMERICAL MODELLING

This chapter contains the results and observations made for the two and three dimensional numerical models, which have been developed to simulate a specimen which has been subjected to a single impact, using the ANSYS Finite Element Analysis (F.E.A.) software. This was carried out in order to observe the residual surface and subsurface stresses produced in the specimen as a result of the impact. Comparisons are also made between the numerical and experimental results in order to validate the numerical results obtained.

5.1 ANSYS

The main purpose of any F.E.A. is to replicate numerically the behaviour of an actual engineering/physical system and also to predict experimental results. Finite element analysis, is the solution of algebraic matrix equations that approximate the relationships between load and deflection in static analyses, and velocity, acceleration, and time in dynamic analyses. Further information on the mathematical theory of finite element analysis can be found in "Chapter 3 FEA Capabilities and Limitations" of "Building Better Products with Finite Element Analysis" (Adams *et al.* 1999).

The outcomes of the numerical models produced for this study can be compared with the experimental results, and then used to visualise parameters such as residual compressive and tensile stresses. There are several F.E.A. software packages commercially available, but for the purposes of this research the ANSYS Academic Research release 11.0 F.E.A. software was used.

It is possible to use the ANSYS software in two ways; via the graphical user interface, where the user inputs data with the use of a menu system, or with the use of an input file, where the user writes an input file using ANSYS commands. Due to the complex model geometry and element attributes, such as the material

properties, and also the similar geometry and boundary conditions for the specimen and the various impactor hammer head sizes, as well as the number of runs to be made, it was decided that input files written using ANSYS commands would be the most appropriate method to generate the numerical model.

5.2 Two Dimensional Numerical Model

Initially, a plane strain analysis was developed that modelled, in two dimensions, the impact of a cylinder on an elastic plate, in order to gain familiarisation with the F.E.A. software. The residual von-Mises stresses produced in this analysis are shown in Figure 5.1.

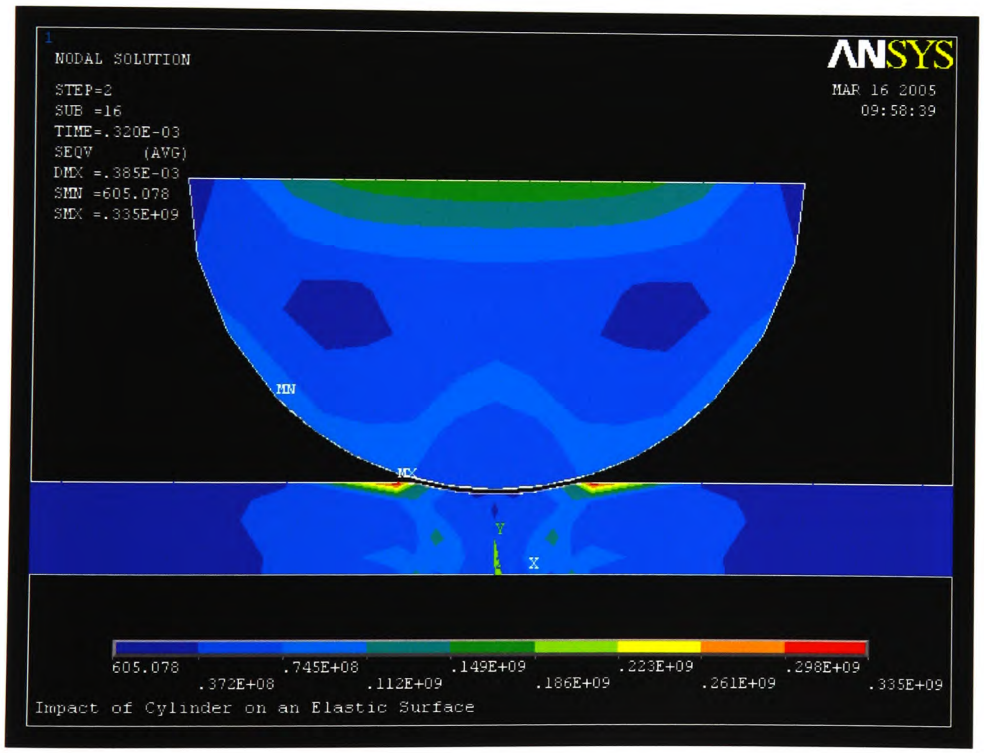

Figure 5.1: 2D analysis of a cylinder impacting an elastic plate showing von Mises stresses (Units - N/m^2)

Once familiar with the F.E.A. software, it was possible to develop an axi-symmetric model of a spherical impactor hammer head impacting a specimen. For the spherical impactor to be represented in two dimensions, it took the form of a semi-circle, with the specimen represented as a rectangle. As an axis of symmetry exists through the centre of the sphere and the specimen, they can be modelled as a sector of a circle impacting a disc.

The dimensions of both the experimental impactor hammer heads and the experimental specimens were used in the finite element analysis, to obtain the most accurate results possible.

The finite element analysis can be used to determine the velocity on contact, the duration of impact, exit velocity, depth and width of the impacted area, the coefficient of restitution, and also to produce images of the residual stresses within the specimen. An example of the residual stresses produced in these analyses is shown in Figure 5.2.

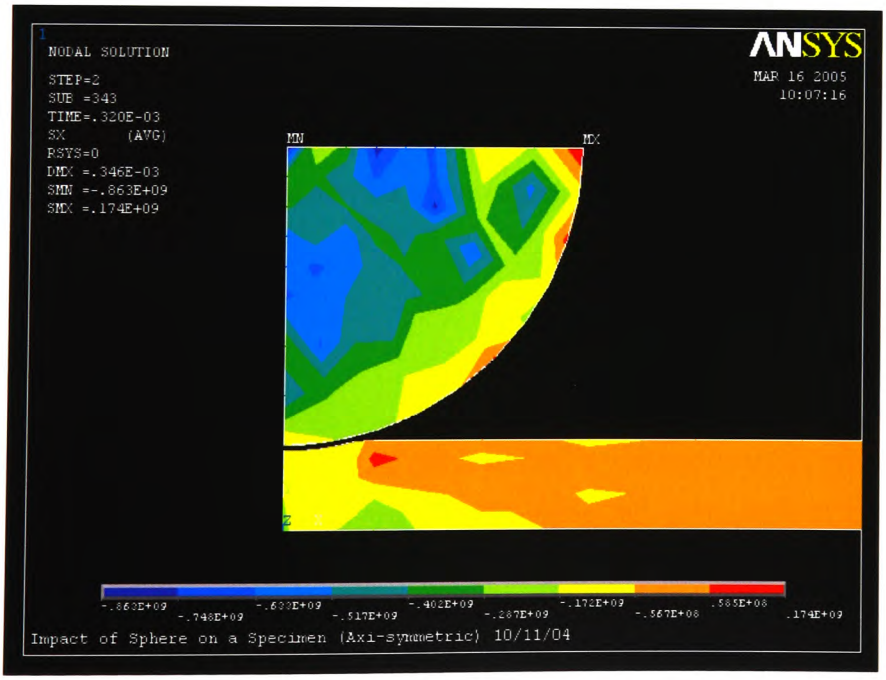

Figure 5.2: Axi-symmetric analysis of a sphere impacting a specimen showing x-directional residual stresses (Units - N/m^2)

Using a velocity of impact of 3.7m/s and a Young's Modulus for steel of 200GN/m^2, as the actual velocity of impact and material properties were not yet confirmed at this stage of the study, the axi-symmetric analysis showed the following results:

- Time of impact = 0.24 milliseconds
- Depth of impact = 0.346mm
- Width of impact = 6 mm.

The validation of these results was not possible as only preliminary experimental work had been carried out at this stage of the study.

5.3 Three Dimensional Numerical Model

The complexity of the two-dimensional model was then expanded into a 3D numerical model, in order to replicate as accurately as possible the actual impact tests. In total, seven three-dimensional numerical models were produced to simulate the single impact damage created by the various impactor hammer head sizes tested, for each of the materials in the experimental programme.

5.3.1 Model Geometry

An important consideration when developing any model geometry is symmetry. Due to the symmetry that exists with the positions and geometries of both the specimens and impactor hammer heads, it was possible to develop an axially symmetric model, which means it was only necessary to model a quarter of both the specimen and the impactor hammer head. One advantage of this is that it will reduced the analysis times, as the number of necessary calculations was greatly reduced.

The actual dimensions of the experimental specimens and impactor hammer heads were used to develop the model geometry. The specimen was generated by constructing three volumes, which were then amalgamated; this was done due to the variation in cross-section of the specimen. The impactor hammer head was generated as a single volume. The specimen and impactor hammer head lines generated are shown in Figure 5.3 and the areas generated are shown in Figure 5.4.

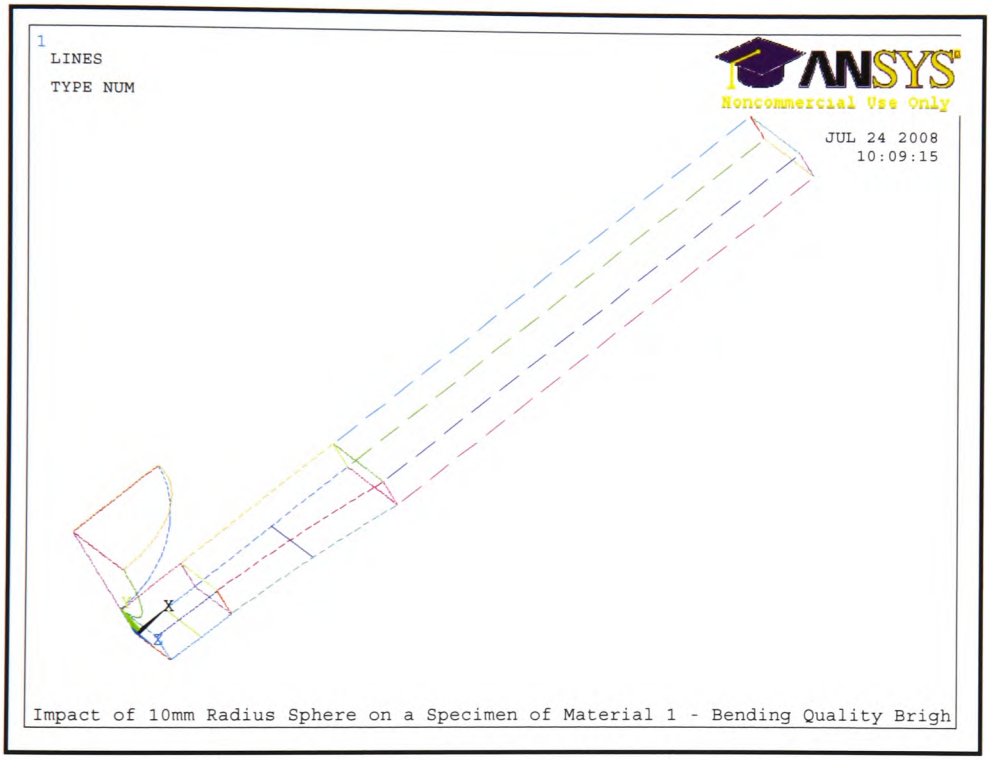

Figure 5.3: Specimen and impactor hammer head lines generated in 3D numerical models

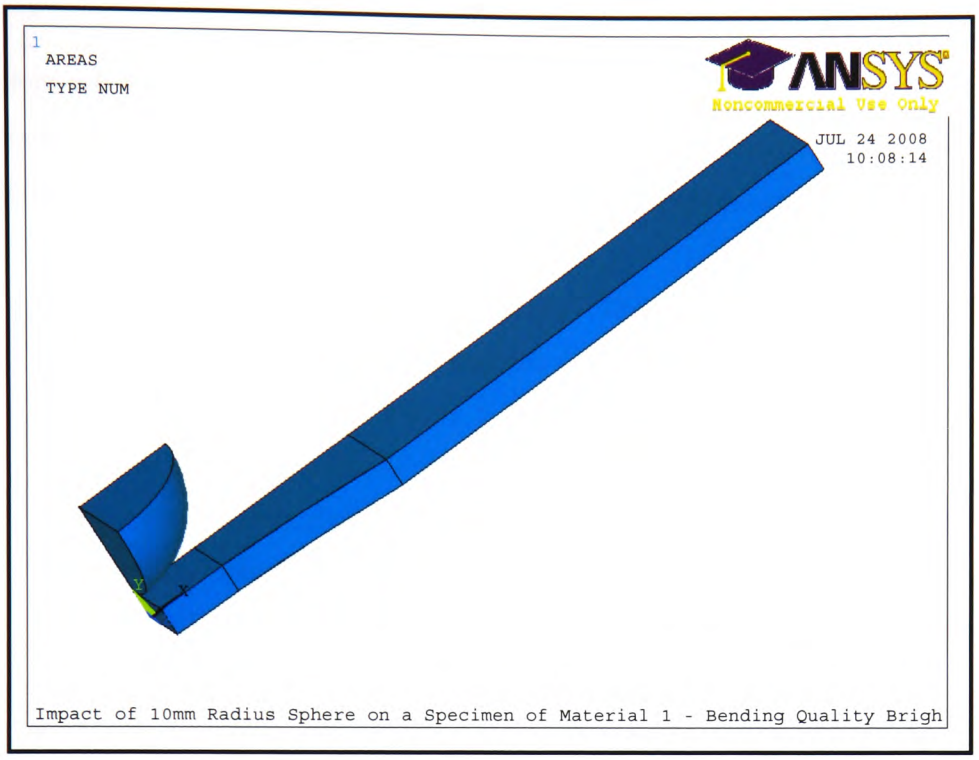

Figure 5.4: Specimen and impactor hammer head areas generated in 3D numerical models

5.3.2 Element Types

For both the specimen and the impactor hammer head, a 20 Node Structural Solid Brick (3D) element type was used, in order to give the most accurate representation of the geometry used. This element type has three degrees of freedom per node, with translations in the x, y and z directions. An important aspect of this element type is its treatment of non-linear transient analysis, which is necessary for the modelling of the problem. Also, this element type is well suited to modelling curved boundaries with a minimal loss of accuracy, and has both plasticity and large deflection capabilities, which are also necessary in this case.

5.3.3 Material Properties and Boundary Conditions

There are various modelling methods available in ANSYS that can be used to model the plastic behaviour of the specimen material. The commands which were considered for the specimen material data are listed below:

- Bilinear Kinematic Hardening (BKIN) - This command assumes that the total stress range is equal to twice the yield stress, so that the Bauschinger effect, as illustrated in Figure 5.5, is included. BKIN is used for most metals or materials which obey the von Mises yield criteria. The material behaviour is described by a bilinear stress/strain curve, which starts at the origin and has positive stress/strain values. The first slope is defined by the elastic modulus of the material and the second is defined by the tangent modulus.
- Multilinear Kinematic Hardening (KINH) - A command which is used to model metal plasticity behaviour under cyclic loading. The material behaviour is described by a multilinear stress/strain curve which starts at the origin and has positive stress/strain values with up to twenty data points for each stress-strain curve. The Bauschinger effect is also included.
- Bilinear Isotropic Hardening (BISO) - This command uses the von Mises yield criteria coupled with an isotropic work hardening assumption and can be used for large strain analyses. The Bauschinger effect is not taken into account. The material behaviour is described by a bilinear stress/strain curve, which starts at the origin and has positive stress/strain values. The first slope is defined by the elastic modulus of the material and the second is defined by the tangent modulus.
- Multilinear Isotropic Hardening (MISO) - A command which can be used for large strain analyses and uses the von Mises yield criteria coupled with an isotropic work hardening assumption. The Bauschinger effect is not taken into account. The material behaviour is described by a multilinear stress/strain curve which starts at the origin and has positive

stress/strain values with up to one hundred data points for each stress-strain curve.

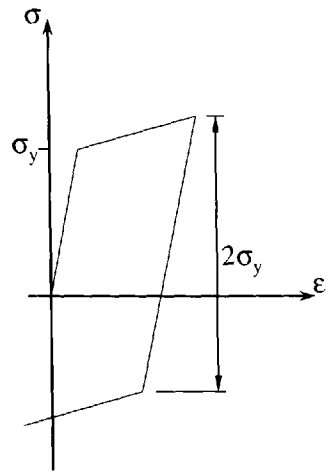

Figure 5.5: Stress/strain behaviour of bilinear kinematic model - Bauschinger effect

The most appropriate modelling method available in ANSYS that can be used to model the plastic behaviour of the specimen material, is the Kinematic Hardening (KINH) command, which allows the user to define multiple stress/strain curves with up to twenty data values for the same material. Data tables were used to define the specimen material data that had been previously obtained in Section 4.1 'Material 1 - Bending Quality Bright Steel' and Section 4.2 'Material 2 - '070M20' Carbon Steel'.

The material data for the specimens of Bending Quality Bright Steel (Material 1) that were used in the data tables for the numerical model are listed in Table 5.1. Further material properties used in the numerical model are listed below:

- Young's Modulus = 194.136GN/m^2
- Yield Stress = 372.29MN/m^2
- Density = 7850kg/m^3
- Coefficient of Friction (static) = 0.4
- Poisson's Ratio = 0.3

Stress (MN/m^2)	Strain
0	0
335.5	0.001713
363.636	0.001932
424.242	0.002291
454.545	0.002928

Table 5.1: Stress/strain data values for the specimens of bending quality bright steel

The material data for the specimens of '070M20' Carbon Steel (Material 2) that were used in the data tables for the numerical models are listed in Table 5.2. Further material properties used in the numerical models are listed below:

- Young's Modulus = $154.312GN/m^2$
- Yield Stress = $391.93MN/m^2$
- Density = $7850kg/m^3$
- Coefficient of Friction (static) = 0.4
- Poisson's Ratio = 0.3

When modelling the impactor hammer head, it is possible to use the linear elastic material properties of the specimen. This is due to the impactor hammer head being much harder and having a higher yield stress than the specimen; therefore, no obvious plasticity occurs after impact, so only the effects on the specimen due the impactor hammer head are considered in the scope of this work. An important parameter to consider when modelling the impactor hammer head is its mass. During the experimental programme, an impactor hammer head of mass 3.52kg was used and it was important to replicate this in the model. In order to achieve this, the volumes generated for each size of impactor hammer head used

in the numerical models were calculated and then using a quarter of the mass, 0.88kg, due to the geometry of the axially symmetric model, the density of each size of impactor hammer head was calculated, therefore ensuring that all of the impacts modelled are consistent.

Stress (MN/m^2)	Strain
0	0
440.545	0.00258
486.875	0.00288
532.635	0.00348
561.282	0.00408
577.939	0.00468
587.021	0.00528
591.965	0.00588
594.945	0.00648
596.699	0.00708
597.715	0.00768
598.241	0.00828
598.416	0.00888
598.520	0.00948

Table 5.2: Stress/strain data values for specimens of '070M20' carbon steel

5.3.4 Mesh Generation

To ensure the accuracy of results, it was important to produce a mesh which was adequate for the model geometry. The entire volume of the specimen and the impactor hammer head were meshed using mapped hexahedron elements of varying element sizes. The impact area on the specimen consists of elements of 0.368mm. Emanating along the specimen from the point of impact, the element size increases to a maximum of 3.3mm. It was important to get as fine a mesh as possible around the point of impact, to ensure the accuracy of results obtained. However, due to the restrictions of the ANSYS software package used it was not possible to make the element size any smaller, as the number of elements generated for this study is very close to the maximum limit of the package. Approximately 24,000 elements (not including contact elements) were generated for each model. The mesh generated on the specimen is shown in Figures 5.6 and 5.7.

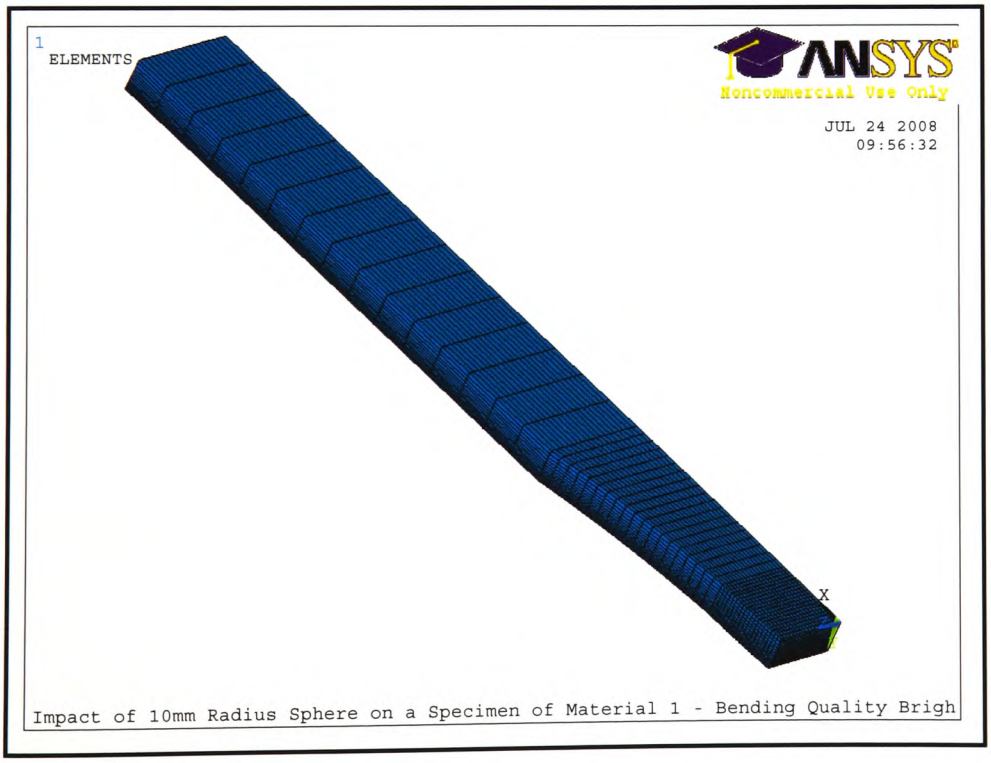

Figure 5.6: Mesh generated on specimen

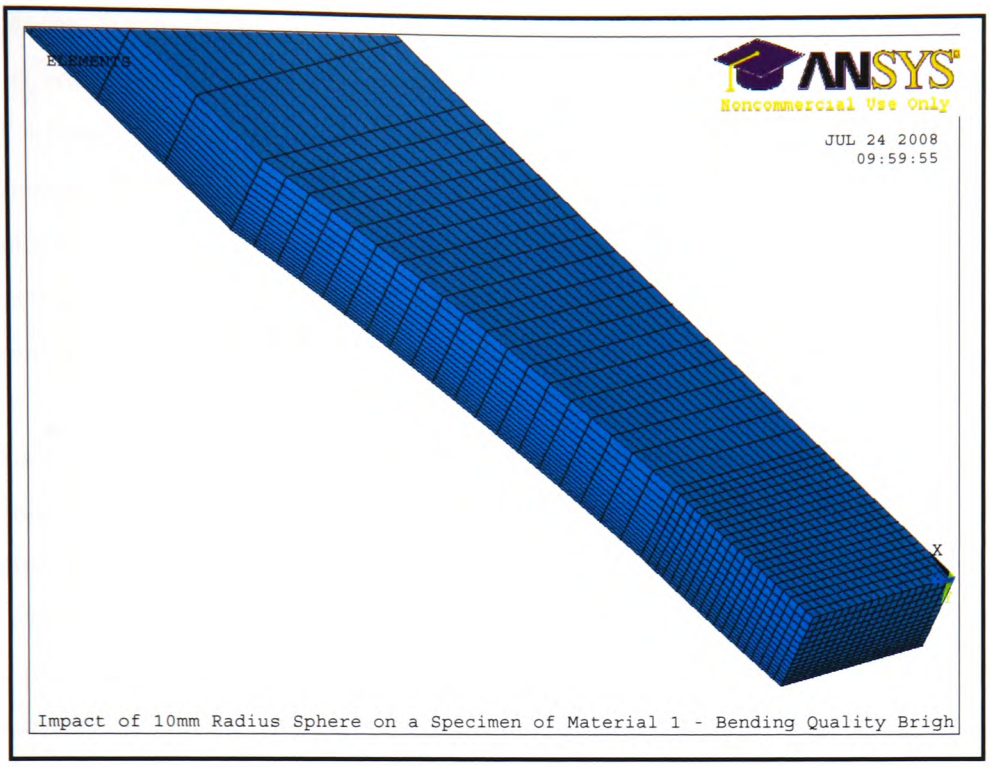

Figure 5.7: Mesh generated on specimen - close up view of impact area

5.3.5 Constraints, Contact and Loads

ANSYS has three main contact capabilities; which are node-to-node, node-to-surface and surface-to-surface. When using node-to-node contact the user must be aware of the exact point of contact on both of the components being modelled. On node-to-surface contact the exact point of contact on the contacting area is not required. Surface-to-surface contact can be used when the exact location of contact on either component is not known, and is most suitable for transient analyses and three dimensional surfaces. Surface-to-surface contact was therefore chosen as the most appropriate type of contact for this problem. The numerical model uses an eight node surface-to-surface contact, with the impactor hammer head being the contact surface and the specimen being the target surface.

For the 10mm impactor hammer head on the Bending Quality Bright Steel specimens, the input velocity used was the average experimental entry velocity of 3.11m/s, as detailed in Section 4.2.2 'Entry Velocity of Impact'. For the six impactor hammer head sizes tested on '070M20' Carbon Steel specimens, the velocity used is the average experimental entry velocity of 2.66m/s, as detailed in Section 4.3.2 'Entry Velocity of Impact'. These values will be used as loading conditions in the numerical models.

Since only one quarter of both the specimen and impactor hammer head were modelled, symmetry boundary conditions needed to be applied, in order that the intersection surfaces were appropriately restrained. As the base of the experimental specimen is restrained, to ensure that no deformation occurs during impact, it was also necessary to restrain the base of the specimen in the numerical model.

A non-linear transient problem can be solved with either implicit or explicit integration algorithms. When the time step size required to obtain convergence is specified by the user, implicit algorithms are used. However, if the time step is adjusted based on the system response then explicit solvers are employed. The three-dimensional, non-linear transient models developed for the current research used implicit time integration algorithms, as the time step size was specified.

The impact produced by the impactor hammer head was modelled over two load steps. The impactor hammer head is modelled so that it is a small distance (0.1mm) above the specimen. In the first time step the impactor moves over the distance specified, thus closing the gap between the impactor hammer head and the specimen and making contact between the two surfaces. In the second load step the constraints for the impactor hammer head are removed, and the impactor moves with the velocity generated by the first time step.

5.4 Model Results

Seven three-dimensional numerical models were produced to simulate the single impact damage created by the various impactor hammer head sizes tested, for each of the materials in the experimental programme. For the Bending Quality Bright Steel specimens (Material 1) the only impactor hammer head used in the experimental procedure was the 10mm radius impactor head, and therefore only one model was produced to replicate this size of impact. Due to the lengthy analysis times of the numerical models (approximately 336 hours per model) and constraints on time for the study, it was only possible to run four of the six models produced for the '070M20' Carbon Steel (Material 2) specimens. The sizes of impactor hammer heads for which numerical results were obtained are 10mm, 11mm, 12mm, and 18mm radii.

5.4.1 Specimen Material 1 – Bending Quality Bright Steel

It is possible to calculate the velocity of the impactor hammer head during contact with the specimen and also the exit velocity of the impactor hammer head from displacement/time results provided by ANSYS. It was possible to use these results to produce the graph shown in Figure 5.8, which can then be used to produce a graph of the displacement of the impactor hammer head against time, as shown in Figure 5.9, the gradient of which gives the contact velocity. It is also possible to produce a further graph, as shown in Figure 5.10, the gradient of which gives the exit velocity.

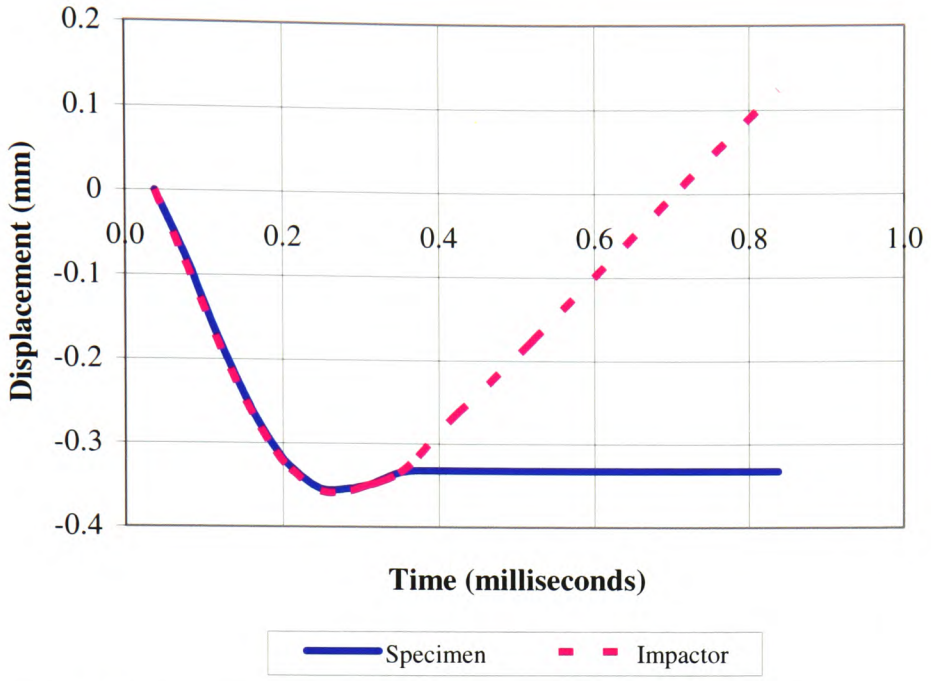

Figure 5.8: Displacement of the impactor hammer head and specimen over time

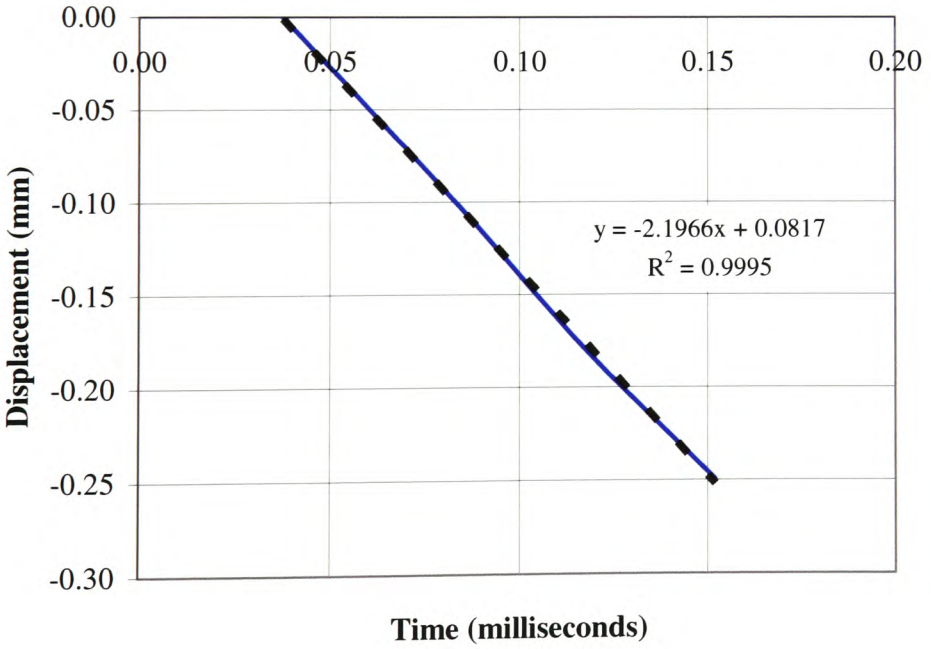

Figure 5.9: Displacement of the impactor hammer head over time - gradient of line provides contact velocity

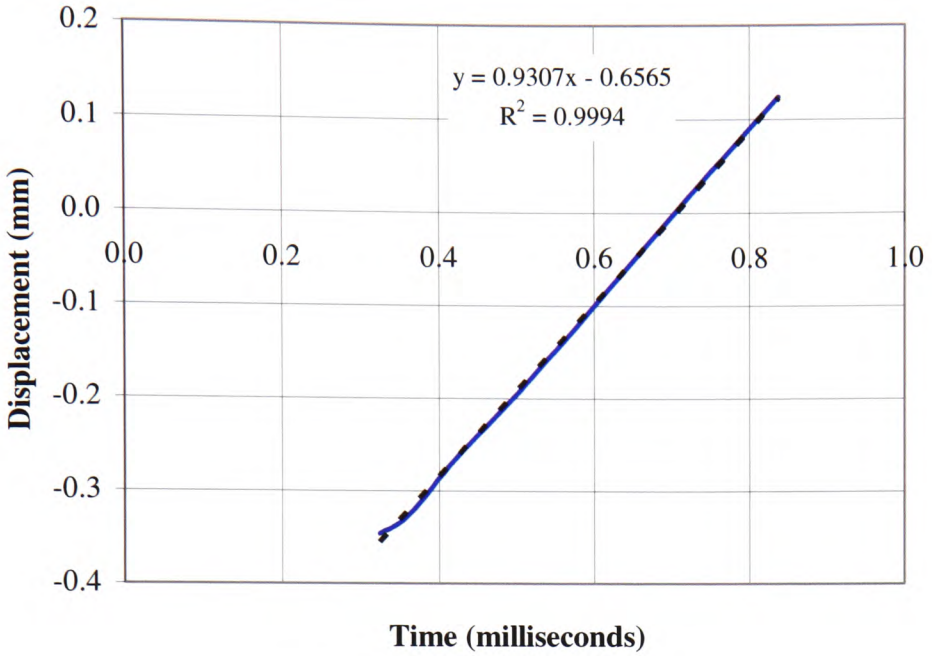

Figure 5.10: Displacement of the impactor hammer head over time - gradient of line provides exit velocity

Table 5.3 shows a summary of both the experimental and numerical modelling results for the bending quality bright steel specimen tests, using the 10mm radius impactor hammer head. On comparison of the results it is possible to say that the experimental results correlate well and validate the numerical results obtained. The contact velocity will be less than the entry velocity as the contact velocity is the velocity of the impactor hammer head during impact, and it will decrease the more it contacts the specimen, as more energy is transformed into strain energy and the deformation of the specimen. The only numerically modelled parameter which does not correlate well with the experimental results is that of the impact contact time. It is possible that the experimental accelerometer readings are inaccurate. The mounting of the accelerometer on the impact rig is extremely critical, and it is believed that if the metal plate on which it is mounted is too thin it will resonate causing the accelerometer to sense erroneous vibrations. It is therefore felt that the impact contact time results produced by the numerical models are the more accurate.

Material Batch – Bending Quality Bright Steel	Impactor Hammer Head Radius (mm)	Entry Velocity of Impact (m/s)	Velocity on Contact (m/s)	Exit Velocity of Impact (m/s)	Coefficient of Restitution	Depth of Impact Crater (mm)	Width of Impact Crater (mm)	Impact Contact Time (seconds)
Experimental Results	10	3.11	N/A	1.02	0.33	0.41	5	0.0000904
Numerical Results	10	3.11	2.58	0.77	0.248	0.482	6.2	0.000293

Table 5.3: Experimental and numerical modelling results for the bending quality bright steel specimens which have been impacted with a 10mm radius impactor hammer head

When considering the residual stresses produced in the specimen as a result of the impact, it is important to consider the von-Mises stress and also the x-directional stress. The von-Mises stress is an equivalent stress which is used to determine if yield has occurred in a complex stress state. It is called an equivalent stress as it takes into account the three principal stresses and equates them to a single stress, which can then be compared to a uniaxial measure of yield and therefore help predict yield and failure. However, the von-Mises stress does not differentiate between tensile and compressive stress states, the nature of these stresses can be determined from the x-directional stress. Residual tensile and compressive stress results are of most interest in the x-direction as this is the direction of the axial loading in the fatigue tests.

Figure 5.11 shows the residual von-Mises stresses on the impacted side of a specimen and Figure 5.12 shows the underside of the same impacted specimen. The maximum residual von-Mises stress recorded was 454MN/m^2 at the base of the specimen, directly under the impact site, and also just outside the impact area on the surface of the specimen. It should be noted that this value is very close to the maximum stress of 454.545MN/m^2 recorded in the material data, Table 5.1, for the numerical model.

Figure 5.13 shows the residual x-directional stresses on the impacted side of a specimen and Figure 5.14 shows the underside of the same impacted specimen. The maximum residual x-directional (tensile) stress recorded was 465MN/m^2 at the region of greatest stress concentration, where the cross-sectional area is the smallest.

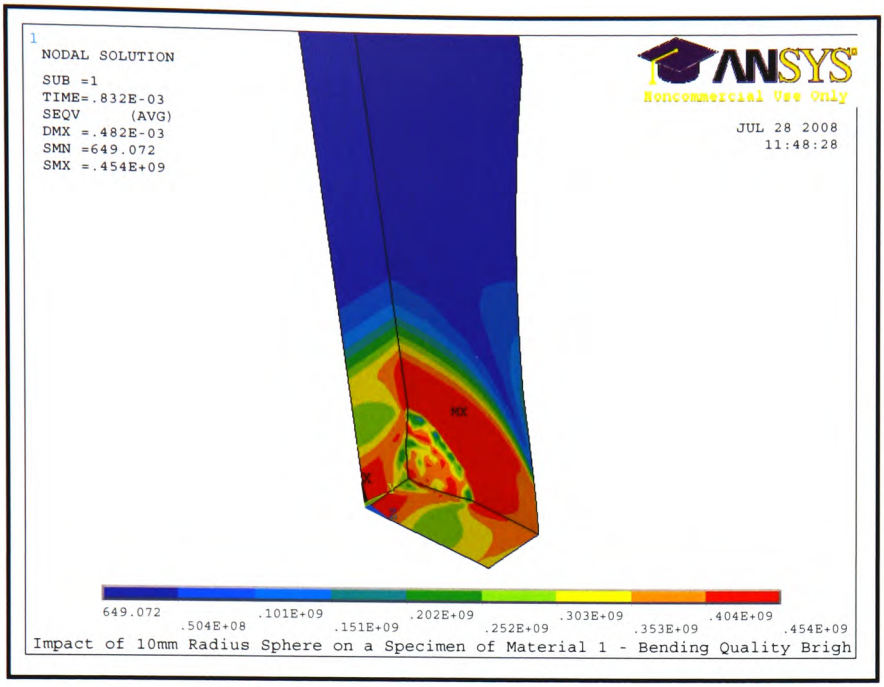

Figure 5.11: Residual von-Mises stresses produced on a specimen of bending quality bright steel impacted with a 10mm radius impactor hammer head (top view) - Units are N/m^2

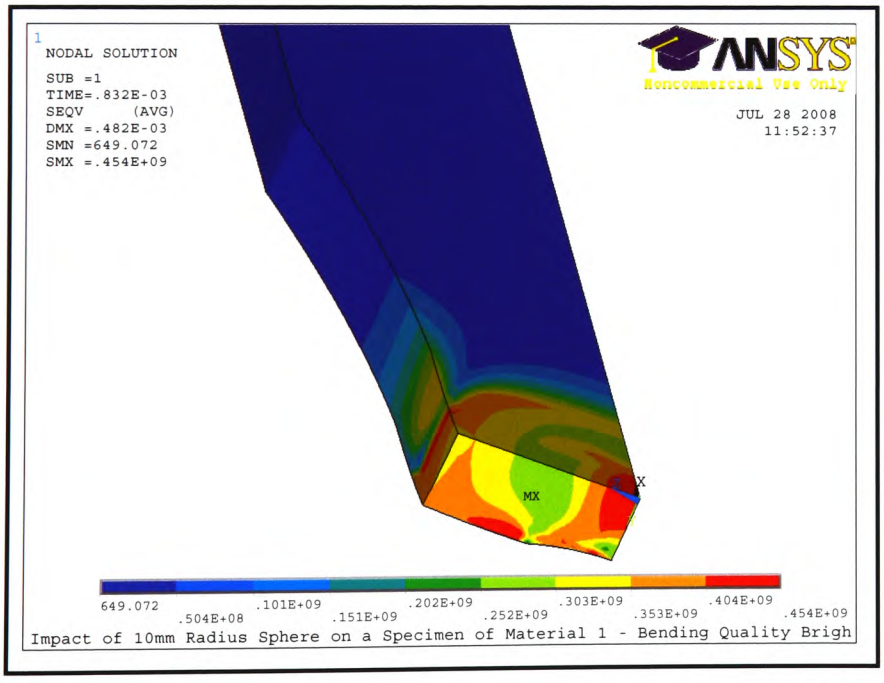

Figure 5.12: Residual von-Mises stresses produced on a specimen of bending quality bright steel impacted with a 10mm radius impactor hammer head (bottom view) - Units are N/m^2

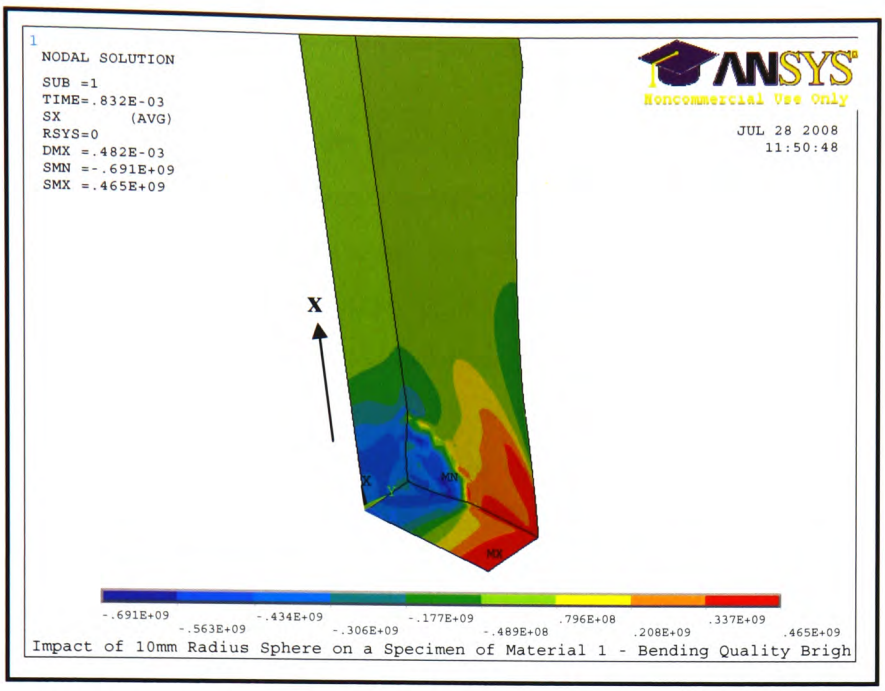

Figure 5.13: Residual x-directional stresses produced on a specimen of bending quality bright steel impacted with a 10mm radius impactor hammer head (top view) - Units are N/m^2

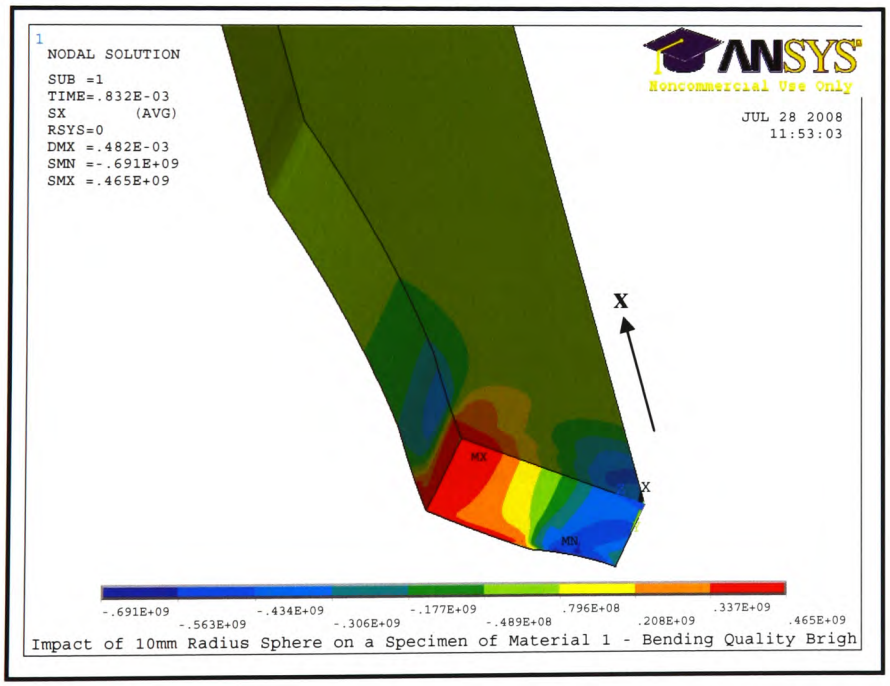

Figure 5.14: Residual x-directional stresses produced on a specimen of bending quality bright steel impacted with a 10mm radius impactor hammer head (bottom view) - Units are N/m^2

5.4.2 Specimen Material 2 – '070M20' Carbon Steel

The velocity on contact for the four impactor hammer head sizes tested are shown in Table 5.4. As previously mentioned these values vary from the entry velocity of 3.11m/s which was used as a set-up parameter, as these are mean values which take into the velocity of the impactor hammer head during its contact with the specimen. The velocity on contact is shown to decrease as the size of the impactor hammer head increases, indicating that more energy is absorbed by the specimen as the size of the impactor hammer head increases. It should also be noted that the velocities for the 11mm and 12mm radius impactor hammer heads are the same, due to the congruity of the impactor geometries and the element size used.

Impactor Hammer Head Radius (mm)	**Velocity on Contact (m/s)**
10	2.20
11	2.12
12	2.12
18	1.99

Table 5.4: Contact velocities generated by ANSYS models

The exit velocities for the four impactor hammer head sizes tested are shown in Table 5.5. With the exception of the exit velocity for the 11mm radius impactor hammer head, the exit velocity is shown to increase with a corresponding increase in the impactor hammer head size, indicating that less energy is absorbed by the specimen on impact as the size of the impactor hammer head increases. It should also be noted that the exit velocities for the 10mm and 11mm radius impactor hammer heads are very similar, due to the congruity of the impactor geometries and the element size used. The numerical and experimental results for exit velocity against impactor hammer head radius are

shown in Figure 5.15. From the trend lines produced it can be seen that the numerical results compare favourably with the experimental results. The numerical results are greater than the experimental results with a maximum difference of 18.3% between the results.

Impactor Hammer Head Radius (mm)	Exit Velocity of Impact (m/s)
10	0.93
11	0.92
12	0.97
18	1.04

Table 5.5: Exit impact velocities generated by ANSYS models

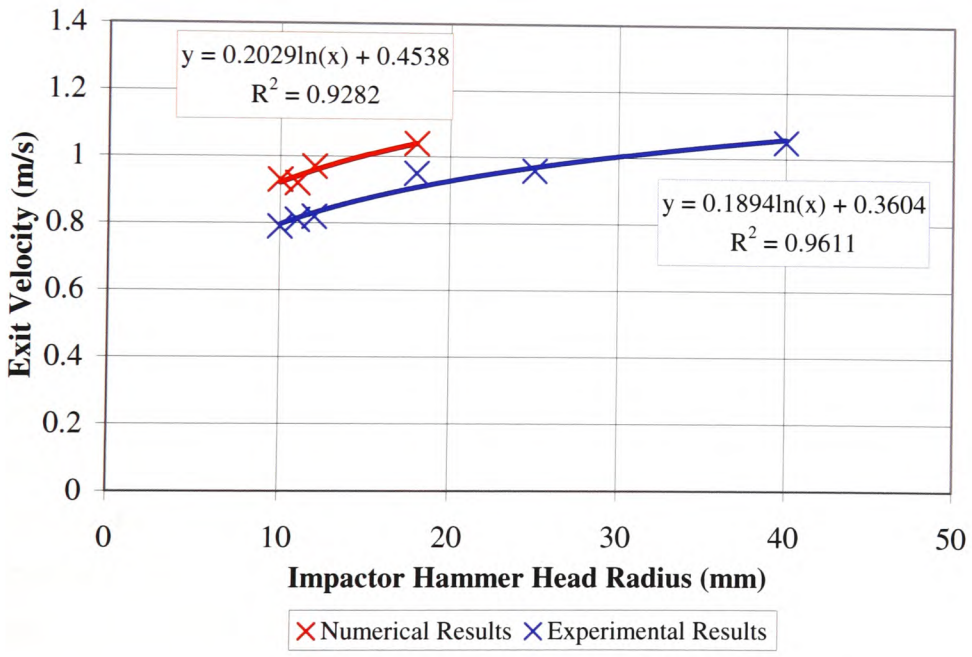

Figure 5.15: Numerical and experimental results for exit velocity against impactor hammer head radius

The COR for the four impactor hammer head sizes tested is shown in Table 5.6. With the exception of the exit velocity for the 11mm radius impactor hammer head, the COR is shown to increase with a corresponding increase in the impactor hammer head size, indicating that the impact can be said to be partially plastic, with some kinetic energy being transformed into the deformation of material, sound and possibly other forms of energy, such as heat. The numerical and experimental results for COR against impactor hammer head radius are shown in Figure 5.16. From the trend lines produced it can be seen that the numerical results compare favourably with the experimental results. The numerical results are greater than the experimental results and with a maximum difference of 17.7% between the results.

Impactor Hammer Head Radius (mm)	**Coefficient of Restitution**
10	0.350
11	0.346
12	0.365
18	0.391

Table 5.6: Coefficient of restitution results generated by ANSYS models

The impact crater depth produced for the impactor hammer head sizes tested are shown in Table 5.7. The depth of crater produced is shown to decrease with a corresponding increase in the impactor hammer head size. The numerical and experimental results for depth of impact crater against impactor hammer head radius is shown in Figure 5.17. From the trend lines produced it can be seen that the numerical results compare favourably with the experimental results. With the exception of the depth of impact crater for the 18mm radius impactor hammer head the numerical results are less than the experimental results. There is a maximum difference of 12.6% between the results.

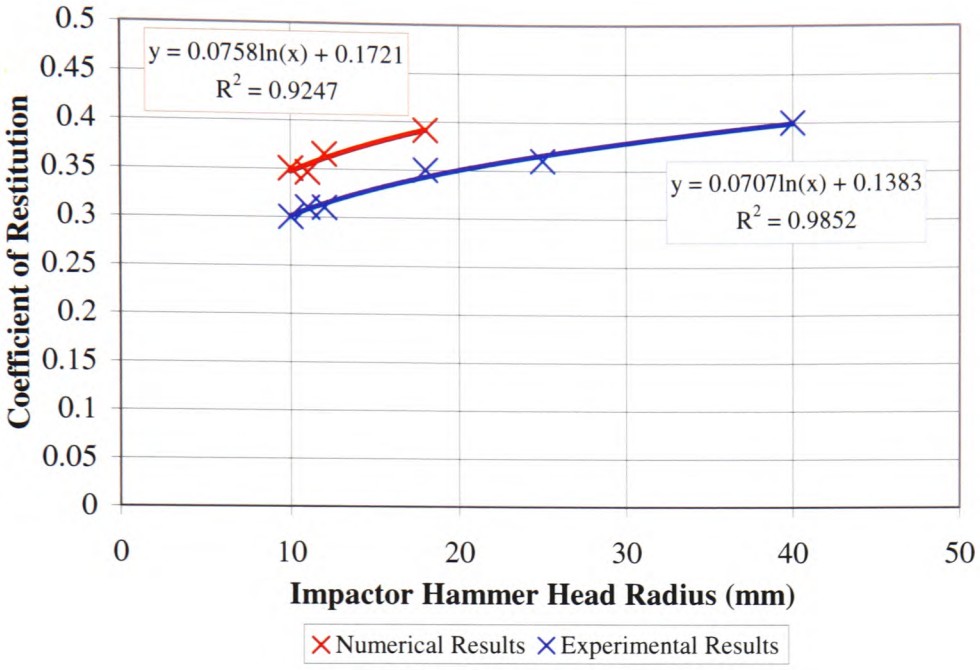

Figure 5.16: Numerical and experimental results for coefficient of restitution against impactor hammer head radius

Impactor Hammer Head Radius (mm)	Depth of Impact Crater (mm)
10	0.332
11	0.322
12	0.310
18	0.261

Table 5.7: Depth of impact crater results generated by ANSYS models

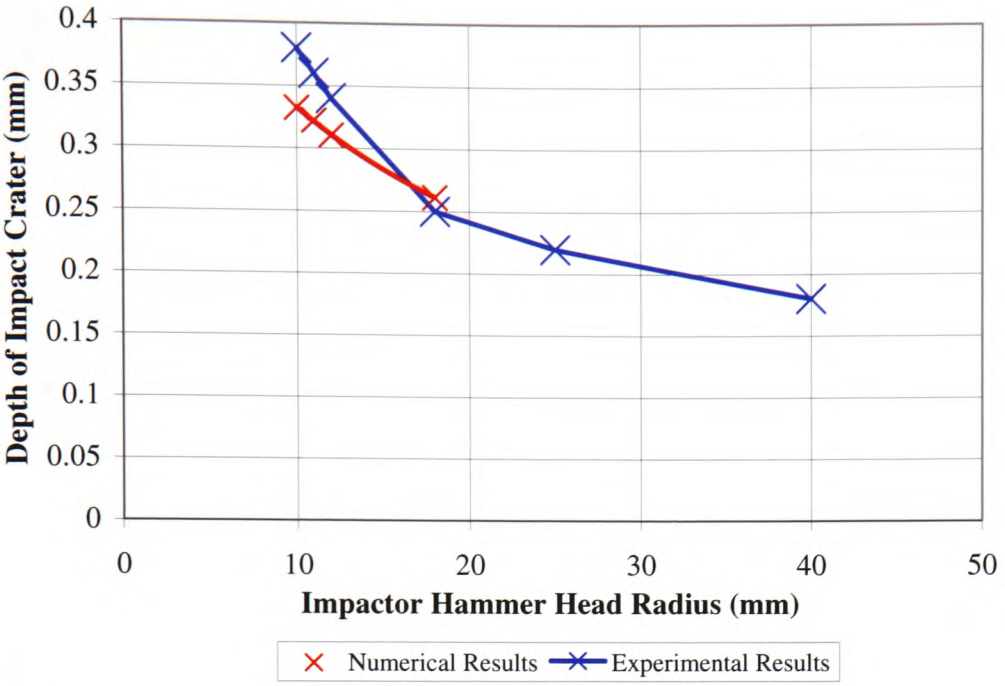

Figure 5.17: Numerical and experimental results for depth of impact crater against impactor hammer head radius

The width of impact craters produced for the various impactor hammer head sizes tested are shown in Table 5.8. The crater width produced is shown to increase with a corresponding increase in the impactor hammer head size. It can also be noted that the width of impact crater for the 10mm and 11mm radius impactor hammer heads is the same due to the congruity of the impactor geometries and the element size used. The numerical and experimental results for width of impact crater against impactor hammer head radius are shown in Figure 5.18. From the trend lines produced it can be seen that the numerical results compare favourably with the experimental results. The numerical results are shown to be less than the experimental results. It should be noted that for the 10mm radius impactor hammer head, the numerical and experimental results are the same and there is a maximum difference of 4.6% between all of the results.

Impactor Hammer Head Radius (mm)	Width of Impact Crater (mm)
10	5.6
11	5.6
12	5.75
18	6.2

Table 5.8: Width of impact crater results generated by ANSYS models

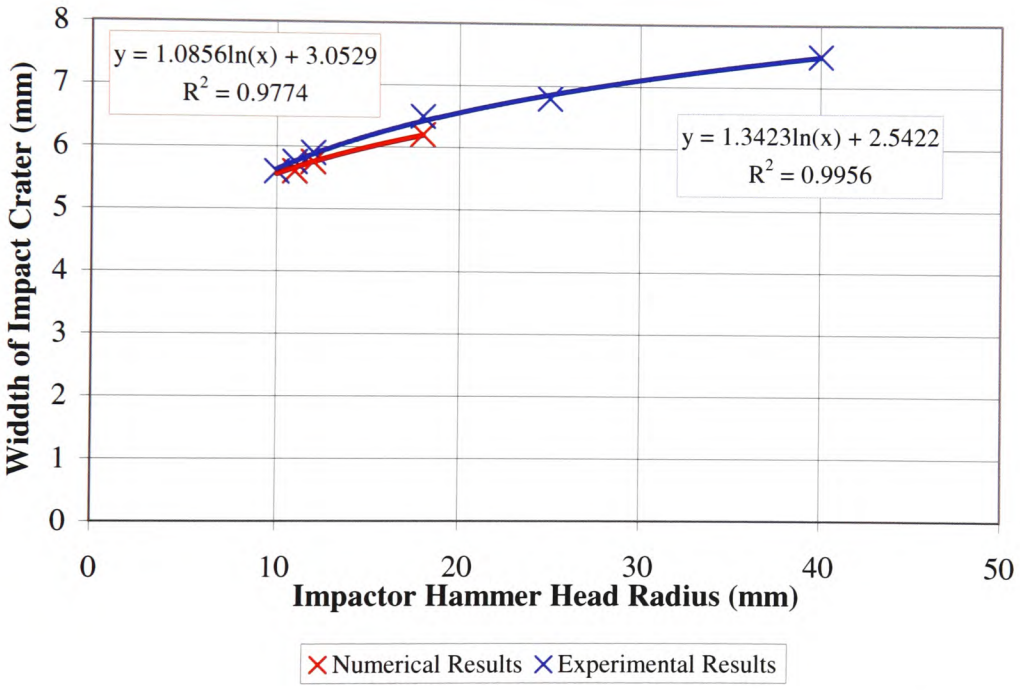

Figure 5.18: Numerical and experimental results for width of impact crater against impactor hammer head radius

The impact contact times for the impactor hammer head sizes tested are shown in Table 5.9. With the exception of the 11mm radius impactor hammer head, the impact contact times are shown to decrease with a corresponding increase in the impactor hammer head size. The numerical and experimental results for impact contact time against impactor hammer head radius are shown in Figure 5.19. From the trend lines produced it can be seen that the numerical results do not compare very favourably with the experimental results. However, as previously discussed in Section 5.4.1, it is felt that the accelerometer was incorrectly mounted, thereby giving erroneous results.

Impactor Hammer Head Radius (mm)	**Impact Contact Time (milliseconds)**
10	0.247
11	0.253
12	0.239
18	0.236

Table 5.9: Impact contact time results generated by ANSYS models

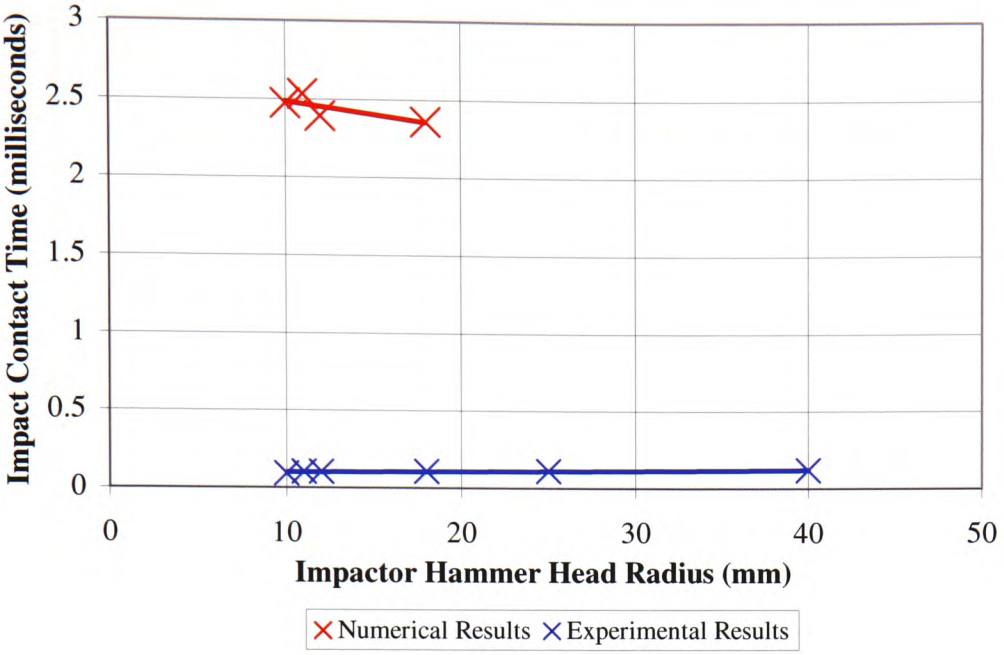

Figure 5.19: Numerical and experimental results for impact contact time against impactor hammer head radius

Figure 5.20 shows the residual von-Mises stresses on the impacted side of a specimen that has been impacted with a 10mm radius impactor hammer head and Figure 5.21 shows the underside of the same impacted specimen. The maximum residual von-Mises stress recorded was 597MN/m^2, which can be seen at the base of the specimen, directly under the impact site, and also just outside the impact area on the surface of the specimen. It should be noted that this value is very close to the maximum stress of 598.52MN/m^2 recorded in the material data, Table 5.2, for the numerical model.

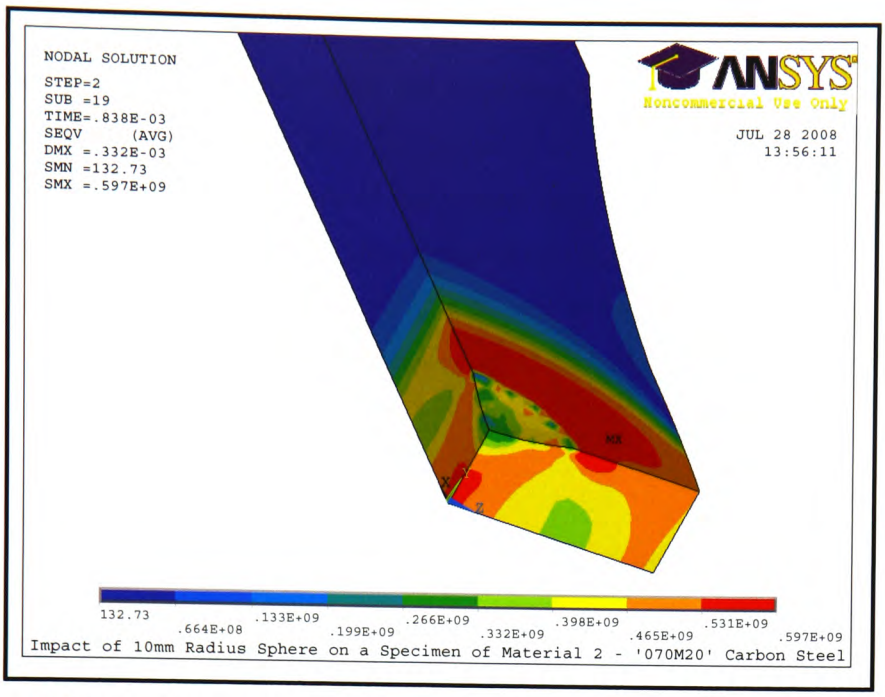

Figure 5.20: Residual von-Mises stresses produced on a specimen of '070M20' carbon steel impacted with a 10mm radius impactor hammer head (top view) - Units are N/m^2

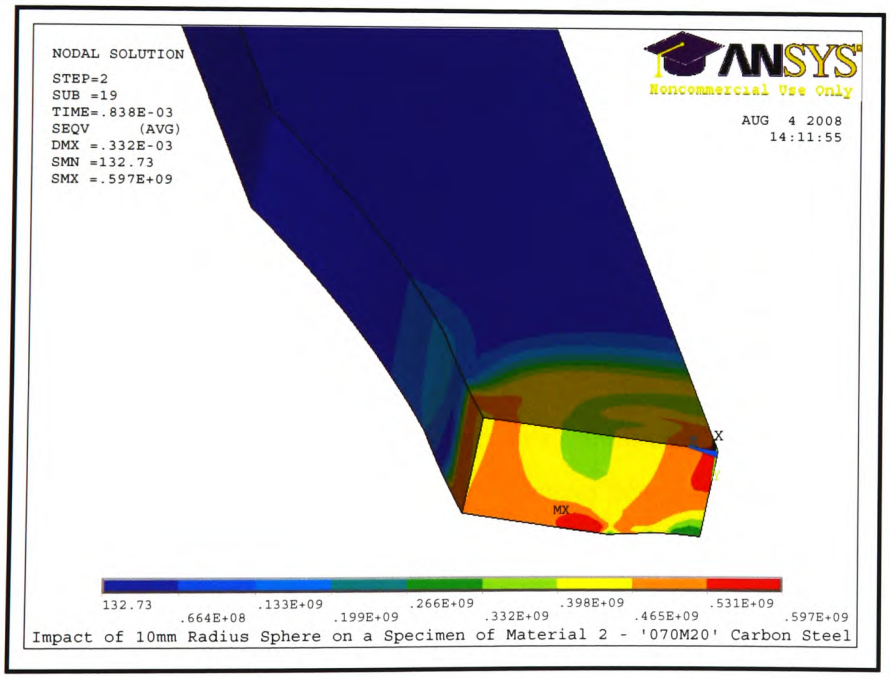

Figure 5.21: Residual von-Mises stresses produced on a specimen of '070M20' carbon steel impacted with a 10mm radius impactor hammer head (bottom view) - Units are N/m^2

Figures 5.22 to 5.30 show the von-Mises stresses on the impacted side of a specimen at various time intervals, from the time of the initial contact between the impactor hammer head and the specimen, to the time of separation after impact. At 0.0948ms, when the initial contact takes place, there is a maximum von-Mises stress directly under the impact site, which diminishes as it radiates outwards, as shown in Figure 5.22. At the point of impact, stresses of 399MN/m^2 are recorded which increase to a maximum stress of 599MN/m^2 directly beneath the impact site.

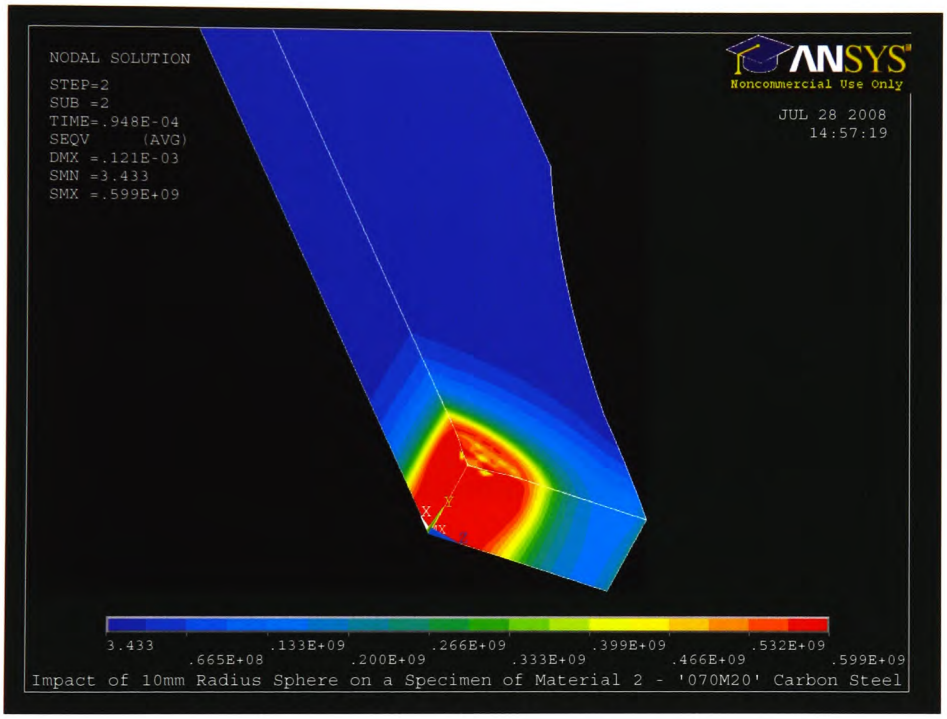

Figure 5.22: Von-Mises stresses produced on a specimen of '070M20' carbon steel impacted with a 10mm radius impactor hammer head (top view) after a time interval of 0.0948 milliseconds - Units are N/m^2

At 0.133ms, the area of maximum stress directly under the impact site has increased, as shown in Figure 5.23. It is also noted that there is a region of high stress at the region of greatest stress concentration, where the cross-sectional area of the specimen is the smallest; this stress is recorded as 532MN/m^2.

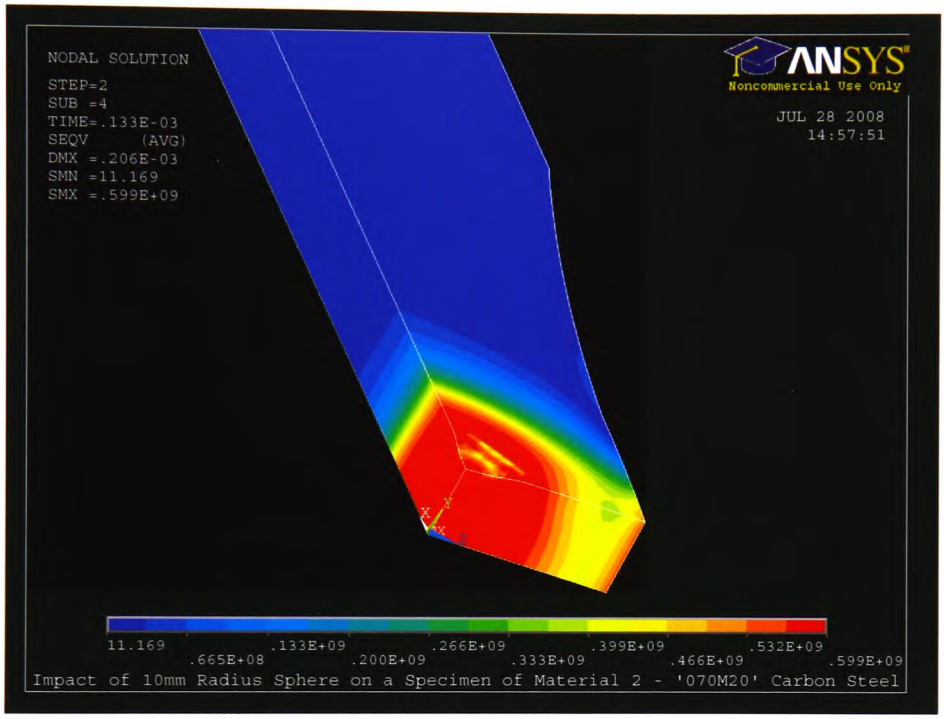

Figure 5.23: Von-Mises stresses produced on a specimen of '070M20' carbon steel impacted with a 10mm radius impactor hammer head (top view) after a time interval of 0.133 milliseconds - Units are N/m^2

At 0.171ms, the stress recorded at the region of greatest stress concentration has increased to 599MN/m^2, as shown in Figure 5.24. The area of stress at the impact site has now greatly increased and has merged with the region of high stress at the region of greatest stress concentration. This area of stress is shown to have increased in size at 0.209ms, as shown in Figure 5.25 and also at 0.285ms, as shown in Figure 5.26.

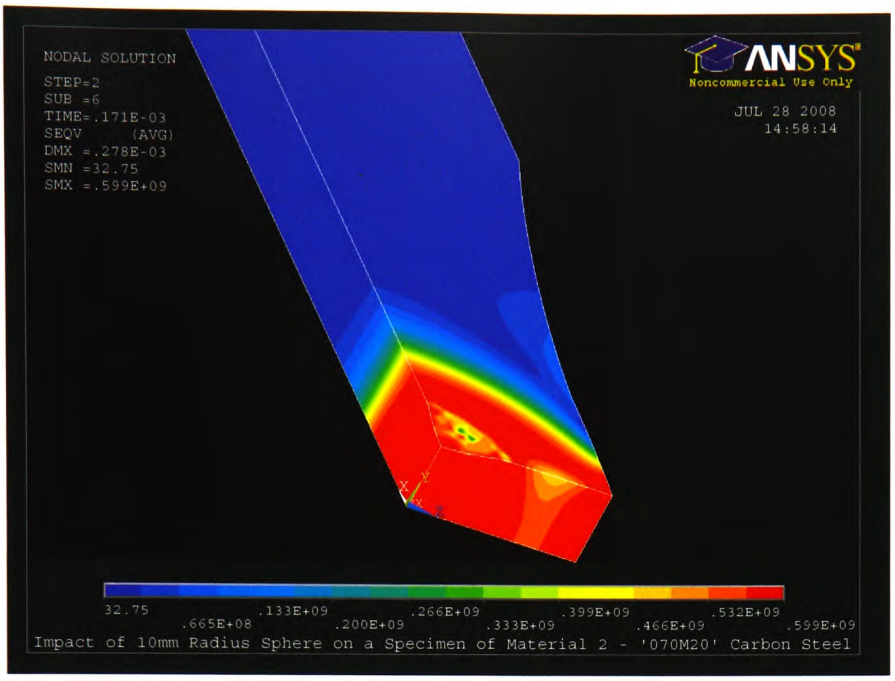

Figure 5.24: Von-Mises stresses produced on a specimen of '070M20' carbon steel impacted with a 10mm radius impactor hammer head (top view) after a time interval of 0.171 milliseconds - Units are N/m^2

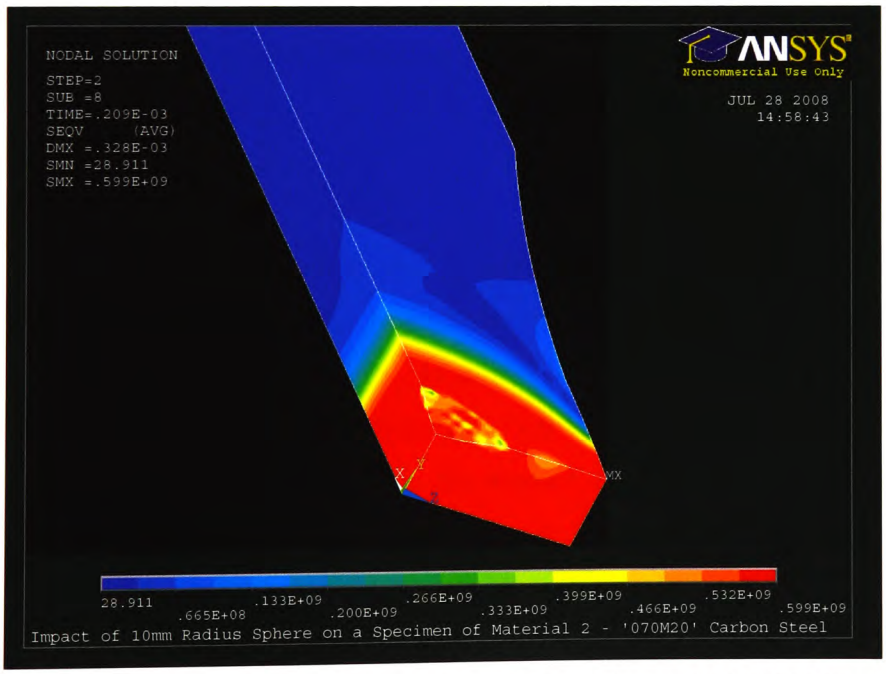

Figure 5.25: Von-Mises stresses produced on a specimen of '070M20' carbon steel impacted with a 10mm radius impactor hammer head (top view) after a time interval of 0.209 milliseconds - Units are N/m^2

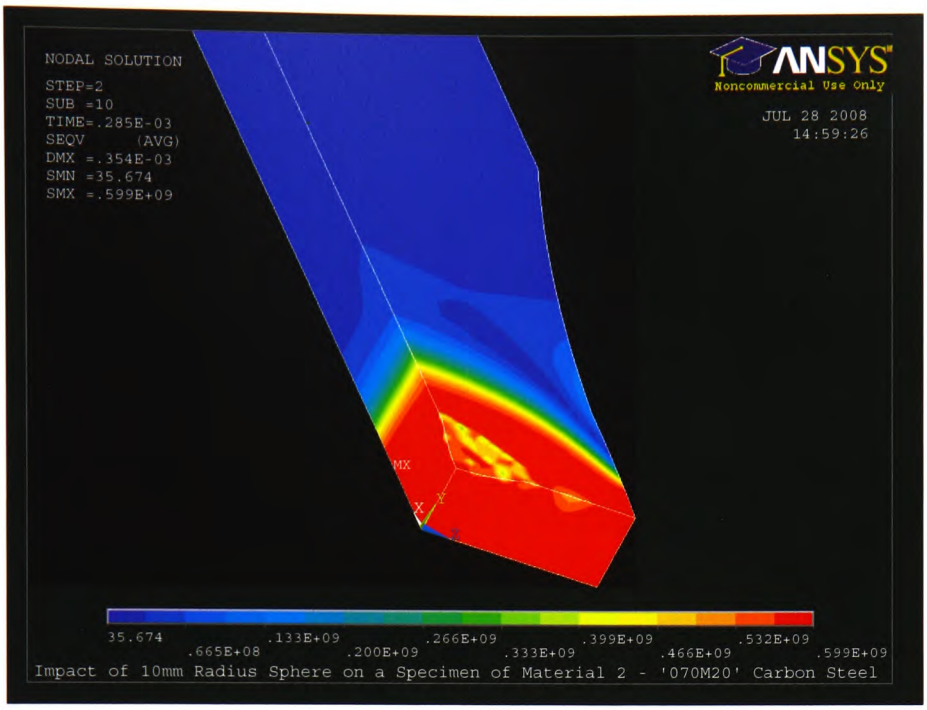

Figure 5.26: Von-Mises stresses produced on a specimen of '070M20' carbon steel impacted with a 10mm radius impactor hammer head (top view) after a time interval of 0.285 milliseconds - Units are N/m^2

At 0.311ms the impactor hammer head is now rebounding out of the specimen. The stresses directly under the impact site have now decreased and range between $200MN/m^2$ and $399MN/m^2$, as shown in Figure 5.27. At 0.348ms, as shown in Figure 5.28, the maximum stress is now visible at the region of greatest stress concentration and just outside the impact area on the surface of the specimen. These regions of maximum stress decrease to $465MN/m^2$, and directly under the impact site the stress decreases to $66.4MN/m^2$ at the top surface of the specimen, and a stress of $531MN/m^2$ at the base of the specimen.

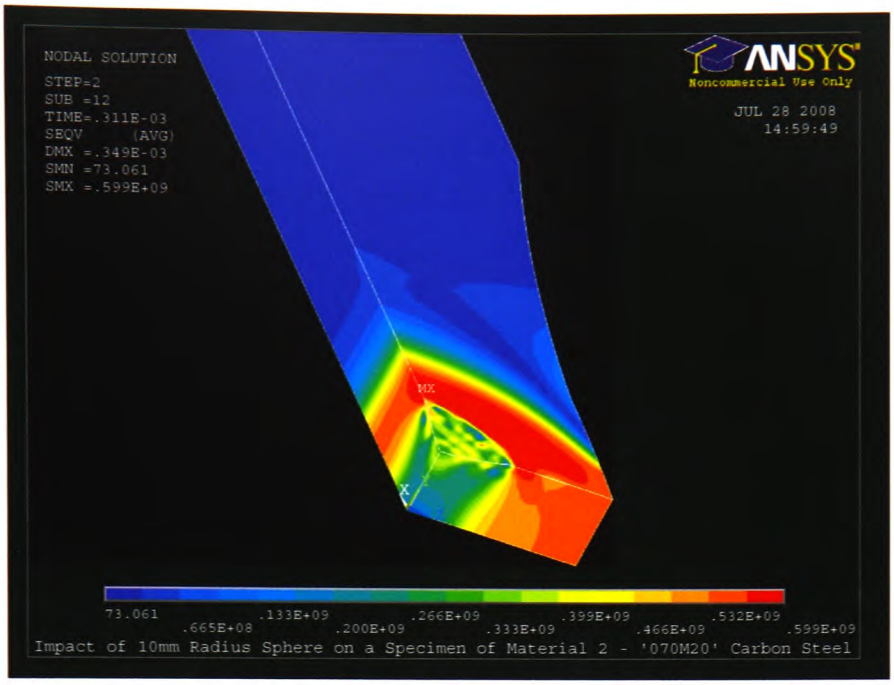

Figure 5.27: Von-Mises stresses produced on a specimen of '070M20' carbon steel impacted with a 10mm radius impactor hammer head (top view) after a time interval of 0.311 milliseconds - Units are N/m^2

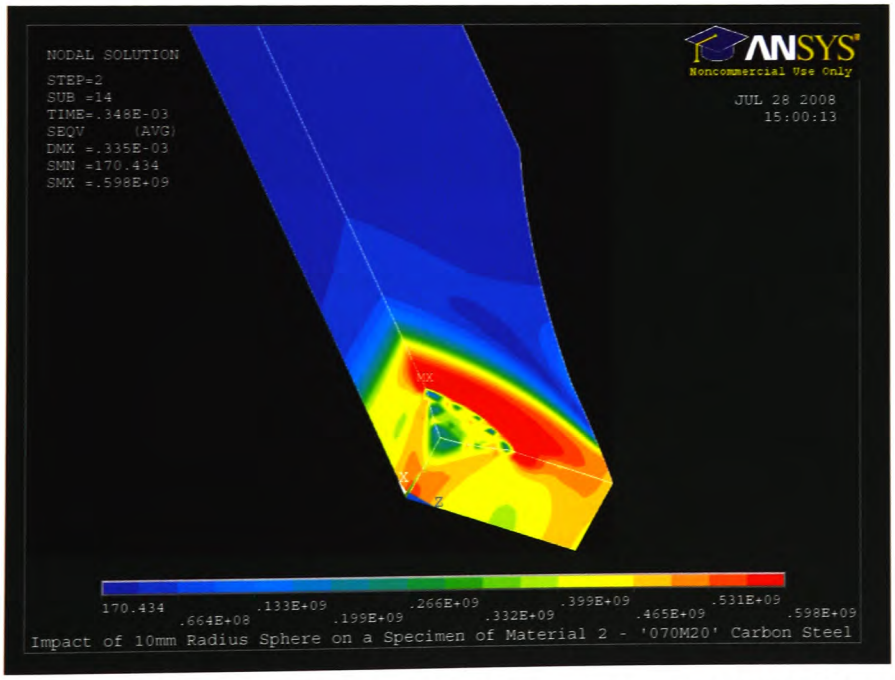

Figure 5.28: Von-Mises stresses produced on a specimen of '070M20' carbon steel impacted with a 10mm radius impactor hammer head (top view) after a time interval of 0.348 milliseconds - Units are N/m^2

The impactor hammer head has now completely separated from the specimen and at 0.421ms the area of stress at the base of the specimen directly under the impact site has increased, as shown in Figure 5.29. At 0.714ms the areas of stress and their corresponding values remain unchanged, as shown in Figure 5.30.

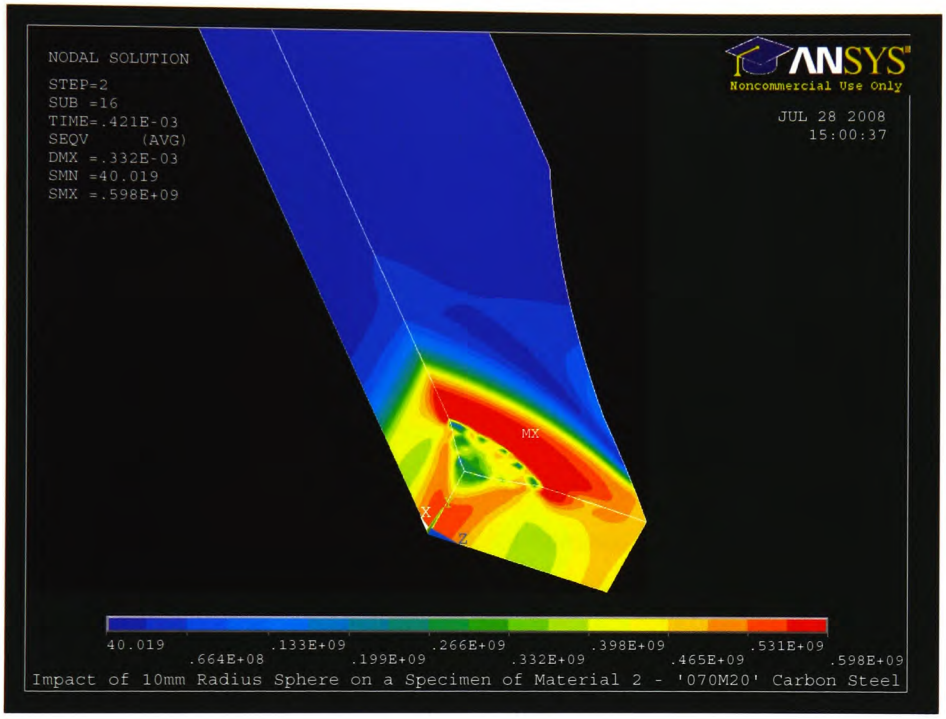

Figure 5.29: Von-Mises stresses produced on a specimen of '070M20' carbon steel impacted with a 10mm radius impactor hammer head (top view) after a time interval of 0.421 milliseconds - Units are N/m^2

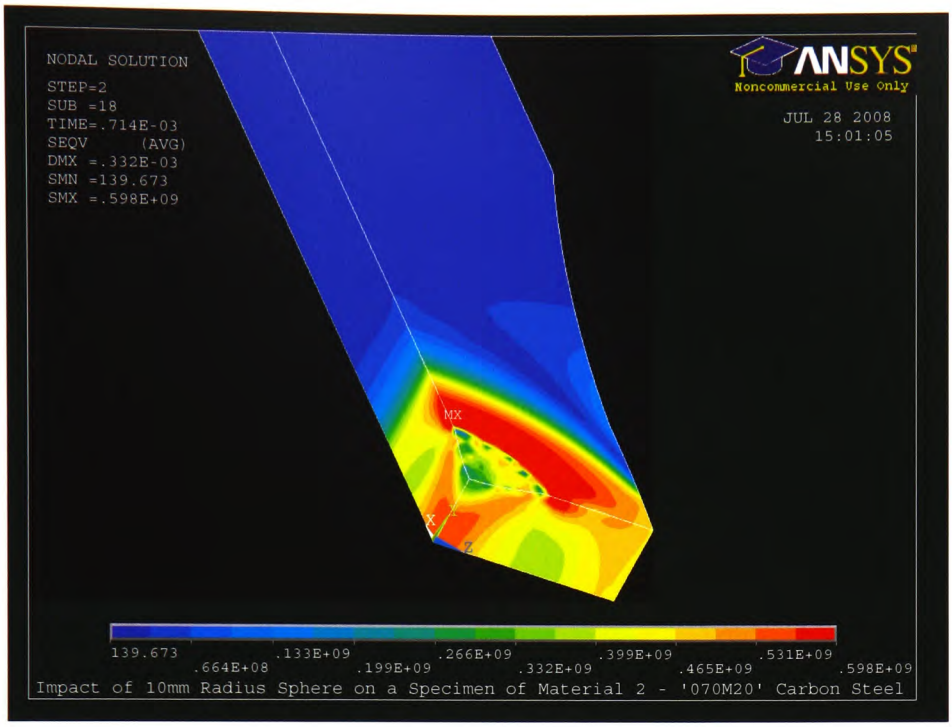

Figure 5.30: Von-Mises stresses produced on a specimen of '070M20' carbon steel impacted with a 10mm radius impactor hammer head (top view) after a time interval of 0.714 milliseconds - Units are N/m^2

The maximum von-Mises stress was recorded at a single nodal position, node 413, which is located just outside the impact area on the surface of the specimen. A graph showing the von-Mises stresses experienced at this nodal position from the beginning of the analysis to the time of separation after impact, is shown in Figure 5.31. The maximum von-Mises stress recorded at this nodal position was $599MN/m^2$. This value decreased and stabilised once the impactor hammer head was fully removed from the specimen, with a residual von-Mises stress of $597MN/m^2$.

A graph of the maximum von-Mises stress recorded at nodal position 413 against von-Mises elastic strain for the duration of the analysis is shown in Figure 5.32.

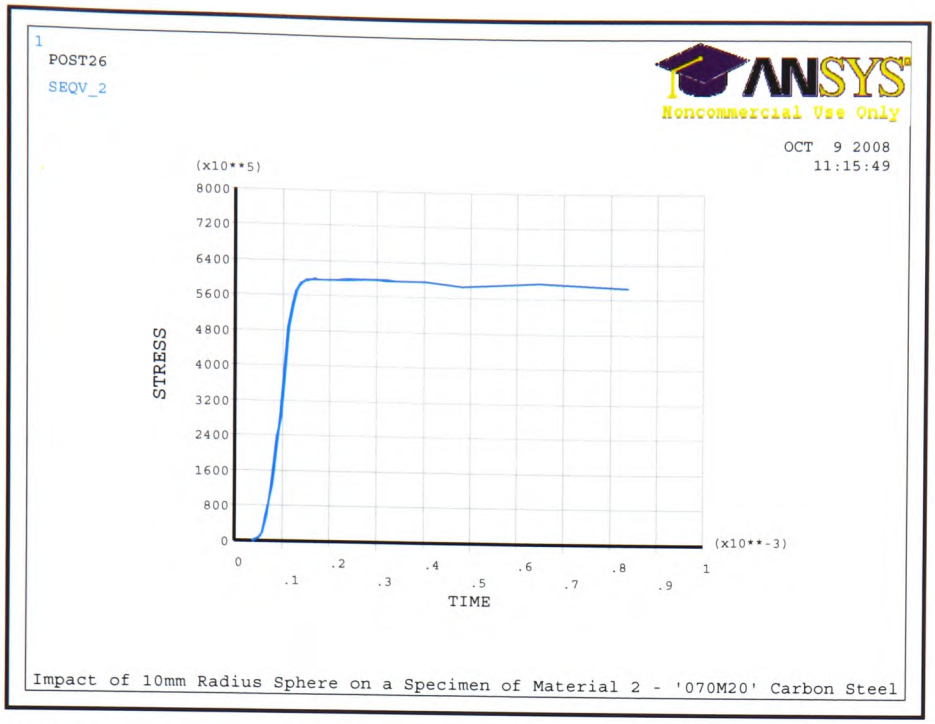

Figure 5.31: Maximum von-Mises stress recorded (N/m^2), occurring at single nodal position (node 413), over time (seconds)

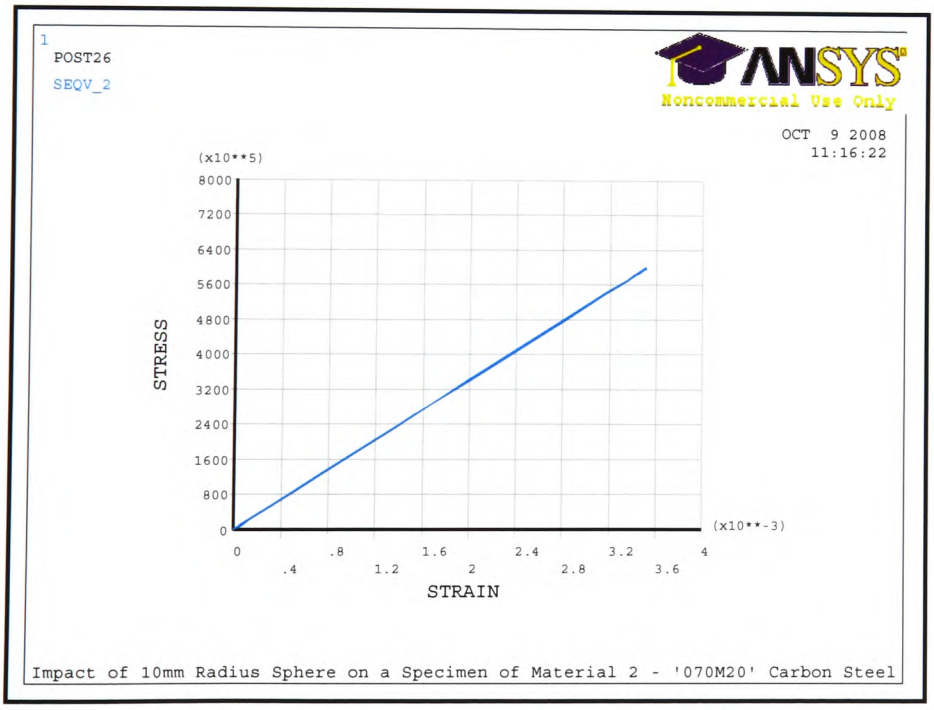

Figure 5.32: Maximum von-Mises stress recorded (N/m^2), occurring at single nodal position (node 413), against von-Mises elastic strain

Figure 5.33 shows the residual x-directional stresses on the impacted side of a specimen that has been impacted with a 10mm radius impactor hammer head. Figure 5.34 shows the underside of the same impacted specimen. The maximum residual x-directional (tensile) stress recorded was 590MN/m^2 at the region of greatest stress concentration, where the cross-sectional area of the specimen is the smallest.

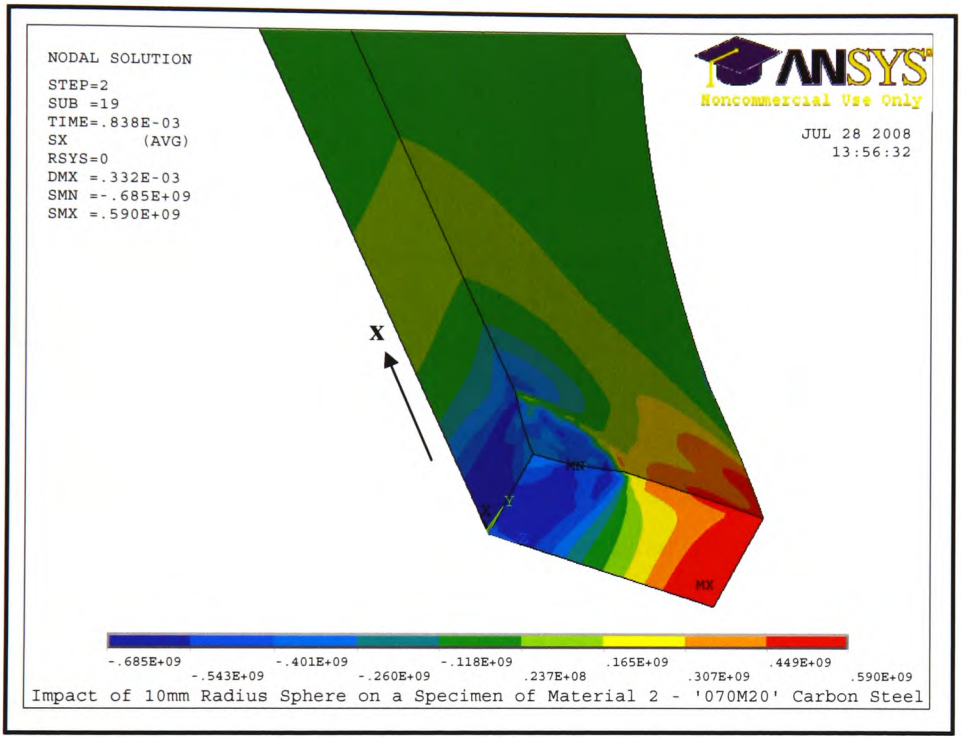

Figure 5.33: Residual x-directional stresses produced on a specimen of '070M20' carbon steel impacted with a 10mm radius impactor hammer head (top view) - Units are N/m^2

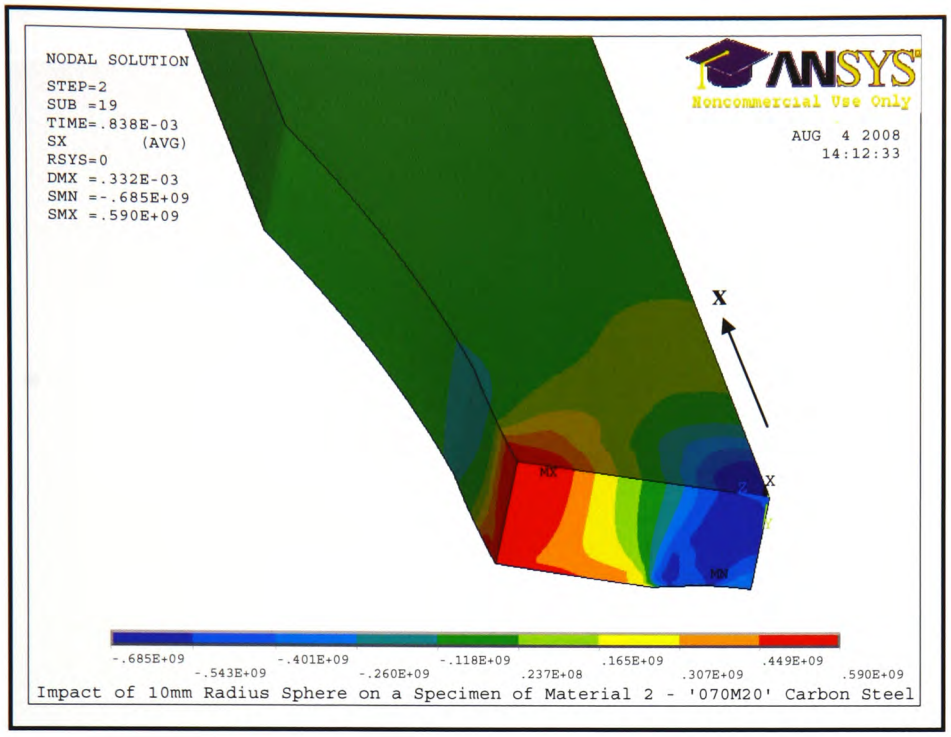

Figure 5.34: Residual x-directional stresses produced on a specimen of '070M20' carbon steel impacted with a 10mm radius impactor hammer head (bottom view) - Units are N/m^2

Figures 5.35 to 5.43 show the x-directional stresses on the impacted side of a specimen at various time intervals, from the time of initial contact between the impactor hammer head and specimen, up to the time of separation after impact. At 0.0948ms, when the initial contact takes place, there is a high compressive stress of $1560MN/m^2$ directly under the impact site and $603MN/m^2$ within the specimen, as shown in Figure 5.35. Additionally, there is a ring of high tensile stress of a magnitude of $594MN/m^2$ just outside the impact area and $354MN/m^2$ at the region of greatest stress concentration. Beyond the shoulder of the specimen, away from the impact site, a compressive stress of $124MN/m^2$ is visible across the length of the specimen.

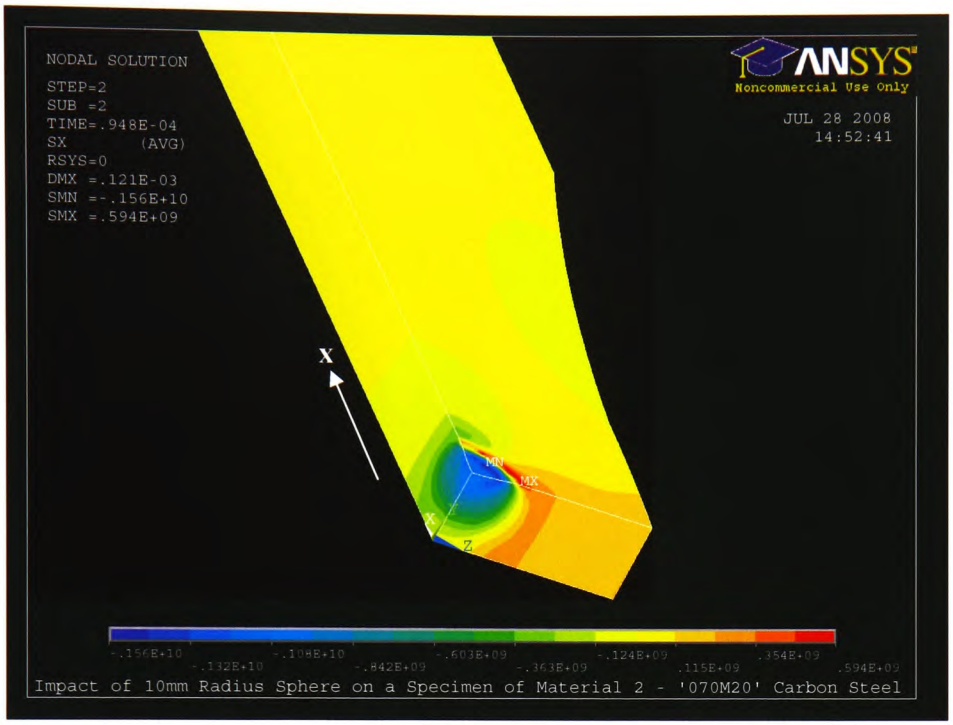

Figure 5.35: X-directional stresses produced on a specimen of '070M20' carbon steel impacted with a 10mm radius impactor hammer head (top view) after a time interval of 0.0948 milliseconds - Units are N/m^2

At 0.133ms, the area covered by the ring of tensile stress just outside the impact area has decreased, as shown in Figure 5.36. The tensile stress at the region of greatest stress concentration has increased to $677MN/m^2$ and the area it covers has also increased. The compressive stress directly under the impact site has increased to $1910MN/m^2$ and the compressive stress visible across the length of the specimen has also increased, to $184MN/m^2$.

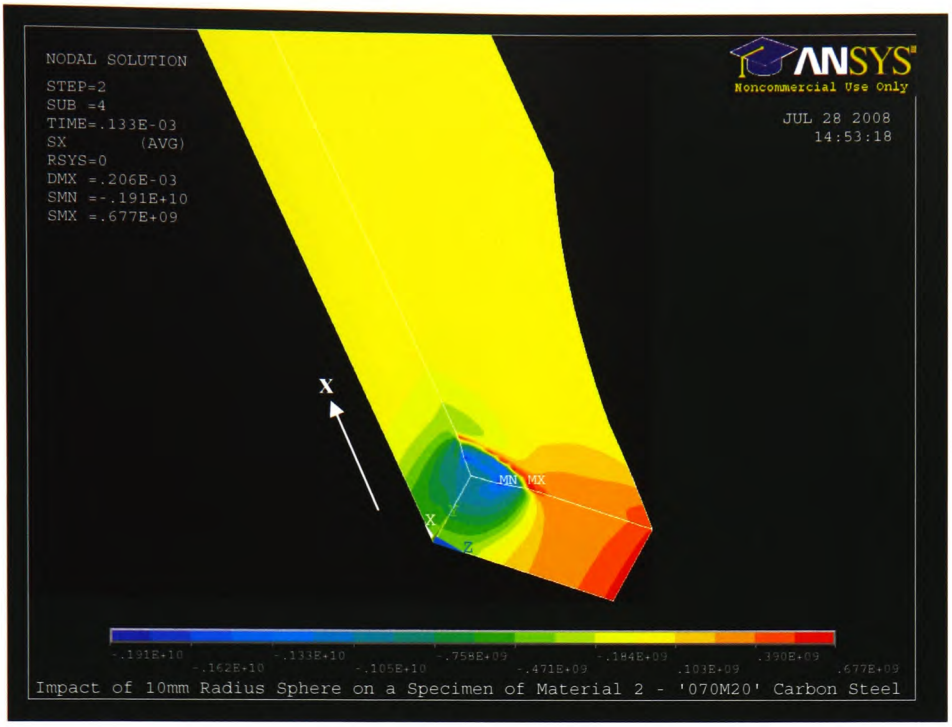

Figure 5.36: X-directional stresses produced on a specimen of '070M20' carbon steel impacted with a 10mm radius impactor hammer head (top view) after a time interval of 0.133 milliseconds - Units are N/m^2

At 0.171ms, the area covered by the ring of tensile stress just outside the impact area has decreased, as shown in Figure 5.37. The tensile stress at the region of greatest stress concentration has increased to $719MN/m^2$ and the area it covers has also increased. The compressive stress directly under the impact site decreased to $1680MN/m^2$ and the area which it covers has increased. The compressive stress visible across the length of the specimen has also increased, to approximately $214MN/m^2$.

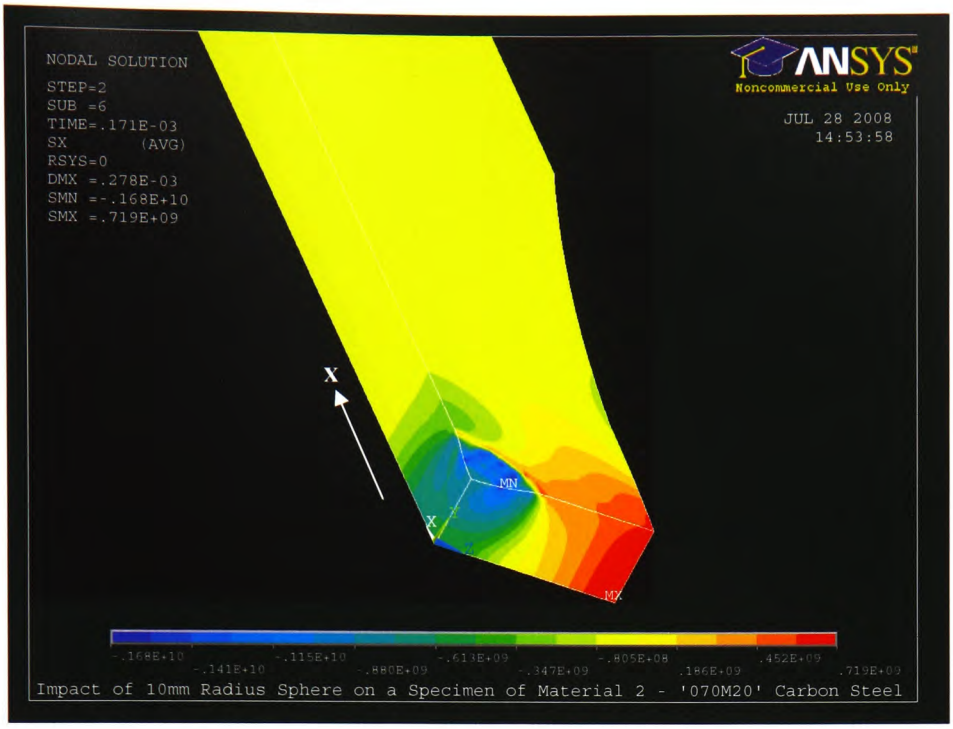

Figure 5.37: X-directional stresses produced on a specimen of '070M20' carbon steel impacted with a 10mm radius impactor hammer head (top view) after a time interval of 0.171 milliseconds - Units are N/m^2

At 0.209ms, the tensile stress at the stress concentration has increased to $738MN/m^2$ and the area it covers has also increased, as shown in Figure 5.38. The compressive stress directly under the impact site increased to $1830MN/m^2$. The compressive stress visible across the length of the specimen has also increased to approximately $259MN/m^2$. At 0.285ms the tensile stress at the region of greatest stress concentration has decreased to $729MN/m^2$, as shown in Figure 5.39. The compressive stress directly under the impact site decreased to $1660MN/m^2$ and the compressive stress visible across the length of the specimen has also decreased, to approximately $198MN/m^2$.

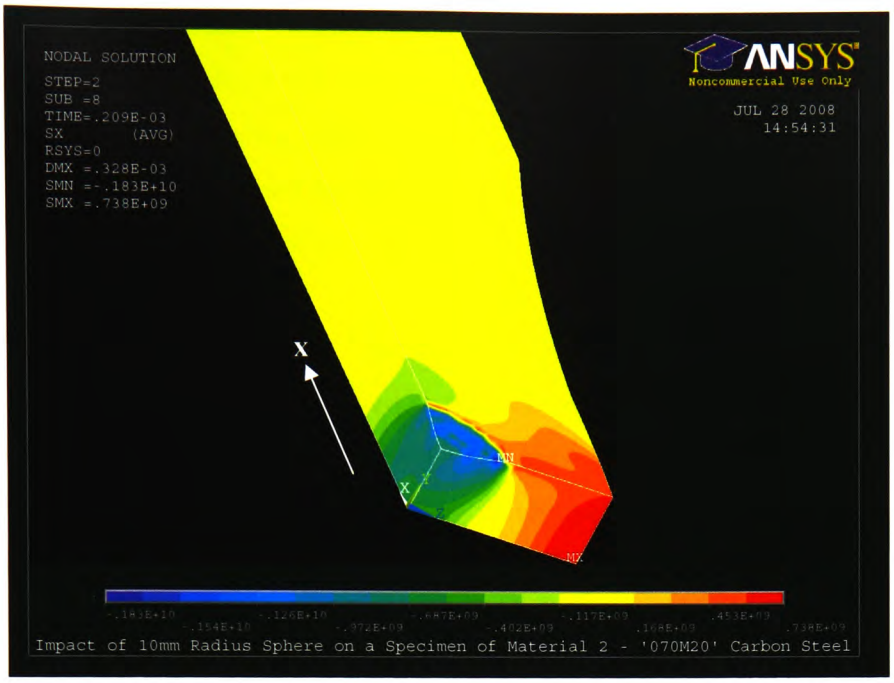

Figure 5.38: X-directional stresses produced on a specimen of '070M20' carbon steel impacted with a 10mm radius impactor hammer head (top view) after a time interval of 0.209 milliseconds - Units are N/m^2

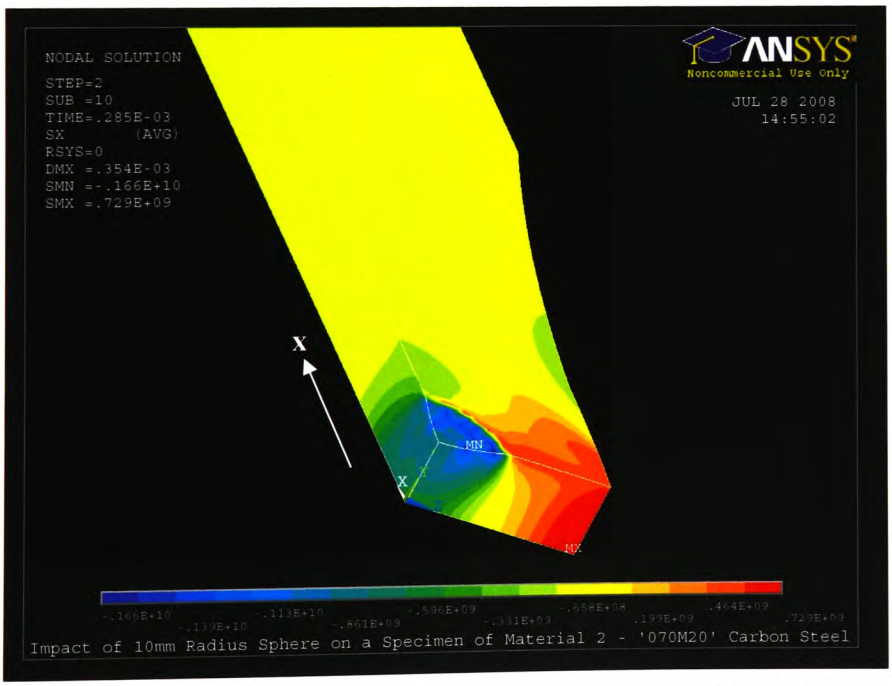

Figure 5.39: X-directional stresses produced on a specimen of '070M20' carbon steel impacted with a 10mm radius impactor hammer head (top view) after a time interval of 0.285 milliseconds - Units are N/m^2

At 0.311ms, the impactor hammer head is now rebounding out of the specimen. The tensile stress at the stress concentration has decreased to 682MN/m^2. The compressive stress directly under the impact site has decreased to 1420MN/m^2 and the area which it covers has also decreased. The compressive stress visible across the length of the specimen has also decreased to 185MN/m^2, as shown in Figure 5.40. At 0.348ms, the tensile stress at the region of greatest stress concentration has decreased to 602MN/m^2. The compressive stress directly under the impact site has decreased to 731MN/m^2 and the area which it covers has increased. The compressive stress visible across the length of the specimen has decreased to approximately 65MN/m^2, as shown in Figure 5.41.

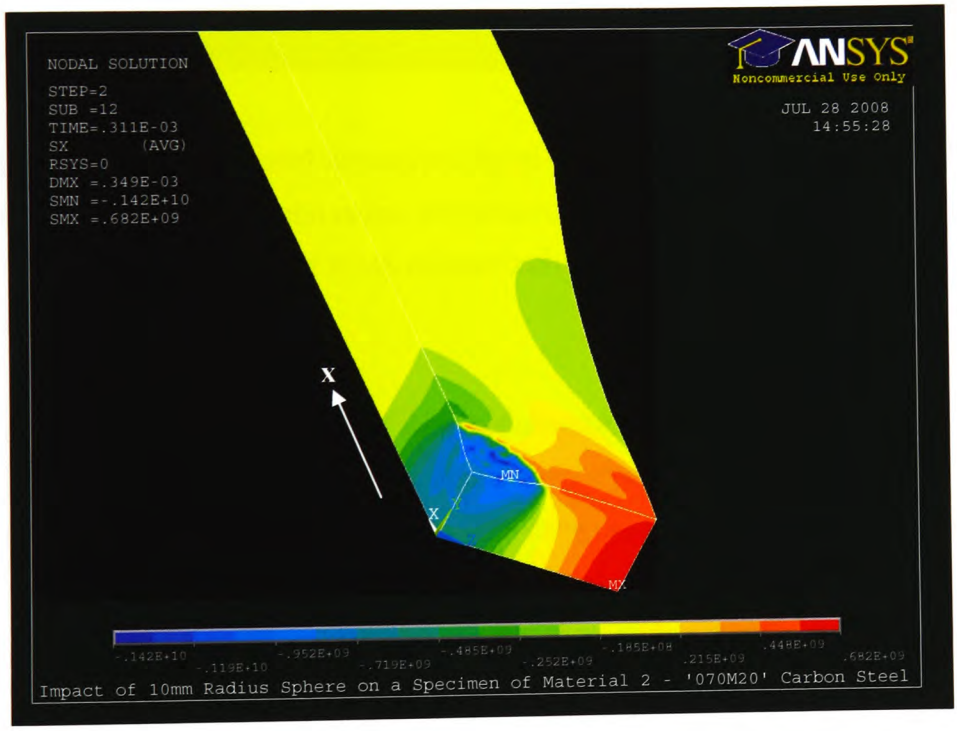

Figure 5.40: X-directional stresses produced on a specimen of '070M20' carbon steel impacted with a 10mm radius impactor hammer head (top view) after a time interval of 0.311 milliseconds - Units are N/m^2

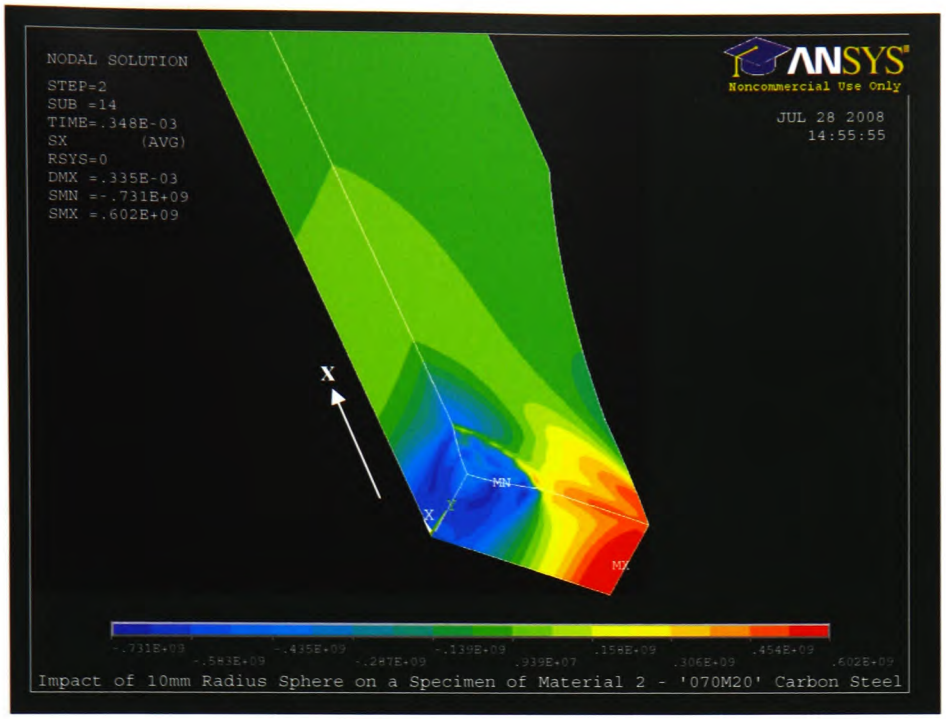

Figure 5.41: X-directional stresses produced on a specimen of '070M20' carbon steel impacted with a 10mm radius impactor hammer head (top view) after a time interval of 0.348 milliseconds - Units are N/m^2

The impactor hammer head has now completely separated from the specimen and, at 0.421ms, the tensile stress at the stress concentration has decreased to $589MN/m^2$, as shown in Figure 5.42. The compressive stress directly under the impact site has decreased to $688MN/m^2$. The compressive stress visible across the length of the specimen has also decreased to approximately $49MN/m^2$. At 0.714ms the tensile stress at the region of greatest stress concentration has decreased to $585MN/m^2$, as shown in Figure 5.43. The compressive stress directly under the impact site has decreased to $691MN/m^2$ and the compressive stress visible across the length of the specimen has increased, to approximately $53MN/m^2$.

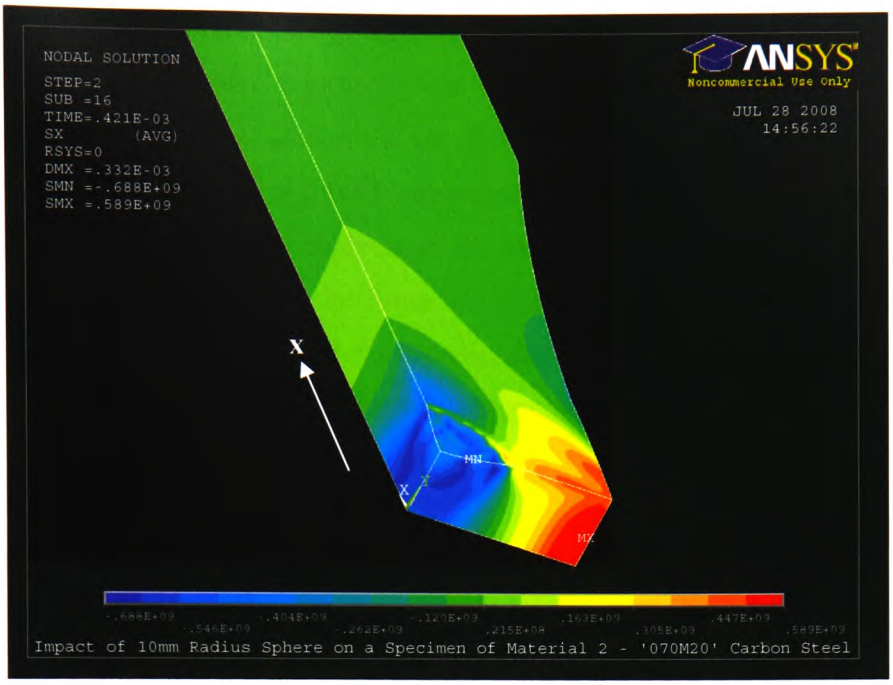

Figure 5.42: X-directional stresses produced on a specimen of '070M20' carbon steel impacted with a 10mm radius impactor hammer head (top view) after a time interval of 0.421 milliseconds - Units are N/m^2

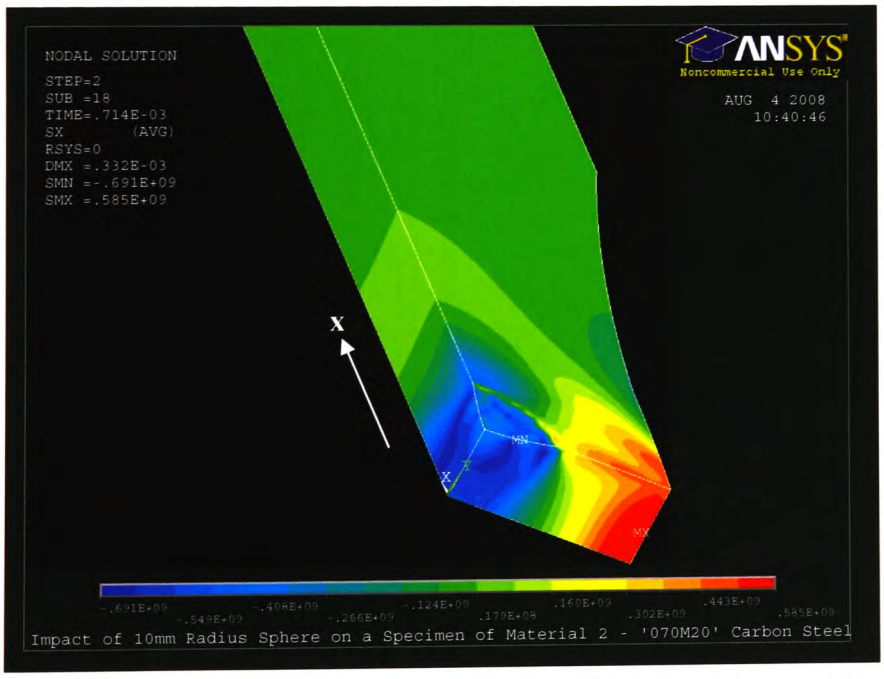

Figure 5.43: X-directional stresses produced on a specimen of '070M20' carbon steel impacted with a 10mm radius impactor hammer head (top view) after a time interval of 0.714 milliseconds - Units are N/m^2

The maximum x-directional (tensile) stress was recorded at a single nodal position, node 553, which is located at the region of greatest stress concentration, where the cross-sectional area of the specimen is the smallest. A graph showing the maximum x-directional (tensile) stresses experienced at this nodal position from the beginning of the analysis to the time of separation after impact, is shown in Figure 5.44. As the impactor hammer head rebounded out of the specimen it can be seen that the x-directional (tensile) stress decreased until it eventually stabilised once the impactor hammer head was fully removed from the specimen, with a residual x-directional (tensile) stress of 590MN/m^2.

A graph of the maximum x-directional (tensile) stress recorded at the nodal position of 553 against elastic strain for the duration of the analysis is shown in Figure 5.45.

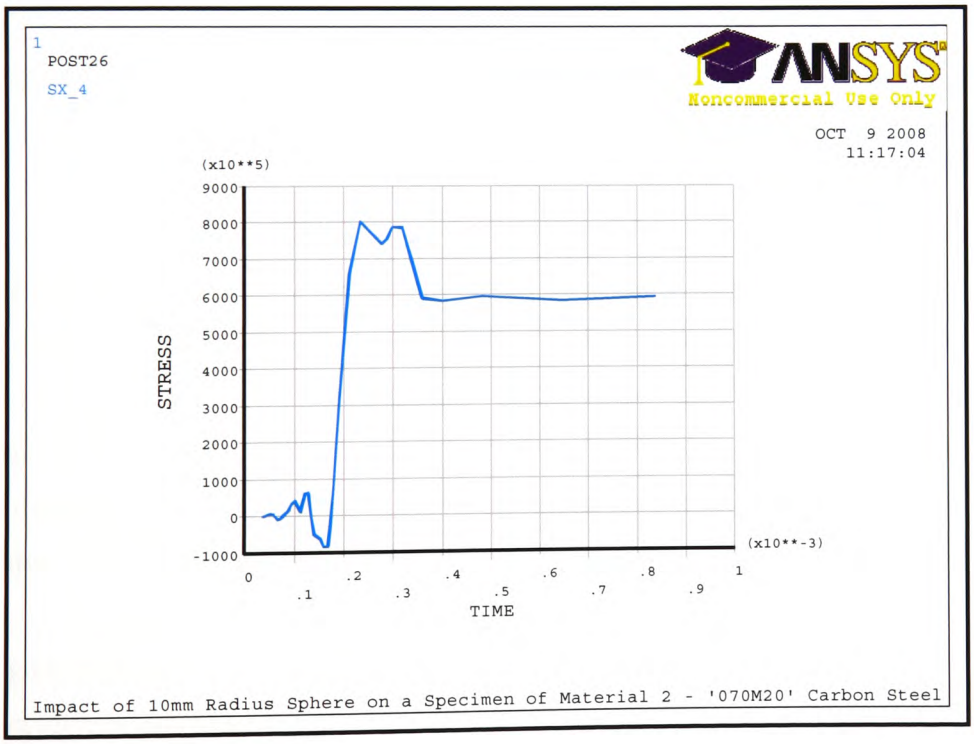

Figure 5.44: Maximum x-directional (tensile) stress recorded (N/m^2), occurring at single nodal position (node 553), over time (seconds)

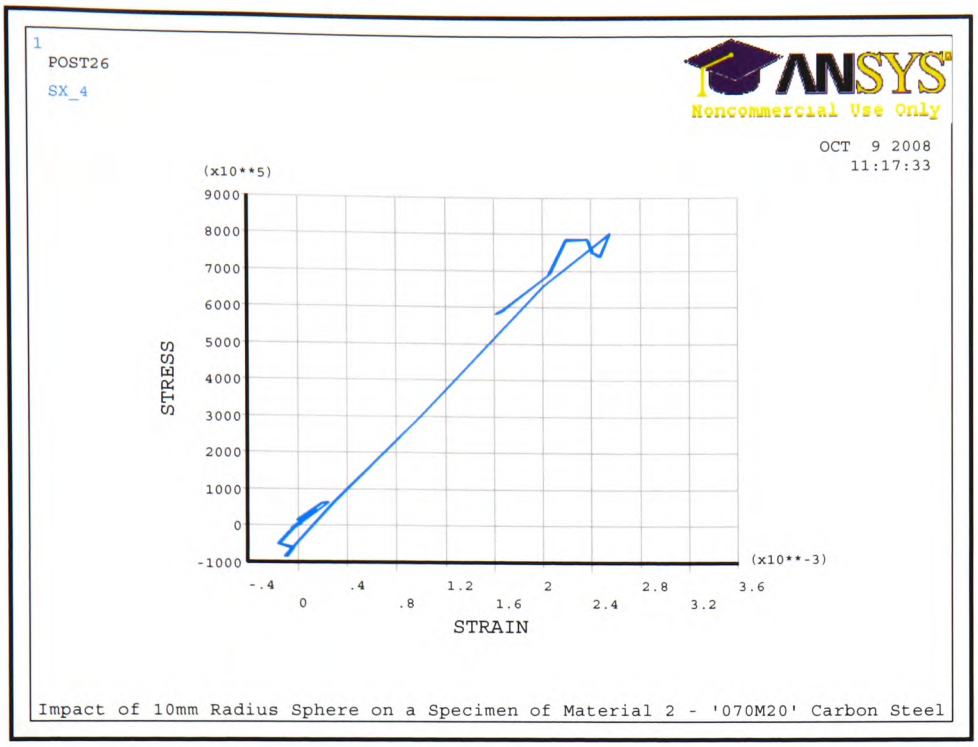

Figure 5.45: Maximum x-directional (tensile) stress recorded (N/m^2), occurring at single nodal position (node 553), against elastic strain

Figure 5.46 shows the residual von-Mises stresses on the impacted side of a specimen which has been impacted with an 11mm radius impactor hammer head and Figure 5.47 shows the underside of the same impacted specimen. The maximum residual von-Mises stress recorded was $597MN/m^2$, which can be seen at the base of the specimen directly under the impact site and also just outside the impact area on the surface of the specimen.

Figure 5.48 shows the residual x-directional stresses on the impacted side of a specimen which has been impacted with an 11mm radius impactor hammer head and Figure 5.49 shows the underside of the same impacted specimen. The maximum residual x-directional stress (tensile) recorded was $588MN/m^2$ at the region of greatest stress concentration, where the cross-sectional area of the specimen is the smallest.

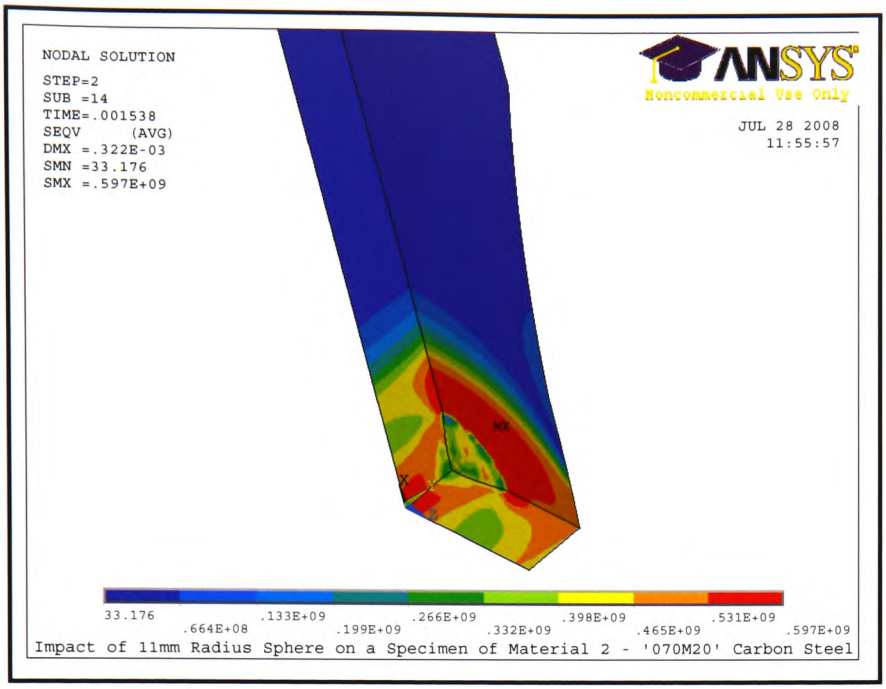

Figure 5.46: Residual von-Mises stresses produced on a specimen of '070M20' carbon steel impacted with a 11mm radius impactor hammer head (top view) - Units are N/m^2

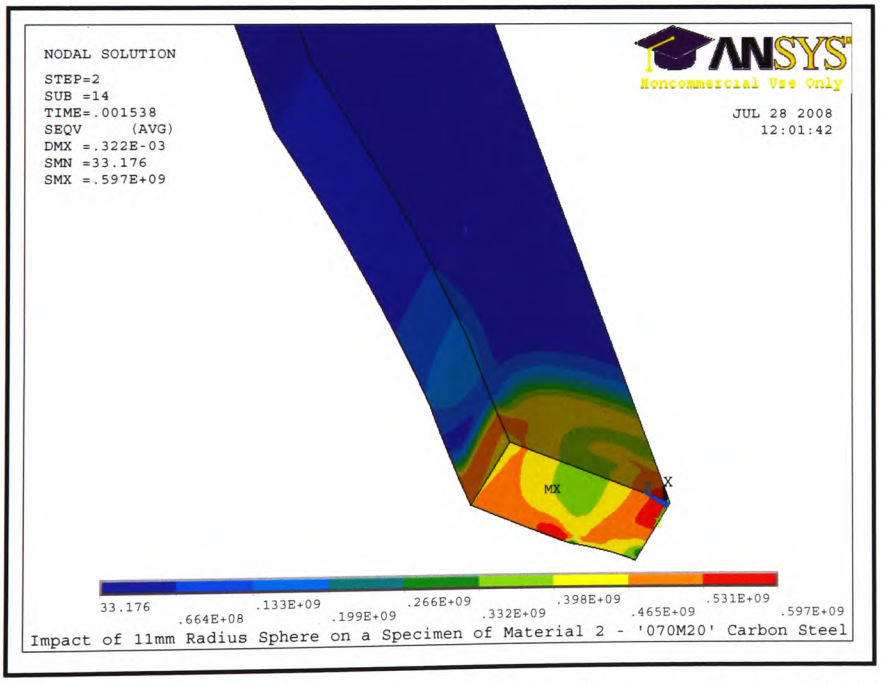

Figure 5.47: Residual von-Mises stresses produced on a specimen of '070M20' carbon steel impacted with a 11mm radius impactor hammer head (bottom view) - Units are N/m^2

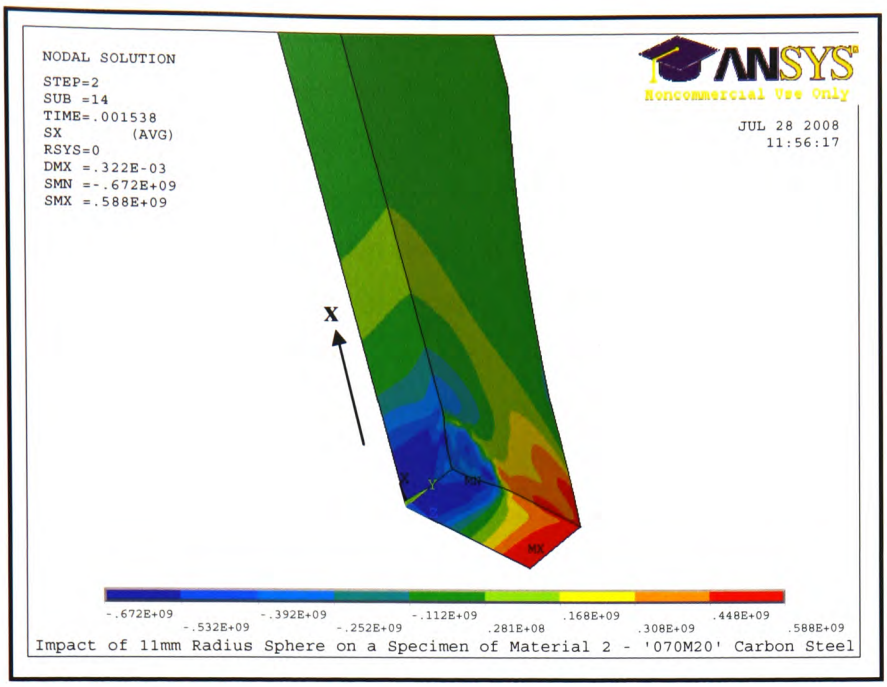

Figure 5.48: Residual x-directional stresses produced on a specimen of '070M20' carbon steel impacted with a 11mm radius impactor hammer head (top view) - Units are N/m^2

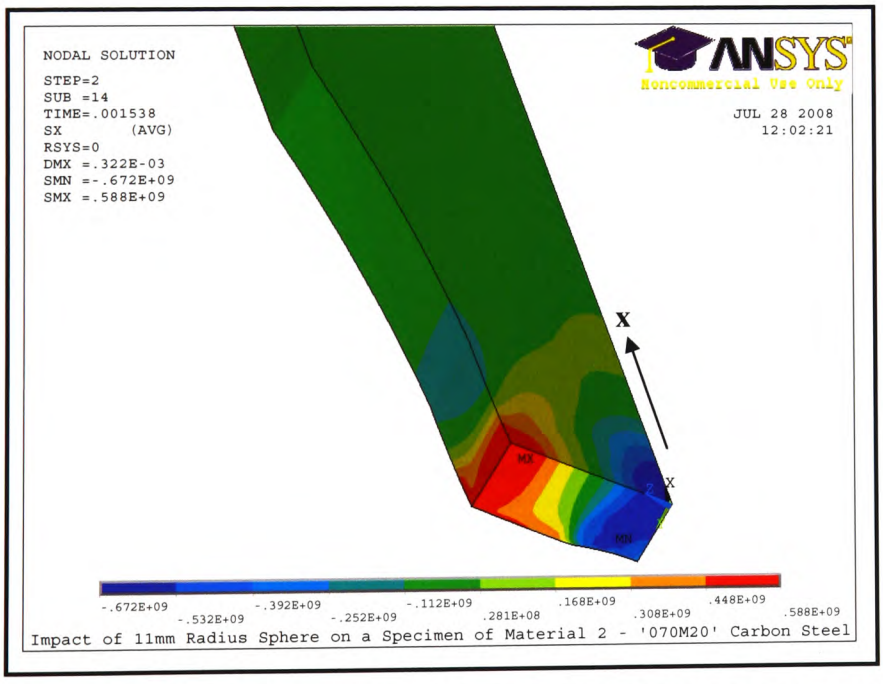

Figure 5.49: Residual x-directional stresses produced on a specimen of '070M20' carbon steel impacted with a 11mm radius impactor hammer head (bottom view) - Units are N/m^2

Figure 5.50 shows the residual von-Mises stresses on the impacted side of a specimen which has been impacted with a 12mm radius impactor hammer head and Figure 5.51 shows the underside of the same impacted specimen. The maximum residual von-Mises stress recorded was 597MN/m^2, which can be seen at the base of the specimen directly under the impact site and also just outside the impact area on the surface of the specimen.

Figure 5.52 shows the residual x-directional stresses on the impacted side of a specimen which has been impacted with a 12mm radius impactor hammer head and Figure 5.53 shows the underside of the same impacted specimen. The maximum residual x-directional (tensile) stress recorded was 589MN/m^2 at the region of greatest stress concentration, where the cross-sectional area of the specimen is the smallest.

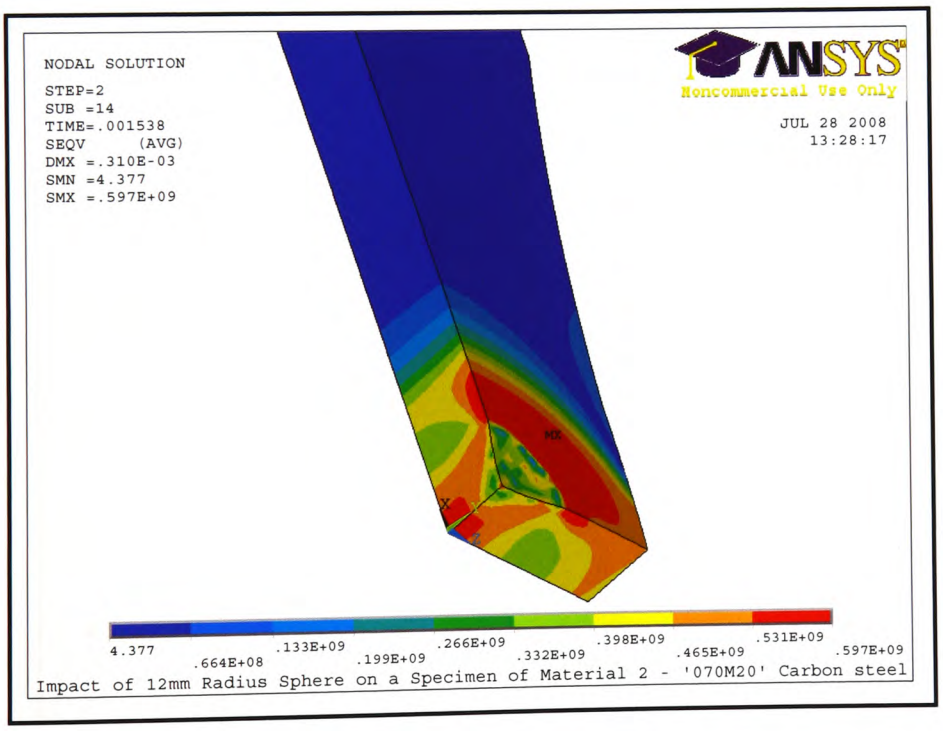

Figure 5.50: Residual von-Mises stresses produced on a specimen of '070M20' carbon steel impacted with a 12mm radius impactor hammer head (top view) - Units are N/m^2

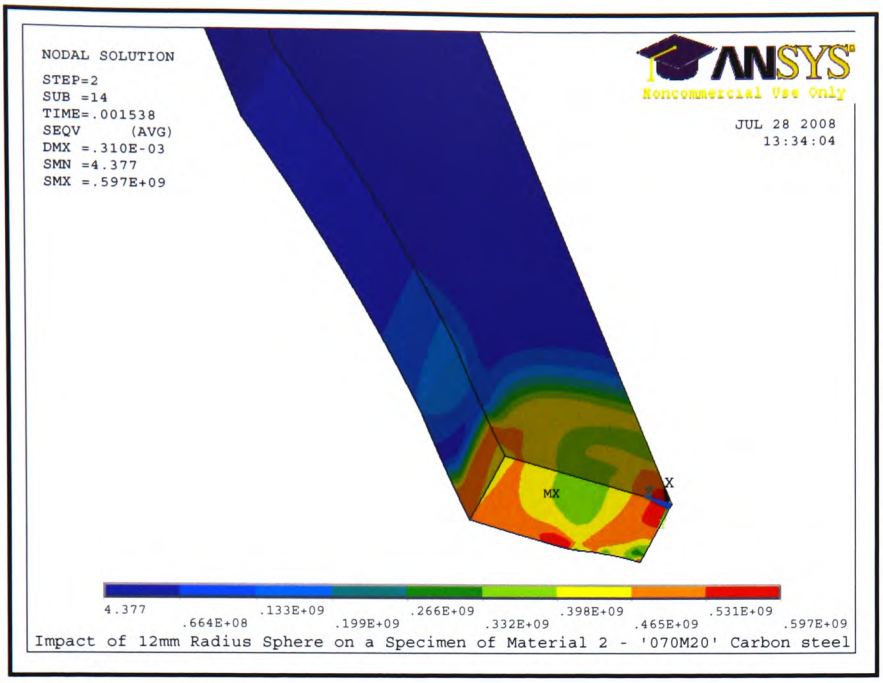

Figure 5.51: Residual von-Mises stresses produced on a specimen of '070M20' carbon steel impacted with a 12mm radius impactor hammer head (bottom view) - Units are N/m^2

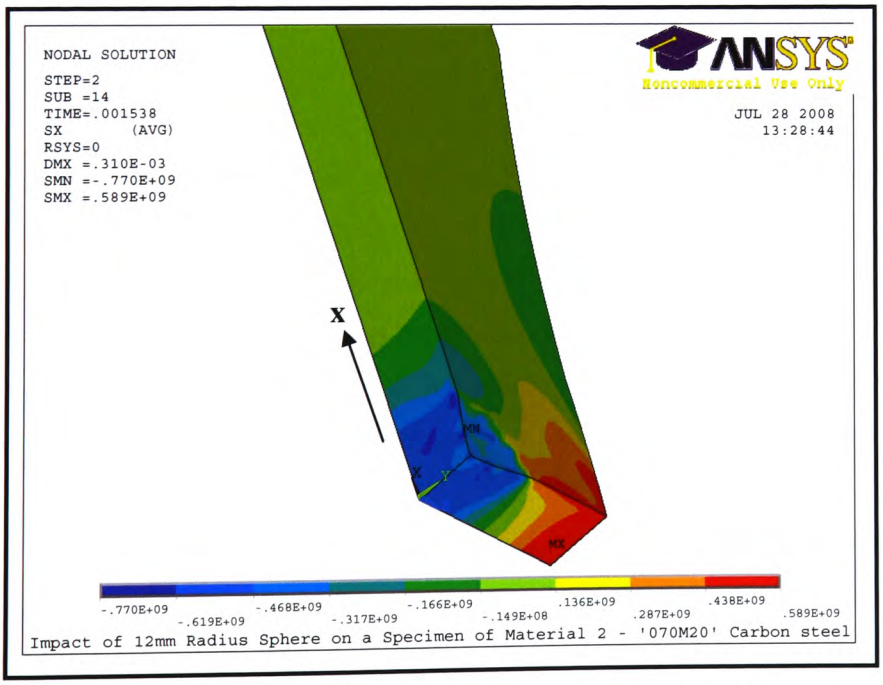

Figure 5.52: Residual x-directional stresses produced on a specimen of '070M20' carbon steel impacted with a 12mm radius impactor hammer head (top view) - Units are N/m^2

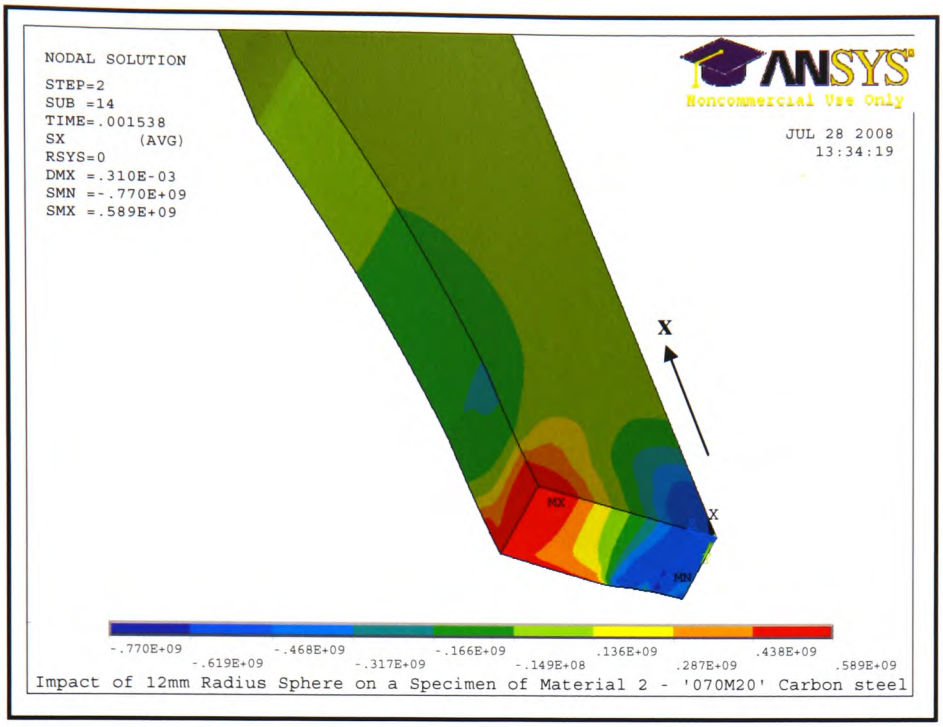

Figure 5.53: Residual x-directional stresses produced on a specimen of '070M20' carbon steel impacted with a 12mm radius impactor hammer head (bottom view) - Units are N/m^2

Figure 5.54 shows the residual von-Mises stresses on the impacted side of a specimen which has been impacted with an 18mm radius impactor hammer head and Figure 5.55 shows the underside of the same impacted specimen. The maximum residual von-Mises stress recorded was $595MN/m^2$, which can be seen at the base of the specimen directly under the impact site and also just outside the impact area on the surface of the specimen.

Figure 5.56 shows the residual x-directional stresses on the impacted side of a specimen which has been impacted with an 18mm radius impactor hammer head and Figure 5.57 shows the underside of the same impacted specimen. The maximum residual x-directional (tensile) stress recorded was $574MN/m^2$ at the region of greatest stress concentration, where the cross-sectional area of the specimen is the smallest.

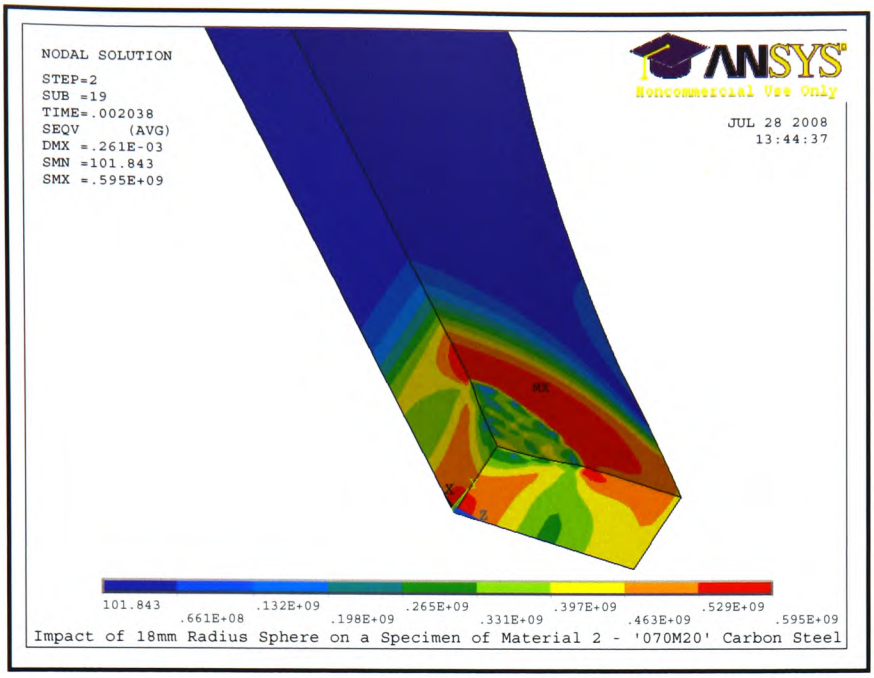

Figure 5.54: Residual von-Mises stresses produced on a specimen of '070M20' carbon steel impacted with a 18mm radius impactor hammer head (top view) - Units are N/m^2

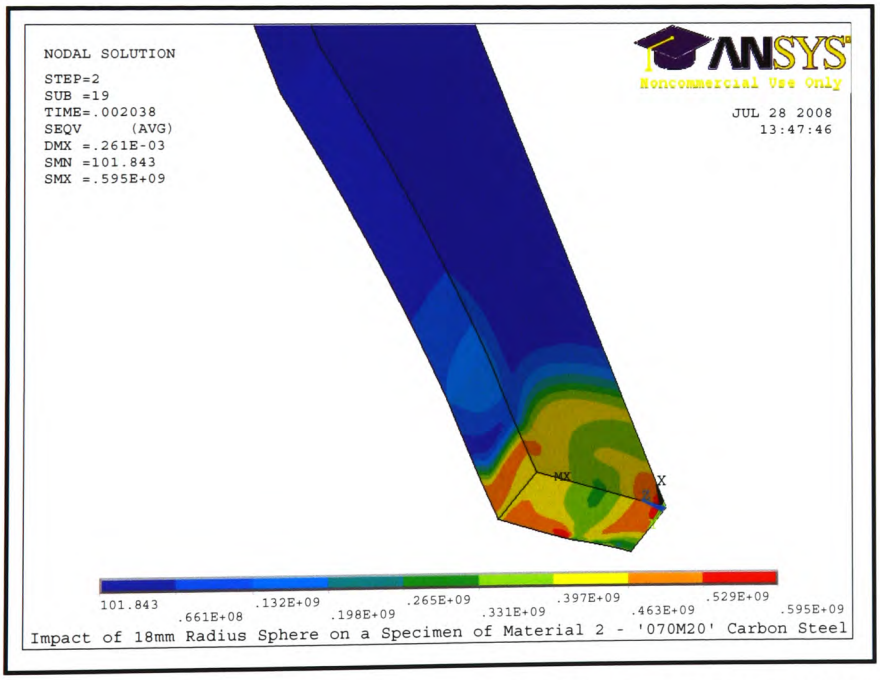

Figure 5.55: Residual von-Mises stresses produced on a specimen of '070M20' carbon steel impacted with a 18mm radius impactor hammer head (bottom view) - Units are N/m^2

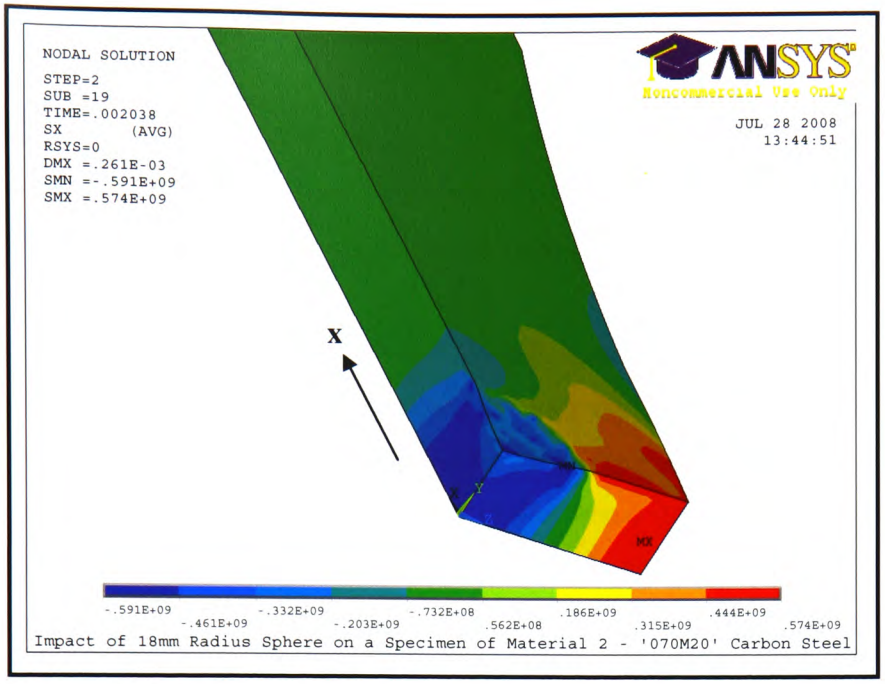

Figure 5.56: Residual x-directional stresses produced on a specimen of '070M20' carbon steel impacted with a 18mm radius impactor hammer head (top view) - Units are N/m^2

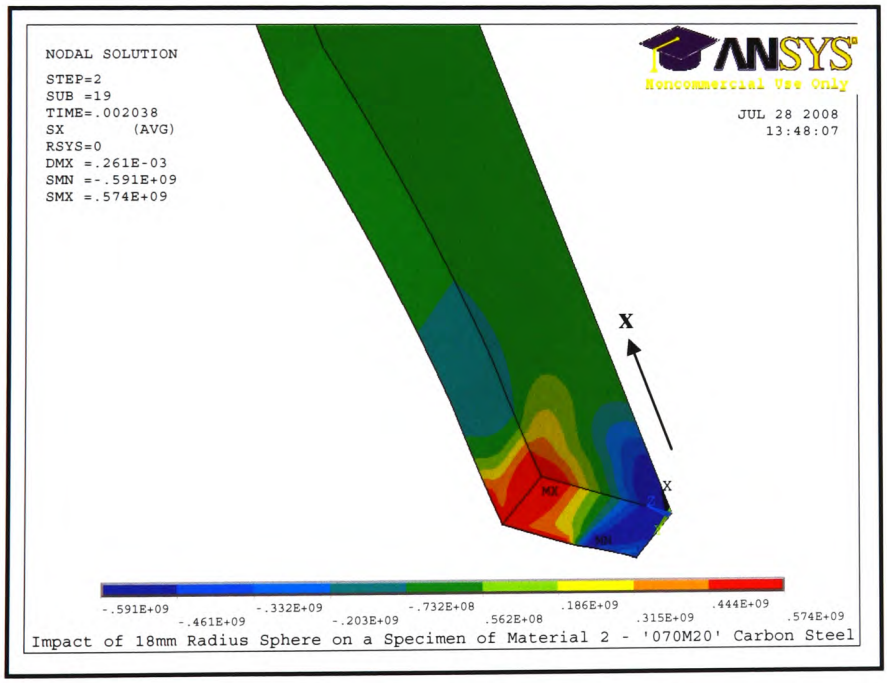

Figure 5.57: Residual x-directional stresses produced on a specimen of '070M20' carbon steel impacted with a 18mm radius impactor hammer head (bottom view) - Units are N/m^2

5. 5 Summary of Numerical Results

Tables 5.10 and 5.11 show a summary of the numerical modelling results for both bending quality bright steel specimen tests and also the '070M20' carbon steel specimen tests, using the various impactor hammer heads sizes modelled.

It can be seen that the residual stress results obtained are very similar due to the congruity of the impactor geometries and the element size used. However, by comparing the results for 10mm and 18mm radius impactor hammer heads only, it can be seen that the maximum residual x-directional (tensile) stress and also the maximum von-Mises stress decrease as the impactor hammer head size increases.

Material Batch	Impactor Hammer Head Radius (mm)	Maximum X Component of Stress - Tensile (MN/m^2)	Maximum von-Mises Stress (MN/m^2)
1) Bending Quality Bright Steel	10	465	454
2) '070M20' Carbon Steel	10	590	597
	11	588	597
	12	589	597
	18	574	595

Table 5.10: Summary of residual stress values obtained from numerical modelling

Material Batch	Impactor Hammer Head Radius (mm)	Entry Velocity of Impact (m/s)	Velocity on Contact (m/s)	Exit Velocity of Impact (m/s)	Coefficient of Restitution	Depth of Impact Crater (mm)	Width of Impact Crater (mm)	Impact Contact Time (seconds)
1) Bending Quality Bright Steel	10	3.11	2.58	0.77	0.248	0.482	6.2	0.000293
2) '070M20' Carbon Steel	10	2.66	2.20	0.93	0.350	0.332	5.6	0.000247
	11	2.66	2.12	0.92	0.346	0.322	5.6	0.000253
	12	2.66	2.12	0.97	0.365	0.310	5.75	0.000239
	18	2.66	1.99	1.04	0.391	0.261	6.2	0.000236

Table 5.11: Summary of numerical results for the various impactor hammer head sizes modelled

Chapter 6: DISCUSSION OF RESULTS

This chapter provides a discussion of the experimental results obtained in Chapter 4, detailing any observations on the possible effect that the size of an impacting object may have on the fatigue life of a specimen. A discussion is also provided on the experimental results obtained for varying heights of impact, in order to determine how the amount of impact energy affects the fatigue life of a specimen. Additionally, the validation of the numerical models carried out in Chapter 5 is discussed, as well as determining links between the fatigue life of a specimen and the residual stresses produced due to impact.

Table 6.1 presents a summary of all the experimental and numerical results obtained for both the bending quality bright steel and also the '070M20' carbon steel specimens, which have been tested with the various sizes of impactor hammer head.

Presented in Table 6.2 are the experimental results obtained from using only the 10mm radius impactor hammer head to impact '070M20' carbon steel specimens at varying heights of impact, in order to determine how the amount of impact energy affects the fatigue life of a specimen.

A summary of the residual stress values obtained from the numerical modelling results is presented in Table 6.3.

Material Batch	Experimental Results												Numerical Results						
	Impactor Hammer Head Radius (mm)	Average Fatigue Life (cycles)	Entry Velocity of Impact (m/s)	Exit Velocity of Impact (m/s)	Coefficient of Restitution	Depth of Impact Crater (mm)	Width of Impact Crater (mm)	Impact Contact Time (secs)	Impact Volume (mm^3)	Entry Impact Energy (J)	Exit Impact Energy (J)	Energy Difference (J)	Entry Velocity of Impact (m/s)	Velocity on Contact (m/s)	Exit Velocity of Impact (m/s)	Coefficient of Restitution	Depth of Impact Crater (mm)	Width of Impact Crater (mm)	Impact Contact Time (secs)
1) Bending Quality Bright Steel	N/A	66,530																	
	10	11,701	3.11	1.02	0.33	0.41	5.00	9.50E-05	5.23	17.08	1.82	15.26	3.11	2.58	0.77	0.248	0.482	6.2	0.000293
2) '070M20' Carbon Steel	N/A	520,822																	
	10	51,070	2.67	0.79	0.30	0.38	5.60	9.04E-05	4.71	12.53	1.09	11.44	2.66	2.20	0.93	0.350	0.332	5.6	0.000247
	11	44,549	2.65	0.81	0.31	0.36	5.75	0.000106	4.70	12.32	1.16	11.16	2.66	2.12	0.92	0.346	0.322	5.6	0.000253
	12	42,812	2.65	0.82	0.31	0.34	5.90	0.000106	4.67	12.34	1.19	11.15	2.66	1.12	0.97	0.365	0.310	5.75	0.000239
	18	49,934	2.68	0.95	0.35	0.25	6.50	0.000107	4.16	12.66	1.59	11.07	2.66	1.99	1.04	0.391	0.261	6.2	0.000236
	25	38,789	2.67	0.96	0.36	0.22	6.80	0.000112	4.00	12.58	1.61	10.97							
	40	48,908	2.64	1.05	0.40	0.18	7.50	0.000119	3.98	12.23	1.95	10.28							

= No results available.

Table 6.1: Summary of numerical and experimental results for the various impactor hammer head sizes tested

Material Batch	Impactor Hammer Head Radius (mm)	Angle of Impactor Hammer Head (degrees)	Height of Impactor Hammer Head (mm)	Average Fatigue Life (cycles)	Entry Velocity of Impact (m/s)	Exit Velocity of Impact (m/s)	Coefficient of Restitution	Depth of Impact Crater (mm)	Width of Impact Crater (mm)	Impact Contact Time (seconds)	Entry Impact Energy (J)	Exit Impact Energy (J)	Energy Diff (J)
'070M20' Carbon Steel	10	90	410	51,070	2.67	0.79	0.30	0.38	5.60	9.04E-05	12.53	1.09	11.44
		67.5	276	73,272	2.04	0.67	0.33	0.28	4.74	9.29E-05	7.35	0.79	6.56
		45	163	181,007	1.42	0.54	0.38	0.19	3.93	1.01E-04	2.96	0.42	2.54
		22.5	87	487,446	0.78	0.35	0.45	0.10	3.05	1.18E-04	1.08	0.22	0.86

Table 6.2: Summary of specimen test results for varying impact heights

Material Batch	Impactor Hammer Head Radius (mm)	Maximum von-Mises Stress (MN/m^2)	Maximum Tensile Stress (X Component) (MN/m^2)
1) Bending Quality Bright Steel	10	454	465
2) '070M20' Carbon Steel	10	597	590
	11	597	588
	12	597	589
	18	595	574

Table 6.3: Summary of residual stress values obtained from numerical modelling

6.1 Discussion of Experimental Results

In the case of Material 1, 'Bending Quality Bright Steel', a single impact with a 10mm radius impactor hammer head lowered the average fatigue life by 82.4%, but increased the average range of standard deviations over which failure could occur by 6.13%. In the case of Material 2, '070M20 Carbon Steel', a single impact with any of the sizes of impactor hammer head tested, (10mm, 11mm, 12mm, 18mm, 25mm or 40mm radius), was again seen to lower the average fatigue life of the specimen, in this case by 91.17%. The maximum average percentage reduction of 92.55% was noted to be for single impacts with the 25mm radius impactor hammer head and the minimum average percentage reduction of 90.19% for single impacts was with the 10mm radius impactor hammer head, as shown in Table 6.4. However, the average range of standard deviations over which failure could occur was found to decrease for specimens of '070M20' carbon steel by 18.36%. Therefore, the experimental results show that a single impact with any of the sizes of impactor hammer head tested, at the

chosen impact energies for this study, lowers the fatigue life of the specimen in both materials. Depending on the hardness of the material, the range of cycles over which the failure can occur may vary, as the average range of standard deviations was found to decrease for the softer specimens of '070M20' carbon steel and increase for the harder specimens of bending quality bright steel. It should also be noted that there was very little variation between the fatigue test results for the '070M20' carbon steel specimens impacted with the various sizes of impactor hammer head, indicating that although a single impact will decrease the fatigue strength of a specimen, the size of impactor used has little effect at the chosen impact energy used in this study. It is felt that the reduction in fatigue life is due to the residual stresses imparted in the specimen resulting from the impact. This hypothesis will be discussed further in Section 6.2, 'Discussion of Numerical Results'.

Impactor Hammer Head Radius (mm)	**Percentage Reduction in Fatigue Life (%)**
10	90.19
11	91.45
12	91.78
18	90.41
25	92.55
40	90.61

Table 6.4: Percentage reduction in fatigue life of specimens of '070M20' carbon steel due to a single impact with various sizes of impactor hammer head

The experimental results for the '070M20' carbon steel specimens show that as the size of the impactor hammer head increased, the exit velocity, COR, exit impact energy and the contact time of impact also increased. This indicates that less energy is absorbed by the specimen on impact as the size of the impactor hammer head increases. The depth of impact crater was found to decrease with an increase in the size of the impactor hammer head and, correspondingly, the width of impact was noted to increase. Research previously discussed in Chapter 2, on the 3D numerical model of shot peening carried out by ElTobgy et al. (2004) using shot of up to 0.5mm in radius, agrees with the trends shown for the depth and width of impact crater. It is possible to use the graphical information obtained from the experimental results to make predictions for any size of impactor hammer head with a radius between 10mm and 40mm at the impact energy chosen for this study. The experimental results also show that subjecting a specimen to a single impact with any size impactor hammer head radius between 10mm and 40mm, does not affect the hardness of the material.

It was decided to extend the experimental programme to determine how the amount of impact energy would affect the fatigue life of a specimen of '070M20' carbon steel. Using only the 10mm radius impactor hammer head, the same procedures were followed as in the original experimental programme. However, for these tests the height of the impactor hammer head was adjusted, thus altering the amount of impact energy imparted onto the specimen. Previously in the experimental programme tests were carried out at 410mm (impact energy of 12.53J). The follow-on tests were conducted at 276mm (7.35J), 163mm (2.96J), and 87mm (1.08J).

It was found that subjecting a specimen to a single impact from a height of 87mm will lower the average fatigue life of the specimen by 6.4% when compared with non-impacted control specimens, and also decrease the average range of standard deviations over which failure could occur by 13.03%. By comparing the fatigue results for the impacted specimens alone, it can be seen that the greater the height of the impact, and therefore the higher the impact

energy, the lower the fatigue life of the specimen becomes. Increasing the height of the impactor hammer head from 87mm to 410mm can lower the average fatigue life of the specimen by 89.5% and, additionally, the average range of standard deviations over which failure can occur is decreased by 1.88%. The graphical trends produced make it possible to predict other rates of failure for all impact heights between 0mm and 410mm.

It was noted that as the height of impact increased, thus increasing the impact energy, the exit velocity, depth of impact crater, width of impact crater, and the exit energy also increased. It is also noted that more energy is absorbed by the specimen on impact as the height of the impactor hammer head increases, as shown in Table 6.5. The COR and also the impact contact time were found to decrease with an increase in impact height, showing that the higher the impact energy the less plastic the material becomes. It is possible to use the graphical information obtained from the experimental results to make predictions for any height of impact between 87mm and 410mm.

Height of Impactor Hammer Head (mm)	**Entry Impact Energy (J)**	**Exit Impact Energy (J)**	**Percentage of Entry Impact Energy Lost During Impact (%)**
410	12.53	1.09	91.3
276	7.35	0.79	89.2
163	2.96	0.42	85.8
87	1.08	0.22	79.6

Table 6.5: Percentage of entry impact energy lost during impact

6.2 Discussion of Numerical Modelling Results

The numerical modelling results for both the materials modelled, namely bending quality bright steel and '070M20' carbon steel, were found to compare very favourably with the experimental results obtained. In the case of the '070M20' carbon steel specimens, it is possible to see that the numerical results follow the same trends as the experimental results, with a maximum percentage difference between the results of 18.3%, which was for the exit velocity of impact, and a minimum percentage difference of 0% for the width of impact crater, as shown in Table 6.6. However, it was found that the experimental results for the impact contact time did not compare favourably with the numerical results, which is possibly because the mounting of the accelerometer may have not been adequate and has therefore produced erroneous results, as discussed in Section 5.4.1.

Parameter Measured	**Percentage Difference between Numerical and Experimental Results (%)**			
	Radius Size of Impactor Hammer Head			
	10mm	11mm	12mm	18mm
Exit Velocity of Impact	17.7	13.6	18.3	9.5
Coefficient of Restitution	16.7	11.6	17.7	11.7
Depth of Impact Crater	12.6	10.6	8.8	4.4
Width of Impact Crater	0	2.6	2.5	4.6

Table 6.6: Percentage difference between numerical and experimental results

The residual stress contours produced by the numerical models are very smooth, indicating that the element size generated was more than adequate for this study. However, some errors may occur due to the element size used, for instance, if the element size is too coarse, it would not be possible to exactly measure the width of impact crater produced. The numerical modelling results would represent the experimental results far more accurately if the mesh generated in the numerical models was finer. However, due to the constraints of the ANSYS package used this was not possible, as the number of nodes generated for this study is very close to the maximum limit of the package.

As non-linear transient numerical models were produced for this study, it is also possible that complications may occur with the numerical stability and non-linearity of the material. ANSYS uses the Newton-Raphson method to solve non-linear transient analysis problems. This method is an iterative process of solving non-linear equations, as illustrated in Figure 6.1 on a load versus displacement curve, where each peak represents a separate stiffness update iteration within each load step. The load is applied in incremental steps and the program performs equilibrium iterations at each time step, repeating these iterations until the problem converges. If the load steps are too large, the error may not be reduced and convergence will fail. Conversely, if the steps are too small the solution may take an excessive amount of time to converge. Equation 6.1 shows the time step equation used in the analyses, which is dependant on both the number of elements generated across the width of the specimen and also the elastic wave propagation speed, detailed in equation 6.2. Convergence of the problem and the accuracy of the results would therefore be improved by increasing the number of elements generated across the width of the specimen, which would in turn increase the time step increment.

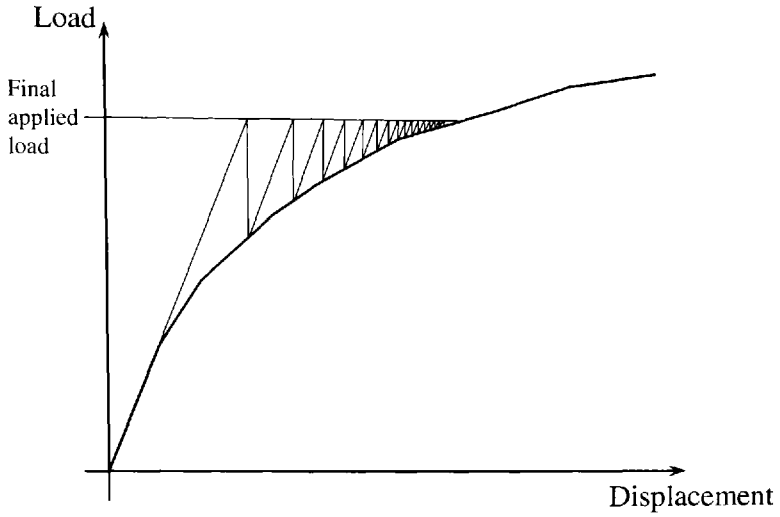

Figure 6.1: Newton Raphson method

$$TEL = \frac{NoE}{CVEL} \tag{6.1}$$

where TEL = time step increment

NoE = number of elements along width of specimen

CVEL = elastic wave propagation speed

$$CVEL = \sqrt{\frac{E}{\rho}} \tag{6.2}$$

where CVEL = elastic wave propagation speed

E = Young's Modulus of specimen material

ρ = density of specimen material

The slight discrepancies between the numerical and the experimental results could also be due to the fact that the numerical models produced do not consider the strain rate effects in the materials. With a strain rate dependant material, the material will deform differently at high speed impacts than at low speed impacts. Cunningham (2007) discusses several cases and how the strain rate of the material can affect numerical results. For instance, in one case study mentioned, Rolls Royce were carrying out a shaft buckling test to establish the ultimate torsional capability of a shaft and found that the numerical model was over-predicting the failure torque by as much as 15%. Another case was described where the numerical model predicted a deformation to be 61mm, but after taking into account the effects of strain rate this was reduced to 29mm, which compared well with a deformation of 30mm that was found experimentally. Therefore, to enhance the accuracy of the results of the numerical model, it may be necessary to consider strain rate effects of the material. However, due to time constraints, this was not a consideration for this research. The effect of strain rate can be taken into account when writing the numerical model by incorporating the Cowper-Symonds, model which describes the relationship of dynamic stress to strain rate using equation 6.3, (MacDonald, 2007).

$$\text{Stress}, \sigma = \sigma_y \left[1 + \left(\frac{\dot{\varepsilon}}{C} \right)^{\frac{1}{p}} \right] \qquad (6.3)$$

where

$\dot{\varepsilon}$ = strain rate

C and P = the Cowper-Symonds strain rate parameters

σ_y = uniaxial yield stress

For both of the materials modelled, the regions of high tensile residual stress were shown to be just outside the crater that had been produced by the impactor hammer head and also at the region of greatest stress concentration, where the cross-sectional area of the specimen is the smallest. It was noted in Section 4.8, 'Macrostructure of Fatigue Cracks', and also illustrated in Figure 4.48, that this region of greatest stress concentration is where the origin of failure occurs during fatigue testing. With such a high intensity of residual tensile stresses in this area, it is inevitable that the fatigue life of the specimen will be reduced. The presence of residual tensile stresses outside the area of impact is in agreement with research carried out by Peters et al. (2002), where it was noted that spherical impacts on a specimen of aluminium alloy produced tensile residual stresses at a distance from the impact site. Finite element analysis on the repeated indentation of a half-space by Kral et al. (1993) noted that in non-hardened materials, a spherical band of tensile hoop stress was produced on the surface of the half-space outside the impact crater, which also compares well with the numerical results produced in the current study.

From the numerical modelling results for the '070M20' carbon steel, it can be seen that for both the residual von-Mises and also the residual tensile stresses, the results obtained are very similar, which is possibly due to the congruity of the impactor hammer head geometries and the element size used. However, by comparing the results for 10mm and 18mm radius impactor hammer heads only, it can be seen that the maximum residual tensile stress and also the maximum von-Mises stress decrease as the impactor hammer head size increases. Thus, the greater the depth and, therefore, the smaller the width of the impact crater produced, then the greater the residual stresses produced in the impacted specimen.

When comparing the experimental and numerical results it can be seen that a single impact, with any size radius impactor hammer head between 10mm and 40mm, causes a reduction in the fatigue life of a specimen, but the size of the impactor used does not affect the amount of reduction in fatigue life, or the size

and extent of the residual stresses produced. However as previously mentioned, the residual stresses produced in the specimens are very similar in size and profile. Therefore, it can be deduced that in this study, the reduction in fatigue life of a specimen is actually due to the energy of the impact and the residual stresses produced in the specimen. Accordingly, a specimen subjected to a single impact with any size radius impactor hammer head between 10mm and 40mm, at the chosen impact energy for this study, will cause a normalisation in the residual stresses produced and also in the reduction of the fatigue life of the specimen.

Chapter 7: CONCLUSIONS AND FURTHER WORK

This chapter contains a summary of the research project, accompanied by the major conclusions from the study. The limitations of the present work are identified and suggestions for further work are also made.

The aim of the research was to investigate the effect of a single impact on the fatigue life of steel. A component subjected to a single impact may have not only noticeable surface damage but also residual stresses in the surface and subsurface layers. These residual stresses may improve or possibly reduce the fatigue life of the component. The objectives of the research were, therefore, to investigate what effect the size of an impacting object has on the fatigue life of a specimen and also to evaluate experimentally the amount of single impact energy required to affect the fatigue life of specimens. Furthermore, numerical models were developed, which were used to show the surface and subsurface residual stresses produced as a result of the impact.

The specimens used in the experimental programme were made from two different types of cold-rolled, mild steel strip. The first material tested was Bending Quality Bright Steel (BS1449), and the second material was '070M20' Carbon Steel (BS970). The materials were chosen as they are both types of mild steel which are easily obtainable and widely used in the manufacture of many engineering components.

To investigate what effect the size of an impacting object has on the fatigue life of a specimen, the hammer heads were produced in six sizes; 10mm, 11mm, 12mm, 18mm, 25mm and 40mm radii. However, due to limitations on material availability, it was only possible to carry out tests using the 10mm radius impactor hammer head on Material 1. In the case of this material, 'Bending Quality Bright Steel', a single impact with a 10mm radius impactor hammer head lowered the average fatigue life by 82.4%, but increased the average range of standard deviations over which failure could occur by 6.13%. In the case of

Material 2, '070M20 Carbon Steel', a single impact with any of the sizes of impactor hammer head tested, (10mm, 11mm, 12mm, 18mm, 25mm or 40mm radius), can again be seen to lower the average fatigue life of the specimen, in this case by 91.17%. However, the average range of standard deviations over which failure could occur was found to decrease by 18.36%. Therefore, the experimental results show that a single impact with any of the sizes of impactor hammer head tested, at the chosen impact energies for this study, will lower the fatigue life of the specimen in both materials. It should also be noted that there was very little variation between the fatigue test results for specimens impacted with the various sizes of impactor hammer head, indicating that whilst an impact will decrease the fatigue strength of a specimen, the size of impactor head used has little effect, at the impact energies used in this study. Depending on the hardness of the material, the range of cycles over which the failure can occur may vary, as the range of standard deviations was found to decrease for the softer specimens of '070M20' carbon steel and increase for the harder specimens of bending quality bright steel.

In order to determine how the amount of impact energy affects the fatigue life of a specimen of '070M20' carbon steel, the height of the impactor hammer head was adjusted, thus altering the amount of impact energy imparted into the specimen. These tests were conducted using the 10mm radius impactor hammer head at impact heights of 276mm, 163mm and 87mm, and compared with the experimental results previously obtained from specimens impacted at an impact height of 410mm. It can be seen that the greater the height of the impact, and therefore the higher the impact energy, then the lower the fatigue life of the specimen. Increasing the height of the impactor hammer head from 87mm to 410mm, can lower the average fatigue life of the specimen by approximately 89.5%. Also, the average range of standard deviations over which failure can occur is reduced by approximately 1.88%.

The results produced by the numerical models were compared with the experimental data for '070M20' carbon steel specimens that had been subjected

to a single impact. The results produced by the numerical models do follow the same trends as the experimental results, and the maximum percentage difference recorded between the numerical and experimental results was 18.3%.

Regions of high residual tensile stress were shown to be just outside the crater produced by the impactor hammer head and also at the region of greatest stress concentration, where the cross-sectional area of the specimen is the smallest. From the experimental work it was also noted that failure of the specimens during the fatigue tests initiated at the region of greatest stress concentration.

It was also found that the residual von-Mises and x-directional tensile stresses were found to decrease as the impactor hammer radius size increases. Thus, the greater the depth and the smaller the width of the impact crater produced, the greater the residual stresses produced in the impacted specimen.

It has previously been noted that the size of the impactor hammer head does not have an effect on the fatigue life of an impacted specimen. However, as the fatigue life of a specimen is considerably lowered due to a single impact, it can be said that this is due to the presence of residual stresses resulting from the impact. For both of the materials modelled, a single impact at the chosen impact energy will impart residual stresses in the specimen, which in turn causes a normalisation in the reduction in the fatigue life of the specimen, as well as the residual stresses produced.

Determining the effect of the size and energy of an indenter on the fatigue life of the component could be used in many engineering applications; such as shot peening, aircraft structures and components, boat propellers, car body panels and parts, and numerous other applications in which a metal structure or component may be subjected to an impact. With accurate material properties a numerical model can be used as an aid in determining the state of residual stress before the application of fatigue load.

7.1 Recommendations for Future Research

Considerations in future research would be to ensure that when developing a numerical model, a very fine mesh is used in the area of impact, and also that strain rate effects are considered. The current study could be developed further by carrying out analyses to determine how a variation in impact velocity, and therefore impact energy, would affect the residual stresses induced in the specimen, and correlations could be made with the experimental results discussed in this study.

One recommendation when carrying out studies similar to this in the future would be to run preliminary numerical models, to ascertain the level of the residual stresses at the chosen impact energy, to ensure that only the effect of the impactor size and shape on the fatigue life of the specimen is determined.

Finally, future experimental work could investigate the effect of different shapes of impactor, such as conical or cuboid, on the fatigue life of materials. Varying the thickness and material type of a specimen could also be considered, as well as the effect of multiple impacts at the same impact location.

REFERENCES

BS 3518: Part 1: 1993. "Methods of Fatigue Testing – Part 1: Guide to General Principles". British Standards and Institution.

BS 3518: Part 3: 1963. "Methods of Fatigue Testing – Part 3: Direct Stress Fatigue Tests". British Standards and Institution.

Adams, V. and Askenazi, A. (1999). Building Better Products with Finite Element Analysis. Santa Fe, USA, OnWord Press.

Bailey, F. W. J. (1964). Fundamentals of Engineering Metallurgy, Cassell, London.

Baragetti, S. (2001). "Three-dimensional Finite-element Procedures for Shot Peening Residual Stress Field Prediction." International Journal of Computer Applications in Technology **14**(1/2/3): 51-63.

Bell, R. A. (1984). "Shot Peening Techniques for Greater Fatigue Life in Springs." Springs **23**(2): 61-63.

Bertke, R. S. and Barber, J. P. (1979). Impact Damage on Titanium Leading Edges from Small Soft Body Objects, Air Force Materials Laboratory, Wright Patterson Air Force Base, Ohio.

Bird, G. C. and Saynor, D. (1986). "The Effect of Peening Shot Size on the Performance of Carbon Steel Springs." Springs **25**(2): 69-79.

Boyce, B. L., Chen, X., Hutchinson, J. W. and Ritchie, R. O. (2001). "The Residual Stress State due to a Spherical Hard-Body Impact." Mechanics of Materials **33**(8): 441-454.

Boyce, B. L., Chen, X., Peters, J. O., Hutchinson, J. W. and Ritchie, R. O. (2003). "Mechanical Relaxation of Localised Residual Stresses Associated with Foreign Object Damage." Materials Science and Engineering A **349**(1-2): 48-58.

Brickwood, R. (2002). "The Benefits of Shot Peening." Surface World **9**(6): 30.

Bulat, V. and Majid, L. (1985). Experimental Determination of Factor Affecting Load Imposed on Propellers in Ice, Transport Canada.

Chen, X. and Hutchinson, J. W. (2001). "Foreign Object Damage and Fatigue Crack Threshold: Cracking Outside Shallow Indents." International Journal of Fracture **107**: 31-51.

Chen, X. and Hutchinson, J. W. (2002). "Particle Impact on Metal Substrates with Application to Foreign Object Damage." Journal of the Mechanics and Physics of Solids **50**(12): 2669-2690.

Chen, X. (2005). "Foreign Object Damage on the Leading Edge of a Thin Blade." Mechanics of Materials **37**: 447-457.

Chernuka, M. W., Jateganonkar, R. P., Norwood, M. E. and Warner, J. L. (1989). Development of a Procedure for Predicting Propeller-Ice Interaction Forces, Transportation Development Centre Policy and Coordination Group, Transport Canada.

Cochennec, F., Rouhaud, E., Retraint, D., Rouquette, S. and Roos, A. (2006). "Analysis of the Impact of a Shot at Low Velocity using the Finite Element Method. Application to the Ultrasonic Shot-Peening Process." Residual Stresses VII **524-525**: 337-342.

Cunningham, J. (2007). Simulation makes Big Savings. Professional Engineering. **20:** 39-40.

Diepart, C. P. (1993). Modelling of Shot Peening Residual Stresses - Practical Applications. Materials Science Forum - 2nd ASM Heat Treatment and Surface Conference.

Duo, P., Liu, J., Golshan, M. and Korsunsky, A. M. (2007). "Evaluation and Analysis of Residual Stresses due to Foreign Object Damage." Mechanics of Materials **39**(3): 199-211.

ElTobgy, M. S., Ng, E. and Elbestawi, M. A. (2004). "Three-dimensional Elastoplastic Finite Element Model for Residual Stresses in the Shot Peening Process." Proceedings of the Institution of Mechanical Engineers - B Journal of Engineering Manufacture **218**(11): 1471-1481.

Farrahi, G. H., Lebrun, J. L. and Couratin, D. (1995). "Effect of Shot Peening on Residual Stress and Fatigue Life of a Spring Steel." Fatigue and Fracture of Engineering Materials and Structures **18**(2): 211-220.

Faulkner, A., Tang, K. C., Sen, S. and Arnell, R. D. (1998). "Finite Element Solutions Comparing the Normal Contact of an Elastic Plastic Layered Medium Under Loading by (a) a Rigid and (b) a Deformable Indenter." Journal of Strain Analysis for Engineering Design **33**(6): 411-418.

Firmin, T. and Saadetian, H. (1994). Using Ansys and Adams to Assist in the Prediction of Fatigue. International Conference on Fatigue.

Frija, M., Hassine, T., Fathallah, R., Bouraoui, C. and Dogui, A. (2006). "Finite Element Modelling of Shot Peening Process: Prediction of the Compressive Residual Stresses, the Plastic Deformations and the Surface Integrity." Materials Science and Engineering A **426**(1-2): 173-180.

Glaeser, W. A. (1999). "Failure Mechanisms of Reed Valves in Refrigeration Compressors." Wear **225-229**(2): 918-924.

Gillespie, B. and Fowler, D. B. (1992). "Evaluation of Size and Shape of Shot Peening Media by Image Analysis." SAE Transactions **100**(1/2): 28-39.

Goldsmith, W. and Lyman, P. T. (1960). "The Penetration of Hard-Steel Spheres into Plane Metal Surfaces." ASME Journal of Applied Mechanics **27**: 717-725.

Gordon, R. and Franklin, K. (2006). Finite Element Simulation of an Ice Axe Pick Impact on a Semi-Rigid Surface. The Engineering of Sport, Munich, Germany, Springer Verlag.

Guagliano, M. and Vergani, L. (2004). "An Approach for Prediction of Fatigue Strength of Shot Peened Components." Engineering Fracture Mechanics **71**(4-6): 501-512.

Haake, S. J., Blackwood, W. D. and Yoxall, A. (1997). Photoelastic Analysis of Ice-Axe Impacts. SPIE The International Society for Optical Engineering.

Hammersley, G. (1999). "Laser Shot Peening Comes out of the Lab." Material World **7**(5): 281-282.

Hara, O. (1992). "Taking a Shot at Stress Reduction." Process Engineering **73**(10): 41-42.

Hardy, C., Baronet, C. N. and Tordion, G. V. (1971). "The Elasto-Plastic Indentation of a Half Space by a Rigid Sphere." International Journal for Numerical Methods in Engineering **3**: 451-462.

Her, S. C. and Liang, Y. C. (2004). "The Finite Element Analysis of Composite Laminates and Shell Structures to Low Velocity Impact." Composite Structures **66**: 277-285.

Hills, D. A., Waterhouse, R. B. and Noble, B. (1983). "An Analysis of Shot Peening." Journal of Strain Analysis **18**(2): 95-100.

Hosseinzadeh, R., Shohrieh, M. M. and Lessard, L. (2006). "Damage Behaviour of Fiber Reinforced Composite Plates subjected to Drop Weight Impacts." Composites Science and Technology **66**: 61-68.

Hughes, D. A. (1992). Analysis of Bird Impact on Fan Blade Leading Edges. Engineering Science. Oxford, Oxford University.

Hughes, D. A., Ruiz, C. and Martindale, I. (1994). "Application of High-Strain-Rate Material Testing to the Study of Impact." Journal de Physique IV **4**: 565-570.

Iguchi, H., Tanaka, K. and Taira, S. (1979). "Failure Mechanisms in Impact Fatigue of Metals." Fatigue of Engineering Materials and Structures **2**(2): 165-176.

Johnson, K. L. (1999). Contact Mechanics, Cambridge University Press.

Kaiser, B. (1987). "The Effect of Shot Peening on the Fatigue Strength of Spring Elements." Springs **26**(2): 59-65.

Kawagoishi, N., Nagano, T., Moriyama, M. and Kondo, E. (2007). "Improvement of Fatigue Strength of Maraging Steel by Shot Peening." Fracture and Damage Mechanics VI **348-349**: 537-540.

Kim, H. and Kedward, K. T. (2000). "Modelling Hail Impacts and Predicting Impact Damage Initiation in Composite Structures." AIAA Journal **38**(7): 1278-1288.

Kirk, D. (1999). "Shot Peening." Aircraft Engineering and Aerospace Technology **71**(4): 349-361.

Kobayashi, M., Matsui, T. and Murakami, Y. (1998). "Mechanism of Creation of Compressive Residual Stress by Shot Peening." International Journal of Fatigue **20**(5): 351-357.

Kral, E. R., Komvopoulos, K. and Bogy, D. B. (1993). "Elastic-Plastic Finite Element Analysis of Repeated Indentation of a Half-Space by a Rigid Sphere." ASME Journal of Applied Mechanics **60**: 829-841.

Lawerenz, M. (1991). "Optimum Shot Peening Specification." Gear Technology **8**(6): 15-22.

Levers, A. and Prior, A. (1998). "Finite Element Analysis of Shot Peening." Journal of Materials Processing Technology **80-81**: 304-308.

Li, L. Y., Wu, C. Y. and Thornton, C. (2000). "Impact Behaviour of Elastoplastic Spheres with a Rigid Wall." Proceedings of the Institution of Mechanical Engineers - C Journal of Mechanical Engineering Science **214**(C8): 1107-1114.

MacDonald, B. J. (2007). Practical Stress Analysis with Finite Elements. Dublin, Glasnevin Publishing.

Mann, J. Y. (1967). Fatigue of Materials - An Introductory Text, Melbourne University Press.

Martin, N. F. (1990). "Nonlinear Finite-Element Analysis to Predict Fan-Blade Damage Due to Soft-Body Impact." AIAA Journal of Propulsion and Power **6**(4): 445-450.

Martinez, C. M., Eylon, D., Nicholas, T., Thompson, S. R., Ruschau, J. J., Birkbeck, J. and Porter, W. J. (2002). "Effects of Ballistic Impact Damage on

Fatigue Crack Initiation in Ti-6Al-4V Simulated Engine Blades." Materials Science and Engineering - A - Structural Materials **325**(1-2): 465-477.

Meo, M. and Vignjevic, R. (2003). "Finite Element Analysis of Residual Stress Induced by Shot Peening Process." Advances in Engineering Software **34**(9): 569-575.

Mitsubayashi, M., Takashi, M. and Aihara, A. (1994). "Phenomenal Analysis of Shot Peening: Analysis of Fatigue Strength by Fracture Mechanics for Shot Peened Steel." JSAE Review **15**(1): 67-71.

Murray, R. R. (1984). "Longer Life for Metal Parts by Shot Peening." Machine Design **56**(6): 57-61.

Nicholas, T., Barber, J. P. and Bertke, R. S. (1980). "Impact Damage on Titanium Leading Edges from Small Hard Objects." Experimental Mechanics **20**: 357-364.

Niku-Lari, A. (1987). "Overview on the Shot Peening Process." Advances in Surface Treatments: Technology Applications Effects: 155-170.

Oakley, S. Y. and Nowell, D. (2007). "Prediction of the Combined High- and Low-cycle Fatigue Performance of Gas Turbine Blades after Foreign Object Damage." International Journal of Fatigue **29**: 69-80.

Orbison, J. G., Peterec, R. H., Carhart, J. A. and Rich, T. P. (1989). Development of a Fatigue Crack Initiation Test Specimen. 4th International Ansys Conference Exhibition.

Paik, J. K., Lee, J. M. and Lee, D. H. (2003). "Ultimate Strength of Dented Steel Plates under Axial Compressive Loads." International Journal of Mechanical Sciences **45**(3): 433-448.

Park, W., Huh, S. and Park, S. (2006). "A Study on the Fatigue Characteristics of Al6061-T651 by Shot Peening Velocity." Key Engineering Materials **11**(326-328): 1093-1096.

Peters, J. O., Boyce, B. L., Chen, X., McNaney, J., Hutchinson, W. and Ritchie, R. O. (2002). "On the Application of the Kitagawa-Takahashi Diagram to Foreign-Object Damage and High-Cycle Fatigue." Engineering Fracture Mechanics **69**(13): 1425-1446.

Ruschau, J. J., Nicholas, T. and Thompson, S. R. (2001). "Influence of Foreign Object Damage (FOD) on the Fatigue Life of Simulated Ti-6Al-4 V Airfoils." International Journal of Impact Engineering **25**(3): 233-250.

Schiffner, K. and Droste gen. Helling, C. (1999). "Simulation of Residual Stresses by Shot Peening." Computers and Structures **72**(1-3): 329-40.

Shen, S. and Atluri, S. N. (2006). "An Analytical Model for Shot-Peening Induced Residual Stresses." CMC **4**(2): 75-85.

Slavik, D. C., McClain, R. D. and Lewis, K. (2000). "Stress Intensity Predictions with Ansys for Use in Aircraft Engine Component Life Prediction." ASTM Special Technical Publication **31**: 371-390.

Soininen, H. (1998). A Propeller-Ice Contact Model. Maritime and Mechanical Engineering. Espoo, Finland, Helsinki University of Technology: 1-116.

Steif, P. S., Mckenna, V. T., Jones, W., Smith, R., Harding, T. and Gilchrist, A. (2001). Accounting for Small Particle Impact in the Design of Gamma-TiAl Turbine Blades. Proceedings of the International Symposium on Structural Intermetallics 2001.

Studman, C. J. and Field, J. E. (1977). "The Indentation of Hard Metals: The Role of Residual Stresses." Journal of Materials Science **12**(2): 215-218.

Suresh, S. (1994). Fatigue of Materials, University Press, Cambridge.

Tabor, D. (1948). A Simple Theory of Static and Dynamic Hardness. Proceedings of the Royal Society of Physics.

Teodosio, J. R., Cindra, F. M. and Pedrosa, P. D. (2003). Relaxation of Residual Stresses during Fatigue Cycles in Steels. Thermec 2003.

Torres, M. A. S. and Voorwald, H. J. C. (2002). "An Evaluation of Shot Peening, Residual Stress and Stress Relaxation on the Fatigue Life of AISI 4340 Steel." International Journal of Fatigue **24**: 877-886.

Tsai, S. W. (1974). Behaviour of Cantilever Beam Under Impact by a Soft Projectile, Air Force Materials Laboratory, Wright Patterson Air Force Base, Ohio.

Tyler, D. (1987). "Shot Peening adds Strength to Component Design." Engineering Materials and Design **31**(2): 29-30.

Veitch, B. and Lukia, K. (1993). The Propeller- Ice Impact Process. The 12th International Conference on Port and Ocean Engineering under Artic Conditions.

Veitch, B. (1994). Results of Ice Cutting Experiments with Cutting Tools Representing Propeller Blade Sections. IAHR Ice Symposium 1994, Norway.

Weaver, A. T. (1990). Jet Engine Ingestion Threats. 43rd International Air Safety Seminar Proceedings: Flight Safety Foundation, Rome.

Wick, A., Schulze, V. and Vohringer, O. (2000). "Effects of Warm Peening on Fatigue Life and Relaxation Behaviour of Residual Stresses in AISI 4140 Steel." Materials Science and Engineering A **293**(1-2): 191-197.

Wong, T. and Cornell, R. W. (1978). Test Methodology Correlation for Foreign Object Damage, Air Force Materials Laboratory, Wright Patterson Air Force Base, Ohio.

Wu, C. Y., Li, L. Y. and Thornton, C. (2003). "Rebound Behaviour of Spheres for Plastic Impacts." International Journal of Impact Engineering **28**: 929-946.

Wu, C. Y., Li, L. Y. and Thornton, C. (2005). "Energy Dissipation during Normal Impact of Elastic and Elastic-plastic Spheres." International Journal of Impact Engineering **32**: 593-604.

Yan, S. L. and Li, L. Y. (2003). "Finite Element Analysis of Cyclic Indentation of an Elastic-Perfectly Plastic Half-Space by a Rigid Sphere." Proceedings of the Institution of Mechanical Engineers - C Journal of Mechanical Engineering Science **217**(C5): 505-514.

Yu, J., Liaw, P. K. and Huang, M. (1999). "The Impact Fatigue Fracture of Metallic Materials." Journal of Mechanics **51**(4): 15-18.

APPENDICES

Appendix 1: Impact Rig Manufacturing Drawings

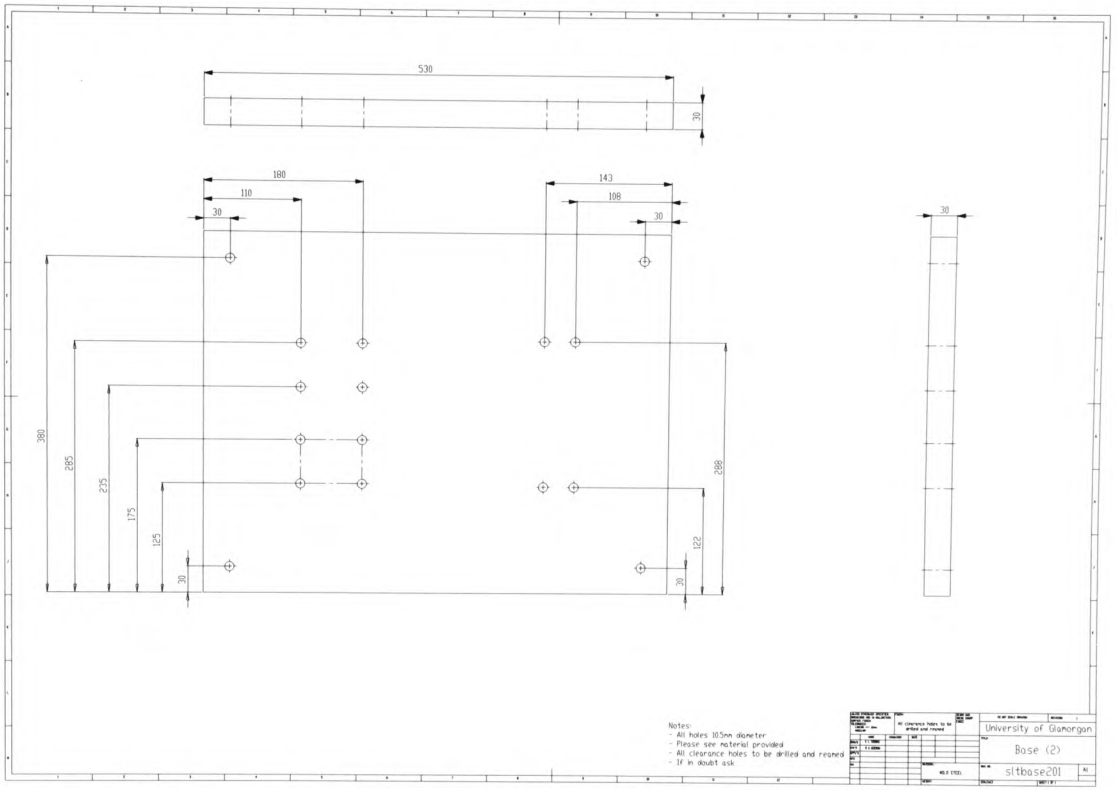

Figure A1.1: Manufacturing drawing of impact rig base plate

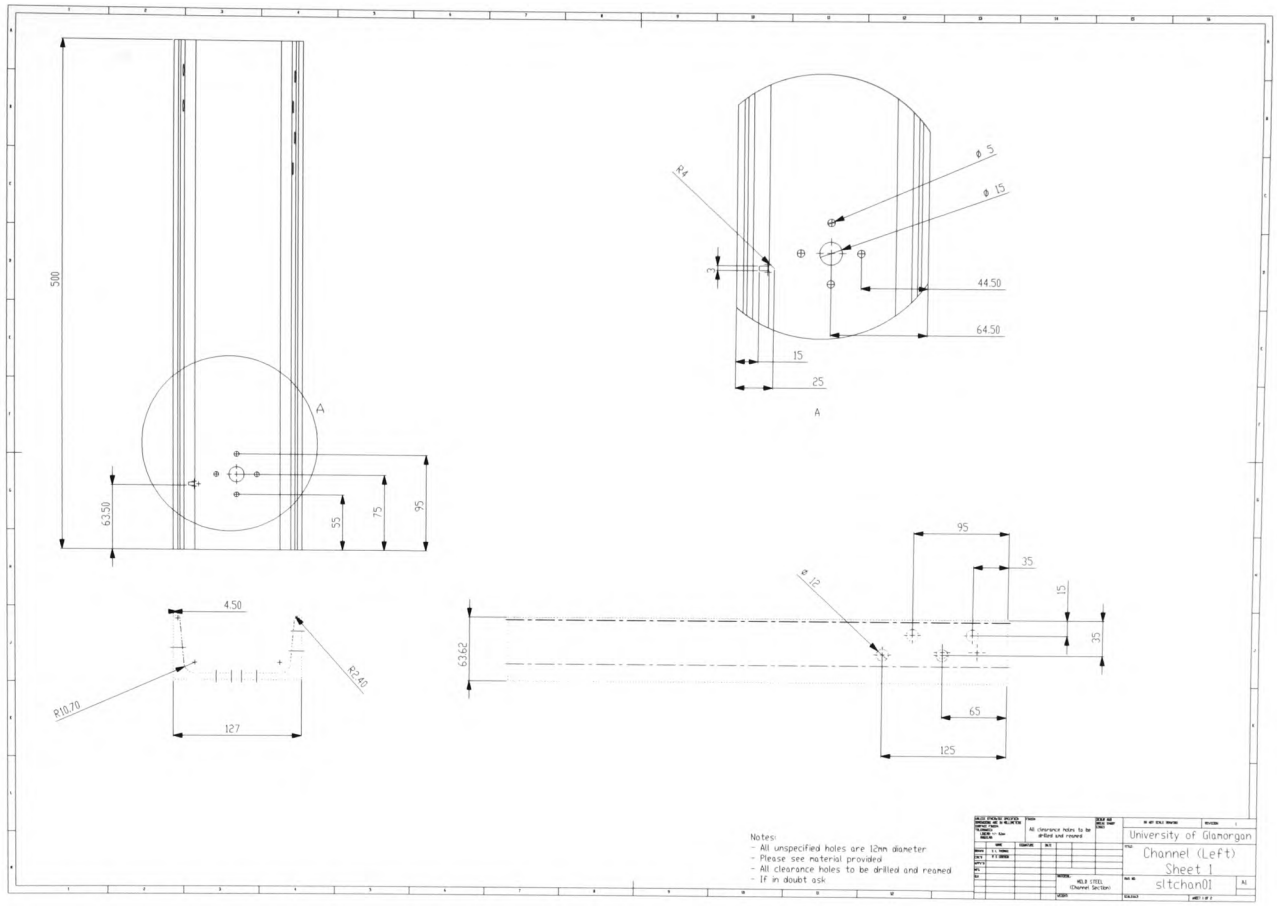

Figure A1.2: Manufacturing drawing of impact rig left hand strut (sheet 1)

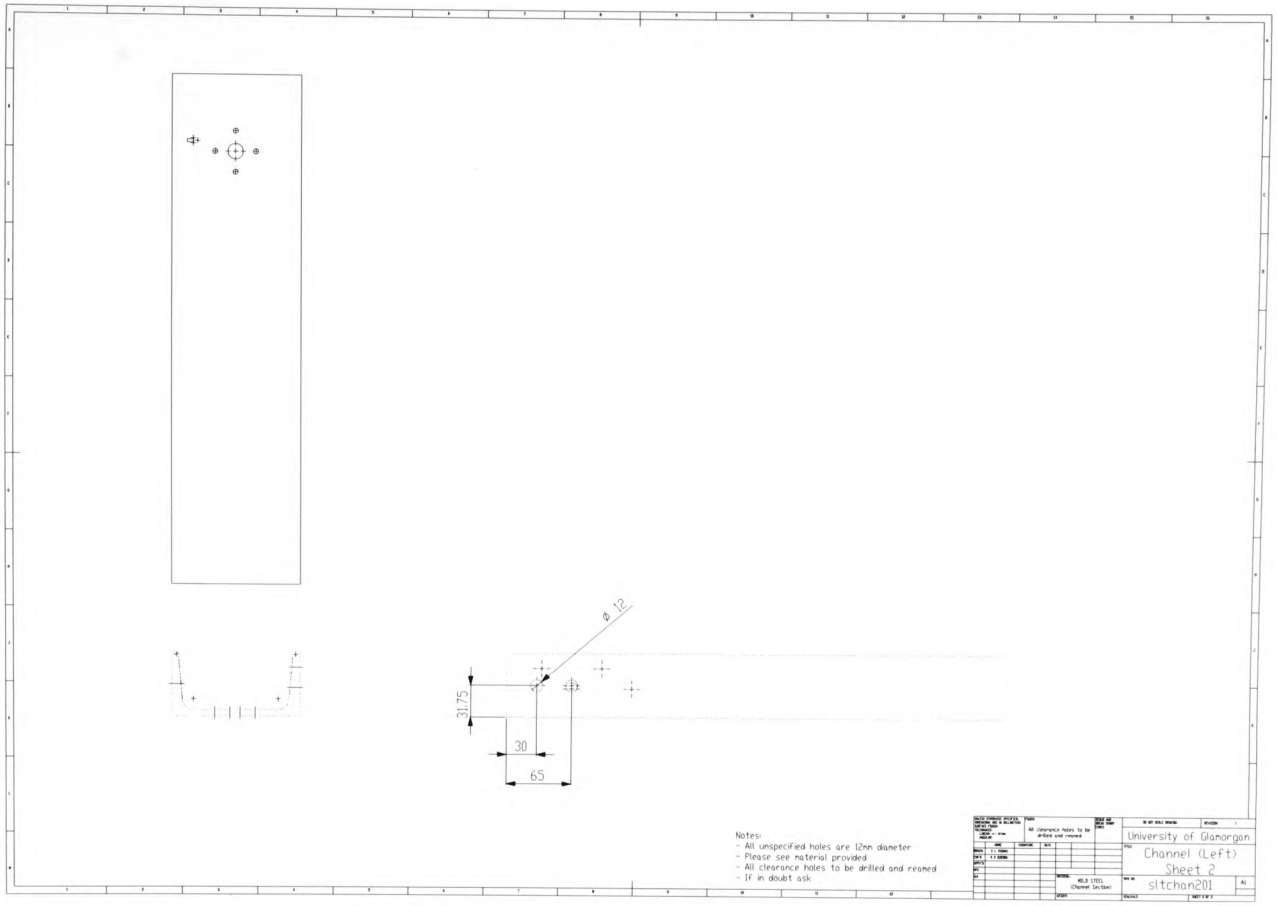

Figure A1.3: Manufacturing drawing of impact rig left hand strut (sheet 2)

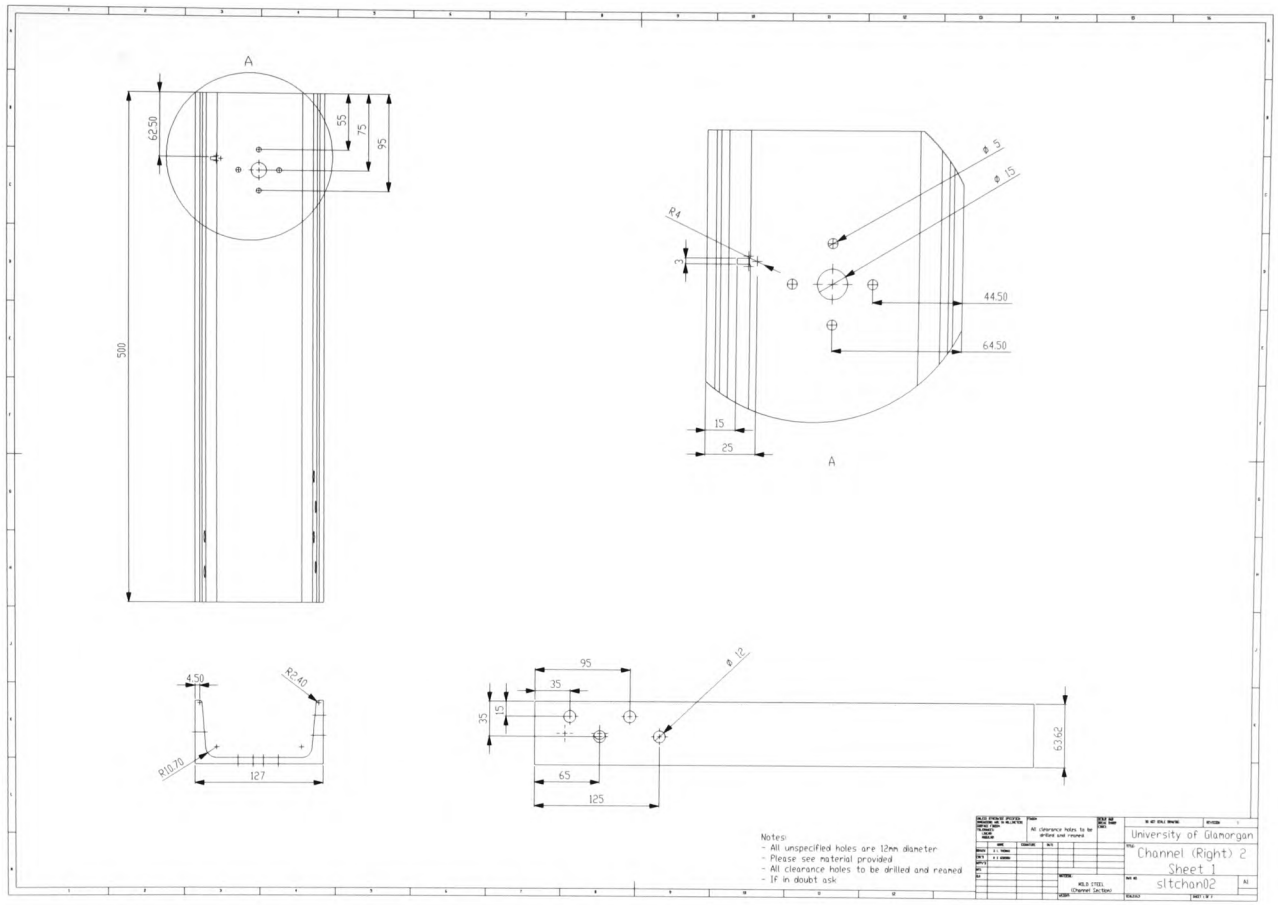

Figure A1.4: Manufacturing drawing of impact rig right hand strut (sheet 1)

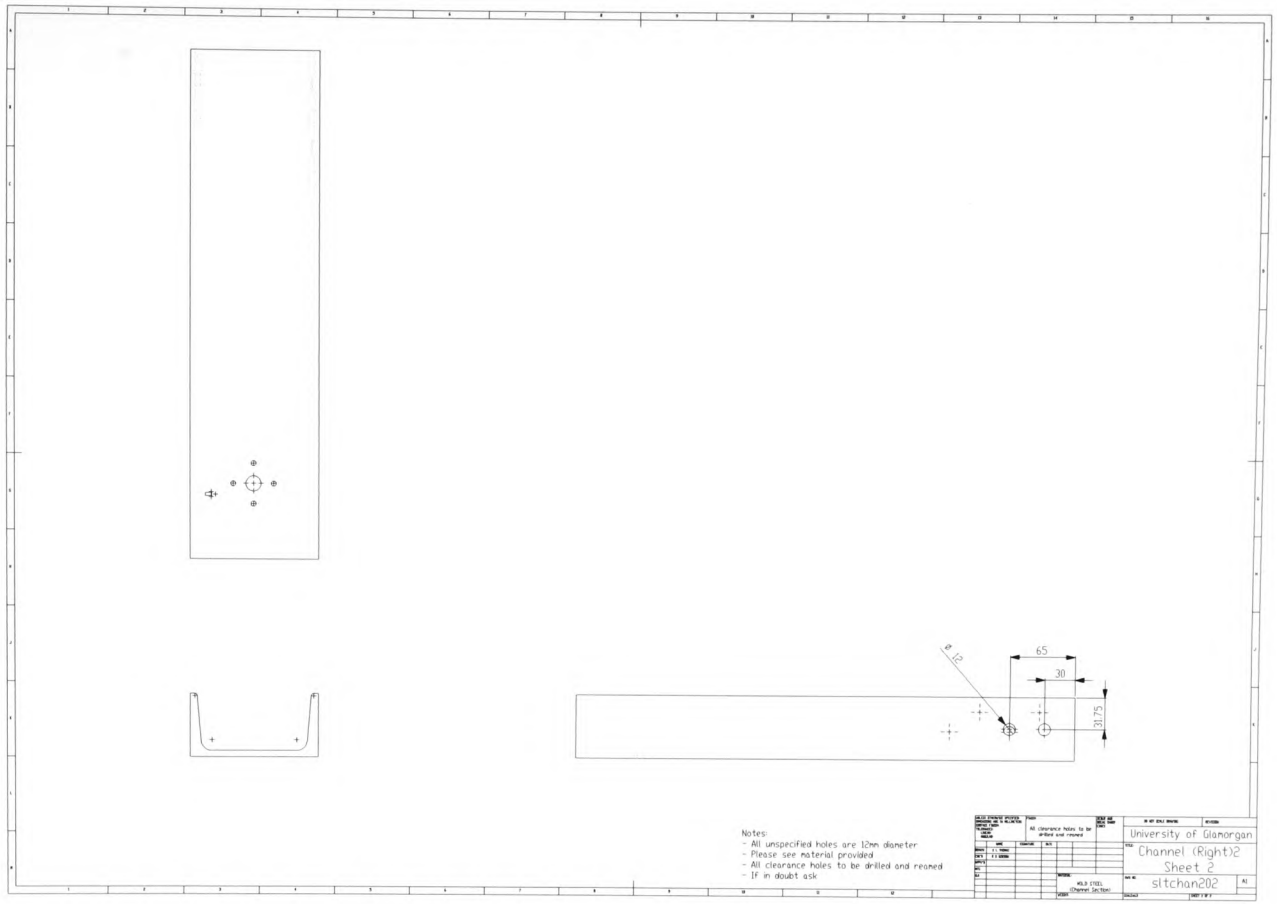

Figure A1.5: Manufacturing drawing of impact rig right hand strut (sheet 2)

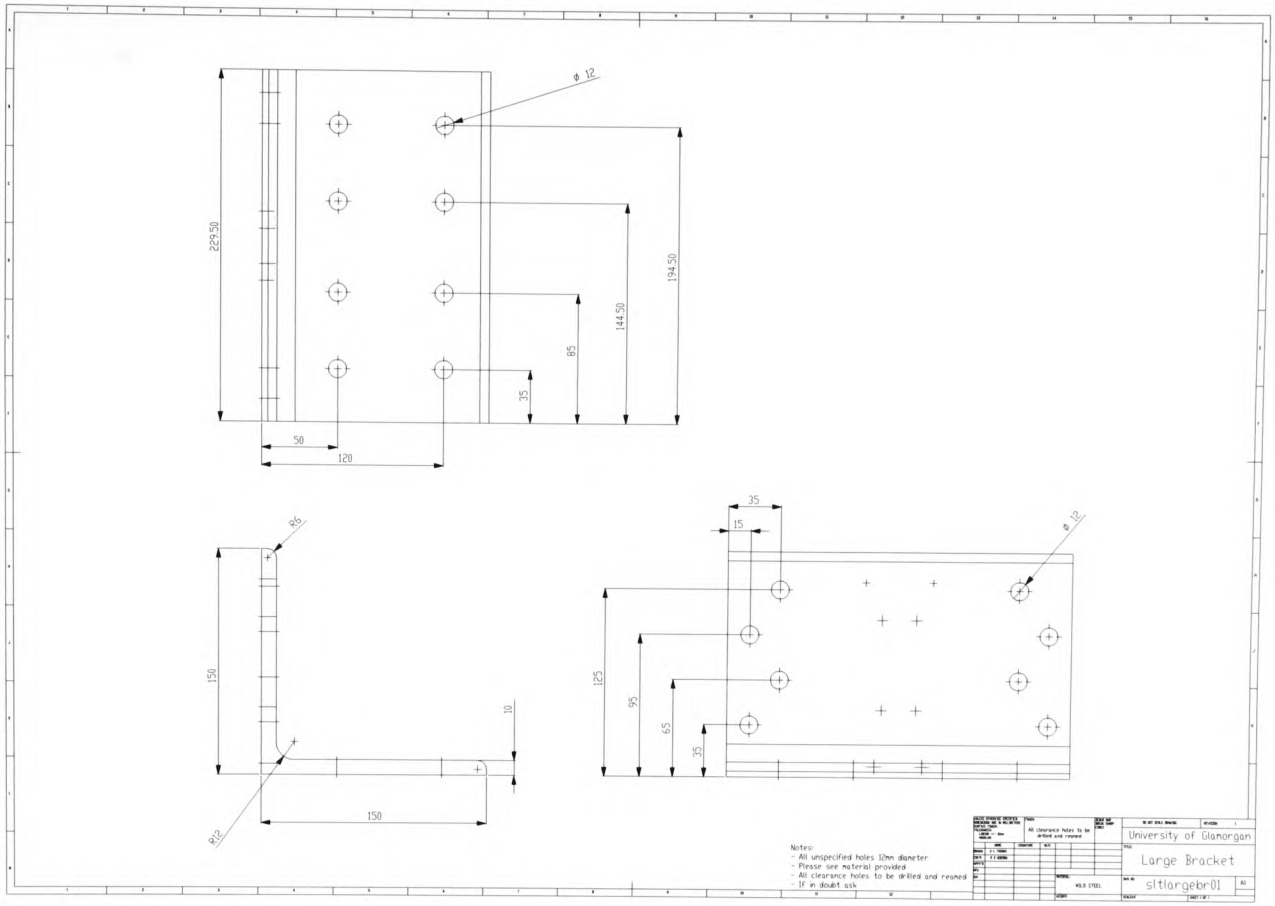

Figure A1.6: Manufacturing drawing of impact rig specimen back plate

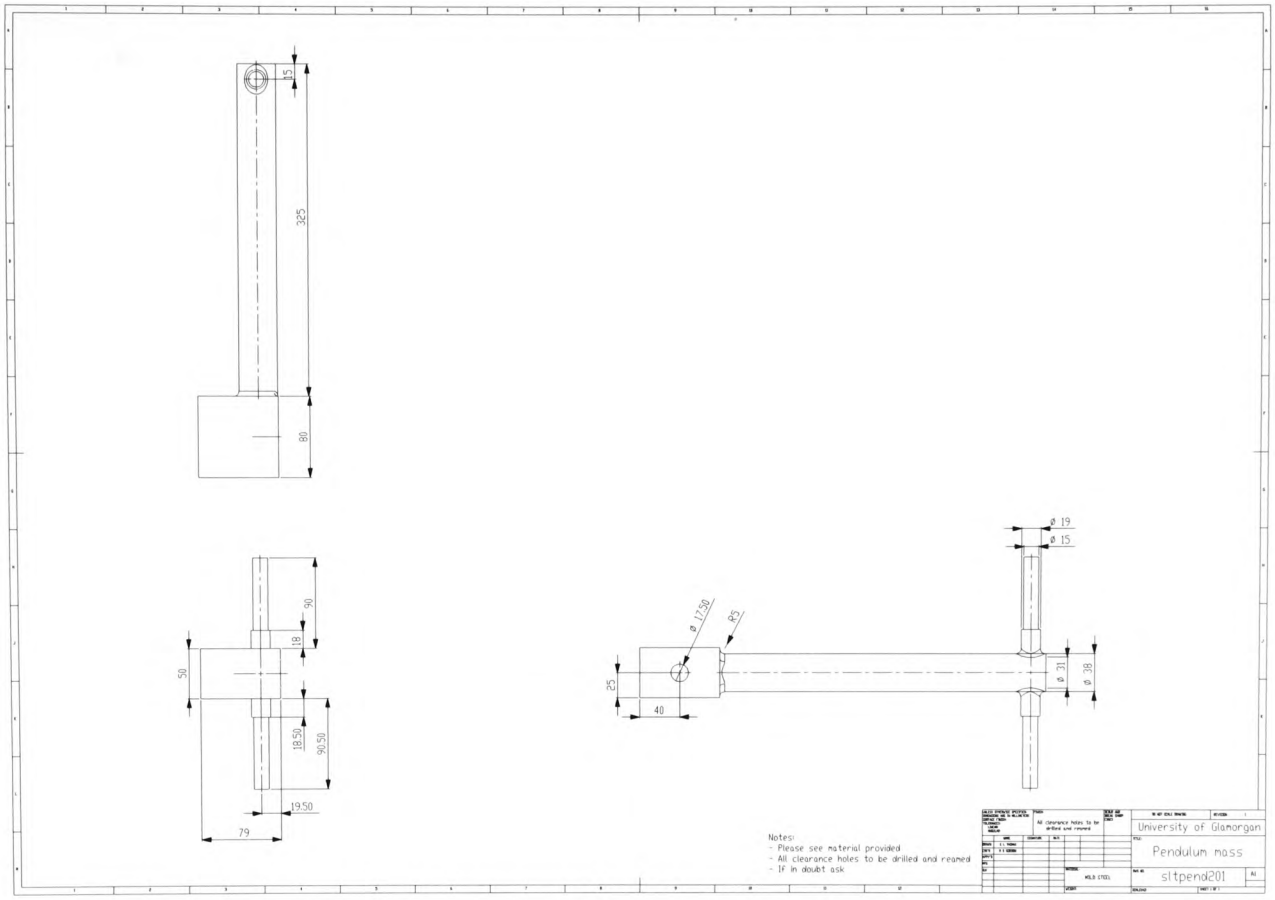

Figure A1.7: Manufacturing drawing of impact rig impactor arm

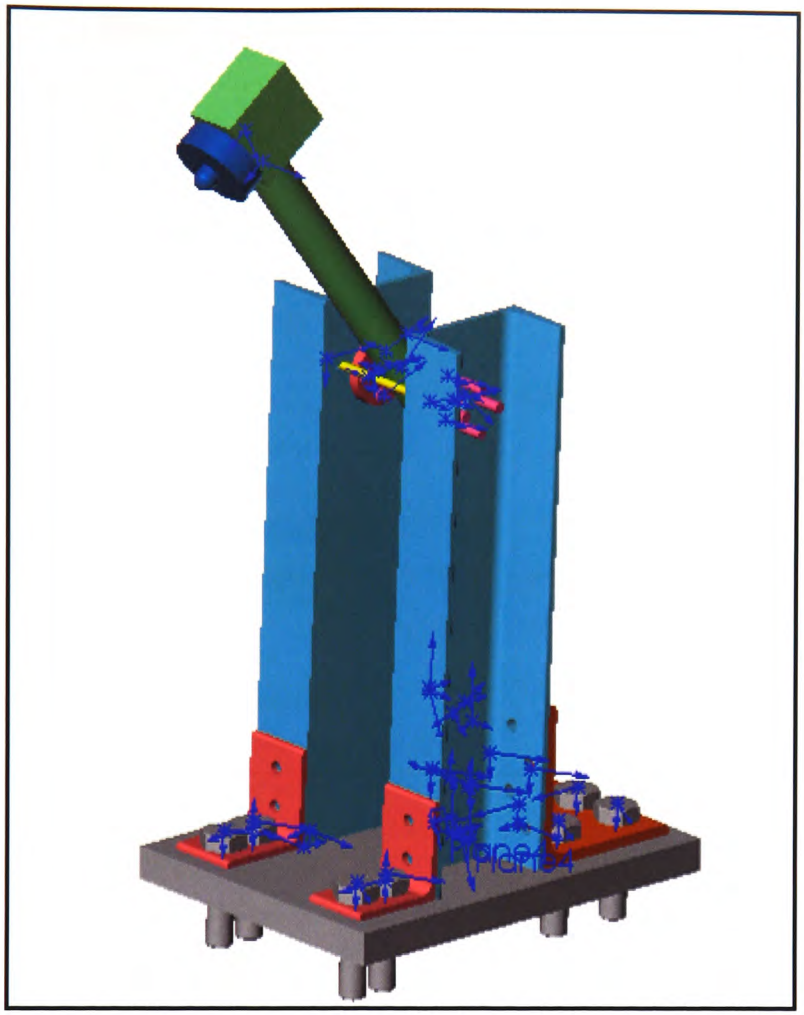

Figure A1.8: Assembly drawing of impact rig

Appendix 2: Error Analysis

Parameter Measured	Equipment	Calibration Date	Error
Depth of Impact Crater	Linear variable displacement transducer (Mitutoyo Absolute ID-F125E)	November 2004 (Calibrated by candidate using gauge blocks)	± 0.01mm
Width of Impact Crater	Microscope (Metallux 2)	N/A	± 0.01mm
Material properties (tensile tests)	Tensometer (Hounsfield H20K-W Tensometer)	17th September 2003	0.54%
Entry Velocity of Impact, Exit Velocity of Impact, Entry Impact Energy, Exit Impact Energy	Potentiometer (Penny and Giles IAPS 762)	November 2004 (Calibrated by candidate as mentioned in Section 4.2.2.)	0%
Impact Contact Time	Accelerometer (Bruel and Kjaer type 4344)	November 2004	5%
Cycles to failure	Fatigue testing (Instron FastTrack 8502)	25th June 2003	0.41%
Specimen dimensions	Digital callipers (Mitutoyo Absolute Digimatic CD-6"CP 500-191U)	September 2004 (Calibrated by candidate using gauge blocks)	± 0.01mm
Surface finish	Surface texture measurer (Talysurf 5-20 Taylor-Hobson)	September 2004 (Calibrated by candidate using calibration blocks)	± 0.001μm
Specimen hardness	Rockwell hardness tester (Wilson)	16th September 2003	± 0.1 Rockwell C
Height of Impact	Digital Height Gauge	October 2004 (Calibrated by candidate using gauge blocks)	± 0.01mm
Angle of Impact	Protractor	N/A	30 minutes (≡ 0.5 degrees)

Table A2.1: Error analysis of parameters measured

Please note that all calibration dates were recorded at the start of the current study and were renewed on an annual basis.